Heriot-Watt University

Doctoral Thesis

Transient natural convection induced by the absorption of concentrated solar radiation in high temperature molten salts

Author:
Ityona Amber

Supervisor:
Dr. Tadhg Sean O'Donovan

A thesis submitted in fulfilment of the requirements for the degree of Doctor of Philosophy

in the

Department of Mechanical Engineering
School of Engineering and Physical Sciences

February 2016

Declaration of Authorship

I, Ityona Amber, declare that this thesis titled, 'Transient natural convection induced by the absorption of concentrated solar radiation in high temperature molten salts' and the work presented in it are my own. I confirm that:

- This work was done wholly or mainly while in candidature for a research degree at this University.
- Where any part of this thesis has previously been submitted for a degree or any other qualification at this University or any other institution, this has been clearly stated.
- Where I have consulted the published work of others, this is always clearly attributed.
- Where I have quoted from the work of others, the source is always given. With the exception of such quotations, this thesis is entirely my own work.
- I have acknowledged all main sources of help.
- Where the thesis is based on work done by myself jointly with others, I have made clear exactly what was done by others and what I have contributed myself.

Signed: 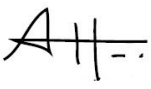

Date: 20-02-2016

ACADEMIC REGISTRY
Research Thesis Submission

Name*:*	Ityona Amber		
School/PGI:	Engineering and Physical Sciences (EPS)		
Version: *(i.e. First, Resubmission, Final)*	Final	Degree Sought (Award **and** Subject area)	Ph.D. Mechanical Engineering

Declaration

In accordance with the appropriate regulations I hereby submit my thesis and I declare that:

1) the thesis embodies the results of my own work and has been composed by myself
2) where appropriate, I have made acknowledgement of the work of others and have made reference to work carried out in collaboration with other persons
3) the thesis is the correct version of the thesis for submission and is the same version as any electronic versions submitted*.
4) my thesis for the award referred to, deposited in the Heriot-Watt University Library, should be made available for loan or photocopying and be available via the Institutional Repository, subject to such conditions as the Librarian may require
5) I understand that as a student of the University I am required to abide by the Regulations of the University and to conform to its discipline.

* *Please note that it is the responsibility of the candidate to ensure that the correct version of the thesis is submitted.*

Signature of Candidate*:*		Date:	20-02-2016

Submission

Submitted By *(name in capitals):*	
Signature of Individual Submitting:	
Date Submitted:	

For Completion in the Student Service Centre (SSC)

Received in the SSC by *(name in capitals):*			
Method of Submission *(Handed in to SSC; posted through internal/external mail):*			
*E-thesis Submitted (**mandatory for final theses)***			
Signature:		Date:	

Please note this form should bound into the submitted thesis.

Updated February 2008, November 2008, February 2009, January 2011

Abstract

Solar-thermal energy systems that involve the deposition of radiation in absorbing high temperature molten salts to harness the entire solar spectrum and achieve high efficiencies and low Levelised Cost Of Energy (LCOE) are of considerable interest for power generation. From a design stand point, to achieve a competitive solar power generation devices, it is imperative to have an accurate knowledge of the inherent physical processes of such a fluid system. Thus under high temperature conditions, detailed understanding of the heat transfer and fluid flow characteristics in an irradiated fluid is considered.

The work investigates the spectral dependent heat transfer and fluid dynamics in a thermal storage concept which uniquely combines a volumetric receiver and a single tank thermal store. The Thermal Energy Storage (TES) is protypical of a small scale concept concentrated solar plant. Advances in computing power, has seen Computational Fluid Dynamics(CFD) consolidated as a powerful tool employed by researchers and engineers to simulate real world behaviour and complex phenomena to a certain degree of accuracy with low effort in time, personnel and resources. This thesis is focused on the development of a realistic numerical model capable of predicting the local volumetric absorption of solar radiation in a fluid layer which provides an improved understanding of the hydrodynamic and thermal conditions in an enclosed fluid layer. Computational Fluid Dynamics is used to simulate the transient heat transfer and fluid flow determined by a combined influence of volumetric absorption and natural convection in a high temperature fluid filled enclosure. The enclosure is studied for the specific case in which a high temperature salt is first heated by direct volumetric absorption of the incident solar radiation and secondly by natural convection from a absorber plate located at the bottom of the enclosure whose sole purpose is to absorb all non-absorbed radiation reaching the lower surface. The current models considers the depth dependence absorption of solar radiation based on (i) a solar weighted absorption coefficient (assumed constant over all wavelengths) and (ii) spectral absorption coefficient characterised by wavelength band based on a standard solar spectrum reference.

A commercially available CFD Package based on Finite Element Method (FEM), COMSOL Multiphysics is used to discretise and solve the Navier Stokes and energy equation under transients heating conditions for a non Boussinesq condition by accounting for the temperature variable properties of molten salts. A time-dependent and Backward Differentiation Formula (BDF) solver using implicit time-stepping methods is combined with refined mesh to solve the non-linear PDE. Validity of the numerical tool has been conducted, by comparing results from published results found in literature with corresponding numerical results. The mesh element optimum sizes and time steps used conform to those obtained in validation models. Simulations have been conducted for

a daily charging period of three hours as used in conjunction with a solar system. The effects of bottom absorber plate, flux Rayleigh number, aspect ratio, variable Air Mass and inclination angle have also been investigated. Numerical results are presented in terms of surface plots, temperature contours, and velocity contours and streamlines which show the thermal field distribution and flow structures, for volumetric absorption of thermal radiation coupled with natural convection. Performance criteria are based on quantification of the level of thermal stratification using the MIX number, the dimensionless exergy and capture efficiency. Three dimensionality effects were studied by considering three dimensional simulation for the same problem.

The results show that the present method and models are capable of capturing the main features of the flow and the overall performance of these turbulence models in terms of predicting time-averaged quantities. Results obtained indicate a nonlinear temperature profile consisting of two distinct layers: a surface layer and a bottom layer. The numerical results reveal natural convection in the cavity follows an initial stage, a transitional stage and a quasi-steady stage. Results indicate that volumetric absorption of solar radiation, when coupled to natural convection has a direct influence on the thermal field through the disparities in absorption and emission phenomena. The isotherms and streamlines show that the natural convective heat transfer and flow are quite different from those obtained in differentially heat enclosures. Thus the heat transfer mechanism destroys a symmetry of the system that relates clockwise and counter clockwise flows. Temperature and flow field are found to be greatly influenced by the aspect ratio (H/D) of the store and the flux Rayleigh number. It is found that the predicted heat transfer from the lower surface in the cavity is increased when the simulation is extended from two to three dimensional. Results obtained indicated that increasing the aspect ratio, Air Mass and inclination angle all result in increasing levels of thermal stratification. Natural convection from the lower absorber surface is found to increase with increasing flux Rayleigh number.

...

Acknowledgements

I would like to express my special appreciation and thanks to my advisor Dr. Tadhg S. O Donovan, for the continuous support of my Ph.D. study and related research, for his patience, motivation, and immense knowledge. I would like to thank you for encouraging my research and for allowing me to grow as a research scientist. His guidance helped me in all the time of research and writing of this thesis. Your advice on both research as well as on my career have been priceless. Also I thank my friends in Heriot-Watt University. Very special thanks to the Petroleum Technology Development Fund (PTDF) for giving me the opportunity to carry out my doctoral research and for their financial support. It would have been impossible for me to even start my study had they not given me a scholarship. A special thanks to my family, your prayer for me was what sustained me thus far. I would also like to thank all of my friends who supported me in writing, and incented me to strive towards my goal. At the end I would like express appreciation to my beloved wife Ichiko and son Azael who spent sleepless nights with me and were always my support in the moments when there was no one to answer my queries. Words cannot express how grateful I am for all of the sacrifices that you've made on my behalf. She has been a constant source of strength and inspiration. There were times during the past four years when everything seemed hopeless and I didn't have any hope. I can honestly say that it was only her determination and constant encouragement (and sometimes a kick on my backside when I needed one that ultimately made it possible for me to see this project through to the end. Finally I thank my God, my good Father, for letting me through all the difficulties. I have experienced Your guidance day by day. You are the one who let me finish my degree. I will keep on trusting You for my future. Thank you, Lord. ...

Contents

List of Figures

List of Tables

Abbreviations

AM	**A**ir **M**ass
BDF	**B**ackward**D**ifferntial **F**ormaula
CFD	**C**omputational **F**luid **D**ynamics
CSP	**C**oncentrated **S**olar **P**ower
DNI	**D**irect **N**ormal **I**ntensity
DNS	**D**irect **N**umerical **S**imulation
FEM	**F**inite **E**lement **M**ethod
FV	**F**inite **V**olume **M**ethod
IR	**I**nfra **R**ed
LCOE	**L**evelised **C**ost **O**f **E**nergy
SMARTS	**S**imple **M**odel**A**tmospheric **R**adiative **T**ransfer
TES	**T**hermal **E**nergy **S**torage
UKATC	**U**nited **K**ingdom **A**stronomical **T**technological **C**enter
UV	**U**ltra **V**iolet

Physical Constants

Speed of Light	c	=	$2.997\ 924\ 58 \times 10^8\ \mathrm{ms}^{-\mathrm{S}}$ (exact)
Math constant	π	=	3.142
Acceleration due to gravity	g	=	$9.81\ \mathrm{ms}^{-2}$

Symbols

C	Concentration ratio	
C_p	Heat capacity	$\mathrm{J(kgK)^{-1}}$
D	Diameter	m
F	Body force	$\mathrm{Nm^{-3}}$
g	Acceleration due to gravity	$\mathrm{ms^{-2}}$
H	Height	m
h	Mesh Element size	m
I	Solar irradiation	$\mathrm{Wm^{-2}}$
k	Thermal conductivity	$\mathrm{W(mK)^{-1}}$
κ	Thermal diffusivity	$\mathrm{m^2s^{-1}}$
Nu	Nusselt number	
P	Pressure	Pa
Pr	Prandtl number=$\mu \mathrm{C}_p/\mathrm{k}$	1
Q	Volumetric heat generation	$\mathrm{Wm^{-3}}$
$\dot{Q}$	Volumetric flow rate	$\mathrm{m^3s^{-1}}$
q	Heat flux	$\mathrm{Wm^{-2}}$
Ra	Rayleigh number	
T	Temperature	K
t	Time	s
u	x velocity component	$\mathrm{ms^{-1}}$
v	y velocity component	$\mathrm{ms^{-1}}$
w	z velocity component	$\mathrm{ms^{-1}}$
α	Absorption coefficient	$\mathrm{m^{-1}}$
β	Intereflection factor	

δ	Attenuation coefficient	
ϵ	Exergy	
ζ	Non dimensionless parameter	
ξ	flow availability	
Γ	Dimensionless height	
γ	Optical depth	
σ	Scattering coefficient	
τ	Dimensionless time	
λ	Wavelength	m
μ	Dynamic viscosity	Nsm^{-2}
ν	Kinematic viscosity	$\mathrm{m}^2\mathrm{s}^{-1}$
ρ	Density	kgm^{-3}
υ	Directional cosine ($\cos\theta$)	
ϕ	inclination angle	
θ	Azimuth angle	
ω	angular frequency	rads^{-1}
η	Efficiency	%

Dedicated to Elijah and Lucy Amber of blessed memory ...

Adoo, Ngodoo, Ngunan, Washima, and Se-ember
Ichiko and Azael aka Digidigi

Chapter 1

Introduction

Electricity generation from solar energy by thermomechanical conversion is currently limited in worldwide implementation [1]. Concentrated Solar Power systems that integrate thermal energy storage systems are renewable energy technologies that are likely to contribute to the world's energy mix and primary energy consumption[2, 3]. Although Concentrated Solar Power plants with storage have been demonstrated to extend operational time beyond sunset, increase dispatchabily, reliability and efficiency is required to translate into reduced LCOE; the cost of produced electricity struggles to attaining grid parity. The high cost of produced electricity from these systems is attributed to firstly relatively poor performance in to the low solar-to-thermal efficiency (i.e a combination of the capture, conversion and field efficiencies) [4] and secondly the high cost of thermal energy storage. When interfaced with Concentrated Solar Power storage constitutes a substantial fraction of overall cost the total plant [5, 6]. For example in a 100 MW parabolic trough with 13.4 hours of thermal energy storage, thermal storage accounts for about 9-20% of the total plant cost [6], while in a the Central Receiver System (CRS) plant thermal storage accounts for between 9 -12%. The current industry driver is to lower the cost of thermal energy storage and subsequently to improve performance in terms of usable temperatures and efficiency [7]. To this end, Thermal Energy Storage (TES) for integration with CSP systems are either been proposed or are currently under development.

Recently, development of solar thermal conversion and storage systems, based on the principle of direct absorption of solar radiation in a working fluid to harness the entire spectrum, has been of particular interest for possible use in power generation. As this method of energy transfer entails the direct deposition of light inside of a working fluid in contrast to its absorption on the outside of a tubular receiver several advantages are derived that translate into a lower capital costs, higher operational reliability and

increased system efficiency [8]. Fig ?? compares the energy conversion steps of in a conventional concentrated Solar Power plant and a solar power plant which uses a direct (volumetric) absorber in a thermal resistance network. In Fig ??a, concentrated solar radiation is intercepted on a surface receiver which is transferred to a working fluid by conduction through the walls of the receiver. The working fluid transports the heated fluid to the boiler and subsequently to the heat engine. In Fig ??b, the concentrated solar radiation is directly deposited in the working fluid in the receiver which directly heats the fluid and to a heat engine. From the figure it can be seen that the introduction of the direct absorption receiver results in a minimisation of the energy conversion steps. Thus, on the basis of the method of energy transfer, the use of volumetric absorption receiver compared with a conventional surface receiver offers several advantages over a conventional surface receiver, which include: a reduction in radiative and convective losses, avoidance of thermal stress, utilisation of high and non-uniform heat flux, higher operational temperatures and simple system designs. Direct absorption of solar radiation by heat transfer fluids has been used by central receiver systems successfully to exploit high operational and storage temperatures which have yielded higher system efficiencies. Taylor et al. [9] reported that approximately 10% improvement in efficiency added up to a 11% improvements in the Levelised Cost Of Energy (LCOE) and a possible 20% improvement in the overall LCOE, when combined with a volumetrically direct steam collection system. The direct absorption of solar radiation by heat transfer fluids in central receiver systems has enabled the exploitation of high operational and storage temperatures which have yielded higher system efficiencies. An integrated Direct Absorption Receiver (DAR) and thermal energy storage systems concept [10] which combines a unique features of volumetric receiver and a single tank storage system are being explored to raise storage temperatures, lower cost of electricity generation and improve efficiency.

1.1 Small Scale Concentrated Power: Direct Capture and Conversion of Solar Energy

There is substantial growth in demand for small-scale Concentrated Solar Power (<10MW) for process heat in a wide range of industrial applications and sectors [11]. However, in contrast to large CSP; small scale CSP are characterised by low efficiencies. At present, technical and economic decisions for the implementation of solar thermal energy storage are in favour of large scale solar power [11]. A break through in the competitiveness in small scale solar thermal electricity may occur if the solar to thermal conversion efficiency can be increased in small scale concentrated solar power plants which include a low cost thermal energy storage.

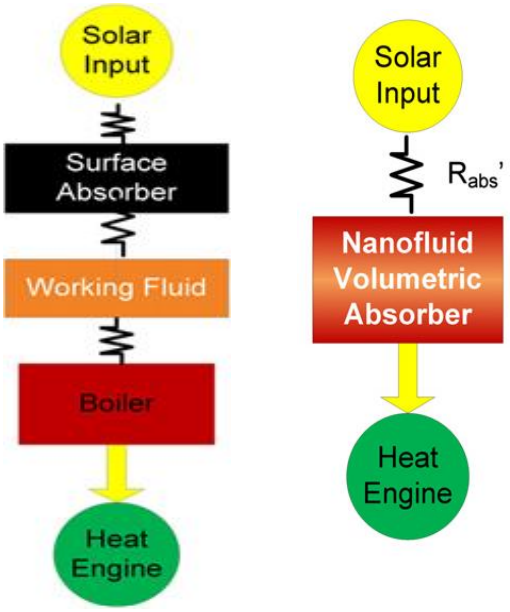

FIGURE 1.1: Thermal resistance network comparison of a conventional solar thermal plant and a volumetric receiver solar thermal plant [9].

A modular, small scale concentrated solar power plant concept that incorporates a novel fixed focus sensible heat thermal energy store has been proposed by the UK Astronomy Technology Centre (UKATC) and Heriot-Watt University [12]. The direct capture and conversion of solar thermal energy concept process flowchart is shown in Fig 1.2. By directly depositing concentrated solar radiation at concentration ratios of up to 1000, directly into a molten salt, permits higher operational and storage temperatures to be obtained.Thus the molten salt acts a) a highly efficient receiver and b) a thermal energy storage medium. The concentrated solar flux charges the storage medium in the tank volumetrically by absorption and subsequently a lower absorber plate develops a natural convective flow which mixes the salt and avoids local hot spots. The energy transfer in the Thermal Energy Store minimises the number of heat transfer interfaces, eliminates the need for pumps and limits thermal degradation of the receiver materials, yielding cost savings and improved efficiency. The thermal energy store would be directly coupled to a heat engine produce electricity [12]. The Direct Capture and Conversion of Solar Energy CSP targets mainly rural and off grid application to offer benefits such as: materials pre-packaged and assembled on site reducing labour requirements; adaptable to different terrains than large scale CSP projects; lower upfront investment and financing is a straight forward matter [12].

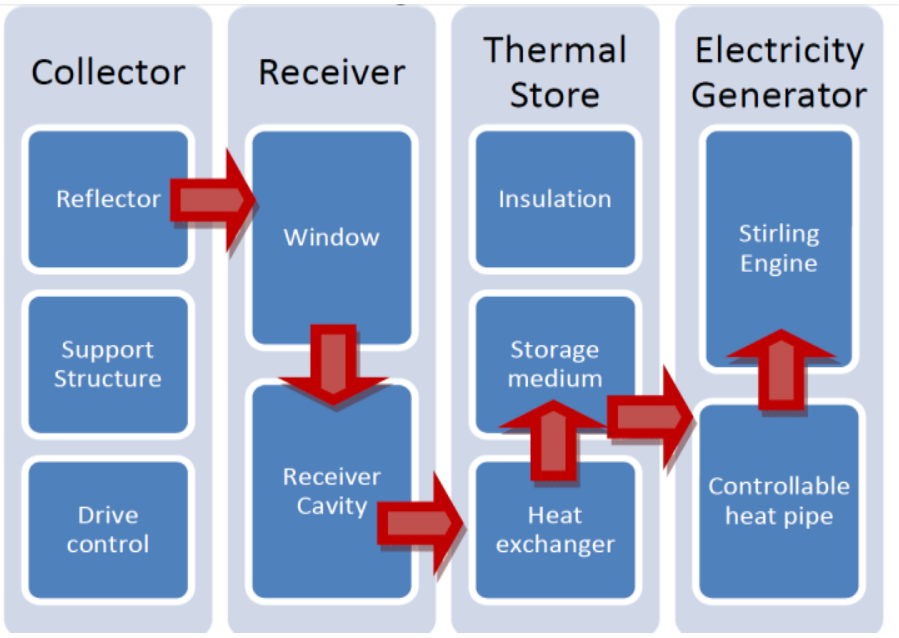

FIGURE 1.2: Flow chart demostrating the process of a Direct Capture and Conversion of Solar Energy concept flow chart.

1.2 Aim

For an effective design and optimisation of a fixed focus Direct Absorption Sensible Thermal Energy storage system, it is of fundamental significance to understand the heat transfer and fluid mechanics under time dependent conditions during charging, discharging and still phases and operational environment. With current advancements in computational power and numerical modelling, virtual prototyping using computational fluid dynamics has become a powerful tool for design and optimisation of storage tanks [13].

The overall aim of this thesis is to develop a numerical tool using Computational Fluid Dynamics (CFD) capable of accurately predicting the local absorption and volumetric heating in a cylindrical enclosure filled with high temperature molten salts. Such a model finds direct relevance for a small scale direct absorption sensible thermal energy system. The objectives in this thesis include:

- Develop numerical model to predict the heat and flow in a high temperature molten salt filled enclosure by accounting from the depth dependent absorption of solar

radiation based on (i) a single weighed values for the incident intensity and absorption coefficient and (ii) using a standard reference for the spectral distribution of solar radiation and wavelength dependence of the absorption coefficient over the wavelength range of interest to solar energy applications. standard reference for the solar radiation based on the SMARTS model and empirical values obtained from experiments.

- Conduct a comparative study between the solar weighted average model and a spectral dependent model.
- Account for the temperature dependence of the thermophysical properties of the molten salts.
- Investigate effect of the absorber plate thickness , flux Rayleigh number and aspect ratio on the temperature and flow field in the enclosure.
- Investigate of thermal performance of the of the enclosure in both models with reference to the studied parameters.
- Investigate the effect of variable Air Mass on the thermal and flow within the enclosure.
- The effect of inclination angle on the radiative induced natural convection is studied. The combined effect of the inclination and air mass on the heat transfer is studied.
- The effect of variable Air Mass in the inclined enclosure on the heat transfer is studied.

1.3 Scope

The present study is confined to the development and application of a novel numerical model for the prediction of spectral dependent temperature and fluid flow fields in a cylindrical enclosure in the charging phase. For the present geometry, understanding the heat transfer and fluid dynamics is of greatest importance to the design of a fixed focus integrated volumetric receiver and sensible heat thermal energy store filled with molten salts for a small scale (5kWe), Concentrated Solar Power (CSP) System. Isothermalisation of the store is required to maximise the storage capacity without damaging the storage medium, which can typically sustain temperatures up to 600^{o}C.

- Chapter 2 is devoted to the review of the direct capture, conversion and sensible thermal energy concept, receivers, molten salts, volumetric absorption, SMARTS model, previous studies in natural convection in enclosures where the driving force is primarily from the absorption of solar radiation,and mixing and stratification as well as capture efficiency.

- Chapter 3 presents the mathematical formulation, equations governing the physical processes and the methodology employed for the resolution of the Computational Fluid Dynamic (CFD) and heat transfer models with emphasis on two and three dimensional coordinates. Numerical discretisation schemes of the governing equations based on Finite Element Analysis (FEA) techniques, boundary conditions and the solution procedure for incompressible and transient flow problems is reviewed.

- Chapter 4 is dedicated to the verification and validation studies carried out to ascertain the software capability in handling the present problem and the accuracy of the solutions. Different test cases are submitted to a process of verification of the numerical solutions involving the techniques described in Chapter 3. The test cases considered include: Direct absorption of radiation in a flow receiver, thermal instability in horizontal fluid layers (Rayleigh Bernard problem), radiation induced natural convection in rectangular convection and unsteady natural convection subject to radiative heating.

- Chapter 5 presents the transient heat transfer and flow phenomena driven by radiation induced natural convection in an enclosure. In this model the depth dependent absorption of solar radiation is accounted for based on weighted values of the solar radiation and the absorption coefficient.

- Chapter 6 presents a spectral dependent radiation model based on a standard reference solar spectrum (SMARTS model). The study accounts for the spectral variation of solar radiation and air mass and its influence on the driving and flow mechanisms.

- Chapter 7 presents the effect of inclination angle on the spectral volumetric heating in an inclined enclosure of unit aspect ratio.

- Chapter 8 summarises the conclusions of the work presented in this thesis; the main achievements and limitations of the studies carried out are also presented. Guidelines for future research work in this applied area are also suggested.

Chapter 2

Literature Review

Today, four main types of concentrated solar power plants are found in operation: Parabolic troughs, linear Fresnel, central receivers (power tower) and parabolic dish; these vary considerably from each other in terms of technical, economic aspects, size, storage, maturity and operational temperature [14]. Irrespective of their individual design or configurations, CSP technologies comprise of four main sub-systems namely: concentrating system, solar receiver, storage, power block and in some cases a supplementary backup system [14, 15]. The highly reflecting mirrors are arranged in a number of different configurations to optimally intercept and focus sunlight on to an absorber which absorbs the energy, converts it to heat and is used to power a turbine or a heat engine [16, 17]. The entire system processes are linked together by radiation transfer or fluid transport. CSP-based plants are presently characterised by high upfront investment resulting in increased electricity generation costs, and as such generated electricity costs struggle to attain grid parity [18]. The rest of this chapter is outlined as follows: Section 2.1 presents a overview of the proposed system for Direct Capture and Conversion of solar energy ; Section 2.2 presents a review of the common receiver systems; section 2.3 presents thermal energy concepts in thermal energy; section 2.4 presents an overview of high temperature molten salts; section 2.5 presents the volumetric absorption in molten salts; section 2.6 presents radiation induced convection in enclosures and section 2.7 presents the energy and exergy analysis in Thermal Energy Storage (TES).

2.1 The Direct Capture and Conversion of Solar Energy

Fig 2.1 shows a schematic of the modular Direct Capture and Conversion concentrated solar power plant concept proposed by the UK Astronomy Technology Centre (UKATC)

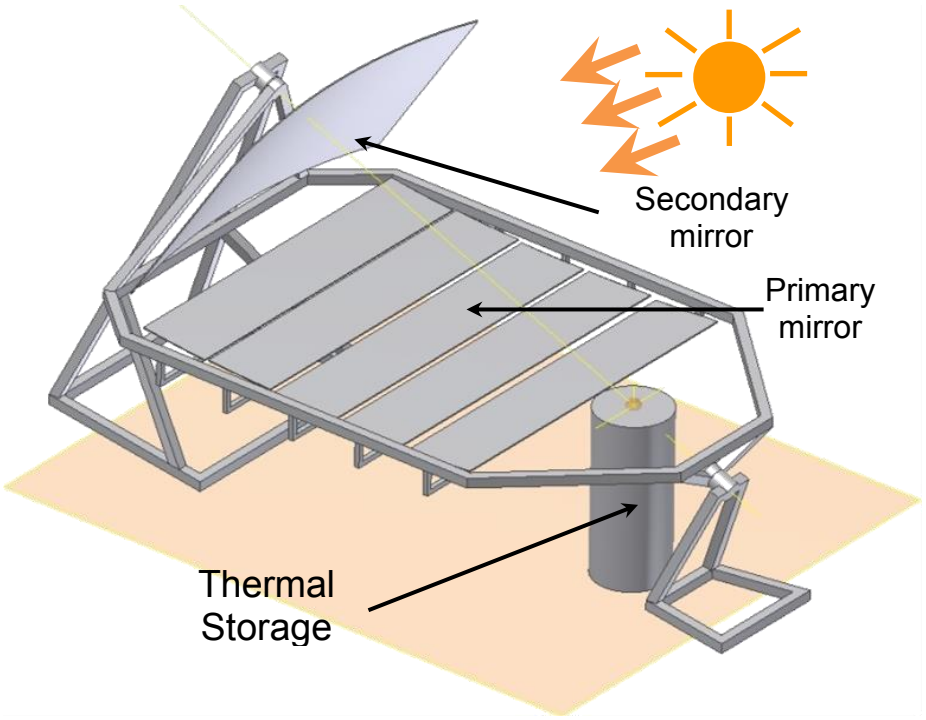

FIGURE 2.1: Schematic of a proposed "Direct Capture, Conversion and storage of Solar Energy" system [12].

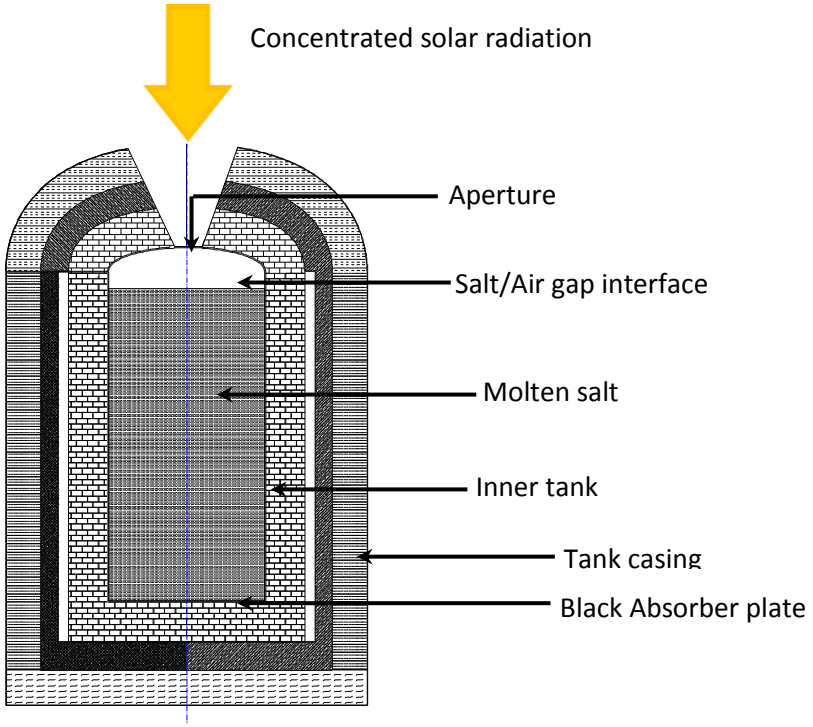

FIGURE 2.2: Schematic of a proposed Direct Absorption Sensible heat Thermal Energy Store (DASTES).

and Heriot-Watt University [12]. The system consists of a primary and secondary reflectors, solar receiver, storage system and power block. In this design concept concentrated solar radiation from highly reflecting mirrors is deposited directly into a volume of high temperature molten salt integrated receiver/sensible thermal store. The thermal energy store would be directly coupled to a heat engine to provides continuous regulated heat to produce electricity. Fig 2.2 shows a schematic of a fixed focus, Thermal Energy System (TES). The cylindrical store combines the unique features of a volumetric receiver and a single tank as an integrated receiver/thermal storage arrangement. The thermal store contains a high temperature salt (Hitec solar salt KNO_3-$NaNO_3$- 60/40% wt.) commonly used in operating and demonstration solar plants around the world. The molten salt storage medium is directly illuminated by the concentrated solar flux incident through a transparent top glass window and heats the molten salt by volumetric absorption. Therefore the molten salt contained in a highly insulated single tank acts as a highly (i) efficient receiver (ii) heat transfer fluid and (iii) a thermal storage medium. The Thermal Energy Storage (TES), accommodates an absorber plate at the bottom tank, whose sole purpose is to absorb all radiation transmitted to the lower surface, thereby subsequently heating the lower fluid and inducing natural convection to mix the fluid in the tank. Therefore, charging of the molten salt will have contributions from: 1) the direct volumetric absorption of incident concentrated solar radiation and 2) a heated bottom absorber plate resulting from the full absorption of residual transmitted radiation radiation. The fixed focus direct absorption integrated receiver/sensible heat thermal energy storage system could help fill a critical need in concentrated solar power.

2.2 Receivers

This section presents an overview of the different receivers used in CSP systems. Surface receivers (tubular and flat plate) are basically heat exchangers that intercept solar radiation on the surface of the receiver and convert into process heat [20]. Surface receivers are crucial design components that influence solar-thermal efficiency. In many CSP systems receivers are placed at the focal point of the collector which may be required to track during the day. As such they are required to withstand harsh operational (high temperatures, incident flux) and environment conditions (dust, rain, humidity, frost), while minimising heat losses. Surface absorbers are generally characterised by low capture efficiencies, high heat losses, thermal fatigue and degradation of receiver materials owing to the fact that the intercept radiation on the outer receiver wall which is then transferred to the working fluid flowing through the receiver. Fig 2.3 shows the temperature of a surface absorber intercepting incoming radiation normal its surface. It is apparent from Fig 2.3, the outer tube wall attain the highest temperatures while the

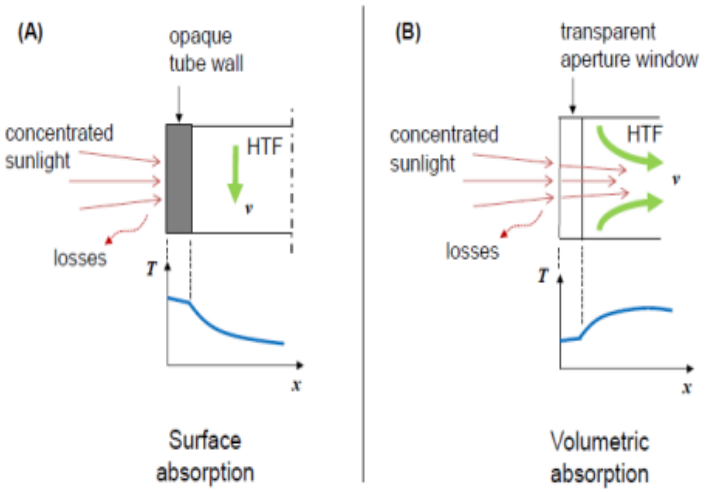

FIGURE 2.3: Flow of a Heat Transfer Fluid (HTF) and temperature profiles in solar receivers (a) surface absorber b) volumetric receiver [19].

inner fluid temperature is lowest. Thus efforts and investments are made to apply spectrally selective solar absorption coatings or rely on surface oxides to grow and reduce the tube reflectivity.

The selection and location of an absorbing plate becomes crucial in terms of thermal performance of the volumetric absorbing system [21]. Thus the location of solar absorbers in solar thermal systems is important for effective harnessing of solar radiation. Siddiqui and Yilbas [21, 22] studied the influence of absorber plate location on thermal performance in horizontal channels numerically. By varying the location of the absorber plate in a horizontal fluid filled water channel, Siddiqui and Yilbas [21], found that the plate location has a significant effect on the system performance. The performance attained the highest value for the absorber location at the mid height of the channel for a low concentration (C=1), while at a concentration, C=5, the performance parameter attained the highest value for the absorber plate location at the top of the channel. This is about 10% higher than those corresponding to other locations. An experimental study found that, by placing a novel material structure for harvesting solar energy developed at Massachusetts Institute of Technology (MIT) on the fluid surface [23], steam can be generated while maintaining low optical concentration and keeping the bulk of the working fluid at low temperature [23].

Volumetric receivers are technological alternatives to convectional surface receivers [24–27]. Volumetric receiver designs permit the bulk of a heat transfer fluid (molten salt) to run closer to its decomposition temperature, thereby realising much higher operational and stage temperatures [28, 29]. Fig 2.3b shows a volumetric receiver design where concentrated sunlight transfers heat to a volume. The sunlight penetrates the volumetric absorber region and is able to directly transfer heat to the medium downstream. Ideal volumetric receivers have a peak temperature located within the Heat Transfer Fluid (HTF) that is hotter than the receiver surface temperature thus reducing radiative losses which is a function of quadratic dependence of thermal radiation on the absorber temperature [24]. Physical systems have additional convective and conductive losses that can be minimised by increasing concentration, thereby reducing exposed surface area and insulating the receiver. Direct absorption of solar radiation in several centimetre thick molten salt water falls have been investigated. However, the cost of pumps, manifold and piping preheaters, and fluid variations as a function of varying solar flux, limits practicality of these receiver designs. Surface and volumetric receivers are both susceptible to reflection losses which can be minimised by applying high absorptivity coatings to receiver surfaces, tuned to be highly absorbing in the visible spectrum and having low emissivity in the infra-red spectrum. It can be seen that the volumetric receiver enables thermal systems with simple and compact designs with increase thermal performance and lower LCOE which is desirable in the thermal energy storage concept.

2.3 Sensible thermal energy storage systems

Solar thermal energy storage can be coupled with solar thermal energy plants as [33, 34] (i) sensible heat storage in oils, molten salts, concrete etc.,(ii) latent heat storage using phase change materials or (iii) thermochemical storage.

Sensible thermal energy storage is the most mature of the thermal technologies, which has been successfully proven from the years of operational experience gained in Andasol-1 and Terresol Germasolar power tower in Spain [30]. Molten salts are preferred as heat transfer fluids in sensible thermal energy storage systems as they generally offer low cost, higher operational temperatures and are more environmentally friendly in contrast to organic heat transfer oils used in parabolic trough systems. Their major limitation is however their relatively high melting temperature which necessitates the use of fossil fuels or air electric heating to maintain the salts above their melting temperatures and avoid serious damage to the equipment when solar power is unavailable at night or in poor weather conditions. Two primary designs are used for sensible heat thermal energy

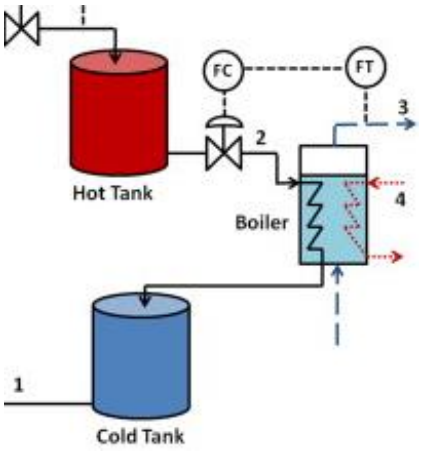

(a)

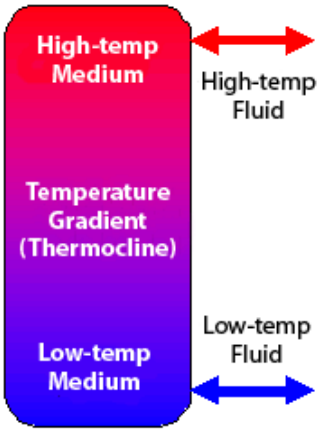

(b)

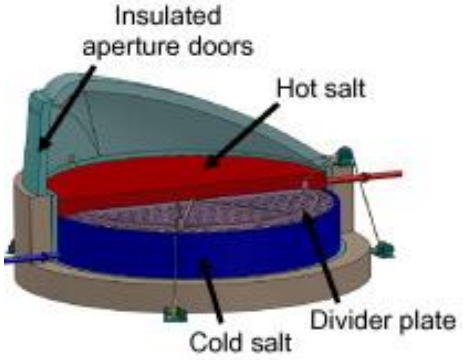

(c)

FIGURE 2.4: Current Sensible heat thermal energy storage systems used in Concentrated Solar Power plants (a) Two Tank Storage [30] (b) Thermocline TES System[31] (c) Integral receiver and storage system CSPonD [32]

storage: two tank systems and single tank thermoclines systems. Fig 2.4 shows current sensible thermal energy storage systems used with Concentrated Solar Plants.

Fig 2.4a, shows a two tank thermal energy storage system. In two tank storage systems, operated in either indirect or direct thermal energy storage, hot and cold heat transfer fluids (molten nitrates, synthetic oils) are actively pumped and stored separately in hot and cold tanks of identical sizes. In the former, the heated Heat Transfer Fluid (HTF) pumped in a closed loop heats up a thermal energy storage medium from the cold reservoir through a heat exchanger which is then stored in a hot reservoir [30]. In the latter, the Heat Transfer Fluid (HTF) in the cold tank is pumped through the solar collectors where it is heated by solar radiation and then pumped into the high temperature tank where it is stored until needed by the solar plant. The advantage to the two tank system is that the cold and hot salts are stored separately (ideal separation). Two tank storage systems currently account for between 9-20% of total plant cost. The high cost is associated with the components associated with the heat transfer at reliable operation at commercial scale [30]. These designs require the two tanks must be constructed with each capable of storing the entire system volume. Also operational risk of a freeze-up if the process temperature drops unexpectedly adds cost to systems that use salt as a heat transfer fluid. Additional hardware must be installed, such as heat tracing, insulation, or emergency water-dilution systems. Gabbrielli and Zamparelli [35] designed internally insulated, carbon steel, molten salt thermal storage tank for a parabolic trough power plant; the study had a 20% lower total investment cost compared to a corresponding ANSI 321H stainless steel tank.

In contrast, is a thermocline thermal energy system shown in Fig 2.4b, which is a packed bed single unit tank which stores hot and cold heat transfer fluid in a single stratified arrangement [36]. Thermoclines tanks are sensible heat TES systems which are marginally larger than one of the tanks in the two tank storages system. They operate by maintaining a thermocline and preventing convective mixing of hot and cold parts in the tank [37]. In traditional CSP systems, 33-35% savings in investment costs have been obtained with single tank systems relying on temperature stratification via natural thermocline formation, relative to the two tank storage system [31, 38]. However at higher temperatures, realisation of the temperature gradient in the thermocline control of thermal stratification becomes difficult as transparent liquid salt offers no resistance to radiative heat transfer, and radiation between a hot ceiling and a cool bottom can induce convection currents that destroy the thermocline [39]. Thus, as the thermocline thermal energy system relies on stratification, maintaining thermal stratification is imperative. This is maintained by careful design if the tank proportions and location of the extraction and return ports so fluid motion does not affect the thermocline [40, 41]. Low cost filler material have been used to fill most of the thermocline tank volume thereby serving as the

primary thermal storage medium, reducing the quantity of the relatively more expensive molten salts [42]. Tests using dual media thermocline tanks with silica particles (sand) in molten nitrate salts, while confirming chemical stability, have shown that filler material tends to settle and pack over time due to the vertical cycling of the thermocline's position, as the system is charged and depleted repeatedly [42, 43]. Various numerical studies using CFD have been reported in literature for thermocline thermal energy storage systems [31, 36–45]. The finding of many of these studies are discussed in the review article of Flueckiger et al. [43] A raft thermocline is a modified thermocline that enables operational temperatures and effectiveness of greater magnitude when compared to traditional (natural) thermoclines [46]. A raft is an insulated platform floating between the hot and cold regions of a liquid in a storage tank which provides and maintains the required thermal stratification between the cold and hot fluid [46].

Recently, an integrated receiver and thermal storage system based on the direct absorption of solar radiation has been developed to lower electricity generated costs while improving efficiency [32, 47]. Fig 2.4c shows a schematic of volumetric receiver with integral storage and modified raft thermocline system designed for the Concentrated Solar Power on Demand (CSPonD) project [32, 47]. Concentrated solar flux from hillside mounted heliostats was directed through the aperture into an open container of molten salt at the base of the hill, or into a one-bounce system with the receiver at the top of the hill. The salt volume in this concept serves as a receiver and also acted as the thermal storage medium in a single storage tank configuration. The concentrated sunlight penetrated and was absorbed by the molten salt in the receiver through a salt depth of 4-5m. The concentrated solar radiation heated the top salt volumetrically and an insulated barrier plate was positioned within the tank to provide a physical and thermal barrier between the thermally stratified layers, maintaining the hot and cold salt volumes required for continuous operation. Hot salt was pumped from the top of the tank through a stream generator and then returned to the bottom of the tank. As a result, high temperature thermal energy could be provided at any desired time. The power block, including salt pumps, heat exchanger/ steam generator and power generation device, for a nitrate salt based CSPonD system will be very similar to those that can be commercially obtained. The tank construction is considered for the low cost carbon steel design of Gabbrielli et al. [35]. On the basis of the National Renewable Energy Laboratory (NREL) Solar Advisor program, the system is estimated to realise cost-competitive levelised production costs of electricity. Maintaining neutral buoyancy at the hot-cold thermocline interface and a near perfect seal; with the side walls to prevent leakage around the divider raft, and the additional cost of the raft the high cost of pumps, manifolds and piping pre-heaters, fluid variations and parasitic power remain major challenges [32].

In general, despite the thermodynamic challenges associated with the single tank (thermocline), significant savings in thermal energy storage are made when compared with two tank storage. It has been demonstrated that further saving in thermal energy storage costs and LCOE can be realised with a combined volumetric combined raft concept developed in the CSPonD project. The feasibility, of internal absorption to induce natural convective heat in integral volumetric and thermal energy system aimed at lowering the cost of a thermal energy system for a small scale power system is of interest in the study.

2.4 Molten salts

Molten salts are attractive and preferred media for high temperature thermal energy storage owing to exhibit densities and specific heats, which increase volumetric storage efficiency. Molten salts can be formulated to operate across various temperatures with low vapour pressures, enabling them to be used in under pressured systems [19]. In general vapour pressures of molten salts are fairly low, for example for chloride salts at 900^{o}C vapour presures is of the order of 0.001 bar. Different molten salts are suitable for high temperature heat transfer and thermal energy storage for solar thermal energy applications. The choice or selection of any molten salt is dependent upon operational temperatures, material compatibility, application, toxicity and cost [48]. Extensive review of molten salts has been complied by Serrano et al. [49], while an engineering database of molten salt thermophysical and thermochemical properties are complied by Sohal [50]. Binary (KNO_3-$NaNO_3$, 60-40%wt M.P 222^o) and ternary (KNO_3-$NaNO_3$-$NaNO_3$ wt 52%-7%-15%, m.p 142^{o}C) molten salts are commonly used for solar thermal applications [51, 52]. Both salts mixtures benefit from higher operation temperature ranges which potentially result in improved efficiency by expanding the working temperature range as well as the convenience of simplifying start-up [53]. However, discrepancy over decomposition and thermal stability temperature of these salts exist [54, 55]. In controlled atmospheres, thermal stability temperatures of molten KNO_3-$NaNO_3$-$NaNO_3$ (wt 52%-7%-15%) have been reported to be raised to up to 610^{o}C in inert atmospheres and up to 650^{o}C-700^{o}C in oxidising atmospheres [56].

Established literature on the light attenuation in molten salts at elevated temperatures (>200^{o}C), over the solar spectrum (250nm-4000nm) is lacking. In particular at the time of writing this thesis, a reliable source of data or extensive study covering precise quantification of transparency and absorbance in terms of neither extinction (attenuation) coefficient, nor established specific data regarding the scattering vs absorption particularly in the entire wavelength range of interest for solar applications at high temperatures

are scarce. There are however, only limited attempts found in the literature concerning light attenuation in molten salt at elevated temperatures (200^{o}C). Amongst these include early investigations of Drotning [57] which reported attenuation coefficients of ternary sodium nitrite, sodium and potassium nitrate (KNO_3-$NaNO_3$- $NaNO_3$ wt 52%-7%-15%) and binary Sodium and Potassium nitrates salts (KNO_3-$NaNO_3$, 60-40 wt, mp 222^{o}C) at 200^{o}C in the wavelength range 0.35-2.5μm based on hemispherical and reflection techniques [57]. Fig 2.5 shows the absorption spectrum for KNO_3-$NaNO_3$, (60-40%wt, mp 222^{o}C) over the wavelength 0.35-2.5um as obtained by Drotning [57]. Dronting [57] found that KNO_3-$NaNO_3$- $NaNO_3$ wt 52%-7%-15% salt absorbs approximately 8% of the solar spectrum per cm of path length and is mostly transparent throughout the solar spectrum, with the exception of strong absorption in the near UV range In binary KNO_3-$NaNO_3$, 60-40% wt, mp 222^{o}C, approximately 3% absorption of the solar spectrum per cm of path length is observed [57]. Following his observations, Drotning [57], concluded by generally describing the two salts as transparent over the visible spectrum.

Drotning [57] also carried out investigations of the temperature dependence of the molten salts absorption over a temperature range of 200-500^{o}C and results are shown in Fig 2.6. The absorption edge wavelength selected for measurement purposes, defined as the wavelength at which the external transmittance through the cell and liquid was 5% of the incident beam. The results shown in Fig 2.6 indicates a shift approximately linearly to longer wavelengths with increasing temperature from to 200-500^{o}C [57]. The increases in the absorption coefficient for pure Hitec salt over this temperature range was approximately 1.5% [57]. On this basis, the variation in solar absorption values due to temperature variations were concluded to be negligible.

Metallic oxides of Cobalt and Copper Cu dopants whose concentration was varied from 0 to 0.1% wt were later used to enhance solar absorption of the salts. Addition of 0.1% wt of $Co(NO_3)_2.6H_2$, increased the absorption form 85% to 90% per cm (2 and 3). The study concluded that particles can increase volumetric absorption of light in salts by an order of magnitude and that CoO_4 dopants offered better solar absorption enhancement. The biggest challenge however, is the stability and the dispersion with agglomeration and sedimentation of the particles suspended in the salt. Experimental errors involved with the small thickness investigated could not allow for a clear quantification of small values of attenuation typical of semi-transparent fluids. Addition of nanoparticles for heat transfer enhancement has been shown to have great potential in forced convection flows [58]. However discrepancy exist regarding of natural convection enhancement in nanofluids within enclosures (enclosed flows). According to some authors, addition of nanoparticles to base fluid implies a more or less remarkable enhancement of the heat transfer rate, while according to others, a deterioration may occur [58]. Reasons for such

conflicting results regarding the heat transfer performance of nanofluids in natural convection flows is attributed to two opposing effects arising respectively, from the increase of the effective thermal conductivity and the increase in the effective dynamic viscosity that occur as the nanoparticle volume is augmented. The economic justification of addition of nanoparticles to enhance volumetric absorption of solar radiation as raised by Bohn and Green [27] remains one of the concerns.

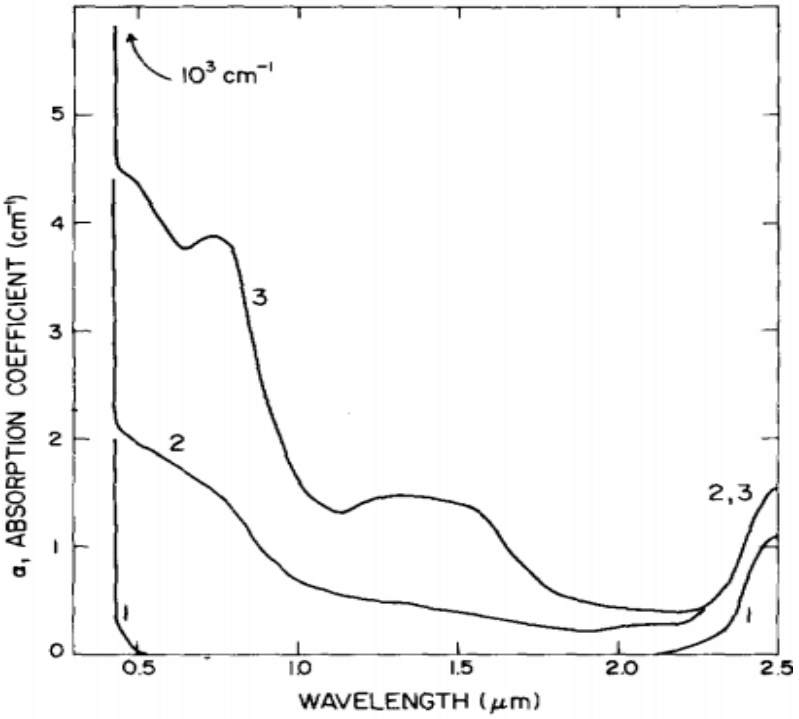

FIGURE 2.5: Absorption coefficient vs wavelength for (1) pure Hitec (2) Hitec 0.032wt Cuo and (3) Hitec 0.061 Co_3O_4 at 200^{o}C based on hemispherical calculation [57].

Passerini [29], experimentally investigated optical properties, thermal, and chemical stability, of high temperature molten salts mixtures considered for direct absorption of solar radiation and thermal storage. In particular, the study carried out chemical stability and material compatibility tests of molten salt nitrate/nitrite, chloride and carbonate salt mixtures with common materials of interest. On the basis of the melting and material compatibility tests, the carbonate salt mixtures were discarded because of undesirable reactions with structural materials or air that made them unsuitable for the CSPonD design project [29]. Experimentally measured attenuation coefficients in the solar wavelength range 400nm- 800nm is shown in Fig 2.7 for KNO_3 - $NaNO_3$, 40- 60% wt temperatures 250^{o}C-500^{o}C and in Fig 2.8 for NaCl-KCl, 50-50% wt at temperatures at 700^{o}C- 800^{o}C respectively. Fig 2.9 shows the attenuation solar radiation in solar salt (KNO_3 $NaNO_3$ 40-60%wt) at 350^{o}C illustrating of radiation attenuation at the reference

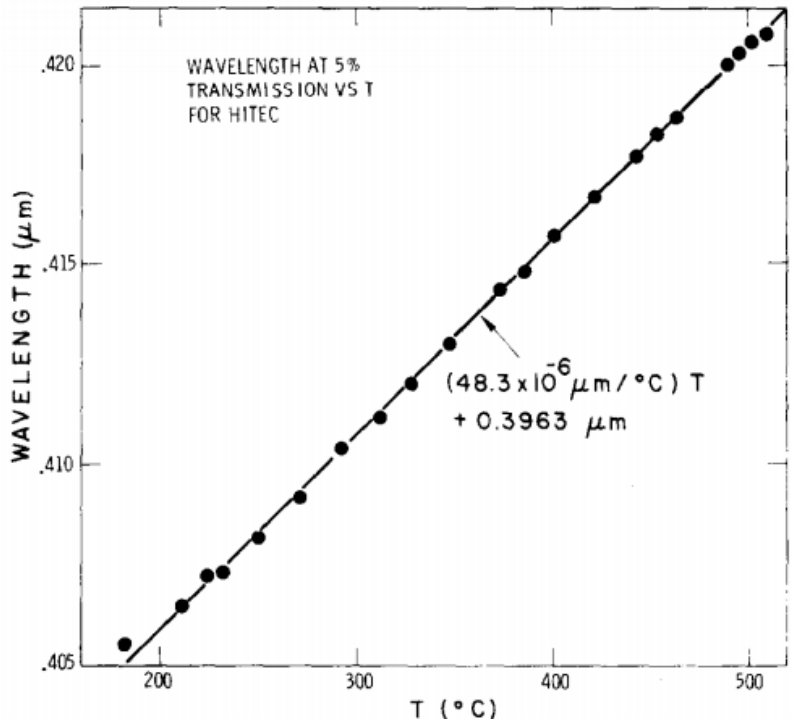

FIGURE 2.6: Fundamental absorption edge location of molten Hitec versus temperature [57].

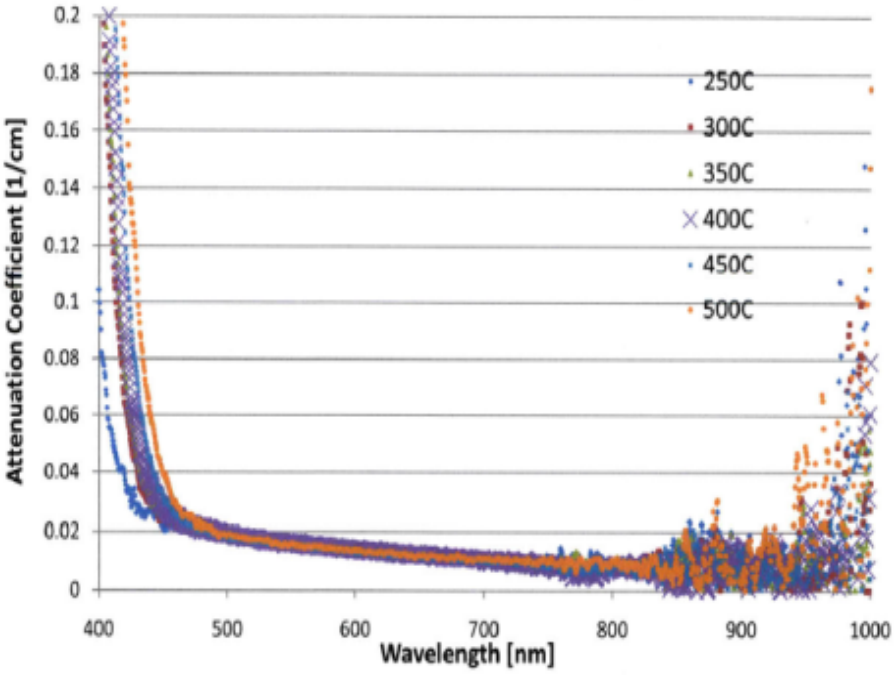

FIGURE 2.7: Attenuation coefficient Average as a function of wavelengths and temperature for Binary potassium nitrate mixture (60/40% wt) [29].

ASTMG173-03 at depths of 0.25, 0.75, 1, 2 and 3m respectively. The absorption spectra for KNO_3-$NaNO_3$, 60-40% is presented for wavelength range of 400 to 800nm (which accounts for 51% of the solar spectrum) and at operating temperatures range 250-500^oC. For example, Fig 2.9 shows that 93% light attenuation at a depth of two metres. Details of the rig construction, experimental procedures and measurements performed can be found in Presseni [29] and Slocum et al. [32].

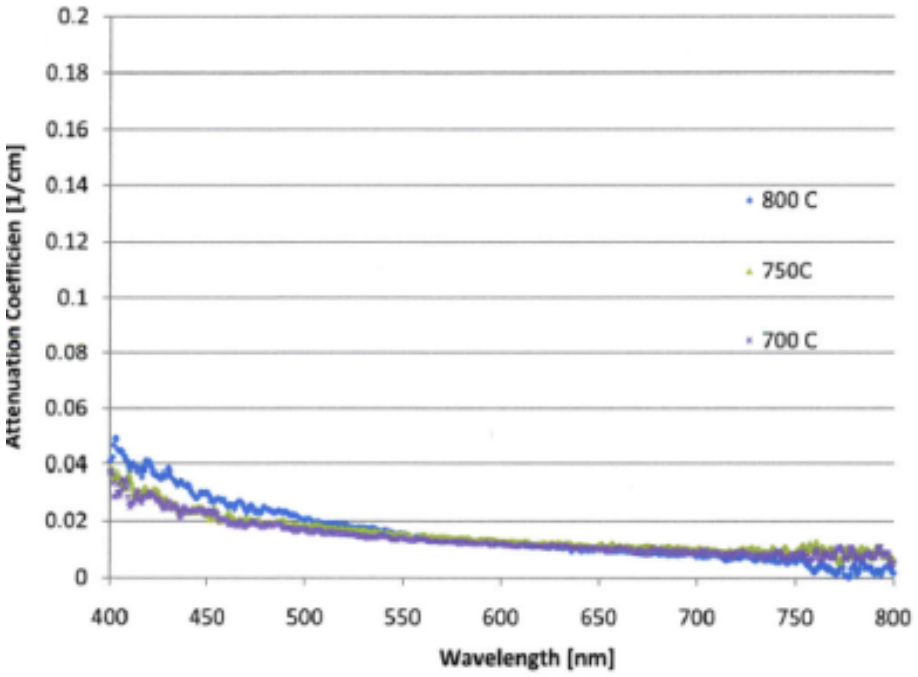

FIGURE 2.8: Attenuation coefficient Average as a function of wavelengths and temperature for 50/50% wt. sodium potassium chloride mixture [29].

Thermal stability of ternary mixtures containing calcium and nitrate additions $Ca(NO_3)_2$-$NaNO_3$-KNO_3 considered for a Heat Transfer Fluid (HTF) and storage application in solar energy systems has been considered by Gomez et al. [59]. Eutectic sodium and potassium nitrates salts mixtures containing $Ca(NO_3)_2$ are less stable at high temperature compared to the binary mixture because pure $Ca(NO_3)_2$ is less stable at high temperature than $NaNO_3$ and KNO_3. This it was found that as the proportion of $Ca(NO_3)_2$ decreases, the salt becomes more thermally stable, and the viscosity decrease. Eutectic mixtures of KNO_3-$NaNO_3$ and $LiNO_3$ which have lower temperatures than binary KNO_3-$NaNO_3$ have been investigated for solar energy thermal storage by authors Mantha et al. [60, 61]. More recently, quaternary molten salts ($LiNO_3$-$NaNO_3$-KNO_3-KNO_2) for thermal storage in a Parabolic Trough Solar Plant has been investigated by Wang et al. [62]. The melting point of the quaternary salt mixture was lower than that

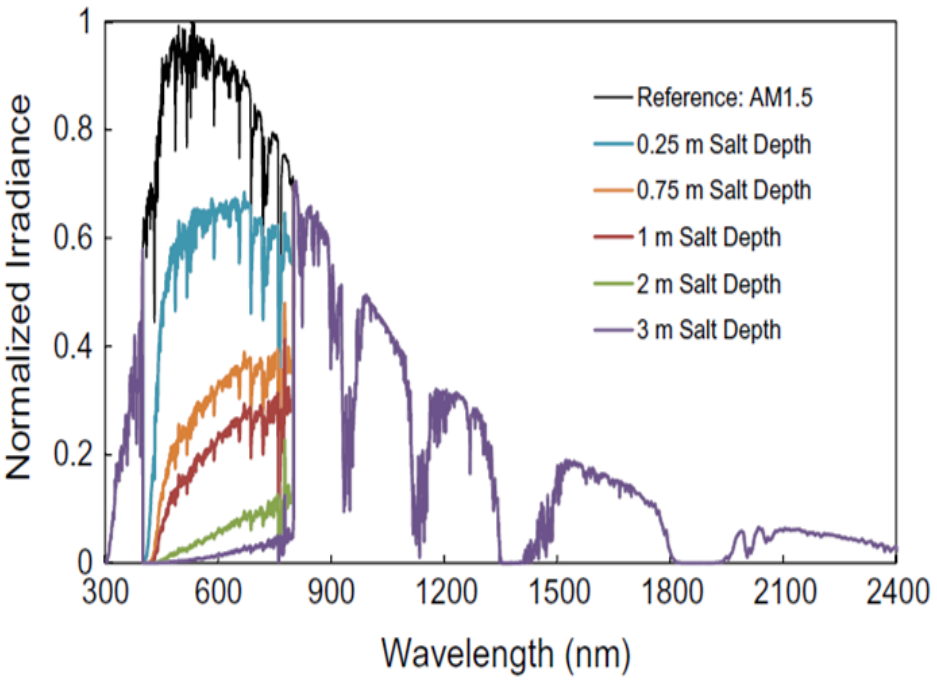

FIGURE 2.9: Solar irradiance attenuation as a function of Wavelength and salt depth at 350^{o}C [29].

of solar salt and Hitec salts which increases the working temperature range of solar energy storage. Compared to the KNO_3-$NaNO_3$ binary solar salt, all the new molten salts present larger thermal energy storage as well as the gravimetric storage density values, which indicate the better thermal energy storage capacity for solar power generation systems [62]. Owing to the scarcity of the light attenuation properties of salts ternary and quaternary mixtures at high operation temperature in wavelengths considered in this thesis, the salts have not being considered in the current study.

Various molten salts suitable for high temperature direct absorption of solar radiation have been identified from literature. Despite the fact that light attenuation at the high temperature of interest in this thesis are lacking, light attenuation within them is selective over wavelengths of interest to solar energy applications. Temperature dependence of radiation absorption was shown to be negligible. In this thesis molten commercially available KNO_3-$NaNO_3$, 60-40%wt, mp 222^{o}C has been used owing to its long term extensive use under high temperatures and excellent thermophysical chemical compatibility and optical properties at such temperatures

2.5 Absorption of solar radiation in fluids layers

When solar rays strikes are at a fluid interface, a small fraction of the incidence radiation will be directly, while most of the radiation will penetrate into the fluid depth. Radiation transmitted into the fluid penetrates to appreciable depths within the fluid as it travels through the medium. Theoretically, absorption of light in a semi-transparent medium follows Beer Lamberts law, which is based on the assumption that the absorbed radiation is a function of the local intensity in medium and the distance x that the radiation has travelled inside the medium. This is mathematically written for a homogeneous medium as:

$$I = I_0 e^{-(\alpha+\sigma)x} \tag{2.1}$$

where I is the intensity transmitted through a layer of material of thickness x, I_0 Intensity before absorption, σ is the scattering coefficient, α the absorption coefficient. The attenuation coefficient δ can be defined in terms of the absorption and scattering coefficient δ=α+σ (cm^{-1}). α is the solar weighted absorption coefficient obtained from equation (2.2), whose nominal value demonstrates a fluids baseline capacity for absorbing solar energy are commonly used to calculate Beer's law [63].

$$\alpha = \frac{\int s_{m\lambda}(1 - e^{-\alpha_\lambda x})}{s_{m\lambda} dx} \tag{2.2}$$

where α_λ, the energy absorption in a fluid layer of thickness x, averaged over the solar spectrum of Air Mass m, $s_{m\lambda}$ is the spectral distribution of the solar intensity through an Air Mass m. The absorption coefficient in equation (2.1) are strongly dependent on the wavelength that are obtained from experiments requiring specialist equipment.

2.5.1 Spectral dependent thermal transport of radiation within a fluid

Equation (2.3) and equation (2.4) present mathematical expressions for the total radiant energy, and the local volumetric rate of solar radiation absorption in water (heat generation) which appear in the energy equation [64]. I_z is the spectral intensity of radiation in the direction (polar angle and azimuthal angle). The RHS of equation (2.3) represents the local rate of absorption of radiation by the water and is the quantity of interest since it appears in the total energy balance. The total radiant energy flux I_z is defined by Viskanta [64] in equation (2.3) as:

$$I_z = \int_0^{2\pi} \int_0^{2\pi} \int_0^{\pi} I_\lambda(z, \theta, \phi) \cos\theta \sin\theta d\theta d\phi d\lambda \tag{2.3}$$

The local volumetric rate of absorption of solar radiation in water (volumetric heating) appears in the energy equation for predicting the temperature distribution in the water is neglected. Equation (2.4) gives the conservation of radiant energy as [64]:

$$S_z = \frac{-dI}{dZ} = \alpha_\lambda \left[\int_0^{2\pi} \int_0^{2/\pi} I_\lambda(z, \theta, \phi) \sin\theta d\theta d\phi \right] d\lambda \tag{2.4}$$

Where λ is the wavelength, α is the spectral absorption coefficient of water. Inspection of equation (2.3) and (2.4) reveals that the radiative flux I_z and the heating rate S_z are given in terms of the spectral intensity. The absence of polarisation and emission, the quasi steady equation of radiative transfer which governs the radiation field spectral intensity in water is given in equation (2.5) [64]:

$$\upsilon \frac{dI_\lambda}{d\tau_\lambda} = -I_\lambda + \frac{\omega_0 \lambda}{4\pi} \int_0^{2pi} \int_{-1}^{1} r_\lambda(\upsilon\phi_1 \rightarrow \upsilon, \phi) I_\lambda(\tau_\lambda, \upsilon, \phi_1) d\upsilon d\phi_1 \tag{2.5}$$

where the optical depth γ_λ is defined as

$$\gamma_\lambda = \int_0^z \beta_\lambda(z) dz \tag{2.6}$$

where σ_λ and δ_λ are the spectral scattering coefficient and attenuation coefficients of water; $\omega_{o\lambda}$, is the the albedo for single scattering; r is the scattering or phase function which is related to the probability that an incoming beam having direction θ, ϕ and confined to a solid angle dΩ=sin θ dθ dϕ=-dυ dϕ will be scattered into a solid angle dΩ around θ, ϕ and sin θ. The first term on the RHS of equation (2.5) accounts for the extinction (absorption and scattering) of radiant energy. The second term represents contributions to intensity by scattering from the elemental volume of water. Equation (2.5) along with boundary conditions is sufficient to determine the radiation field.

2.5.2 Forward scattering approximation

The forward scattering approximation assumes that scattering in fluid layers is highly peaked in the forward direction and can be defined by a scattering function. Omitting the mathematical details, equations (2.7) to (2.8) presents mathematical expressions for the total spectral radiative flux made by assuming that all the scattered energy is scattered strictly in the forward direction is given as:

$$I(z) = \int_0^1 2(\frac{1}{2}\upsilon^o[1 - r_{0\lambda}(\upsilon^o)]I_b\lambda e^{\frac{-\gamma}{\upsilon}}/\beta(\gamma_{D\lambda}, |\upsilon|)I_{d\lambda}T_{3(\gamma_\lambda)} - I_{b\lambda}E_3(\gamma_{D\lambda} - \gamma_\lambda))d\lambda \quad (2.7)$$

The resulting total heating rate can be expressed by:

$$S(z) = \frac{dI}{dz} = \int_0^1 2\kappa_\lambda(\frac{1}{2}(\frac{\upsilon^o}{\upsilon}[1 - r_{o\lambda}(\upsilon^o))]I_{b\lambda}e^{\frac{-\gamma}{\upsilon}}/\beta(\gamma\lambda, |\upsilon|)I_{d\lambda}T_{2(\gamma\lambda)} - I_{b\lambda}E_3(\gamma_{D\lambda} - \tau_\lambda)]d\lambda \quad (2.8)$$

where the spectral radiative flux incident at the bottom is given by:

$$I_{b\lambda} = 2\rho_{b\lambda}(\frac{1}{2}\upsilon^o)[1 - r_{o\lambda}(\upsilon^o]I_b\lambda e^{\frac{-\gamma}{\upsilon}}\beta(\gamma_{D\lambda}, |\upsilon|)I_(d\lambda)T_2(\gamma_{D\lambda}) \quad (2.9)$$

The exponential and transmission integral functions $E_n(x)$, $T_2(x)$ and $T_3(x)$ are given as

$$E_n(x) = \int_0^1 e^{-\frac{-x}{\upsilon}}\upsilon^{n-2}d\upsilon \quad (2.10)$$

$$T_2(x\int[1 - \rho_0(\upsilon_1)]e^{-\frac{-x}{\upsilon}}\frac{\upsilon 1}{\upsilon}d\upsilon|\beta(\gamma, |\upsilon|) \quad (2.11)$$

$$T_3(x\int[1 - r_0(\upsilon)e^{-\frac{-x}{\upsilon}}\upsilon d\upsilon/\beta(\gamma, |\upsilon|) \quad (2.12)$$

The inter reflection factor, $\beta(\gamma,|\gamma|)$ is defined as

$$\beta(\gamma, |\upsilon|) = 1 - r_b r(\upsilon)e^{(-2\gamma_D/|\upsilon|)} \quad (2.13)$$

$$\gamma = \int_0^D \alpha dz \quad (2.14)$$

The first and second terms on the RHS of equation (2.7) represent the contributions of the beam and diffuse components of the incident solar flux, respectively. The third term denotes the contribution to the flux due to reflection from the bottom. Equation (2.8) has been verified indirectly in laboratory experiments by comparing the measured and predicted temperature distributions in a tank of water which was irradiated from radiant heaters located above the water. Equations (2.7) and (2.8) have also yielded

realistic estimates of radiative transfer in natural waters and as such can be used with some confidence for pure water [64].

Viskanta and Toor [64] used discrete ordinate approximations to solve equations (2.9) to (2.10) and predicted the local volumetric rate of solar energy absorption accounting for the absorption and scattering by pond water. The results presented showed the sensitivity of the absorption and distribution of the absorbed energy in the pond to the directional distribution of the incident solar radiation, attenuation of solar radiation by the atmosphere during the diurnal cycle, and the modifications of the spectral radiation characteristics of water by impurities and additives. The model assumed constant material physical properties, and accounted for the depth dependent absorption of solar radiation using a solar weighted absorption coefficient. Viskanta and Toor [64], extended the earlier works of Cengel and Ozişik [65], developed a fourth order degree polynomial solution form of the RTE and presented them in a form readily usable in the energy equation [65]. By determining radiation intensity and flux quantities at each wavelength the total quantities over the entire spectrum are obtained by superposition, and the equation was used to compute the solar absorption at various fluid depths at different angles of incidence (0^o to 75^o at 15^o intervals).

Equations (2.5), (2.7) and (2.8) can be simplified by neglecting the directional dependency, to obtain Beer Lambert's law (equation 2.1). By using a solar weighted average absorption coefficient, Beer's law has been applied to spectral bands models, where the spectrum can be divided into several spectral bands, each having an average attenuation coefficient α_j and energy component, I_j have been used to account for the spectral nature of light attention. Two [4], three [66] and six [67], spectral band models have been applied to volumetric receivers. However, according to Cengel [65], estimation of the depth dependent absorption of solar radiation based on a single bulk value can lead to serious errors. Decrepancies in results of spectral radiation flux calculations based on absorption coefficient band models was illustrated in the study of Webb and Viskanta [68] using two and three band models. From their results, shown in Fig 2.10 the two band model gave higher system performance compared with the three band model. Differences in models such as these with regards to the attenuation band models are expected to vary based on the band number model.

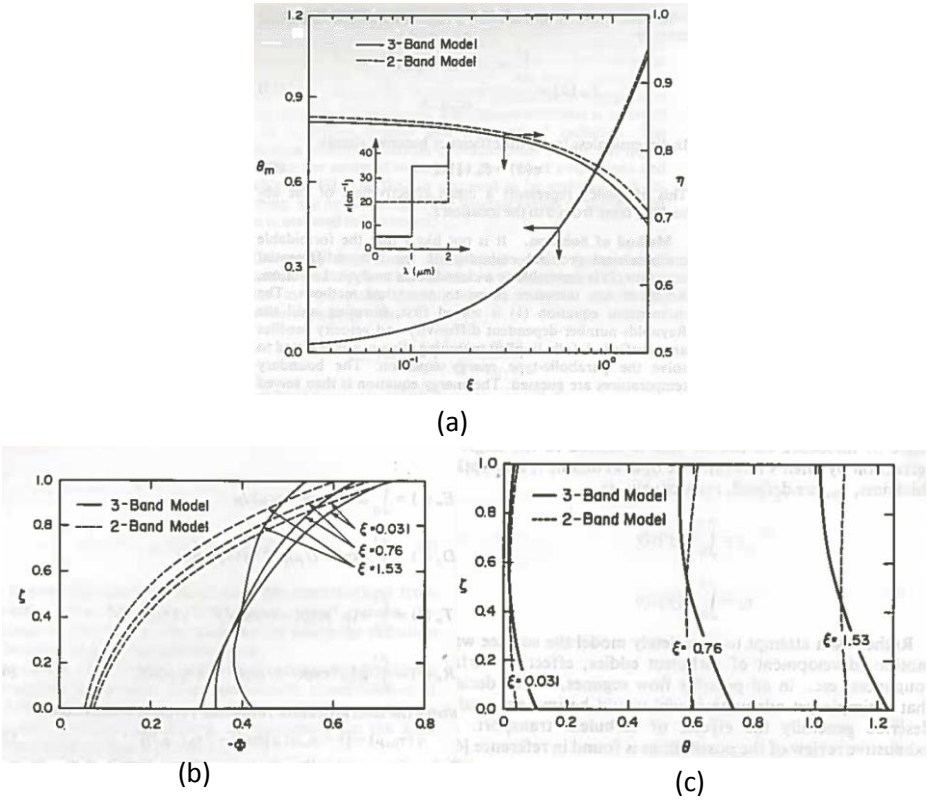

FIGURE 2.10: Effects of absorption coefficient band model on (a) mean temperature and collector efficiency (b) local radiation flux (c) local temperature [68]

2.6 Standard Spectral Irradiance distribution reference: The Simple Model of the Atmospheric Radiative transfer of Sunshine (SMARTS) model

Recalling that the intensity and absorption coefficient in equation (2.1) and (2.2) are strongly dependent on the wavelength, thus all wavelengths are not affected by solar energy activity equally. In particular, for applications where spectral solar radiation needs to be evaluated from atmosphere to ground level to estimate performance, precise knowledge of the extraterrestrial spectrum (ETS) is of primary importance [20]. Reference spectra represents terrestrial solar spectral irradiance on a specific surface, under one set of specified atmospheric conditions. Terrestrial spectra can be evaluated through the use of Radiative Transfer Models (RTMs), which describe atmospheric extinction processes on a spectral basis. Over the years various fixed reference solar spectra have been developed for standard reporting conditions of such spectrally selective devices.

Amongst these include:

- ASTM891-82 for direct normal spectral irradiance is one of the early standard spectra produced are th.
- E892-82, for total hemispherical spectral irradiance on a south facing 37^{o}‘ tilted surface.
- ASTMa,b: EM424-71 standard spectrum replaced the 82 and 87b spectra.
- EM892-87 was adopted in the International Standards Organisation (ISO) adopted both the 82b spectra.
- Spectra was moved to ASTM G159-98(combination of E-892-92 E892-92) to conform to ISO standard.

G159-98 was adopted and has had a successful application, however challenges of its reproducibility, solar geometry, spectral range, spectral resolution (step size)are drwwas backs of the G159-98. Details of the listed deficiencies are presented and fully discussed in Gueymard [69].

Improved atmospheric radiative transfer models with improved parametrisation of the absorption properties of aerosols in the environment have been developed. The Simple Model of the Atmospheric Radiative Transfer of Sunshine, (SMARTS), is a medium resolution (0.5-5nm) spectral radiative model, versatile enough to cover a variety of solar energy applications [69–71]. The SMARTS model evaluates the spectral solar irradiance components of the short wave and long wave spectrum, taking into account the effect of the atmosphere. Fig 2.11 shows the spectral irradiation data obtained from reference spectra derived from Simple Model of the Atmospheric Radiative transfer of Sunshine (SMARTS v. 2.9.2) (NREL) at Air Mass AM1.5. Three resolutions and spectral intervals are now used in SMARTS: 0.5nm in the UV(280-400nm), 1nm in the visible and part of the near infra red (400nm-1700nm) and 5nm beyond, up to 4000nm [70]. The SMARTS model incorporates 10 widely used reference atmospheric profiles and accounts for Rayleigh scattering absorption from 19 different gases (e.g ozone, nitrogen dioxide, water vapour and aerosol) extinction properties, using individual parametrisations of the optical mass for each constituent. An advantage of the SMARTS model is that it is easy to implement and execute; its results compare favourably with high resolutions models. Its library offers a large number of user options [72–75].

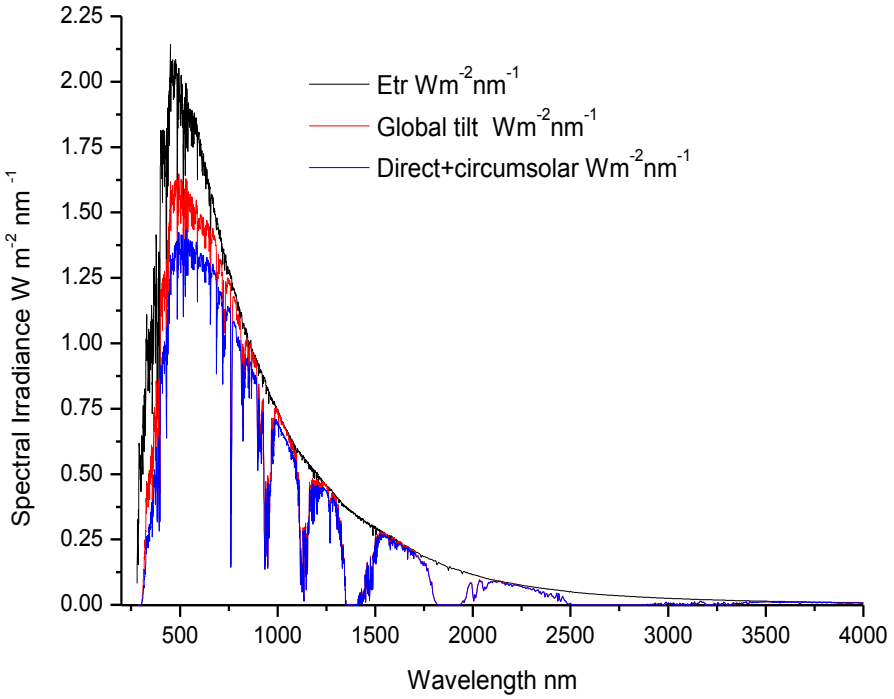

FIGURE 2.11: ASTM G173-03 Reference Spectra Derived from SMARTS v. 2.9.2 [76]

2.7 Air Mass

The Air Mass characterises the solar spectrum after solar radiation has travelled through the atmosphere. It is defined as the ratio of the mass of the atmosphere through which a beam of radiation passes to the mass it would pass through if the sun were at the Zenith. The solar intensity and Zenith (sun) angles vary with Air Mass coefficient. The relationship between Air Mass and zenith (sun) angle and air mass is given by equation and a brief explanation of the respective Air Mass and zenith is presented in Table 2.1.

$$AM = \frac{1}{\cos\theta_z} \tag{2.15}$$

The intensity of the direct component of sunlight throughout each day can be determined as a function of air mass from the experimentally determined equation:

$$I = 1.353 \times 0.7 \times AM \times 0.678 \tag{2.16}$$

where I is the intensity on a plane perpendicular to the sun's rays in units of Wm^{-2} and AM is the Air Mass. The value of 1353 Wm^{-2} is the solar constant and the number 0.7 arises from the fact that about 70% of the radiation incident on the atmosphere

is transmitted to the Earth. The extra power term of 0.678 is an empirical fit to the observed data and takes into account the non-uniformities in the atmospheric layers [69–71].

TABLE 2.1: Air Mass vs Zenith angle.

Air Mass	Comments
AM0	The Air Mass referred to at zero atmospheres such as in space power applications. Generally characterized using AM0 corresponds to the Zenith angle 0^o.
AM1	means "one atmosphere", is the spectrum after travelling through the atmosphere to sea level with the sun directly overhead. It corresponds to a zenith angle 5^o.
AM1.5	1.5 atmosphere thicknesses, corresponds to a solar zenith angle of 48.2^o. AM1.5 is useful to represent the overall yearly average for mid-latitudes. The specific value of 1.5 is adopted as the standard testing.
AM2	Corresponds to a solar zenith angle of 60^o. useful range for estimating the overall average/ performance of solar cells installed at high latitudes.
AM3	useful range for estimating the overall average performance of solar cells installed at high latitudes.
AM4	Corresponds to zenith angle 75
AM5-AM15	Corresponds to zenith angles greater than 80^o and less than 90^o.

2.8 Natural convection in enclosures induced by absorption of radiation

Buoyancy driven convection in cavities plays a vital role in a variety of physical and engineering applications such as in energy storage [77]. Since the classical works of Rayleigh and Bernard understanding the interaction between heat transfer and fluid flow in convective thermal transport has been of primary interest and remains the subject of many investigations. Differentially heated cavity models with idealised isothermal or iso flux end walls have formed the fundamental studies for understanding thermal and flow interactions in enclosures. The differential heated cavity problem has been extensively studied experimentally and numerically in various contexts (aspect ratios, geometries, orientation, fluids and control parameters) and several boundary conditions. Three thermal boundary conditions based on the heating phase angles, ϕ are commonly found in literature [78, 79]:

(a) Heating from below ($0^o < \phi < 90^o$), typical Rayleigh Bernard flows are obtained in which an unstable fluid layer is formed and a small disturbance in this layer leads

to the onset of convection owing to the density gradient being parallel but opposed to the gravity vector. The fluid remains in a state of unstable equilibrium due to the heavier fluid being above the lighter fluid. The critical Rayleigh number for the onset of convection is found to be Ra>1708 for rigid boundaries and Ra>1101 for rigid free boundaries [80].

(b) Lateral heating from the side (ϕ=90^o) causes recirculating or cellular boundary layer flows near the rigid wall, ascending along the hot wall and descending along the cold wall and enclosing a core region is typical [79]. At this heating angle, the density gradient is normal to the gravity vector.

(c) Heating from above (90^o < ϕ <180^o) causes the density gradient to be parallel but in the same direction as the gravity, and the fluid becomes stratified. It is however possible that both conventional and unstable (stratified) mode can interact in a given configuration.

While a large body of literature exists for the typical Rayleigh Bernard convection in differentially heated cavities, literature for the fluid mechanics and heat transfer problem in enclosures, where the primary driving force for the natural convective motion, is the volumetric absorption of thermal energy is very limited. Unlike in the differentially heated cavity problem, where steady state solutions are obtained for idealised isothermal or flux boundaries conditions by time stepping from a prescribed initial state, radiation induced buoyancy driven flow boundary conditions are transient and complex. Thus, in radiation induced natural convection problems, it is of fundamental significance to understand the heat and flow behaviour in the enclosure under time dependent heating conditions. As such this is expected to be quite different from the convention in differentially heated cavity problems described above. Considerable numbers of investigations have been found in literature amongst which include works of Webb and Viskanta [81] who carried out experimental and numerical investigations to predict the heat transfer and the natural convection in rectangular enclosures. The test cell and conditions are presented and described in chapter 4 (section 4.3). The experimental tests were then simulated numerically by solving the conservations equations of mass momentum and energy with the radiative divergence flux equation using the control volume scheme and the SIMPLER algorithms [82]. Incident solar radiation was considered for constant isotopic radiation incident at the transparent vertical wall. Results obtained showed that at high Rayleigh numbers, the heat transfer near the base were very low while most of the heat transfers occurred at the top of the enclosure where the warm fluid first contacts the isothermal wall [82]. Results also showed that at higher optical depths absorption of the incident flux in the fluid will be completely attenuated before reaching the opaque walls and the flow and heat transferred are expected to be minimal. The maximum fluid

temperature in the cavity was found to increase with increasing aspect ratio, as a higher area is exposed. High fluid opacity did not permit the penetration and transmission of incident radiation through the fluid. This in turn eliminates the development of buoyancy induced fluid flow as the volumetric rate of radiant energy deposition approaches a uniform heat flux boundary condition. The incident radiation within the fluid directly heats the core of the flow and results in the flow pattern losing the characteristic centrosymmetry of natural convection solutions in cavities with differentially heated walls. The eddy centre is displaced to a position very near the cooled side wall [82].

Numerical and experimental investigations of unsteady natural convection induced by absorption of radiation have been reported for shallow triangular enclosures with sloping bottoms. These find relevance in buoyancy driven flows with respect to the daytime natural convection in a side arm and in littoral regions [83–87]. From these studies, the driving mechanisms and major features of the flow development were observed. On this basis the flow regimes were classified: early flow transition characterised by the thermal boundary layer, a transitional stage marked by irregular occurring rising plumes and a quasi-steady state stage. Scaling analysis of unsteady natural convection induced by absorption of radiation in a triangular enclosure verified by numerical simulations are reported by Mao et al. [88, 89]. Scaling analysis carried out revealed the features of the flow regimes which were dependent on Rayleigh numbers (natural convection) and a relative value of certain non-dimensional parameters describing the flow. Proper scales were said to be have been established to quantify the flow properties in each of these flow regimes. A three-dimensional numerical simulation was conducted by Lei and Patterson [90] to investigate the natural convection in a shallow wedge subject to solar radiation absorption. The study revealed three distinct stages of the flow development from an isothermal and stationary state: an initial stage, a transitional stage and a quasi-steady stage. The heat transfer at the initial stage was dominated by conduction from the sloping bottom. The transitional stage started with the onset of instabilities, and the quasi-steady state was characterised by steady growth of a spatially averaged temperature. The results obtained were in good agreement with observations from a flow visualisation experiment and a two-dimensional simulation.

In more recent studies two and three dimensional enclosures filled with water were subjected to solar radiation and have been reported by Hattori et al. [91, 92]. The simulated geometry finds relevance in deep water bodies subjected to a top solar radiative heating where the authors infer investigations are scarce [91]. Direct Numerical Simulations (DNS) were applied in solving the coupled mass, momentum and energy equations. Results revealed non-linear temperature distributions characterised by two distinct layers: an upper stratification region, due to internal heating, provided by the

direct absorption of radiation, and a potentially unstable boundary layer due to the absorption and re-emission of the residual radiation by the bottom surface [91]. A direct consequence of the non linear temperature stratification is the limitation of the mixing driven by rising thermal plumes as well as limiting the maximum height to which thermal plumes could attain. This in turn determines the penetration length scale of the plumes and by extension determining the lower mixed layer thickness. The study also theoretically determined the lower mixed layer thickness, which is suggested to be equal to the attenuation length of the radiation [91] and has been shown to have important implications for water quality, including the transport of pollutants and nutrients. In a three-dimensional enclosure (parallelopiped), filled with water and subjected to solar radiation, the authors [92] used scaling analysis and a numerical model to study the early stage of the flow development.

Penetrative convection owing to selective absorption of radiation belongs to a wider class of the Rayleigh Bernard problem which has been the subject of many researches [93]. According to Moroni and Cenedese [94] penetrative convection entails the motion of a vertical thermal plume or dome into a fluid layer of stable density and temperature stratification when the plume has enough momentum to extend into that fluid layer for a significant distance from the original interface [94]. The authors simulated penetrative convection and the mixing layer in a stratified fluid in a laboratory experiment aimed at 1) predicting mixing layer growth as a function of initial and boundary conditions 2) understanding the interaction between the mixing layer and the stable layer and 3) describing the fate of contaminant dissolved in the fluid phase [94]. Fig 2.12 shows images of the mixing layer and its interface acquired during the experiment. The portion viewed is a vertical slab of about 1cm thick, centred near the middle of the test section. From their study, it was demonstrated that the flux through the interface between a mixing layer and the stable layer play a fundamental role in characterising and forecasting the quality of water in stratified lakes and in the oceans, and the quality of air in the atmosphere.

Fig 2.13 shows typical characteristic zones for penetrative convection: boundary layer, mixing layer, the transitional layer and stable stratified layer, as established by vertical profiles of mean temperature, density and convective heat flux over the convective layer height z_i. In the mixing layer, with a typical height of $0.85z_i$, the temperature and density profiles are constant, in space due to vertical mixing of all these quantities. In the transitional layer, at around $0.85z_i < z < 1.2z_i$, the temperature profile increases and reaches a stable behaviour, while the convective heat transfer is a minimum. The mixing layer grows within the transitional layer. In the transitional layer the convection is characterised by narrow plumes in the form of domes of rising horizontal surfaces balanced

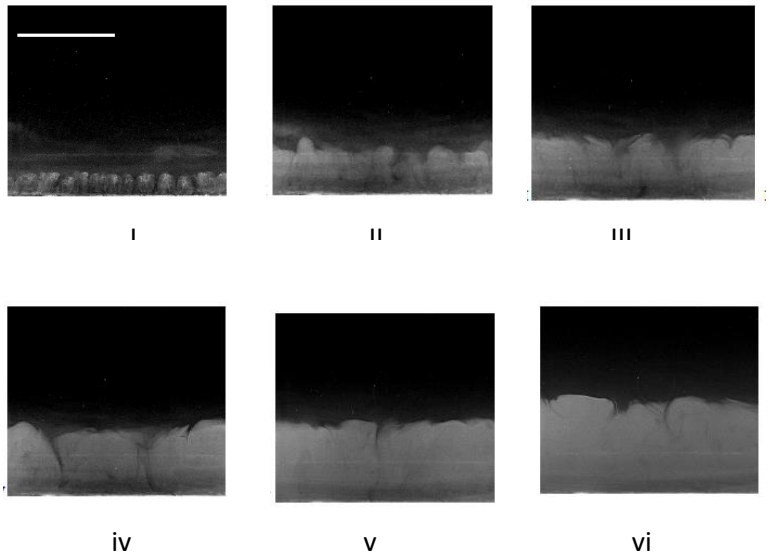

FIGURE 2.12: Visualisation of mixing layer evolution .Each snap shot corresponds to a progressive time (white line in frame is 10cm); I:180s,II: 400s III: 600 IV: 700 V: 919 VI: 1260 [94].

by larger regions of descending motion. In the stable layer, where the temperature shows a stable profile with constant gradient, the convective heat flux is zero.

Convection due to selective absorption of radiation has also been shown experimentally by Krishnamurti [95] for a viscous fluid. In this study convective instability was found to occur in the fluid as long as the radiative heating is sufficient to exceed the higher ambient temperatures. Convective plumes were found to be unable to penetrate far into the fluid depth and remained shallow in a strongly stratified layer. However, for a weakly stratified layer, plumes grow tall and further collect in a large convective cluster which persist as a steady coherent flow.

Hill [96], using the linear and nonlinear analysis based on the nonlinear energy theory simulated Krishnamurti's [95] experiment. A concentration based internal heat source is modelled quadratically. A linear analysis and conditional nonlinear analysis are performed. Due to the presence of significantly large regions of potential subcritical instabilities, the results indicate that linear theory may only be accurate enough to predict the onset of convective motion when the model for the internal heat source is predominantly linear. This lends much credence to the use of a linearly modelled internal heat source as used by Krishnamurti [95], within the constraints of the parameter

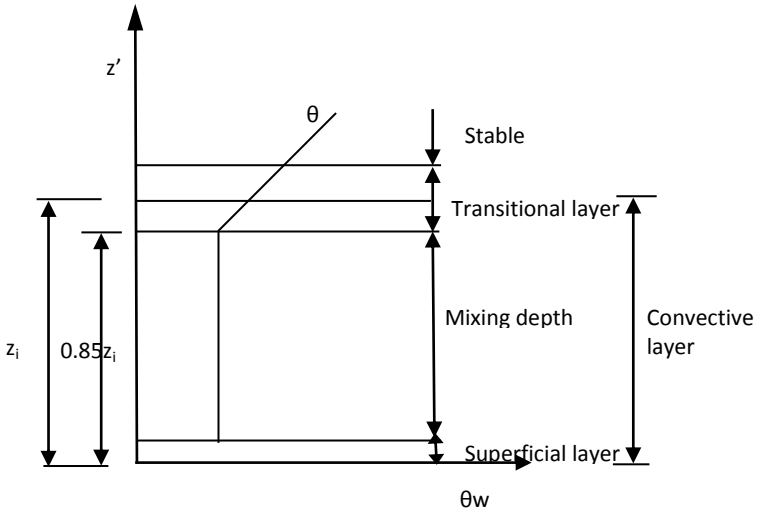

FIGURE 2.13: Schematic of the atmospheric boundary layer under convective condition, with profiles of the vertical kinematic heat flux [94].

ranges. More recently Harfash [97, 98] advanced the earlier works of Hill [96] in three dimensional numerical simulations. Using the linear stability and the nonlinear energy stability analysis convection induced by the selective absorption of radiation in a fluid layer in a three dimensional box was investigated. From the results obtained it was found that due to the inherent nature of the linear theory, it only provides boundaries for instability, but does not predict anything about instability, because of the presence of nonlinear terms. Thus making the development of the nonlinear stability theory highly desirable, as full assessment of any regions of subcritical instabilities between the two respective theories can be made. Table 2.2 summarises the various investigations for natural convection in enclosures driven by absorption of solar radiation.

2.8.1 Finite Volume Method vs Finite Element Method

In the Finite Volume Method (FEM), the governing equations are integrated over a volume or cell assuming a piece-wise linear variation of the dependent variables (u, v, w, p, T) [106]. The piece-wise linear variation determines both the accuracy and the complexity. Using these integrations, fluxes across the boundaries of the individual volumes can be balanced. The flux is calculated at the mid-point between the discrete nodes in the domain. In contrast Finite Element Method (FEM), uses a Galerkin's method

TABLE 2.2: Summary of the numerical investigations on the natural convection induced by the selective absorption of radiation in a fluid layer in various enclosures

Investigation	**Geometry**	**Method/Remarks**
Webb and Viskanta [81, 82]	Rectangular	• Two dimensional mass, momentum and energy equations were discretised using the control volume scheme of Patankar. • SIMPLE algorithm was used to couple pressure and momentum. Volumetric heat source accounted for based on weighted mean absorption coefficient and constant isotropic solar radiation.
Lei and Patterson [83–86]	Triangular	• Two dimensional system of equations solved with Finite volume method. • SIMPLE scheme adopted for pressure velocity coupling and QUICK scheme applied for spatial derivatives. • Second order implicit scheme used for time discreisation. Three dimensional mass, momentum and energy equations solved with Finite Difference Method. • System of equations were discretised using second order differencing and upwind scheme. Second order time accurate backward differencing scheme applied to time integration. • The system equations are solved implicitly with iterative procedure. • Over relaxation method applied to all equations include Poisson equation.
Hattori et al. [91, 92]	Paralleoplied	• Non-staggered, Cartesian mesh, finite volume SNS code , based on a fractional step method, with the Adams-Bashforth and Crank–Nicolson time discretisation schemes used for the advection and diffusion terms. • The spatial discretisation of the diffusion terms uses second-order central differencing, whilst the spatial discretisation of the advection terms uses second-order central differencing with the ULTRA (universal limiter for tight resolution and accuracy) flux limiter. • The strongly implicit procedure (SIP) (Stone 1968) is used for solving the momentum and energy equations, while the bi-conjugate gradient stabilised method (BICGSTAB using a SIP preconditioner is used for solving the Poisson pressure correction equation, which is formed directly from the Navier–Stokes equations.
Hill [96]	Rectangular	• Governing equations reduced to eigenvalue value problems using compound matrix and Chebyshev-tau techniques. • Linear internal heat source from absorption of radiation based on constants of proportionality.
Harfash [97, 98]	cubiod	• Three dimensional mass, momentum and energy equations were carried out velocity-vorticity formulation.
Onyegegbu, [99, 100]	Rectangular	• Finite difference method was used to solve the coupled mass, momentum and energy equations. • Elliptic system of PDEs equations solved by implicit method. • Internal heat generation based on combined mean Planck, Roseland and scattering coefficients
Verevochkin and Startsev [101]	Rectangular	• Governing equations were discretised using Finite volume method with expansion of variables in a Fourier series with time dependent coefficients.
Salmun [102]	cuboid	• Three dimensional mass, momentum and energy equations were solved using Finite Volume method with the SIMPLE scheme. • Linear first and second derivatives approximated by second order center differencing scheme. • Advection terms discretised by QUICK scheme. • Time integration discretised by second order backward difference scheme .
Coates and Patterson [103, 104]	rectangular	• Finite Volume method with the SIMPLE scheme. second derivatives approximated by second order center differencing scheme. • Advection terms discretised by QUICK scheme. • Time integration discretised by second order Crank-Nicholson predictor corrector method.
Cui et al. [105]	triangular	• Velocity-vorticity formulation three dimensional simulations for convection induce by selective absorption of radiation.

of weighted residuals where the governing partial differential equations are integrated over an element or volume after having been multiplied by a weight function [107]. The dependent variables are represented on the element by a shape function, which is the same form as the weight function and may take any of several forms. [107]. The main advantage as well as the main disadvantage of finite elements is that it is a mathematical approach that is difficult to put any physical significance on the terms in the algebraic equations. The finite volume method, always deals with fluxes and this is not the case with finite elements. The table below summarizes the advantages and disadvantages of the various methods [106, 107]:

TABLE 2.3: Summary of the numerical investigations on the natural convection induced by the selective absorption of radiation in a fluid layer in various enclosures

Method	Finite Element	Finite volume
Advantages	More mathematic approach	Fluxes have more physical significance
	Natural boundary conditions (for fluxes)	Use techniques like skew upwinding and QUICK schemes
	Any shaped geometry can be modelled with the same effort	
	More suited to Multiphysics modelling.	
	More degrees of freedom	
Disadvantages	More mathematics involved- less physical significance	Irregular geometries require far more effort
	Application of FE on any geometrical shape is the same	

2.9 Mixing and stratification

Thermal performance of solar thermal systems is strongly influenced by natural convection and thermal stratification [108, 109]. Therefore quantification of the level of mixing and stratification occurring in thermal storage is of practical interest. System performance with regards to thermal stratification has been extensively studied [108–112], especially in water storage thermal storage systems [109, 110]. Numerous methods have been proposed for the characterisation of thermal stratification in thermal store. An extensive review on methods to determine stratification efficiency of thermal energy storage processes and theoretical comparative study of the various methods was reported in Haller et al. [111]. The authors focus on the methods that can be used to determine the ability of storage to promote and maintain stratification during charging, storing and discharging. Fig 2.14 shows a summary of the different approaches found in literature as presented in Haller et al. [111]. The approaches shown in Fig 2.14 are

classifieds according to two main groups: 1) density approach which is commonly used by environmental scientists and 2) the temperature approach used by thermal engineers.

Indices or metrics for the degree of stratification based on the latter approach can be based on the first law of thermodynamics or based on the second law of thermodynamics. Davison et al. [112] developed the dimensionless MIX number which expresses the degree of mixing that occurs during a charging process. The method is based on the momentum of energy which characterises storage tank performance in terms of both total energy stored in the tank and its vertical temperature profile. The MIX number is defined by the dimensionless expression as shown in equation (2.17):

$$MIX = \frac{M_{st} - M_{actual}}{M_{st} - M_{mix}} \tag{2.17}$$

where M_{st},M_{actual} and M_{mix} are the momentum of energy of a perfectly stratified tank, experimental and a fully mixed tank and is obtained from equation (2.18). The energy of each layer of the tank, E_k=$\rho V C_p$ dT is weighted by the vertical distance from the bottom of the tank to the centre of each layer, y_i. The momentum of energy is:

$$M = \sum_{i}^{n} y_i E_i \tag{2.18}$$

The MIX number equals zero for an actual tank with equal amounts of energy at vertical locations identical to those predicted by the unmixed tank model. If the actual tank has an equal amount of energy at heights identical to that predicted by the fully mixed tank model, MIX equals 1. As the MIX number is based on the height weighted energy (i.e) moment of energy, in the tank, it is a measure suitable to assessing the level of mixing in an enclosure. As such, it can be considered as a suitable estimate of the level of mixing and stratification formed within an enclosure.

For thermal energy storage, the MIX number generally gives a good indication of the level of mixing and stratification within over time. However, a major drawback of this method is that it does not show, at what time mixing was most severe; this is due to the way the MIX number is evaluated. The non-dimensional exergy is used to overcomes the weaknesses of the MIX number as its evaluation is independent of the amount of energy stored in a tank. It allows for a better estimation of the transient evolution of the level of stratification. Dincer and Rosen [13] argued that traditional energy analysis may be inadequate as it cannot account for the degradation of the energy and proposed that the second law of thermodynamics offers an alternative measure of the quality of

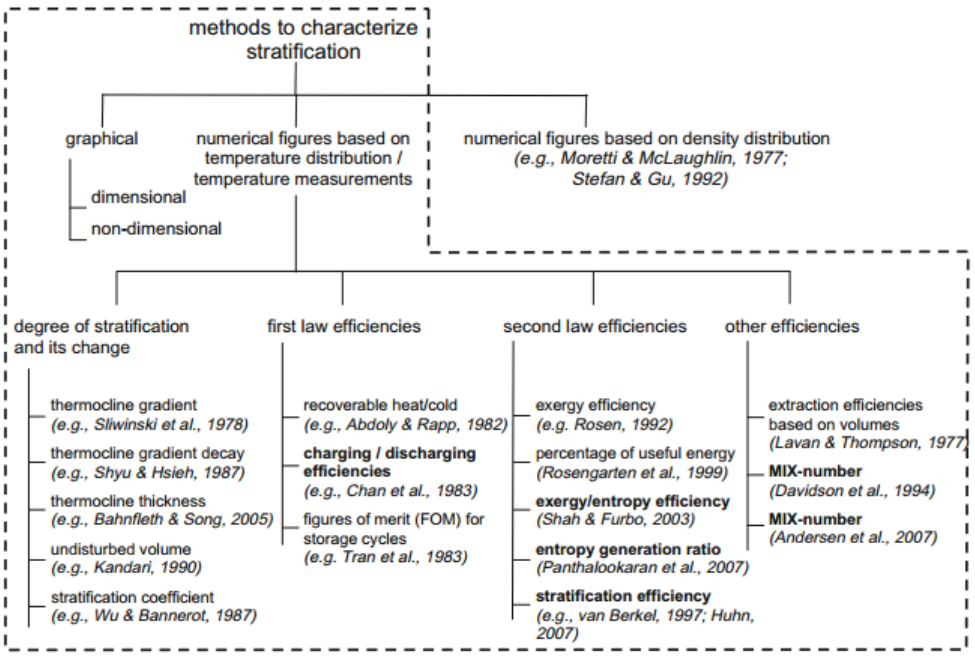

FIGURE 2.14: Different methods proposed to characterise thermal stratification in water storage [111].

the energy stored. The process of loss of stratification creates entropy through mixing and environmental losses and as a consequence, degradation of the energy stored [113].

For natural convection in enclosure problems determination of the entropy generation is important for an exergy analysis. Magherbi et al. [114] studied the entropy generation at the onset of natural convection. Entropy generation gives a measure of destruction of available work of the system is important. As such entropy generation in fundamental natural convection and for evaluating the performance of sensible heat thermal energy storage are also of primary interest. Oztop and Al-Salem [115] presented an extensive review of entropy generation minimisation or thermodynamic optimisation in enclosures due to buoyancy induced flows for energy systems. The authors present a comprehensive table list of available literature on entropy generation studies in square, rectangular and cylindrical enclosures. Their review highlights the relationships of thermodynamic and Energy Generation Minimisation (EGM) method and the interaction between heat transfer, engineering thermodynamics and fluid mechanics. Basak et al. [116] studied entropy generation during conjugate natural convection within a square cavity. In a numerical study the author applied finite element carried out entropy generating analysis (using FEM) during conjugate natural convection within a differentially heated square cavity enclosed by vertical walls of different thicknesses. Their results showed that

maximum entropy generation due to heat transfer occurred near the solid fluid interface region due to a high temperature gradient. The maximum magnitude of the entropy generation due to fluid friction occurred near the cavity due to friction between the circulation walls and cavity walls. Increased values of the heat transfer and flow intensity resulted in larger values of entropy. A numerical investigation of the transient natural convection and entropy generation in a differentially heated enclosure using a finite volume method was reported by Magherbi, et al. [114]. The study found that the total entropy generation attained a maximum value at the onset of the transient state which increased with the Rayleigh number and the irreversibility ratio. Entropy generation in rectangular cavities of constant area and varying aspect ratios were studied numerically by Ilis et al. [113]. The study reports that, for a cavity with high value of Rayleigh number, the total entropy generation due to fluid friction increased with increasing aspect ratio, attains a maximum and then decreases. The aforementioned studies show that the exergy efficiency gives better insights into the thermal performance than energy efficiencies. They are seen as useful tools in guiding Research design and decisions and a true representation of the associated internal system losses. They also provide a measure of how the operation of a system approaches the ideal or theoretical upper limit. However energy and exergy analysis for radiation induced natural convection in enclosures driven by the volumetric absorption of solar radiation appear to be lacking. The instantaneous exergy within a storage tank can be evaluated by equation 2.19 is defined as:

$$\epsilon = \int \xi \rho dV \tag{2.19}$$

where ϵ is the instantaneous exergy (J), V is the volume of the storage tank (m^3) and ξ is the flow availability (J/kg), which is calculated by:

$$\xi = (h - h_0) - T_0(s - s_0) \tag{2.20}$$

In which the enthalpy (J/kgK), h_0 is the enthalpy at a reference state (J/kgK), s is the entropy, s is the entropy (J/kg), s_0 is the entropy at reference state (J/kg), and T_0 is the temperature at reference state. Dincer and Rosen [13], defined an exergy based non dimensional parameter ξ to quantify the degree of stratification in the tank by comparing it two ideal extreme states, a perfectly stratified tank and a perfectly mixed tank. The non-dimensional exergy parameters ζ is defined as

$$\zeta = 1 - \frac{\epsilon - \epsilon_{mix}}{\epsilon_{st} - \epsilon_{mix}} \tag{2.21}$$

where $\epsilon_{\ mix}$ is the instantaneous exergy of a perfectly mixed tank (J) and $\epsilon_{\ stat}$ is the instantaneous exergy of a perfectly stratified tank (J). ζ=0, for a perfectly stratified tank and ζ=1. For a perfectly mixed tank. For a non perfect thermal stratification, ζ will be between 0 and 1. Assuming both density and specific heat are constant, the global instantaneous exergy difference between the actual tank and perfectly mixed tank can be evaluated by:

$$\epsilon - \epsilon_{mix} = C_p \rho V[(\bar{T} - T_{mix}) - T_0 ln(\tilde{T}/T_{mix})] \tag{2.22}$$

where C_p is the specific heat of the fluid (J/kg K), $\bar{T}$ is the volume averaged temperature (K) and $\tilde{T}$ is the equivalent temperature (K). Similarly, the global instantaneous exergy difference between a perfectly stratified tank and a perfectly mixed tank can be evaluated by

$$\epsilon_{st} - \epsilon_{mix} = C_p \rho V[(T_{stra} - T_{mix}) - T_0 ln(T_{stra}/T_{mix})] \tag{2.23}$$

where $\bar{T}_{\ stra}$ and $\tilde{T}_{\ stra}$ are the volume averaged temperature and the equivalent temperature in a stratified tank (K), respectively. The mixed temperature, T_{mix} is calculated using the net energy balance that includes energy losses to the ambient and net energy addition or withdrawal during the loading or unloading phases, as represented by the following equation:

$$\rho C_p V \frac{dT_{mix}}{dT} = m_i C_{p,in}(T_i - T) - UA(T_{mix} - T_{amb}) \tag{2.24}$$

where U is the overall heat transfer coefficient (W/m^2K), A is the surface area (m^2) and T_{amb} is the ambient temperature (K). $\bar{T}$ is defined below, where the summation is extended into all control volumes

$$\bar{T} = \frac{1}{V} \sum_{cv} T_i V_i \tag{2.25}$$

where T_i (K) is the temperature in the i_{th} CV(m^3) and V_i is the volume of the i_{th} cv(m^3). Physically, $\tilde{T}$ represents the equivalent temperature of a mixed thermal energy system that has the same exergy as a stratified thermal energy system. It is defined as:

$$\tilde{T} = \frac{1}{V} \sum_{cv} V_i ln T_i \tag{2.26}$$

In a similar manner, $\bar{T}_{stra}$ and $\tilde{T}_{stra}$ are calculated by:

$$\bar{T}_{stra} = \frac{1}{V}\sum_{CV} T_{stra,i}V_i \tag{2.27}$$

$$\tilde{T}_{stra} = exp\left[\frac{1}{V}\sum_{CV} V_i ln T_i\right] \tag{2.28}$$

After extensive comparisons among these parameters/approaches with the numerical simulation data obtained for this paper, it is found that the non-dimensional exergy parameter best quantifies the level of thermal stratification in the storage tank, and hence it will be used in this thesis as the parameter to quantify the level of thermal stratification in the tank.

2.10 Capture efficiency

Capture efficiency is defined as the fraction of incoming energy entering through the aperture that is retained by the receiver to heat the fluid body and retained. Equations (2.16) and (2.30) present assessment metrics based on the first and second law efficiencies applicable to stationary receivers undergoing transient heating [117]. Khullar et al. [117] have recently applied energy and exergy metrics defined above to stationary receivers undergoing transient heating. In volumetric absorption capture performance evaluation is of interest as these systems are required to efficiently convert concentrated solar radiation and achieve the highest possible temperatures while retaining high efficiencies [4].

$$\eta_I = \frac{E_{stor}}{Q_{in}} = \frac{\int_0^t mC_p(T - T_0)}{CIAt} \tag{2.29}$$

$$\eta_{II} = \frac{Ex_{stor}}{Q_{in}} = \frac{\int_0^t mC_p[(T - T_0) - T_0 ln(T/T_0)]t}{CIAt} \tag{2.30}$$

The aforementioned MIX number, exergy and capture efficiency metrics have been successfully applied in gaining insights into the thermal performance. A combination of these metrics can serve as useful tools in guiding designs and assessing performance of thermal storage systems. Hence, in the present study these metrics will be applied to give an indication of the capacity of the thermal system.

Chapter 3

Model geometry and numerical formulation

This chapter presents the mathematical formulation, governing equations, and numerical implementation of the governing equations describing the physical phenomena encountered in a sensible thermal energy storage system, charged by absorption of concentrated solar radiation in high temperature molten salt. The components and operation of a Direct Absorption Sensible heat Thermal Energy System described in Chapter 2 involves complex physical processes which entails radiation coupled to natural convection which can be broken into representative constitutive equations obtained in many classical textbooks. The governing equations and derived non linear partial differential equations are solved using Finite Element Methods (FEM).

Section 3.1 presents the description of the geometry and mathematical formulation of transient volumetric heating of a fluid in a Direct Absorption Sensible Thermal Energy System. In section 3.2 the governing equations of the representative physics are presented, while in section 3.3 assumptions and constraints,as applied to the numerical formulation are discussed. Section 3.4 presents the numerical implementation along with its boundary and initial conditions in COMSOL Multiphysics, this section also presents the derivation of the lower surface boundary condition.

3.1 Geometry and Mathematical formulation

In Chapter 2, a schematic and general description of a direct absorption thermal energy storage system . Fig Fig 3.1a shows a schematic of a direct absorption thermal energy storage system consisting of an insulated inner steel tank , accommodating a black

absorber plate at its lower surface and contains commercially available mixture of sodium (Na) and potassium (K) nitrate salts was presented. The molten salt in the TES is directly illuminated by concentrated solar radiation, which in turn heats it by: 1) the direct volumetric absorption of incident concentrated solar radiation in a non linear manner and 2) a natural convection driven by transmitted radiation absorbed by an absorber plate radiation at the bottom surface.

Under consideration is a two dimensional equivalent (Fig 3.1b) of the direct absorption thermal energy storage system (Fig 3.1a) containing approximately $2m^3$ of molten salt. The domain consists of rigid adiabatic vertical walls of height H and a black rigid conductive bottom wall of finite thickness (dx) and width D. The dimensions of the domain are given in Table 3.1 for various H/D ratios, while the list of thermophysical properties of the lower absorber surface is presented in Table 3.2. The domain is filled with high temperature molten salt which is in contact with the lower boundary surface, while the top surface, the salt air interface is an open, stress free adiabatic surface. Initially, the molten salt is at rest and at a temperature T_0=250K, corresponding to a temperature above salt crystallisation temperature. The thermophysical properties of the molten salt are taken for temperature dependent properties which have been collected from molten salts handbook and binary molten salt KNO_3-$NaNO_3$ has long operational experience in thermal transport and storage handling. Table 3.3 gives the following temperature dependence for the viscosity, density, thermal conductivity, heat capacity and viscosity as extracted from Janz [48]. Fig 3.2 shows measured attenuation coefficients for molten salt KNO_3-$NaNO_3$ at 250^oC; the measurements were obtained with a Elmer Perkins EPP2000-UVN-spectrophotometer from StellarNet, in a high temperature quartz cuvette. In Fig 3.2 a comparison of the measured values obtained in the present study with experimentally determined attenuation coefficient as obtained for Passerini's [29] study in the visible wavelength region (400-800nm) are presented. Results show a good agreement and is used with confidence in the present study.

At the time t=0, non-uniform concentrated flux at 700X is initiated at the top surface and thereafter maintained. The downward penetrating radiation within the salt depth directly illuminates it and heats the salt volume in a non-uniform manner by volumetric absorption. The non-absorbed radiation transmitted to lower surface is assumed to be to be fully absorbed by the lower absorber. The absorber plates accumulates the absorbed energy which subsequently heats the lower plate up by conduction. The heated absorber heats the fluid adjacent to it initially by conduction and then subsequently Rayleigh Bernard type convection once the criterion for onset of thermo instability is satisfied.

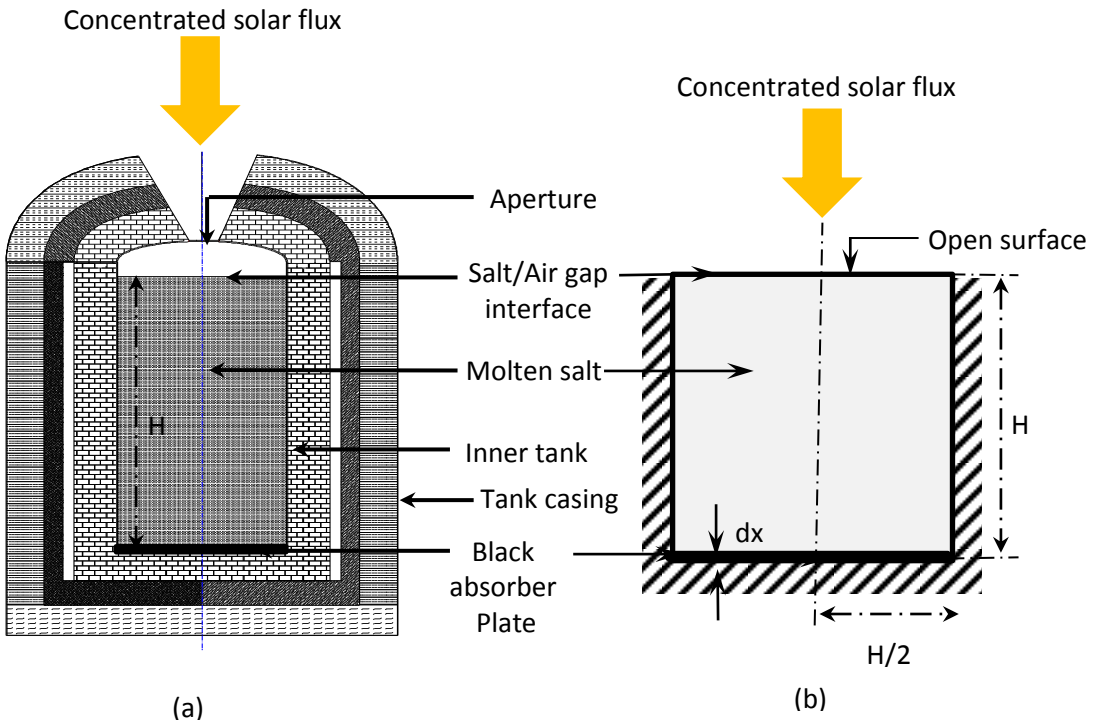

FIGURE 3.1: Schematic showing (a) Direct absorption Thermal Energy storage system and (b) Two dimensional equivalent of problem under study.

TABLE 3.1: Dimensions of the computational domain for a fixed molten salt volume at different aspect ratios (H/D).

H/D	H(m)	D(m)
0.5	0.71	1.4
1	1.1	1.1
2	1.76	0.8

TABLE 3.2: Properties of lower plate material.

Materials property	Symbols	Dimensions
Density	ρ	8960(kg/m^3)
Specific Heat	C_p	385(J/kgK)
Thermal conductivity	k	400(W/(mK)

3.1.1 Assumptions

The following assumptions were made in the present numerical model formulation:

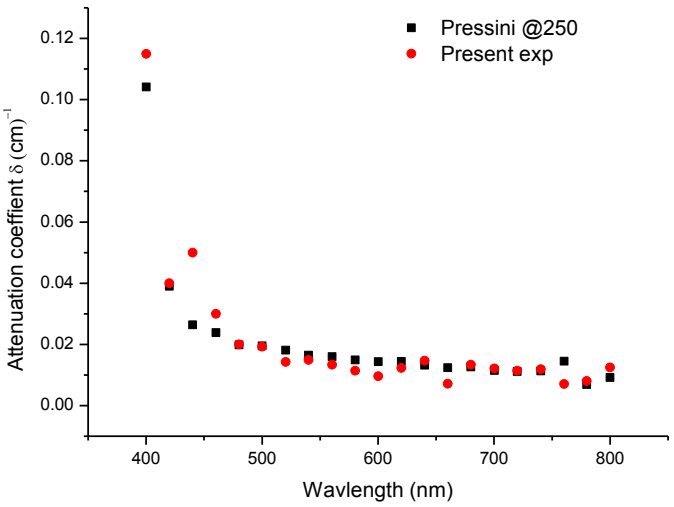

FIGURE 3.2: Comparison between measured attenuation coefficient for KNO_3-$NaNO_3$ (60%-40%) from present study (red) with values determined obtained from Passerini2010 (Black) [29]

TABLE 3.3: Thermopysical properties of molten KNO_3-$NaNO_3$ salt [48].

Property	Symbols	Dimensions
Density (ρ)	2090-0.636T	kgm^{-3}
Thermal conductivity (k)	$0.443+1.9 \times 10^{-4}$T	W $(mK)^{-1}$
Heat capacitance (C_p)	1443-0.172T (1396.044+0.172T)	$J(kgK)^{-1}$)
Dynamic viscosity (μ)	$22.714-0.12T+2.281\times10^{-4}T-1.474\times10^{-7}T$	$kg(ms)^{-1}$

1. A two dimensional computational domain is used to represent the TES geometry.
2. The flow is assumed to be two dimensional.
3. The working fluid is molten binary KNO_3-$NaNO_3$ salt and is considered to be Newtonian.
4. Molten binary KNO_3-$NaNO_3$ has a crystallization temperature of 222^oC with a maximum operational temperature 600^oC and its vapour pressure is taken to be zero as assumed in many thermal energy applications.
5. The fluid top surface is assumed to be optically smooth, so that the reflection and transmission characteristics follow Fresnel equations of classical electromagnetic theory.
6. The non uniform incident radiation is described to have a Gaussian profile and approximates the flux distribution from the concentrator system shown in Fig 2.2.
7. The fluid depth studied is taken to be within depth such that the an adequate amount

of radiation is transmitted to the lower surface sufficient induce convection and mixing.
8. The directly deposited concentrated solar radiation absorbed is assumed not generate temperatures which exceed operational temperatures of the salt (600^oC).
9. All radiation transmitted to the lower surface is assumed to be fully absorbed at this surface.

3.2 Governing Equations

The interaction of heat and flow and the subsequent temperature and flow fields generated within the enclosure are governed by the continuity, momentum (Navier-Stokes) and energy transport equations with a source term as given below equations (3.1) to (3.3) [118]:

$$\nabla \cdot \vec{V} = 0 \tag{3.1}$$

$$\rho \frac{\partial(\vec{V})}{\partial t} + \rho(\vec{V} \cdot \nabla) \cdot \vec{V} = -\nabla p + \mu \nabla^2 \vec{V} + \rho g \tag{3.2}$$

$$\rho C_p \left(\frac{\partial T}{\partial t} + \nabla \cdot \vec{V} T \right) = \nabla \cdot (k \cdot \nabla T) + S \tag{3.3}$$

where $\vec{V}$ is the velocity vector consisting of the velocity components u v and w. T is the spatial temperature in the domain from the resulting heating. P is the pressure. S is the source term representing the rate of absorption of solar radiation given in equation 3.4 below. The source term is determined by solving the Radiative Transfer Equation (RTE) subject to the appropriate radiative boundary conditions. The radiative transfer equation in its exact form is an Integro-differential equation which is algebraically very difficult to solve, especially when the effects of scattering are included, as they must be for this problem. Solution to this problem was derived in equations (2.4)-(2.7) in Chapter 2 (section 2.5) and was given in form readily employed in the energy equation.

$$S = \sum \left(\alpha_\lambda \left([1 - \rho_a(\gamma_i)] \frac{I_\lambda}{\gamma} e^{\frac{\alpha_\lambda y}{\gamma_r}} + \frac{1}{1 - r_B} \left([1 - r_a(\gamma_i)] \right) I e^{\frac{\alpha_\lambda L}{\gamma_r}} \right) \right. \tag{3.4}$$

The first terms on the RHS of equation (3.4) represent the contributions of the direct absorption of radiation within the fluid body while the second term denotes the contribution to the heated absorber plate at the bottom.

In terms of weighted average values for solar intensity and absorption coefficient, equation (3.4) can be written, neglecting directional cosines to obtain equation (3.5):

$$S = [1 - \rho_a]\alpha I(e^{\alpha y} + \kappa e^{\alpha L}) \tag{3.5}$$

The governing equations given in equation (3.1) to (3.3) are non dimensionlised using the following scales: H $\sim$ α (length scale); t$\sim$ $\kappa\alpha^2$ (time scale); T $\sim$ g $\beta \mathrm{I}_0/\mathrm{C}_p\kappa\alpha^2$ (temperature scale); V(u,v,w) $\sim$ κ α (velocity scale).

$$\rho\frac{\partial(\overrightarrow{V})}{\partial t} + \rho(\overrightarrow{V} \cdot \nabla)\overrightarrow{V}) = -RaPr\nabla p + RaPr\nabla^2\overrightarrow{V} + PrRaT \tag{3.6}$$

$$\rho C_p\left(\frac{\partial T}{\partial t} + \nabla.\overrightarrow{V}T\right) = \nabla \cdot (k \cdot \nabla T) + S \tag{3.7}$$

The controlling parameters describing the flow in an enclosure is given by the Rayleigh number which prescribes the buoyancy effect in comparison to viscous effect in a fluid. The threshold for convection is Ra_c=1708 in an enclosure with two rigid wall while in an enclosure with rigid bottom and free top Ra_c=1101 [80]. The Prandtl number which prescribe the viscous effect to the thermal diffusivity. In terms of flux Rayleigh number is given by equation [91, 92].

$$Ra = \frac{\rho^2 C_p g\beta q H^4}{\mu k^2} \tag{3.8}$$

where g, ρ, μ, k, and β are the gravitational constant, density and coefficient of volumetric expansion respectively.

$$Gr = \frac{g\beta I_0 h^4}{\rho^2 C_p \nu^2} \tag{3.9}$$

The Prandtl number is a fluid property:

$$Pr = \frac{\mu C_p}{k} \tag{3.10}$$

Initial conditions

1. u,v(t=0)=0
2. T(t=0)=250K melting point temperature of salt t$\leqslant$0

Boundary conditions

1. Vertical wall is rigid adiabatic, and impermeable. No slip occurs at the side walls. The velocity components and normal temperature gradients being zero, (u=v=w=dT/dn=0).
2. The top boundary (y=0) is a stress free and adiabatic surface i.e (du/dy=dv/dy=dw/dy=0) and (dT/dy=0).
3. The lower boundary is rigid wall with no slip (u=v=w=0) and of finite thickness and thermal conductivity, where the transmitted flux to this surface is absorbed and heats the lower fluid at temperature obtained from equations (4.1).

Consider a solid plate of finite thickness, dx and length L as shown in Fig 3.3. The top surface is subjected to the heat flux with adiabatic conditions at the lower surface (Fig 3.3). For dx<< H and uniform conduction ,one dimensional heat transfer in the plate is assumed. Thus, applying the one dimensional transient heat conduction equation in dimensional form as given in equation (6.6) and the following boundary conditions [119], the top plate surface temperature is assumed as follows:

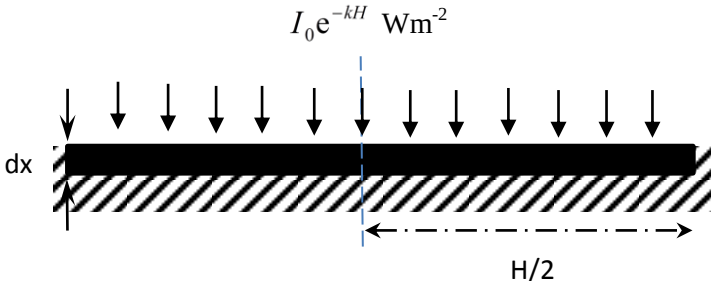

FIGURE 3.3: Lower plate absorber.

$$k_a \frac{d^2 T_a}{dy^2} + I_z = \frac{1}{k} \frac{dT}{dt} \tag{3.11}$$

where y is the plate thickness The initial and boundary conditions applicable are:

$$-k \left. \frac{dT}{dy} \right|_{y=0} = I_0 e^{-\eta H} \tag{3.12}$$

$$T\Big|_{t=0} = T_i \tag{3.13}$$

$$-k\frac{dT}{dy}\Big|_{y=dx} = 0 \tag{3.14}$$

Omitting, the mathematical details for which can be found elsewhere [119] the temperature of the lower plate for a fully insulated lower absorber surface and side walls,is given as:

$$T(x,t) - T_i = \frac{2I}{k}\left[\left(\sqrt{\frac{\alpha t}{\pi}}\right)^{\frac{1}{2}} e^{\frac{x^2}{4\alpha t}} - \frac{x}{2}xerfc\left(\frac{x}{\sqrt{4\alpha t}}\right) - xerfc\left(\frac{x}{2\alpha t}\right)\right] \tag{3.15}$$

The temperature of the top surface x=0, y=H is given by

$$T(x,t) - T_i = \frac{2I}{k}\left(\sqrt{\frac{\alpha t}{\pi}}\right)^{\frac{1}{2}} \tag{3.16}$$

where, I is the intensity described by the Total Solar Intensity(TSI) and the SMARTS model and α is attenuation coefficient taken for a weighted value equations (2.2) for spectral values .

3.3 Numerical implementation

Commercial Finite Element Method (FEM) software COMSOL Multiphysics version 4.4 is employed to solve the derived, time dependent system of nonlinear partial differential equations (PDEs) [120]. COMSOL Multiphysics software is a commercial numerical software package that uses finite element method (FEM) to solve systems of partial differential equation derived from different Multiphysics problems. COMSOL Multiphysics is supplied with different pre-configured solvers, (fluid flow, heat transfer, structural etc) [120].

The conjugate heat transfer physics interface combines the heat transfer phenomena with the nonisothermal physics equation with the equations for laminar flow described in section 3.2 and solves nonlinear partial differential equations (PDEs) by prescribing appropriate initial and boundary conditions as outlined in section 3.4. Second-order elements for the velocity and linear elements for the pressure field, (P_2 + P_1) discretisation are used [120]. A time-dependent Backward Differentiation Formulas (BDF) solver was employed to obtain solutions to the time-dependent nonlinear partial differential

equations using implicit time-stepping methods. The BDF solver applies the backward differentiation formula (backward Euler) with order of accuracy varying from one to five. BDF methods offer high stability but have severe damping effects, especially the lower-order methods [120]. Simulations in COMSOL using the Backward Differential Formula solver in combination of Navier Stokes (NS) equations on a fine mesh, a transient solver with small time steps and time-averaging of results [120] were used to model heat transfer and flow fields. The Convergence of the solution at each time step was obtained for the convergence criteria for the residuals of continuity equation, velocity components, and energy equation solutions obtained when the difference between normalised residual of the algebraic equation and the prescribed value is less than ϵ_ϕ. i.e max $\mid \phi^{m+1} - \phi^m \mid < \epsilon_\phi$ were satisfied i.e where ϕ is a dependent variable and m is the iteration number. The simulations are performed on a HP Compaq with the following specification; Quad core Intel® Core(TM) i7-3770 CPU @ 3.40GHz, 16GB RAM.

Chapter 4

Validation

This chapter is primarily concerned with the verification of the numerical tool and validation of the developed numerical models. Verification and validation is carried out in this chapter by evaluation of the software suitability in simulating established analytical and experiments found in literature, and comparing the numerical simulated results with those obtained from published literature. The procedures implemented in the verification, validation and mesh refinement conform to the processes outlined in [121–125]. Mesh refinement and time dependence studies was conducted systematically for all test cases by varying numerical results over mesh element sizes ranging from a coarse mesh to fine mesh so that the difference between in output solution at the respective mesh size and the solution at the finest mesh considered converged and remained constant for the mesh and time dependence tests. The relative error has been calculated by reference to the results given by the finest mesh. The compared quantities for the mesh size dependence study are the maximum velocity and the average temperature within the domain The relative error for either of the quantities in reference to the results of the finer mesh is obtained from the mesh convergence plots. Convergence of the solution was checked at each time step, and the convergence criteria for the residuals of continuity equation, velocity components, and energy equation were specified as stated in section 3.3. The solution convergence is met when the difference between normalised residual of the algebraic equation and the prescribed value is less than 10^{-x} for all variables where x is an integer

Five tests cases have been considered for the verification and validation study in this study. The chapter is set out in the following order: section 4.1 presents the verification of the volumetric absorption of radiation in a working fluid in a flow receiver, directly irradiated from the top by isotropic radiation. The reference experimental test on an open film solar collector conducted by Beard, et al. [126]. The numerical results and

the experimental results are then compared. In section 4.2, the verification study for a buoyancy flow problem is presented. In this test case, the classical Rayleigh Bernard convection for the stability of an infinite horizontal fluid layer heated from below and cooled from the top is simulated in COMSOL. The result obtained from the numerical solution is then compared with the analytical solution as found in studies by Drazin [80] and Chandrasekhar [118]. Section 4.3 presents the validation for the radiation induced natural convection due to volumetric absorption of solar radiation in a rectangular enclosure against the experimental results of Webb and Viskanta [82]. Section 4.4 presents the validation of the numerical results from COMSOL with experimental results of Coates and Patterson [104] for the unsteady natural convection in a cavity with non-uniform absorption of radiation. Lastly, Section 4.5 presents validation of numerical simulation natural convection in a reservoir sidearm subject to solar radiation with experimental results of Lei and Patterson [84].

4.1 Solar radiation Absorption validation

4.1.1 Experimental test

In this section, an experimental investigation on a direct absorption, open fluid film solar collector carried out by Beard et al. [126] is presented. The study which is modelled with COMSOL Multiphysics software used to ascertain the software capability in solving the system of equations along with its initial and boundary conditions representative of the direct absorption of solar radiation in a working fluid. Fig 4.1 shows a schematic of the low cost open fluid-film solar collector (Solaris open water trickle solar collector). The collector consists of a top glass of single glazing, and a black collector bottom steel plate over which near uniform laminar film flow of silicone oil was pumped. The top glass is transparent to the incident solar radiation and allows incident radiation to be transmitted to the working fluid and the collector plate, whose sole purpose is to absorb the transmitted radiation. The collector was tested under various ambient and fluid flow conditions. Each test was run for ten to fifteen minutes, during which the isolation and inlet and outlet temperatures were measured [126]. Full details of the design, construction and experimental tests for the open fluid film solar collector can be found in [126]. Table 4.1 shows the collector dimensions, material properties and reference operating conditions used in the experiments.

TABLE 4.1: Open fluid-film solar collector geometry parameters and operating conditions [126].

Property	Symbols	Dimensions
Collector Length	l	4.9
Collector width	w	1.1
Plywood deck thickness	thickness	(kg/(ms))
Glass thickness	g thickness	3(mm)
Insulation thickness	Ins thickness	8.99
Aluminium thickness	Al thickness	8.99

Materials property	Symbols	Dimensions
Density	ρ	880(kg/m^3)
Specific Heat	C_p	1.63(J/kgK)
Thermal conductivity	k	k(W/(mK)
Dynamic viscosity	μ	7.0(kg/(ms))
Absorption coefficient	α	3.31m^{-1}
Vapor pressure@40/100^{o}C		4×10^{-4}/0.6mmHg

Materials property	Symbols	Dimensions
Collector eff factor		0.98
Overall thermal loss coff	U	12 (W/m^2 K)
Heat removal factor	F_R	0.88
Flow rate	$\bar{Q}$	0.0150.022 (kg/m^2)
Avg wind speed		4m/s
Heat transfer coefficient	h	5 (W/m^{2}K)
Ambient temperature	T_{amb}	293 (K)
Max and Min Intensity	I	920 (W/m^2)

4.1.2 Numerical model

Fig 4.2 shows a schematic of the numerical domain which is a single channel of one segment of the flow valleys of the open film collector presented in Fig 4.1. The receiver consists of two parallel walls, one of which is top glazing is a 3mm transparent glass is transparent to the incident solar radiation and the other i.e the bottom wall was opaque. At the inlet silicone oil at a constant temperature enters and flows between the top and bottom walls. Solar radiation incident at the top glazing and transmitted through the transparent glass cover is absorbed in the silicone oil flowing through the troughs. The silicone oil flowing through the domain is then heated by the incoming radiation and the bottom plate. Table 4.1 presents dimensions, properties of the material and input parameters used in the present simulation.

$$\left.\frac{dT}{dy}\right|_{y=0} = I_0 e^{-\eta y} \tag{4.1}$$

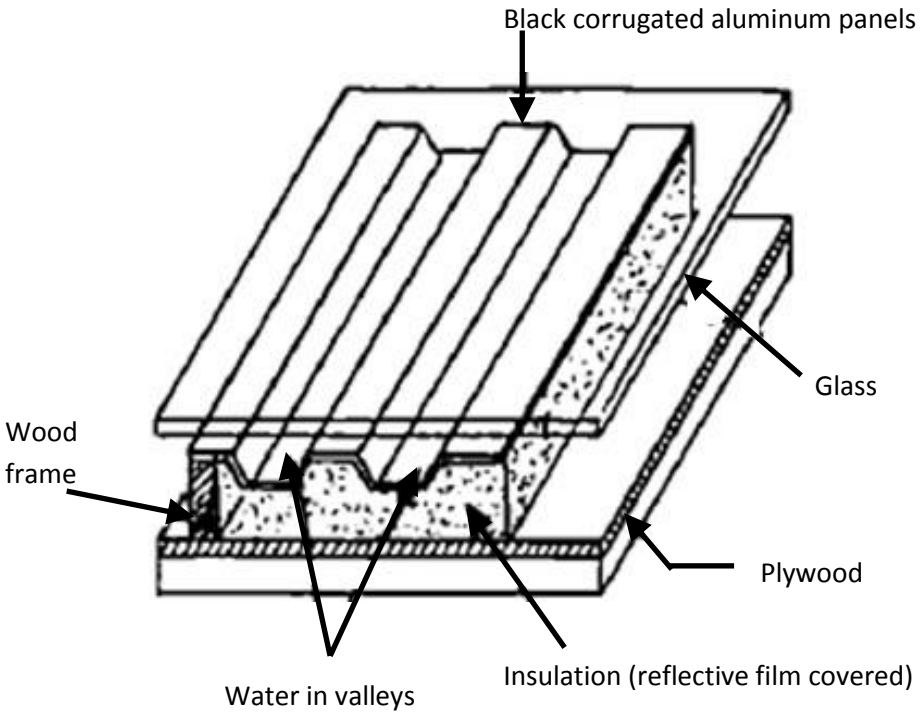

FIGURE 4.1: Open fluid film collector(Solaris)[126].

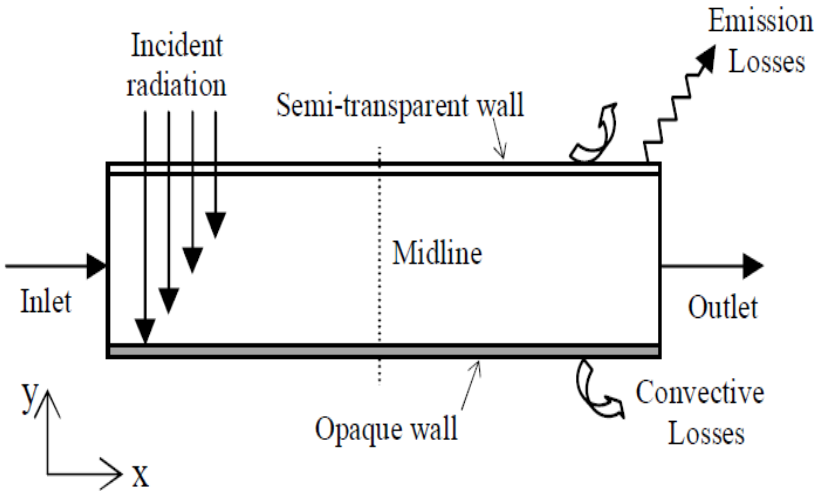

FIGURE 4.2: Two dimensional flow domain considered for the present study [127].

$$\left.\frac{dT}{dy}\right|_{y=H} = 5W/m^2 \tag{4.2}$$

$$u(y) = \frac{3}{2}u\left(1 - \left(\frac{y}{h}\right)\right) \tag{4.3}$$

The physical processes occurring in the flow receiver are governed by the two dimensional mass (equation 3.1) momentum (equation 3.1) and energy equations including the volumetric heating source term (equation 3.3) for two dimensional steady state incompressible laminar flow [127]. Equation 4.1 to 4.3 present the initial and boundary conditions applied. Assumptions considered in the following formulation are: flow within channel is developed, Scattering of energy within the fluid is ignored, solar radiation is uniform and isotropic and fluid absorptivity is approximated by a single value.

The coupled governing equations mass, momentum and energy for two-dimensional steady-state, incompressible, laminar flow from the above numerical compilation is solved in COMSOL Multiphysics environment [120].

Fig 4.3 shows a schematic of the computational mesh made up of triangular element meshes with nodes effectively clustered to the vicinities of all boundaries in the x,y plane.

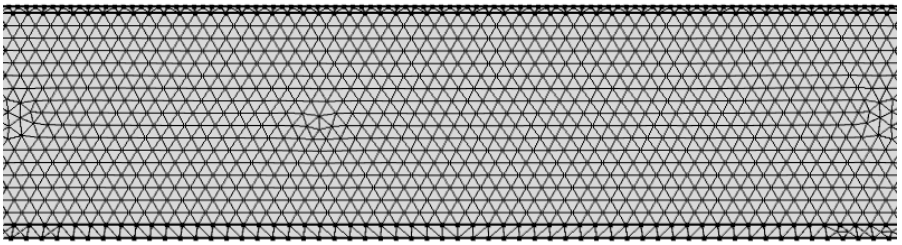

FIGURE 4.3: Mesh of the computational domain

A test of mesh and time-step dependence is conducted prior to the calculation, check of the independence of the numerical result on the mesh element size. Different mesh sizes which ranged from a coarse mesh (100mm) to a fine mesh (5mm), obtained by dividing the maximum mesh size by a mesh refinement ratio (N) i.e(h/N). The solution to the output variable in this case the difference in the solution to the average temperature at

the various mesh element sizes and at the finest mesh is monitored until it converged and remained constant as shown in Fig 4.4. It is clearly seen that as the difference in the average temperature converged at N=5 after which the solution remains fairly constant value at finer element sizes. A mesh is selected at N=8, corresponding to a mesh element size 10mm, above which further reductions in element size did not change the average temperature significantly and the differences of the numerical results were within 4.7%, which indicated that the total amount of 6148 elements was adequate enough to save the computing time without losing the numerical accuracy. The convergence criteria for the residuals of continuity equation, velocity components, and energy equation were 10^{-5}, 10^{-5} and 10^{-5}, respectively. The solutions were obtained once the convergence criteria were satisfied.

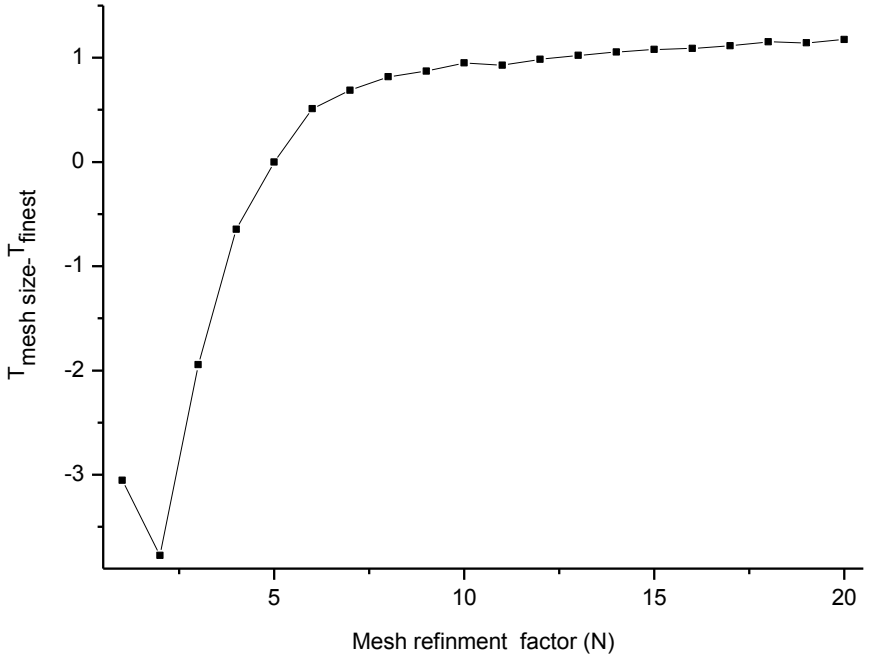

FIGURE 4.4: Mesh refinement plot for test case 1: A plot showing the difference in the maximum temperature for the different mesh densities versus mesh refinement factor (N)

Fig 4.5 shows the experimental results average bulk outlet temperatures of Beard et al. [126] (blue) compared to the predicted steady state numerical solutions (green) obtained using COMSOL. The input condition for each test simulated is presented on top of the results for the respective cases. Direct comparisons to the experimental and numerical results reveals satisfactory agreement between them with errors less than 5% for all five cases.

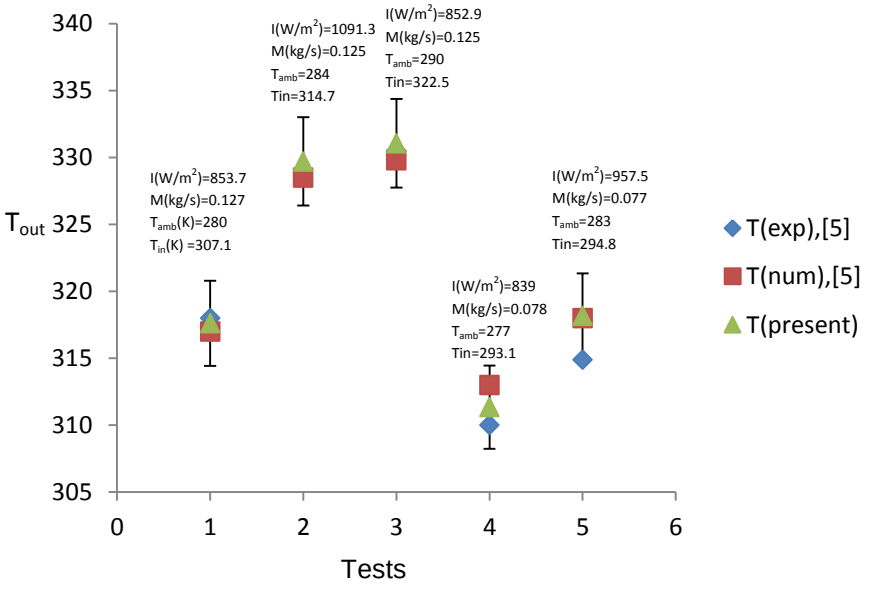

FIGURE 4.5: Comparison of bulk outlet temperature (T_out) between experimental [126] and numerical data [127] and present numerical data for five different cases (see [127]). The error bars show 5% deviation.

4.2 Rayleigh Bernard Convection

In this section, the analytical solutions of the classical Rayleigh Bernard problem for stability of the quiescent state of an infinite fluid layer heated from below and cooled at the top was presented by Drazin [80] and Chandrasekhar [118]. The hydrodynamic flow of a viscous fluid of varying density and temperatures is obtained from solving equations of mass momentum and energy given in equation 4.4 to 4.6:

Continuity:

$$\nabla \cdot \vec{V} = 0 \tag{4.4}$$

Momentum:

$$\frac{1}{Pr}\left(\frac{du}{dt} + u\nabla u\right) = \frac{dP}{dx} = \nabla^2 u \tag{4.5}$$

$$\frac{1}{Pr}\left(\frac{dw}{dt} + w\nabla w\right) = \frac{dP}{dz} - RaT = \nabla^2 w \tag{4.6}$$

Thermal diffusion:

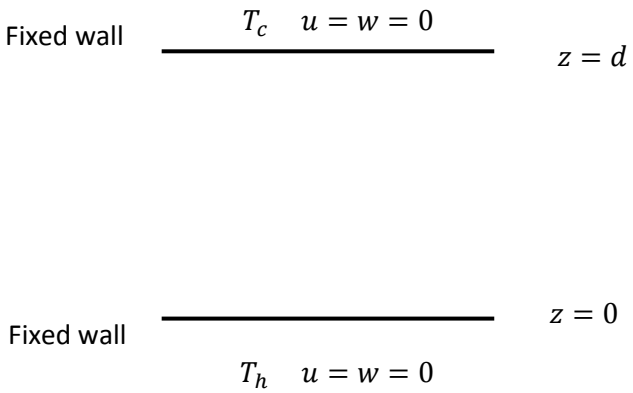

FIGURE 4.6: Rayleigh Bernard problem with two rigid walls.

$$\rho Cv\left(\frac{dT}{dt} + v\nabla T\right) = -k\left[\frac{1}{r}\frac{d}{dr}\left(r\frac{dv_r}{dr}\right)\right] + q \tag{4.7}$$

where u, v and w are the dimensionless velocities in the x,y, and z directions. T is, temperature; pressure p, and heat source q. Ra and Pr are the Rayleigh number and the Prandtl number defined in equation (3.8) and (3.10) respectively.

Full details for the linear stability derivations, perturbed equations and non-dimensional variables, can be found in the study of Drazin [80] and Chandrasekhar [118]. The equations governing the marginal state transition from stability to instability occurring via a stationary state is obtained from equation 4.8 to 4.14 [80]:

$$(D^2 - a^2)W = \left(\frac{g\alpha}{\nu}\right)a^2\Theta \tag{4.8}$$

$$(D^2 - a^2)\Theta = \left(\frac{\beta}{\kappa}\right)d^2 \tag{4.9}$$

where Θ and W are the dimensionless temperature and velocity respectively. Eliminating Θ between these equations, we obtain:

$$(D^2 - a^2)^3 W = Ra^2 W \tag{4.10}$$

Analytical solutions to equation (4.10) exists for three cases: two rigid boundaries, one rigid and one free boundary and lastly, two free boundaries [118]. Parameters characterising the marginal state for the three cases: (the critical Rayleigh number) i.e. the Rayleigh value above which instability sets in and the wave number for the three cases are shown in Table 4.2. Solving the problem for the two rigid boundaries the preceding solutions the case where the bounding surfaces, z=0 and z= 1 are rigid, the following can be found:

TABLE 4.2: Parameters characterising the marginal state for the three cases, Pr=7 [118].

Nature of the bounding surface	Ra_c	a	$2\pi/a$
Both free	657	2.2214	2.828
Both rigid	1708	3.117	2.026
One rigid one free	1101	2.682	2.342

$$W = (D^2 - a^2)^2 W = 0 \text{ for z=0 and 1} \tag{4.11}$$

The solution

$$DW = 0 \text{ for z=0 and } \mathrm{D}^2 W \text{ for z=1} \tag{4.12}$$

The solution

$$W = A_0 \sin q_0 z + A \sinh qz + A \sinh q_1 z \tag{4.13}$$

$$W = \sin q_0 z - 0.045302 \sinh q_1 z \cos q_2 z + 0.00121173 \cosh q_1 z \sin q_2 z \tag{4.14}$$

$$w = W(z) \cos \frac{2\pi}{L} x \tag{4.15}$$

$$u = \frac{DW}{a^2} \frac{2\pi}{L} \sin \frac{2\pi}{L} x \tag{4.16}$$

where the solution to the cell patterns (rolls) are given by:

$$w = W(z) \cos \frac{2\pi}{L} x \tag{4.17}$$

where L is constant corresponding to a particular wave number, a:

$$L = \frac{2\pi}{a} \tag{4.18}$$

4.2.1 Numerical model

A schematic representation of the numerical domain for the Rayleigh Bernard problem investigation is shown in Fig 4.7. The domain consists of sides of dimensions H. The gravity vector is directed in the negative y coordinate direction, and the fluid is assumed to be water with Pr=7. The non-dimensional governing equations for the Rayleigh Bernard convection problem are conservation of mass, the incompressible Navier–Stokes equations, and the energy equation given in equation 4.4 to 4.6and the Boussinesq approximation is assumed to be valid.

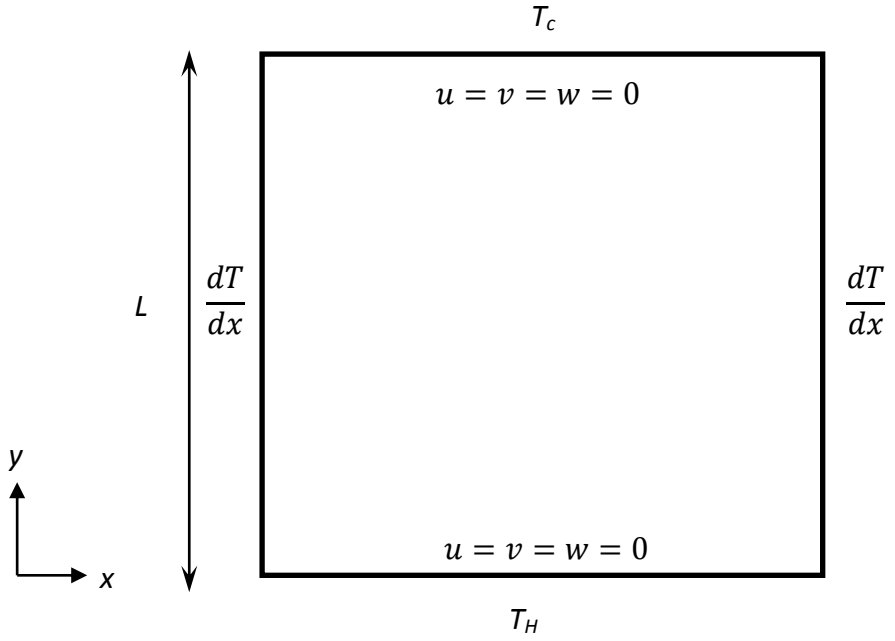

FIGURE 4.7: Rayleigh Bernard problem with two rigid walls Schematic diagram of the physical model and coordinate system.

A finite Element Method [120] is used to discretise the coupled Navier–Stokes and energy equations. The velocity and pressure terms are discretized using a second order and linear elements (P_1+P_2) scheme [120].

In order to ensure mesh independence of solutions, a mesh sensitivity tests for the case Ra = 1078 and Pr = 7 were conducted for different mesh element sizes, which ranged from a coarse mesh (200mm) to a fine mesh (5mm). Fig 4.11 shows the convergence of the

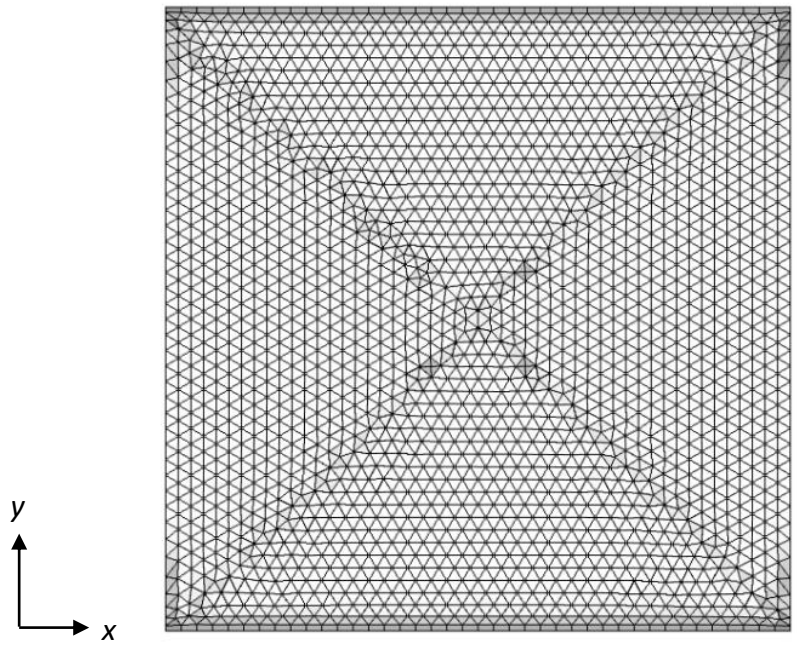

FIGURE 4.8: Computational mesh.

difference in the maximum value of the vertical velocity, (w_{max})at the respective mesh sizes and the solution at the finest mesh element size, with mesh refinement. The plot shows convergence at the mesh refinement factor N=5 which corresponds to an element size 20mm . Thus an element size 20mm is selected, which gives 1% error which is considered to be fine enough to get accurate solutions. Fig 4.8 shows the computational mesh used consisting of 6586 elements mesh elements. A convergence criterion of 10^{-6} was imposed on the residuals of all the governing equations.

The numerical model was also checked for accuracy against the published numerical solution of Chandrasekhar [118] for natural convection of fluid in an enclosure of aspect ratio (A) of 1 heated from below. A comparison of the streamlines and vertical velocity, are presented in Fig 4.9 and Fig 4.10. Results obtained from numerical results are in quite good agreement with those of Chandrasekhar [118].

4.3 Radiation-Buoyancy driven flow in rectangular enclosure.

In this section, the experimental works of Webb and Viskanta [82] on radiation induced natural convective motion in a vertical rectangular tank is simulated with COMSOL. For

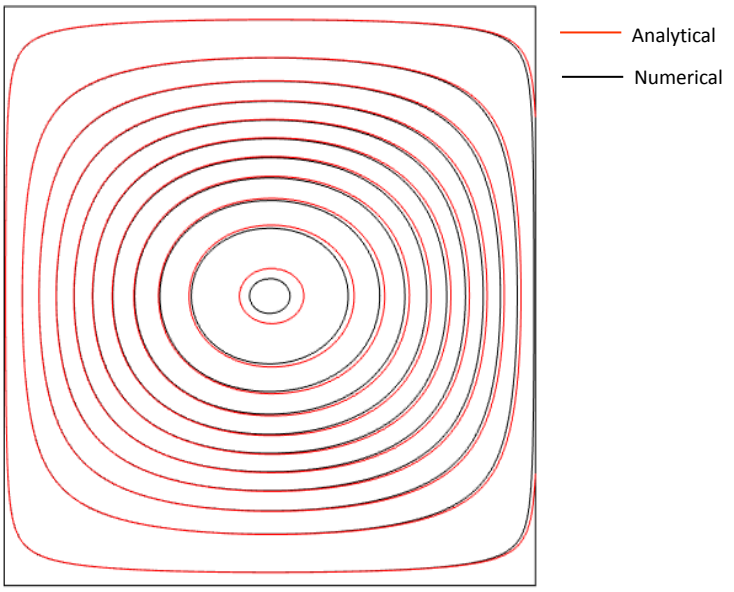

FIGURE 4.9: Solutions: analytical [118] and numerical Streamlines for Rayleigh Bernard problem with two rigid walls.

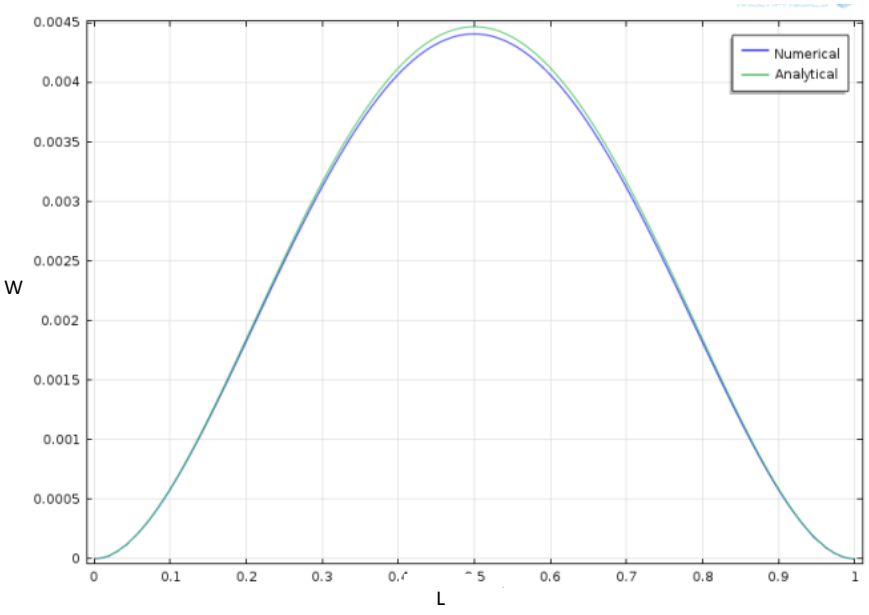

FIGURE 4.10: Analytical [118] and Numerical results for the velocity for Rayleigh Bernard problem with two rigid walls.

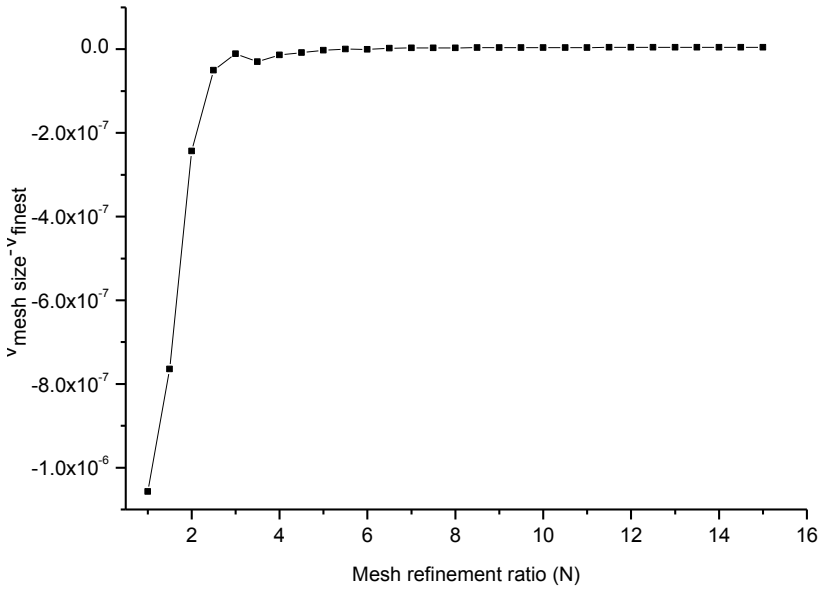

FIGURE 4.11: Mesh refinement plot for test case 2: A plot showing the difference in the maximum velocity for the different mesh densities versus mesh refinement factor (N).

brevity, a brief description of the experiment is presented below and the full description of the experimental study can be found in Webb and Viskanta [82]. Fig 4.12 shows a schematic of the test cell and its components. The test cell has dimensions of 48 by 145 by 41mm and is made up of optically transparent windows which form the front and back walls of the enclosure. The optically transparent windows provide access for flow visualisation using a Mach Zehnder interferometer system [82]. A heat exchanger fabricated from a 12.7mm thick copper block, and painted black with 3M Brand ECP 2200 solar absorber coating formed one of the interior vertical walls (Fig 4.12). The exterior surface of the test cell was insulated with 5cm Styrofoam insulation, while the inner compartment contains degassified water. The top of the acrylic test cell was left open for filling the enclosure. The test cell was illuminated with Quartz halogen lamps, with parabolic dichroic mirrors (Philips 13117) which estimated the solar spectrum at sea level. A spatial uniformity of the radiation of 9% on the average was achieved over a typical 90mm exposed test fluid height after eight to ten hours when the system reached steady state. The optical quality window and Mach Zehnder interferometer to which the test cell was mounted, were adjusted to achieve the infinite fringe condition so that any subsequent variation in intensity will result in thermal disturbances in the system. Mach Zehnder interference images were recorded as well as the flow visualisation performed by

injection of fluorescence dyes [82]. Interferograms showing fringes for enclosure aspect ratios 1 and 2 are presented in Fig 4.16a and Fig 4.17a respectively.

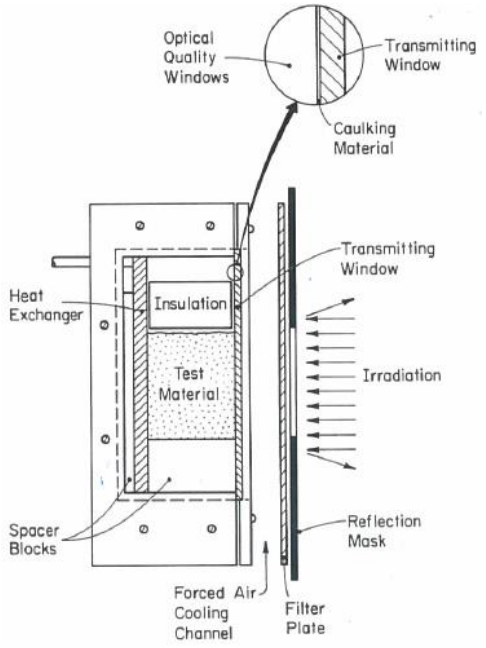

FIGURE 4.12: Schematic of test apparatus[82].

4.3.1 Numerical simulation.

Fig 4.13 shows a two dimensional computational domain for the test cell (Fig 4.12). The left vertical wall is opaque and is at held at a constant temperature, while the right vertical wall is transparent and transmits radiant energy incident upon it, while confining the test fluid. The top and bottom wall are rigid and adiabatic boundaries. Incident radiation at x=D, penetrates the fluid layer and is absorbed. The absorbed radiation then heats the fluid volumetrically and subsequently develops a buoyancy driven flow. The temperature and fluid flow developed in the enclosure are solved for using the 2 dimensional steady state, conservation of mass, momentum and energy equations assuming Boussinesq approximations (equations 3.1 to 3.3). The input parameters and boundary conditions include: at the transmitting wall ϵ =1, r=0 incident radiation flux incident I_0= 1300W/m^2, temperatures of the cooled wall and cooling air temperatures were 23.1^{o}C and 22.3^{o}C respectively [82]. The vertical transmitting wall is considered to be infinitely thin, perfectly transparent and absorbs none of the incident radiant energy as such the conjugate effects are neglected. Assumptions: Incident flux at x=D, penetrates the fluid layer and is absorbed within the fluid resulting in local volumetric

heating and subsequent buoyancy driven flow. The radiation flux is assumed to be one dimensional. Flow is assumed to be stead, two dimensional and laminar. Thermophysical properties are taken to be constant and Boussinesq approximation applies. The spectral parameter, dimensionless governing equation (equations 4.19 to 4.22) and their boundary conditions were solved using COMSOL Multiphysics. P_1+P_2 discretisation schemes were applied to the velocity and pressure fields. For the discretisation of the flow domain, non uniform triangular meshes are constructed within the flow domain with elements clustered toward all interior surface of domain. Fig 4.14 shows a schematic of the computational mesh.

$$\frac{\partial U}{\partial \xi} + \frac{\partial V}{\partial \eta} = 0 \tag{4.19}$$

$$U\frac{\partial U}{\partial X} + V\frac{\partial U}{\partial Y} = -\frac{\partial P}{\partial X} + Pr\left[\frac{\partial^2 U}{\partial X^2} + \frac{\partial^2 U}{\partial Y^2}\right] \tag{4.20}$$

$$U\frac{\partial V}{\partial X} + V\frac{\partial V}{\partial Y} = -\frac{\partial P}{\partial X} + Pr\left[\frac{\partial^2 V}{\partial X^2} + \frac{\partial^2 V}{\partial Y^2}\right] + RaPr\Theta \tag{4.21}$$

$$U\frac{\partial \Theta}{\partial X} + V\frac{\partial \Theta}{\partial Y} = -\frac{\partial \Phi}{\partial X} + \frac{\partial^2 \Theta}{\partial X^2} + \frac{\partial^2 \Theta}{\partial Y^2} \tag{4.22}$$

where X,Y = (x,y)/D dimensionless coordinates , U,V= (u,v)D,κ dimensionless velocities, Θ=(T-T_w)k /(I_0D)

Boundary conditions are:

$$U = V = \left.\frac{\partial \Theta}{\partial Y}\right|_{Y=0} \tag{4.23a}$$

$$\frac{\partial U}{\partial Y} = V = \left.\frac{\partial \Theta}{\partial Y} = 0\right|_{Y=A} \tag{4.23b}$$

$$U = V = \Theta = 0\Big|_{X=0} \tag{4.23c}$$

$$U = V = \Theta = 0\Big|_{X=1} \tag{4.23d}$$

$$k\frac{\partial \Theta_g}{X} = \left.\frac{\partial \Theta}{X}\right|_{\Theta=\Theta_g} \tag{4.23e}$$

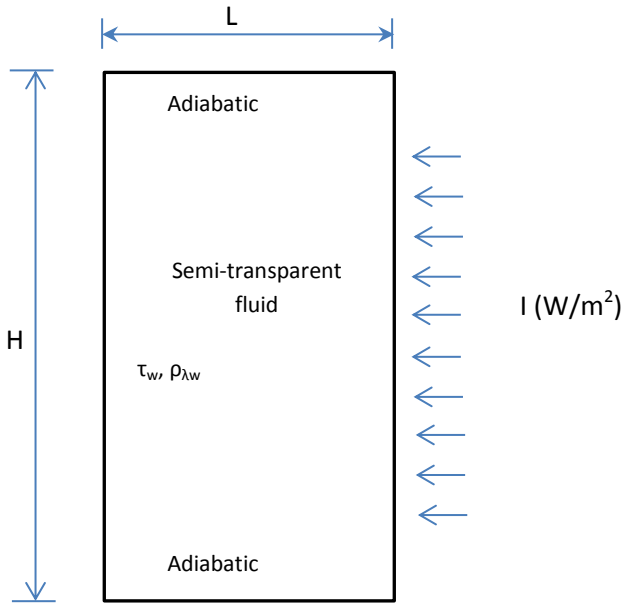

FIGURE 4.13: Numerical domain representing test cell.

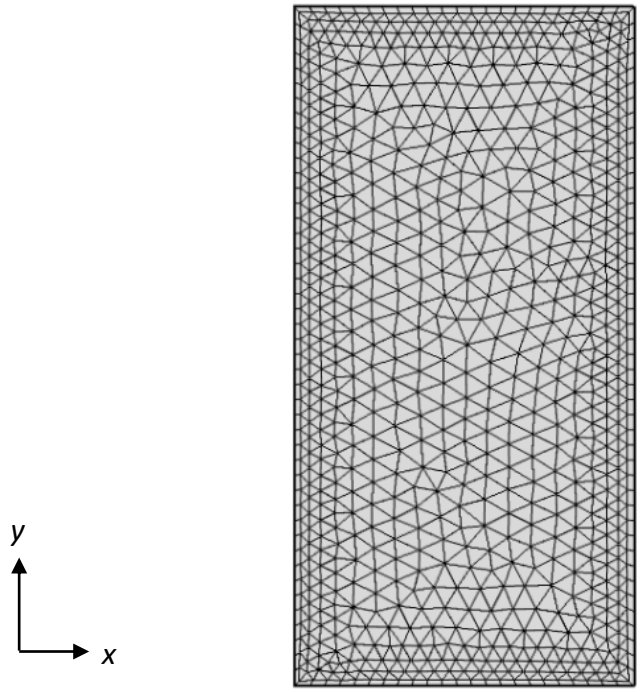

FIGURE 4.14: Computational domain.

Fig 4.15 shows the mesh convergence for the solution of the average temperature against the mesh refinement ration for $1 \leqslant N \leqslant 15$. From Fig 4.15 the difference in average temperature solution converges at N=5 equivalent to an element size of 20mm consisting of 3826 elements, above which there is little changes the solution for the maximum temperature.Thus selection of this mesh element size gives a 2.2% error with reference to the solution at the finest mesh element size. A convergence criterion of 10^{-5} was imposed for the residuals of continuity equation, velocity components, and energy equation respectively.

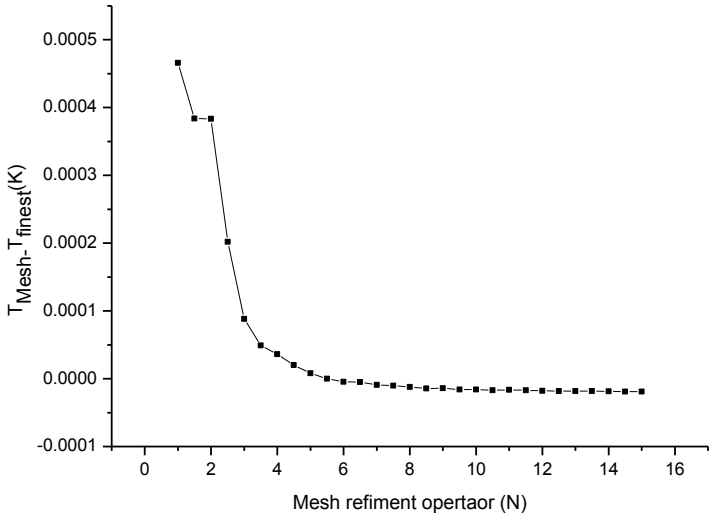

FIGURE 4.15: Mesh refinement plot showing the difference in the average temperature for the different mesh densities versus mesh refinement factor (N).

We also carried out some numerical simulations to check the validation of the numerical scheme. The comparison of the numerical results are carried out against experiments results of Webb and Viskanta [82].

Fig 4.16a and Fig 4.17a show interferograms for enclosures aspect ratio of 1 and 2 as obtained from experiments [82]. Fig 4.16b and Fig 4.17b shows the isotherms obtained from numerical simulations for identical aspect ratios 1 and 2. In Fig 4.16a and Fig 4.17a, the difference in the fringe densities at the two vertical walls is indicative of the absorption of the radiation; higher fringe density at the cooled wall (heat exchanger) indicates the higher convective heat transfer [82]. In both experimental and numerical studies identical features are observed. Boundary layers are present on both vertical walls, with

the boundary layer at cooled wall being the thinnest. The interior core of the enclosure is stagnant and stably stratified. Fig 4.18 shows the plot of the predicted and experimentally measured temperature profile in the test cell at the vertical line L/2, for Ra=2.268 and aspect ratio (A) equal to 2.0. The results show good agreement, except near ι =2, where heat loss from the free surface effects were present. ι and Θ are the dimensionless height and temperature respectively.

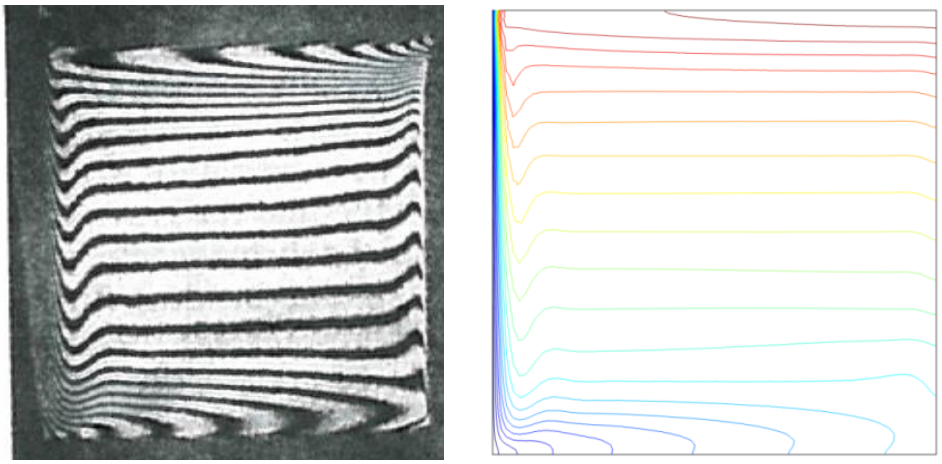

FIGURE 4.16: Experimental and numerical isotherms at H/W=1. Left: Inferrograms [82] and right:Present study.

4.4 Unsteady natural convection in a cavity with non-uniform absorption of radiation

This section considers the validation of the unsteady natural convection problem in an enclosure, where the primary driving force is the absorption of a top incident radiation incident by the fluid. Coates and Patterson [104], experimentally investigated the unsteady natural convection in a rectangular tank shown in Fig 4.19 generated by the absorption of radiation. The tank consists of three chambers of internal size of height=300mm, width l =200mm and total length (le+l)=600mm (Fig 4.19), where l is the length of the opaque region, and le is the length of the transparent region through which radiative energy enters. A perspex lid was directly placed at the water surface

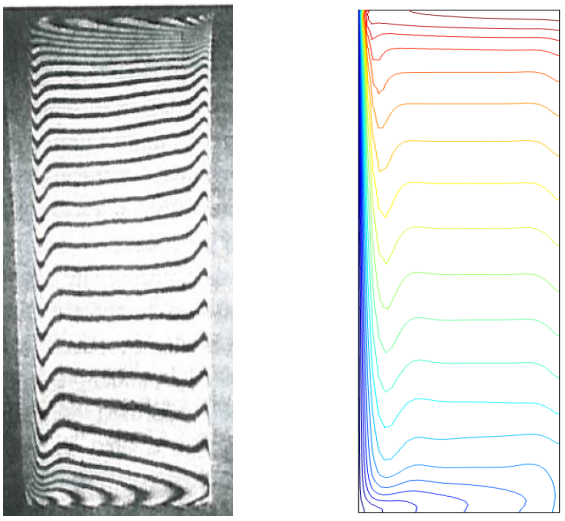

FIGURE 4.17: Experimental and numerical results at H/W=2. Left: Inferrograms [82] and right: Present study.

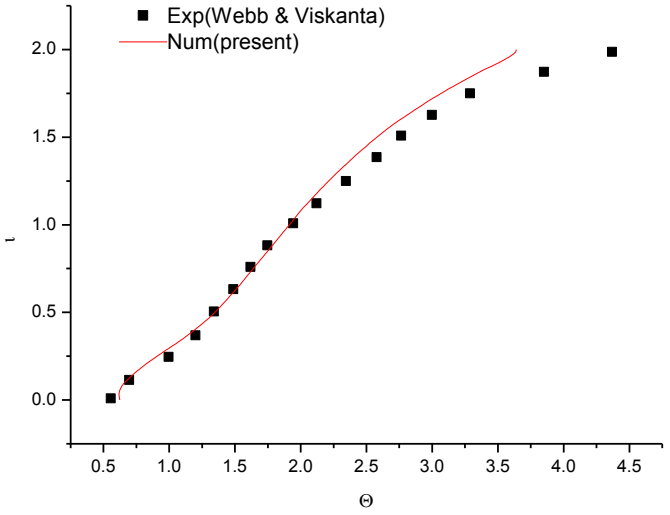

FIGURE 4.18: Comparison of predicted and experimentally determined vertical temperature profile at x=L/2 for water, Ra=2.26×10^8 and A=2.0.

which formed a non-slip boundary and held the blocking layer and the section of aluminium film foil covering the part of the surface, where radiation was restricted from entering the tank (Fig 4.19). The tank was filled with filtered water supplied and maintained by a constant temperature bath to ensure that the tank and bath were isothermal. A 1000W quartz globe, spot theatre lamp (light source) characterised by uniformity and parallicity simulated the solar spectrum and illuminated water within the tank. Temperatures were measured using thermistors placed at fixed locations at the unshaded distance as shown in Fig 4.19. Fluid velocities were measured by a pattern tracking technique using 75μm particles of Pliolite tracer. Details of the functions and operation of the other components and parts readers are referred to Coates and Patterson [104]. Table 4.3 and Table 4.4 show the experimental data.

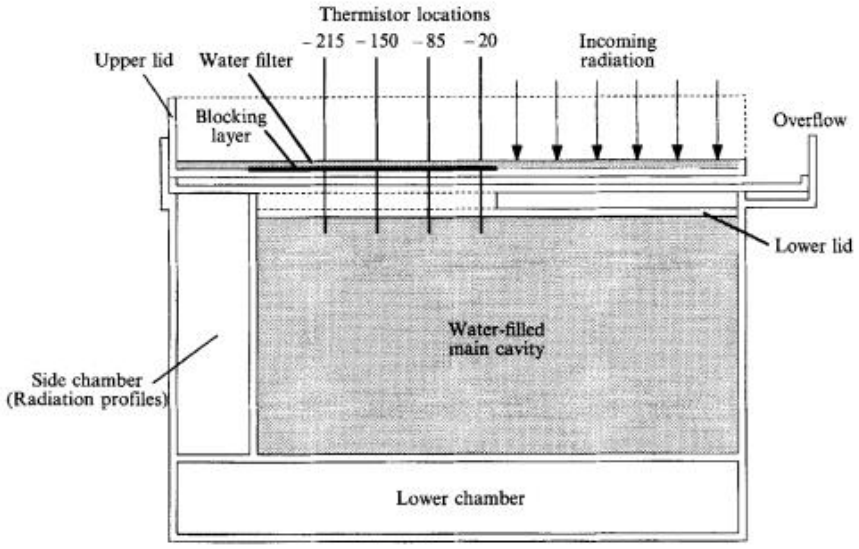

FIGURE 4.19: A schematic of the experimental set up which shows the two lids in place and with the experimental cavity filled (the shaded region in the sketch). The blocking layer ensures that the left side is not illuminated. [103].

4.4.1 Numerical

A two dimensional schematic of the experimental tank of Coates and Patterson [104] is presented in Fig 4.20. The domain has a depth h and and total length L (L_e+L) and contains a Newtonian fluid (water) initially at rest at a temperature T_0. The side walls and lower walls are rigid, adiabatic side and non slip boundaries. Side walls are

TABLE 4.3: The best fit three band model for the surface energy flux Ii and attenuation coefficient η to the temperature/depth data. The surface fluxes for the three experiments are given in the columns MAX (maximum intensity), WF (water filter) and ND (neutral density filter) [104].

Band	wavelength	percentage of total energy	MAX	WF	ND	nt
1	>1200	~50	64.5	18	48.5	145
2	800-1200	30	39	33.5	29	15
3	<800	20	24	23.5	18	2.5

TABLE 4.4: The bulk values for the surface flux I, and the attenuation coefficient η for the three experiments. The equivalent Grashof number and dimensionless attenuation coefficient are also given [104].

Experiment	I_0	Gr	η	η *
Maximum intensity	115	4.33e8	21.6	6.48
Water filter	64	2.41e8	15.6	6.68
Neutral density filter	87	3.28e8	21.6	6.48

maintained at isothermal condition. The upper boundary is isothermally insulated. The left top surface is opaque to solar radiation, while the right top surface is transparent to incident radiation at this surface. The test considered was for the parameter values Gr= 4.33×10^8, Pr=7.04 and A=A_E. Incoming radiation was divided into three bands with (nondimensional) intensities and attenuation band as given in Table 4.3 and Table 4.4, respectively. The temperature and velocity fields are obtained from solving the coupled energy, momentum and continuity equations along with the Boussinesq assumption and including the source term (equations 4.24 to 4.27) . The spectral parameters were accounted for by a single value and three spectral band models.

$$\frac{\partial u}{\partial x}+\frac{\partial w}{\partial z}=0 \tag{4.24}$$

$$\frac{\partial u}{\partial t}+A_E\left(u\frac{\partial u}{\partial x}+w\frac{\partial u}{\partial z}\right)=-\frac{\partial p}{\partial x}+\left(\frac{A_E^2}{Gr}\right)^{\frac{1}{3}}\left(\frac{\partial^2 u}{\partial x^2}+\frac{\partial^2 u}{\partial z^2}\right) \tag{4.25}$$

$$\frac{\partial w}{\partial t}+A_E\left(u\frac{\partial w}{\partial x}+w\frac{\partial w}{\partial z}\right)=-\frac{\partial p}{\partial x}+\left(\frac{A_E^2}{Gr}\right)^{\frac{1}{3}}\left(\frac{\partial^2 w}{\partial x^2}+\frac{\partial^2 w}{\partial z^2}\right)+A_E T \tag{4.26}$$

$$\frac{\partial T}{\partial t} + A_E\left(u\frac{\partial T}{\partial x} + w\frac{\partial T}{\partial z}\right) = -\frac{1}{Pr} + \left(\frac{A_E^2}{Gr}\right)^{\frac{1}{3}}\left(\frac{\partial^2 T}{\partial x^2} + \frac{\partial^2 T}{\partial z^2}\right) + H(x)\sum_{i=1}^{N}\alpha I_i exp[-\alpha z] \tag{4.27}$$

Variables in equation equations (4.24) to (4.27) are non dimensionlised using the following schemes

$x = x^* h^{-1}$, $z = z^* h^{-1}$, $t = vt^* h^{-2}\left(\frac{A_E^2}{Gr}\right)^{\frac{1}{3}}$, $u = hu^* v^{-1}(GrA_E)^{-1/3}$, $w = hw^* v^{-1}(GrA_E)^{-1/3}$, $T = (g\beta h^3(T^* - T_0))(v^2(GrA_E)^{2/3})^{-1}$, $I = I^* I_0^{-1}$, $\alpha = \alpha^* h$. where the stared variables are dimensional. H(x)= 0 for $0 \leqslant x \leqslant A^{-1}$ and 1 for $0 \leqslant x \leqslant A^{-1} + A_E^{-1}$. Gr the Grashof number is defined as $Gr = (g\beta I_0 h^4)(\rho^2 C_p \nu^2)^{-1}$

The governing equation and their boundary condition were solved using COMSOL Multiphysics. P_1+P_2 discretisation schemes were applied to the velocity and pressure fields.

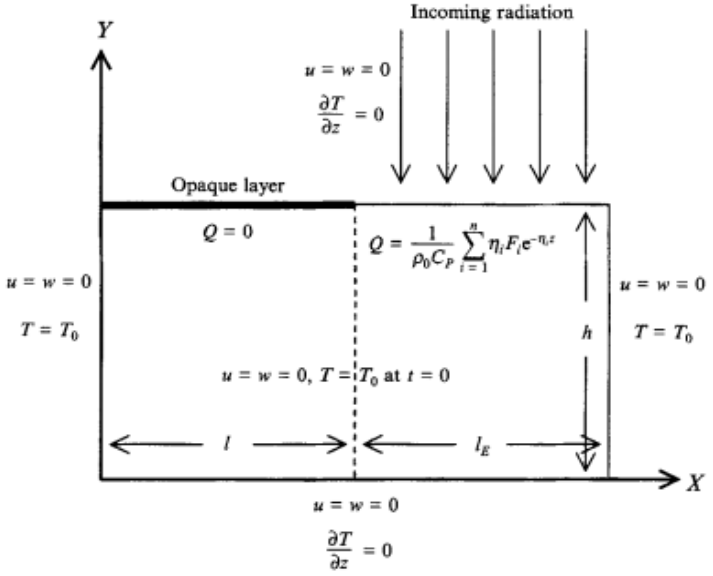

FIGURE 4.20: Schematic of the cavity and boundary conditions [104].

4.4.2 Validation

Fig 4.22 shows the plot of the experimental and numerical results for the maximum velocity against the square root of the dimensionless time. Good agreement can be

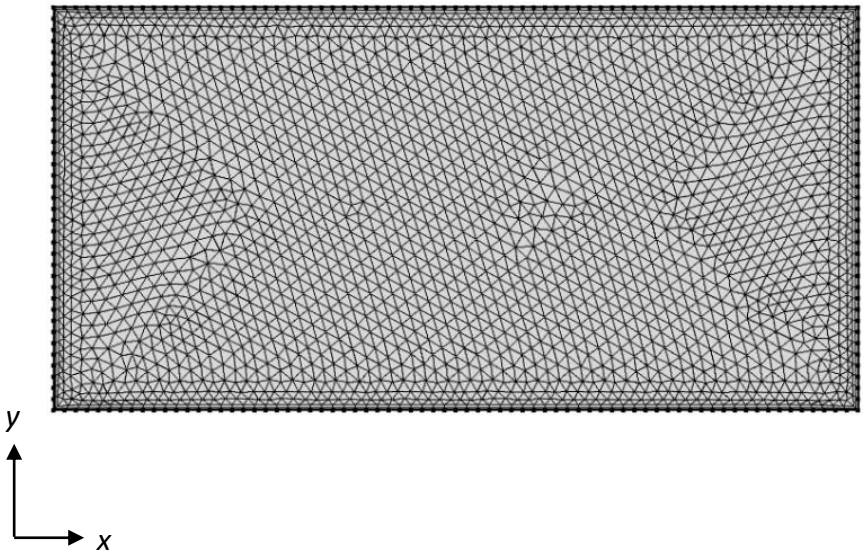

FIGURE 4.21: Refined Mesh arrangement.

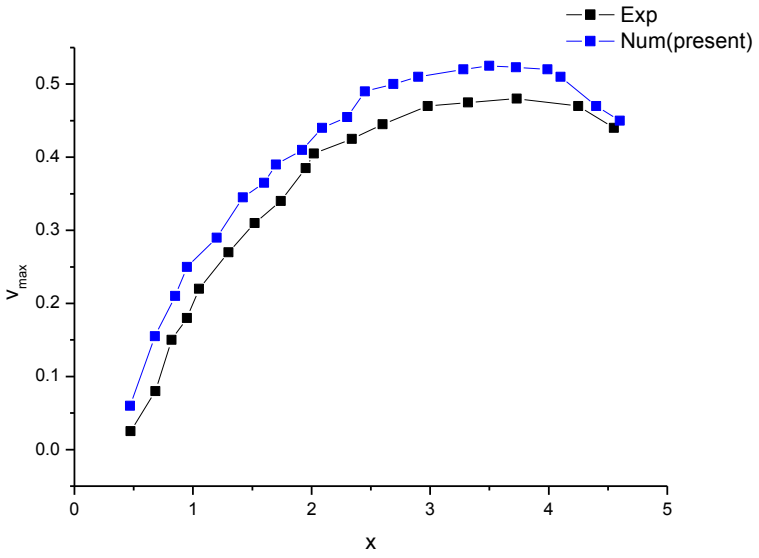

FIGURE 4.22: Maximum velocity plotted against square root of time for experiments and numerical simulation.

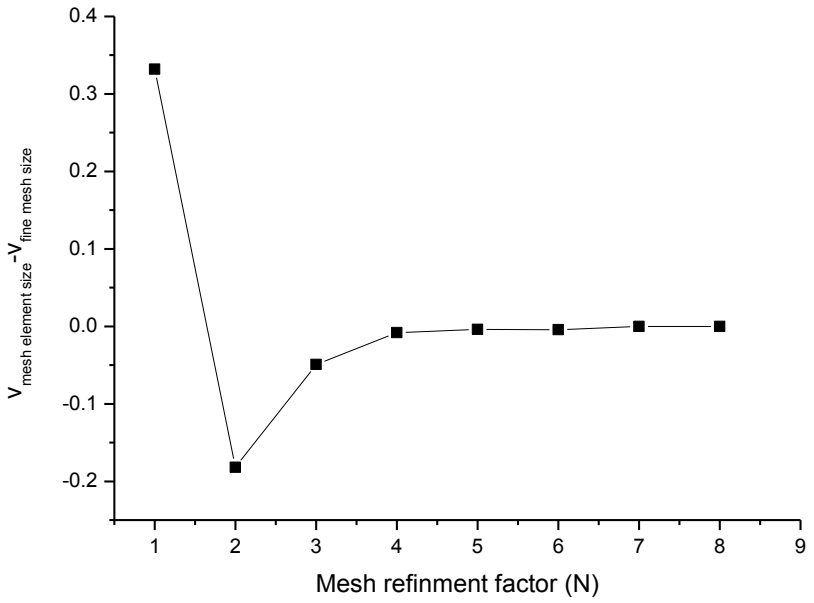

FIGURE 4.23: Mesh refinement plot showing the difference in the maximum velocity for the different mesh densities versus mesh refinement factor (N)

seen between the experiments and the simulations results thus, giving confidence in the numerical code. The mesh dependence has been conduced by tracking the solution in the difference in maximum velocity at different mesh sizes from a coarse mesh and the solution of the maximum velocity at a fine mesh. Fig 4.23 shows convergence in the solution is attained at N=3 corresponding to an element size 10mm. Fig 4.21 shows the computational domain at selected mesh consisting of 4698 mesh elements. Selection of this mesh size gives approximately a 2% deviation from the numerical result obtained at the fine mesh. The solution convergence is met when the difference between normalised residual of the algebraic equation and the prescribed value is less than 10^{-4} for all variables.

4.5 Natural convection in a reservoir sidearm subject to solar radiation

Laboratory experiments Lei and Patterson conducted to investigate the daytime natural convection in a side arm is presented in this section. The experiment the side arm was modelled using a triangular tank with sloping and absorptive bottom, which, contained water at an isothermal and stationary state. A spot theatre lamp was used to simulate

solar radiation incident in the flow domain, which was switched on instantaneously and maintained at constant intensity throughout the duration of the experiment. The tank had a length of 600mm and side arm height of 60mm. The water temperature in the wedge then increases as a consequence of absorption of the radiation. The convective flow was visualised using a shadow techniques, while the temperature were measured simultaneously at discrete locations along the sloping bottom. Shadow graphs showed three distinct stages of the flow development; initial transitional and quasi steady stages

4.5.1 Numerical formulation

Fig 4.24 shows a schematic of the two dimensional flow domain under consideration. The triangular wedge has a length L = 600mm, maximum depth h= 60 mm, and bottom slope A = h/L =0.1 (see Fig 4.24), dimensions corresponding to those of the experimental model . Singularity at the tip in the numerical simulations was avoided by cutting the tip of at x = 60 mm. The flow domain is filled with water initially at rest and at temperature T_0. At time t = 0, a surface radiation of intensity I_0 is initiated and thereafter maintained. When the surface radiation travels through a water column, the radiation intensity at a particular wavelength decreases with depth according to Beer's law: $I=I_0e^{-ay}$, where I_0 is the incident solar radiation , a is the attenuation coefficient for water which is strongly dependent on the wavelength of the radiation. Similarly as found in most limnological applications this value is be characterised by a single bulk attenuation coefficient, and that assumption is also adopted in this study. Equations (4.28) to (4.31) govern the developing temperature and flow fields.

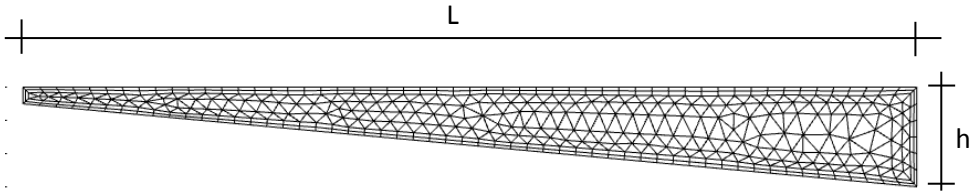

FIGURE 4.24: A schematic of the geometry and mesh.

$$\frac{\partial u}{\partial x} + \frac{\partial v}{\partial y} = 0 \tag{4.28}$$

$$\frac{\partial u}{\partial t} + u\frac{\partial u}{\partial x} + v\frac{\partial u}{\partial y} = -\frac{1}{\rho_0}\frac{\partial P}{\partial x} + v\nabla^2 u \tag{4.29}$$

$$\frac{\partial v}{\partial t} + u\frac{\partial v}{\partial x} + v\frac{\partial v}{\partial y} = -\frac{1}{\rho_0}\frac{\partial P}{\partial x} + v\nabla^2 v + g\beta(T - T_0) \tag{4.30}$$

$$\frac{\partial T}{\partial t} + u\frac{\partial T}{\partial x} + v\frac{\partial T}{\partial y} = -k\nabla^2 T + I_0\alpha e^{-\alpha y} \tag{4.31}$$

Boundary conditions for velocity and temperature are described follows: On the sloping bottom, rigid nonslip velocity conditions (u = v = 0) apply. The same velocity conditions apply to the end wall at x = L, which is also insulated (dT=dx = 0). On the water surface, it is assumed that any heat loss through the surface is small compared with the heat capture via absorption of radiation. In other words, it is assumed that the water surface is insulated (dT=dy = 0). It is also assumed that the water surface is stress-free (v = 0 and (du=dy = 0).

$$\frac{\partial u}{\partial x} + \frac{\partial v}{\partial y} = 0 \tag{4.32}$$

$$\frac{\partial u}{\partial t} + u\frac{\partial u}{\partial x} + v\frac{\partial u}{\partial y} = -\frac{1}{\rho_0}\frac{\partial P}{\partial x} + v\nabla^2 u \tag{4.33}$$

$$\frac{\partial v}{\partial t} + u\frac{\partial v}{\partial x} + v\frac{\partial v}{\partial y} = -\frac{1}{\rho_0}\frac{\partial P}{\partial x} + v\nabla^2 v + g\beta(T - T_0) \tag{4.34}$$

$$\frac{\partial T}{\partial t} + u\frac{\partial T}{\partial x} + v\frac{\partial T}{\partial y} = -k\nabla^2 T + I_0\alpha a^{\alpha y} \tag{4.35}$$

Equations **??** to 4.35 present the nondimesionlised governing equations based on the scales x,h $\sim \alpha$ (length scale), t $\sim (\mathrm{kH}^2)^{-1}$ (time scale), T $\sim$ I/kα (temperature scale), u,v $\sim$ kα(velocity) which is solved using a finite element method in COMSOL Multiphysics. The velocity components and temperature are directly obtained from the Navier-Stokes equations and the energy equation. Second-order elements for the velocity field and linear elements for the pressure field, (P_2+P_1) discretisation is used [120]. To define the size of a mesh to ensure the independence of computational results and gives a good compromise between accuracy and CPU cost, mesh refinement tests were performed. The mesh convergence test plot for two-dimensional simulations for the convective Flow is calculated for the case of I_0=50Wm^2 at a reference temperature 21.5^{o}C, which gives Gr = 2.51 $\times$ 10^6 and Pr = 6 and measured bulk attenuation coefficient is 6.16 m^{-1}. It can be seen from Fig 7.3 that as the mesh was refined from a coarse mesh to a fine mesh,

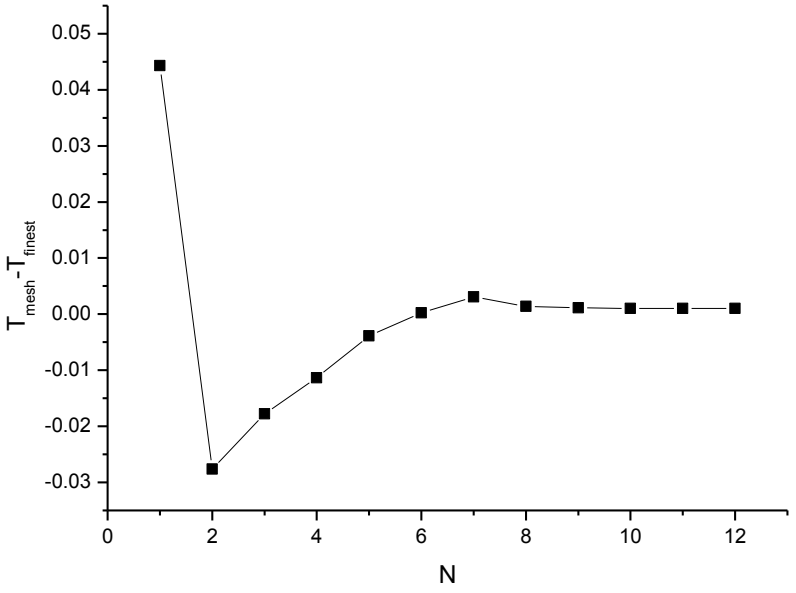

FIGURE 4.25: Mesh convergence plot)

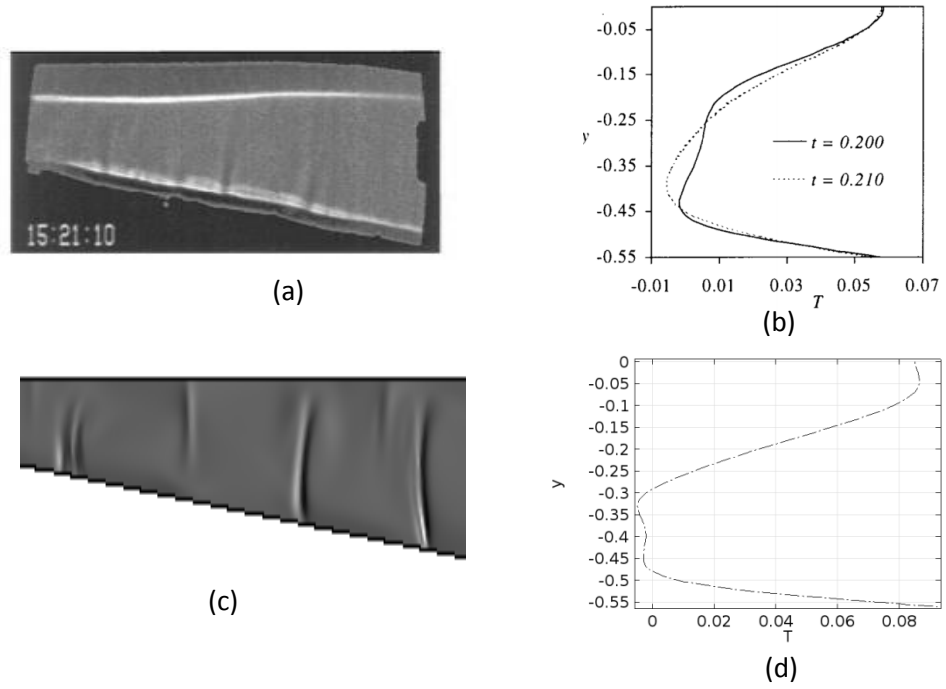

FIGURE 4.26: Flow structures and temperatures in the quasi steady state for experiments (top) and numerical simulation (bottom): (a) shadow graph from experiment at 600s [84] (b) vertical temperature profile at x=5.5 [84] (c) shadowgraph for numerical simulation at 710s (d) vertical temperature profile at x=5.5 (numerical)

seen by the increasing value of the refinement ratio (N), the difference in the solutions at the respective mesh element sizes converged at N=7. Thus a mesh element size of 3mm (N=8), was the selected and considered sufficient for the accurate simulation. A mesh of 3mm gives a domain consisting of 8272 elements and an error in the average temperature of 0.01% compared solution at the finest mesh element size considered the convergence criteria for the residuals of continuity equation, velocity components and energy equation were 10^{-5}. The solutions were obtained once the convergence criteria were satisfied. Results obtained from the numerical simulation of the experiments of Lei and Patterson [84] are compared with the corresponding results. Results presented show the flow structures and temperature profiles in the quasi steady. From the results presented a good agreement is observed.

In summary, since neither analytical solutions nor experimental data currently exist (to the authors knowledge) of the exact problem, verification and validation of the numerical model has been based on a comparison between the numerical model against the published analytical solutions and experimental data of similar problems. Numerical error of 4.7%, 1%, 2.2%, 2.2% and 1% are associated with numerical results for all validation cases studied. In conclusion, in all cases the overall error stays less or equal to 5%. Such a deviation is considered as acceptable in order to have a reasonable level of accuracy for the current problem, thus the present radiation induced absorption models are considered validated.

Chapter 5

Heat transfer in a cavity filled with high temperature molten salt absorbing concentrated solar radiation

Numerical simulation of the transient heating of a high temperature molten salt filled enclosure of unit aspect ratio and subjected to concentrated solar radiation is presented in this chapter. Non-uniform concentrated flux deposited into a body of molten salt from the top of the enclosure heats the salt in two ways: (1) the volumetric absorption of the penetrative radiation as it passes through the fluid depth, and (2) convection from a lower boundary surface absorber plate, heated from the full absorption of transmitted (non absorbed) radiation reaching this surface. The enclosure is studied for a specific case in which the radiatively heated bottom surface develops a temperature gradient sufficient to generate natural convection to enhance heat transfer, mix the salt and improve energy storage. Understanding the heat transfer and fluid dynamics in this system is of greatest importance to the design of a thermal store for a small scale (circa 5kWe) Concentrated Solar Power (CSP) system. Isothermalisation of the store is required to maximise the storage capacity without damaging the storage medium, which can typically sustain temperatures up to 600^{o}C.

In the present study the driving mechanism and flow features in radiation induced natural convection flows in a cylindrical geometry is considered. The model accounts for depth dependent volumetric heating of the fluid domain by using a single bulk attenuation coefficient value and an isotropic incident solar radiation, which is consistent with previous studies [81–86, 91, 92]. Numerical results are presented in terms of isotherms,

streamlines, surface and line plots. In section 5.1 a two dimensional geometry and mathematical formulation of the transient heating problem is presented. Section 5.2 presents the governing equations, boundary and initial conditions. The validation and the mesh and time step dependency study conform to the test cases presented in chapter 4. Finally, numerical results for the heat transfer and fluid flow features arising from the radiation induced natural convection is presented in section 5.3-5.8.

5.1 Radiation induced natural convection in a cylindrical enclosure: Solar average weighted model

Fig 5.1 shows a schematic of the computational domain with unit aspect ratio (H/D=1) containing high temperature molten KNO_3-$NaNO_3$. Absorption of radiation imposes a natural length scale appropriate to radiation and the fluid at a unit depth. The length scale for the radiative transport process is therefore comparable with the size of the enclosure. The domain side walls and bottom boundary are rigid and adiabatic while the top surface is an open and adiabatic boundary. The lower boundary is a perfectly black absorber plate of known capacitance, thermal conductivity and finite thickness (dx) as illustrated in Fig 5.1. The fluid is initially in a quiescent state and at a temperature T_0. At t=0, non-uniform concentrated solar radiation incident at the top is initiated and thereafter maintained. The non-uniform solar flux is transmitted along the central axis which coincides with its optical axis and is concentrated over a fixed area (diameter, d = 0.2m). The depth dependent absorption of radiation within the domain is accounted for by using a single bulk attenuation coefficient value and an incident isotropic solar radiation. The light attenuation within the fluid body is estimated from Beer's law given by equation 5.1:

$$I = I_0 e^{-(\alpha)y} \tag{5.1}$$

where I_0 is the bulk radiation intensity incident at the salt surface (y=0), taken for a single value of 1000W/m^2, C_p is the specific heat of the molten salt and δ the bulk attenuation coefficient (solar weighted absorption coefficient) [63]. Application of a bulk vertical absorption coefficient for molten salt in the present model, is consistent with literature where the absorption of solar radiation of many fluids is characterised by a single bulk attenuation coefficient [91, 92]. The direct deposited radiation heats the fluid body and the lower surface, which subsequently generates natural convection which creates plumes and mixes the salt.

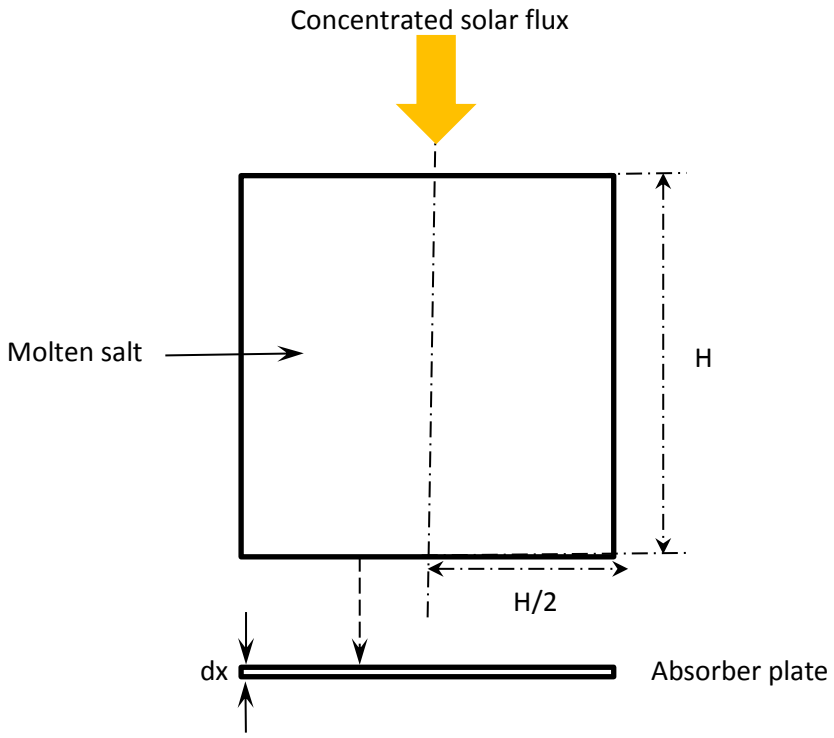

FIGURE 5.1: Numerical domain of unit aspect ratio filled with fluid of Prandtl number 6.

5.1.1 Governing equation

The transient temperature and flow field in the present formulation is governed by the conservation equations for mass, momentum and energy equations equations 3.1 to 3.3 discussed in chapter 3. The governing equations expressed in non-dimensional form are given in equations 6.5 to 6.6, by using the following scales; x,h $\sim \alpha$ (length scale), t $\sim$ $(\mathrm{kH}^2)^{-1}$ (time scale), T $\sim$ I/kα (temperature scale), u,v $\sim$ kα(velocity).

$$\nabla \cdot \vec{V} = 0 \tag{5.2}$$

$$\rho \frac{\partial(\vec{V})}{\partial t} + \rho(\vec{V} \cdot \nabla)\vec{V}) = -RaPr\nabla p + RaPr\nabla^2 \vec{V} + PrRaT \tag{5.3}$$

$$\rho C_p \left(\frac{\partial T}{\partial t} + \nabla . \vec{V} T \right) = \nabla \cdot (k \cdot \nabla T) + S \tag{5.4}$$

where u and w are the velocity components in the x and y directions as shown in Fig 5.1. T is the spatial temperature in the domain from the resulting heating. P is the pressure and the gravitational acceleration; density kinematic viscosity, thermal diffusivity and bulk expansion coefficient are g, ρ, μ,β and κ respectively; mg is the body force (N/m^3). The absorption coefficient is used as the characteristic length due to the absorption of incident radiation imposing a natural length scale appropriate to the radiation and the fluid, i.e. the attenuation length, and from equation 5.1, it can be seen that there will be limited radiation transmitted to the lower surface beyond the penetrative depth. Ra is the Rayleigh number, Ra= $\rho^2 C_p g\beta/\mu k^2$ and Pr is the Prandlt number, fixed at 6. The Rayleigh number used here is the flux Rayleigh number [91], and it differs from the Rayleigh number used in the classical Rayleigh-Bénard convection where the fluid is bounded by rigid and fixed-temperature walls. S is the volumetric heating source term in equation 5.5 is given by:

$$S = \frac{1}{\rho_0 C_p}\frac{dI}{dz} + \frac{2I}{k}\left(\sqrt{\frac{\alpha t}{\pi}}\right)^{\frac{1}{2}} \tag{5.5}$$

where I is as given by equation 5.1 The boundary conditions are: rigid, non-slip and adiabatic side walls where the velocity components and normal temperature gradients are zero. The fluid depth is bounded by a stress free (u=v=w=dT/dn=0) and adiabatic top at y=0 (dT/dy=0). The lower boundary is a rigid plate of finite thickness and fixed thermal conductivity, whose top surface is considered to be a non slip conditions and the lower surface and end walls are adiabatic. The temperature at the lower surface is given by $T=T_0+\Delta T$, where ΔT is the transient perturbation temperature arising for the full absorption of all radiation transmitted to the lower surface. The derived time dependent system of non-linear partial differential equations (PDEs) are solved using the commercially available Computational Fluid Dynamics, Finite Element Method (FEM) based software COMSOL version 4.4 [120]. Second-order elements were applied for the velocity and linear elements for the pressure field, (P_2+P_1) discretisation [120]. Validation of the present model is based Webb and Viskanta's [81] experimental study on the radiation induced natural convection in a cavity which is presented in chapter 4. In order to ensure mesh-independent solutions, mesh sensitivity tests for the case concentration ratio C = 700X, I_0 = 1000 Wm^{-2}, and α 2 m^{-1}, attenuation coefficient for molten KNO_3 $NaNO_3$ salt.

Different mesh element sizes were tested to ensure mesh independence of the numerical results. Mesh element sizes (h) in the range 5mm$\leqslant$N$\leqslant$ 200mm were obtained by dividing a maximum mesh element by a mesh refinement factor N, for 1$\leqslant$N$\leqslant$ 10. Fig 5.1 shows the plot for the mesh convergence test. From this figure, it can be seen that the results

for the difference in average weighted temperature at the respective mesh sizes and the finest mesh element size i.e (h_N-h_{10}), against the mesh refinement factor N, converged when N=3. Using the mesh element size corresponding to N=3 results in 5578 domain elements and gives a relative error calculated by reference to the results given by the finest mesh within 0.1%. Thus selecting a mesh of this size was adequate enough to save computational time without losing numerical accuracy. Fig 5.2 shows the mesh used in the numerical simulations of the present work. Effects of time step on the solution were carefully examined in the preliminary calculations, where three time steps viz: 0.2, 0.5, and 1 s were tested. As a compromise between the computational time and the accuracy, 1 s was adopted as the time step in the numerical calculation. A convergence criteria of 10^{-5} was imposed for the residuals of the governing equation were.

The validation of the present simulation is conducted against 1) the experimental investigation of Webb and Viskanta [82] which is described presented in Chapter 4, section 4.3. However as the chamber in this study was illuminated from the side, their results are not readily applicable to the problem investigated here but does show the importance of fully incorporating a non-uniform absorption of the incoming radiation accounted for by weighted average values for the incident solar radiation and absorption coefficients. To provide further verification two-dimensional numerical simulation of the flow in a horizontal fluid layer of shallow depth of less than 3 metres subject to constant and uniform radiation at the water surface with the Rayleigh number equivalent to the physical scenario with solar radiation of I_0 =1000 Wm^{-2}, and α=10 m^{-1}, a typical attenuation coefficient for water. The considered range of the fluid domain corresponds to typical water depths used in laboratory-scale experiments of Coates and Patterson [104]; Lei and Patterson [83, 87].

5.2 Result

Fig 5.4 shows the transient temperature profile in a unit aspect ratio fluid domain arising from the direct absorption of the incident solar radiation and the heated lower boundary for Pr=6 and Ra=8.9×10^{11}. In the current geometry, the transmitted radiation to the bottom surface, heats the lower surface and thereby developing an adverse temperature gradient so that the heat transfer from this surface is achieved entirely by convection. Fig 5.4 a-d shows the non-dimensional temperature profile for the fluid domain at various times of heating. Fig 5.4a shows the temperature profile at an early heating time, τ=1.5×10^{-5}, shortly after the solar radiation is initiated and thereafter maintained. The fluid is observed to be heated non-uniformly from the top. The end walls force the heat to be transferred downwards along the end walls. While a boundary layer develops

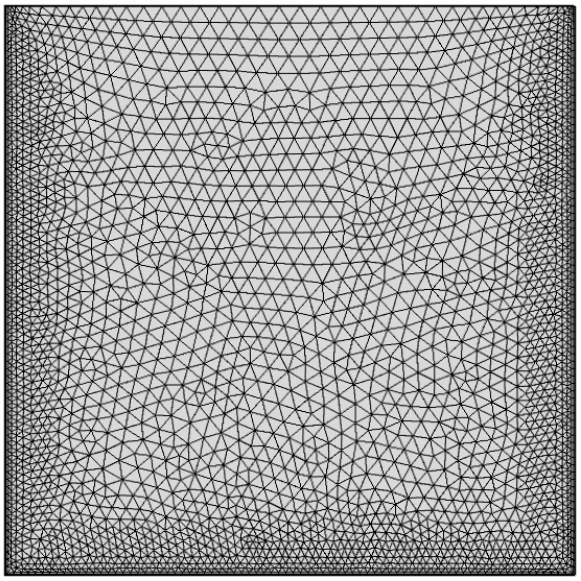

FIGURE 5.2: Computational mesh.

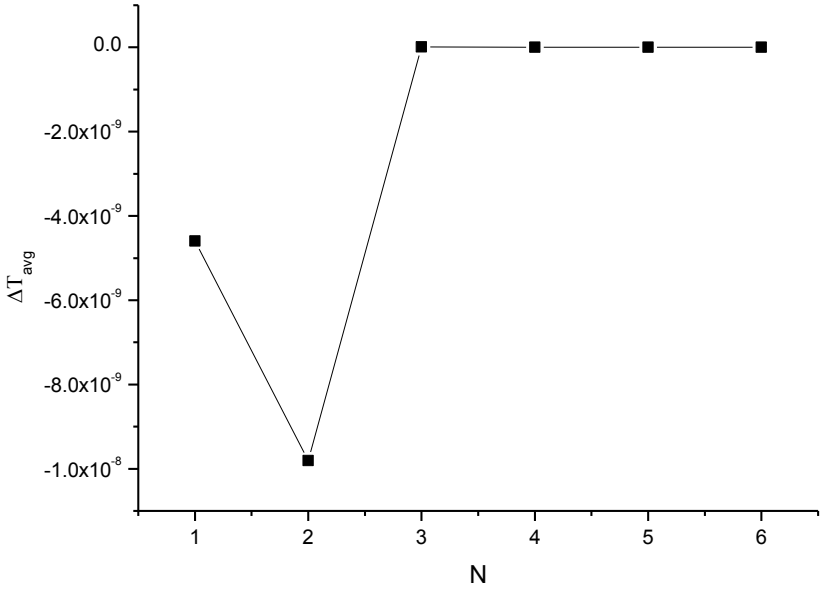

FIGURE 5.3: Mesh refinement results.

at the lower surface. Fig 5.4b shows the temperature distribution in the domain at a heating time, τ=3.795×10^{-5}. In the top fluid column the non- uniform depth dependent heating is found to develop a unique thermal feature. While in the lower column, thermal plumes are observed to emerge from the thermal boundary layer. In Fig 5.4c, (τ=4.55×10^{-5}) for continued heating, the establishment of a distinct top stratified layer of hot fluid is observed. In the lower fluid column, plumes extend into the fluid layer for a significant distance, introducing vertical fluid velocities and initiating mixing. Fig 5.4d (τ=7.58×10^{-4}), a non linear temperature profile is observed, revealing stable stratified surface layer of hot fluid above a layer a cooler fluid. At this transient, homogenised temperatures are realised in the lower mixing layer and the thermal plume becomes drastically reduced. The surface layer is due to the direct absorption of the incident solar radiation in the fluid which has stabilizing effects. Thus, this develops a stable stratification owing to the density gradient being parallel but in the same direction as the gravity vector. On the other hand, the convection layer has a destabilizing effect which sets up an unstable Rayleigh Bernard type instability.

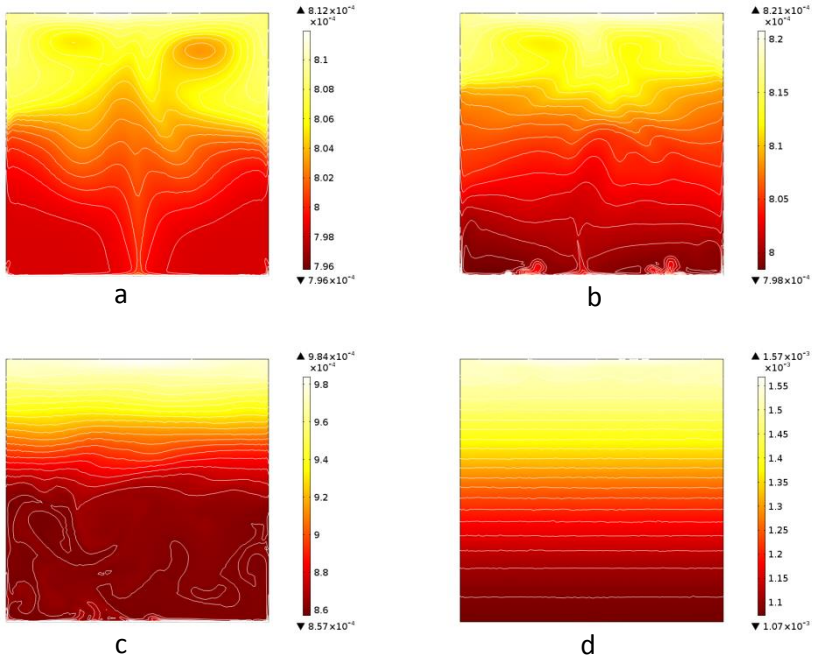

FIGURE 5.4: Transient surface temperature plots at (a) τ=1.593×10^{-5} (b) τ=4.55×10^{-5} (c) τ=5.31×10^{-4}(d) τ=7.58×10^{-4}

Fig 5.5 shows the velocity vectors corresponding to the surface temperature plots presented in Fig 5.4 a-d. In Fig 5.5a, it can be seen that fluid velocity is generated below the top surface and along the decaying beam. In Fig 5.5b, velocity is initiated in the lower fluid, whose magnitude can be seen to increase in Fig 5.5c. At this transient,

regions with no mixing and mixing can easily be seen. At τ=7.58×10^{-4} (Fig 5.5d), bulk mixing in the lower fluid column is diminished. Fluid velocities become localised to the boundary layer at the lower surface and in the region below the top surface.

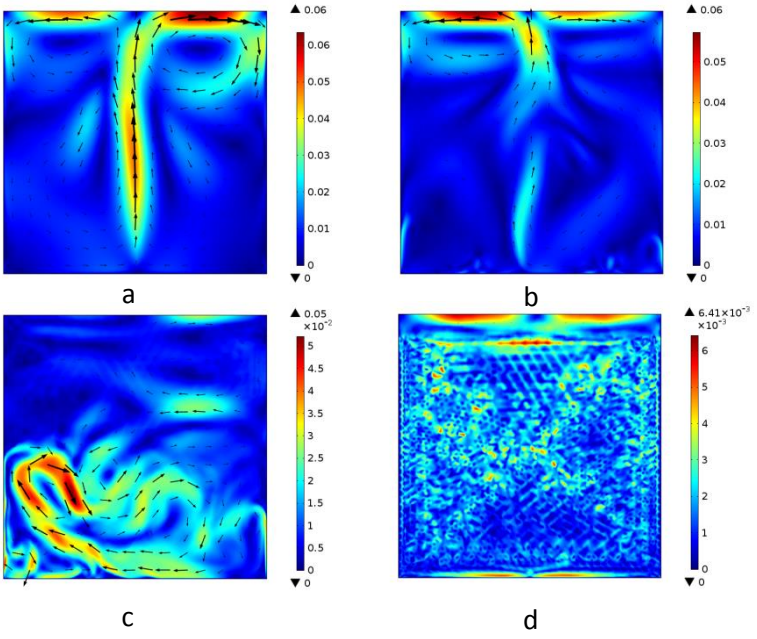

FIGURE 5.5: Transient surface temperature plots at (a) τ=1.593×10^{-5} (b) τ=4.55×10^{-5} (c) τ=5.31×10^{-4}(d) τ=7.58×10^{-4}.

5.3 Surface and boundary layers.

The fluid temperature in the enclosure increases owing to the absorption of the radiation in the upper fluid column. In the bottom boundary region, the fluid temperature increases owing to heat being conducted from the lower surface. From Fig 5.4d the establishment of a non-linear temperature profile, characterised by two distinct layers can be seen; stable surface layer and convection layer. This section describes in the detail the driving mechanisms and flow features identified in the surface layer and the mixing layer.

5.3.1 Surface Layer

Fig 5.4 d, clearly shows a stable stratified surface layer at the top of the fluid column which results in strong vertical stratification. The surface layer is generally characterised

by no bulk fluid movement [91], however in the current results tangential fluid velocities below the interface in the radial direction are observed. This is attributed to the fact that the interface between a liquid and ambient atmosphere is subjected to very high temperature differences and fluid motion is induced [128]. An identical phenomenon was observed in experiments of Cramer et al.[128], while heating molten salts in a cylindrical experimental cell placing the heater just below the free surface [128]. As the induced tangential velocities drive flow along the top surface and along the lateral wall, in the early stages vortices are formed that are found to be a main mechanism in establishing and maintaining this layer. Velocity vectors shown in Fig 5.5 a-c; the induced flow transports heat into the top fluid column which is subsequently seen to become the stable surface layer. Thus it is suggested here that the induced vortices below the interface promotes vertical stratification. Heat is however transferred primarily in the surface layer by conduction. The psuedo convection is caused by temperature gradients in a radiation beam in the fluid. Previous scaling has shown that the surface layer temperature growth scales according to Hattori et al.[92].

5.3.2 The Convection layers

As seen in Fig 5.4 b & c and Fig 5.5 b & c, a convection layer occurs in the lower fluid column. This convection layer is formed due to the bottom boundary being unstable due to Rayleigh Bernard type instability, owing to the transmitted radiation to the lower surface. The time series of the vertical velocities at the middle of the lower boundary, (x,y)=(0.5H,-0.9H) are presented in Fig 5.6a in linear and logarithmic scale for Ra=8.33×10^{11}. From these plots the three different flow regimes can easily be identified and are marked according to their instantaneous perturbation temperature and velocity fields shown in Fig 5.4 a-d and Fig 5.5 a-d.

- The initial/early flow: This is the flow before the initial peak at a,which is marked by the development of the diffusive growth of a bottom boundary layer. This stage occurs immediately after the radiation is initiated; part of the penetrative radiation is absorbed by the fluid body and the rest is transmitted to the lower surface. The transmitted solar radiation is completely absorbed at the lower surface absorber plate and it increases in temperature accordingly. As the lower surface continues to absorb radiation, heat is conducted into the lower surface absorber plate and subsequently a thermal boundary layer develops. The growth of the thermal boundary layer marks the early flow regime in the boundary layer. Surface plots in Fig 5.4a shows the existence of the distinct thermal boundary along the entire length of the lower plate and along the lower height of the vertical left and right

walls owing to end wall effects. The thermal boundary layers development is primarily due to conduction from the lower surface and secondarily to the radiation absorption in the layer. The characteristics of the boundary layer development are similar in many respects to those observed by Lei and Patterson [83, 84, 90], where the boundary layer and temperature growth are expected to scale according to [88, 89, 92]. Thermal boundary layer growth continues until the heat conducted from the lower surface is balanced by that convected to the bulk fluid. In the linear scale the magnitude of flow velocity increases smoothly during the stable development stage. The minimal flow velocity at the respective times suggest a minimal contribution to the heat transfer. Thus as the fluid flow is weak, this indicates that conduction is the dominant heat transfer mechanism at this point.

- The transitional stage: The onset of the thermo convective instability characterised by the formation and occurrence of rising plumes. Thus, the occurrence of the thermal plumes marks the onset of the transitional stage and its primary form is seen as irregular occurring plumes rising from the lower surface which can be clearly seen from the isotherms and streamline at Fig 5.4 b & c. Thermal plumes occur when the temperature gradient within the boundary layer exceeds some critical value, this leads to thermal instability. Stability of a fluid layer heated from below is characterised by a Rayleigh number Ra, defined in Drazin [80] Chandrasekhar [118]. The critical value of the Rayleigh number exists, above which Rayleigh Bernard instability occurs and is dependent on the geometry and applied boundary conditions [80]. Instability in a horizontal fluid layer with a free top and rigid lower boundary is found to occur at the critical value, Ra_c=1101 and for a horizontal fluid layer with rigid-rigid boundaries the critical value is Ra_c=1708 [80]. In the present case the thermal boundary layer is bounded by a rigid surface at the bottom and an open surface at the top, which is equivalent to the free rigid boundary configuration. A time scale for the onset of Rayleigh Bernard type instability in the present study follows the scaling developed in Hattori et al.[91]. Typical mixing layer depths of about 0.85H are observed. Hattori et al.[91] estimated the maximum height and thickness of the mixing layer to be approximately equal to the attenuation length of the radiation in deep waters and that the penetration length scale of the plumes determined the lower mixed layer thickness [92]. The time series of velocities within the boundary layer in the transitional regime show that the flow velocity fluctuates with time in an irregular manner indicating the occurrence of the convective instability. The fluctuations correspond to the development of rising plumes, as observed in the temperature and velocity plots. The flow velocity exhibit 3 distinct stages in the transitional regime and can be further sub-divided into the early middle and late transitional stages. At the early

transitional stage, the fluctuations are irregular and varies widely in magnitude. In the middle transitional stage, the magnitude of the velocity decreases and takes on more regular values. In the late transitional stage the fluctuations become more regular and much lower than at the middle transitional stage. Fig 5.7a shows the early stage to the middle transitional stage velocities. The transition is characterised by an increasing fluctuation magnitude in a non-periodical fluctuations. The magnitude of the fluctuations becomes reduced and regular from the middle transitional regime to the late transitional regime (Fig 5.7b).

- Quasi-steady state: For a maintained constant surface radiation, the penetrative radiation continues to heat the domain and since there is no heat loss through the boundaries, the fluid temperature increases without a limit. As such there will be no steady state in terms of the temperature. However, a quasi-steady state may be reached in which the temperature increases at the same rate everywhere whereas the temperature gradients and flow velocities become steady. At the quasi steady stage, a two layer non-linear temperature structure are evident. In the upper layer strong stabilisation exists, and the lower (boundary) layer destabilising stratification exists. Typical flow pattern as observed in Fig 5.7 c shows the velocity becomes localised to the boundary layer region. As the quasi steady state is reached fluctuating velocity amplitudes become reduced with almost periodically oscillatory pattern (Fig 5.7 c).

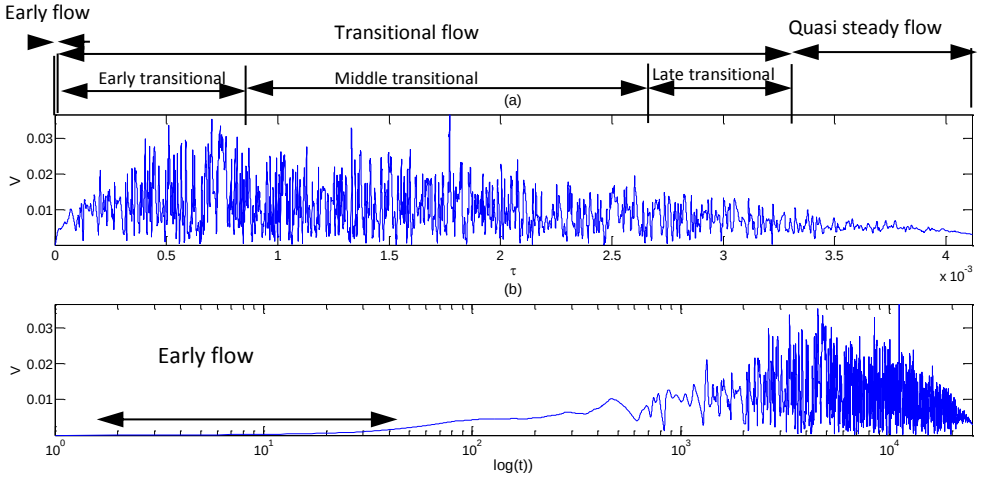

FIGURE 5.6: Time series of velocity at a position (0,H), and the spectra of different sections of the time series for Ra=8.3×10^{11}.(a) Time series with linear scale (b) Time series with logarithmic scale.

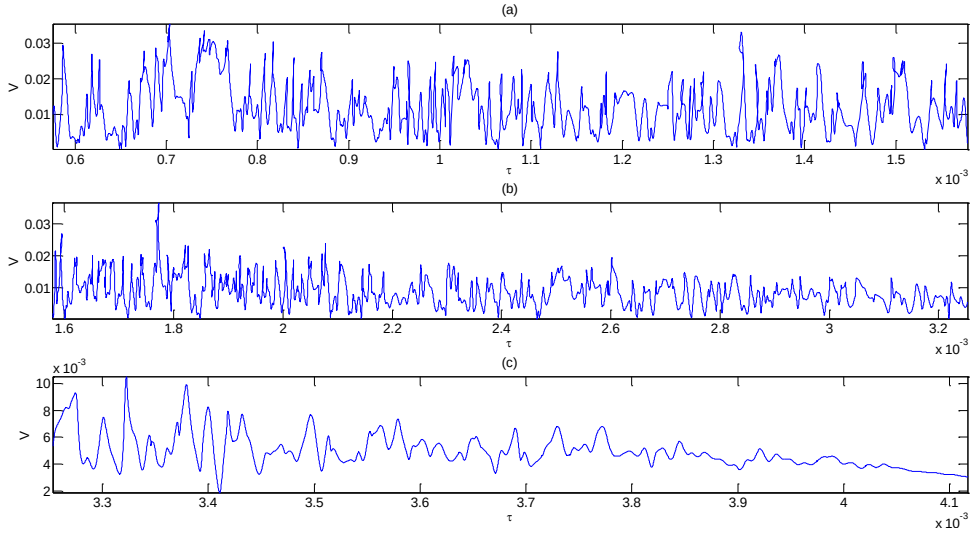

FIGURE 5.7: (a) Time series corresponding to the early to the middle transition regime. (b) Time series corresponding to the middle to late transition regime (c) Time series corresponding to the late to quasi steady state.

5.4 Spectral analysis

Fig 5.8 shows the power spectrum corresponding to the early to middle transition stage. The present results were post processed with Matlab version 2013 software [129]. Two significant peaks in the frequency spectrum are identified at f_1=0.5Hz and f_2=0.48Hz. Other frequencies are visible within the power spectrum; their amplitudes are one order smaller than the amplitude of the two main frequencies however. In the middle to late transition stage (Fig 5.7 c), several peaks in the frequency spectrum may be identified, however peaks with significant amplitudes are seen at f=1.014, 1.044, and 1.114Hz. The interaction between the different frequency modes is non-harmonic, thereby indicating characteristics of chaotic flows. At the quasi steady state, the spectrum exhibits spectra reduced peaks.

Fig 5.9 shows the time series for the volumetric flow rate across a vertical section plane at a given x location obtained from equation 5.6 and equation 5.8 The overall flow development is comprised of three distinct stages which is consistent and can easily be matched with the major fluid developments and features identified from the surface plots (Fig 5.4a-d), velocity plots (Fig 5.9), plot indicate that the steady state is reached around τ=3.25$\times$ 10^{-3}.

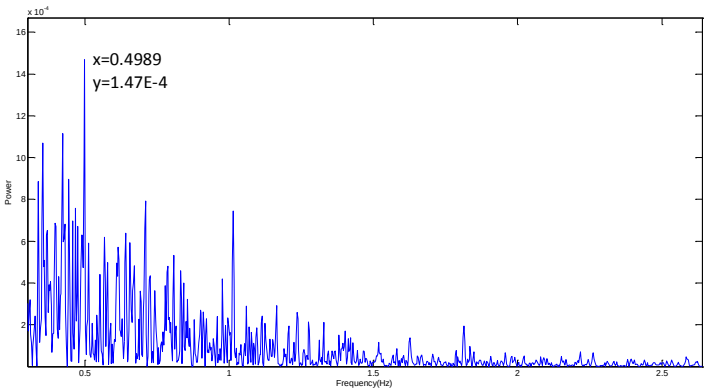

FIGURE 5.8: Spectra analysis of flow in the transitional flow stage.

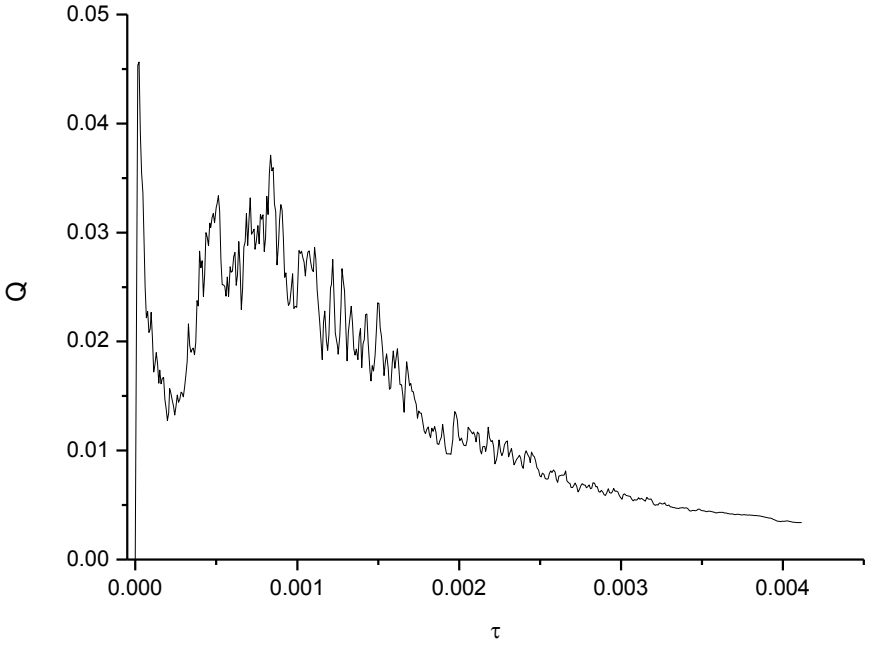

FIGURE 5.9: Time history of the volumetric flow rate which indicates the strength of circulation.

$$\dot{Q}(x) = \frac{1}{2}\int_{-H}^{0} |V| dy \tag{5.6}$$

The averaged volumetric flow rate $\dot{Q}_m$ is obtained by integrating these quantities along the horizontal direction. $\dot{Q(x)}$ and $\dot{Q}_m$ are normalised using the scale κ.

$$\dot{Q}_m = \frac{1}{L}\int_{-H}^{0} Q(x) dx = \frac{1}{L}\int_{0}^{L}\int_{-H}^{0} |V| dy dx \tag{5.7}$$

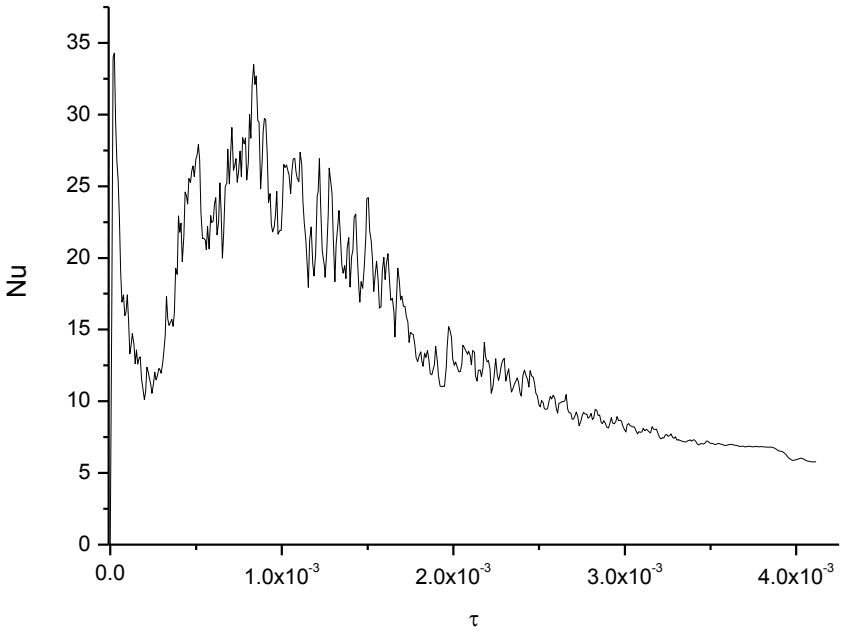

FIGURE 5.10: Time history of the heat transfer from the lower surface.

Fig 5.10 shows the time history for the dimensionless convective heat transfer from the lower surface. This plots is for a position on the bottom surface and near the centre of the enclosure (x =0.25H and y = 0.95H) for the Rayleigh flux number (Ra)= 8.9×10^{11}. The plot reveal features that are consistent with those presented in Fig 5.4 a-d, Fig 5.5 a-d and in Fig 5.9. It can be seen in Fig 5.10, that the heat transfer increases gradually at the initial/ early stage where the heat is transferred predominantly by conduction. In the transition regime high rates of heat transfer with sharp and irregular fluctuations of large amplitudes occur, that corresponds to the occurrence of thermal plumes (Fig 5.4b & c). The change from the initial stage to the transitional stage at $\tau = 3.795 \times 10^{-5}$, corresponds approximately to the presence of the first dip where thermal plumes are initiated, as observed from isotherms. After the transition stage, a quasi-steady state is reached, where heat transfer becomes steady, oscillating about a stable mean value with reduced amplitude. The fluid flow induced from heating of the salt/air interface results in a sharp increase in the heat transfer to a maximum at the early stage. The change from the initial stage to the transitional stage corresponds approximately to the presence of the first dip in the plots of the volumetric rate (Fig 5.9). The heat transfer rate remains constant over the quasi-steady state. The increase and decrease in heat transfer is consistent with increments and reductions in the number of thermal plumes and circulation cells during the heating process. The average heat transfer rate

is obtained from the average Nusselt number (equation 5.10) based on the height of the enclosure as:

$$Nu = \frac{H}{\Delta T}\frac{\partial T}{\partial x} \tag{5.8}$$

$$Nu = \int_0^H Nu \ \mathrm{dy} \tag{5.9}$$

5.5 Mixing

Of practical interest in design and performance prediction in thermal energy storage systems is quantification of the level of stratification and mixing. Fig 5.11 presents the vertical profiles of the density expressed in terms of the dimensionless density across the fluid domain depth. From Fig 5.11 the zones of no mixing and complete mixing can be established which correspond to the two layers identified earlier: surface layer and the convecting layer.

The transition layer between the surface layer and the mixing layer is a zone of practical interest and relevance in thermocline thermal energy storage systems. Its occurrence in either the charging or discharging phase can be to indicate thermal performance.

Detailed analysis shows that the surface layer can be further dividend into a stable surface layer and a themocline region while the convection layer divided into a mixing layer and a boundary layer. The thermocline is the transition layer between the surface layer and the mixing layer. This layer is of practical interest thermocline storage systems as its limit defined as the zone where local temperatures are in the middle $98 \leqslant \theta \leqslant 99$ of operational temperature range $0.01 \leqslant \theta \leqslant 0.99$ has been applied to investigate thermal performance.

In comparison with the temperature profiles the occurrence of the non-mixing and mixing zones are consistent with observation from the surface plots and isotherms. In the non-mixing zone; (the surface layer), the density and temperature show a stable profile with constant density gradient through the fluid depth; the convective heat flux is zero. Thermal plumes are important mixing mechanisms which initiate and drive vertical convection [91]. From surface plot in Fig 5.4 c, the presence of nonlinear temperature stratification imposes limits on the mixing driven by rising thermal plumes. In the mixing layer, which occupies a typical maximum mixing height of 0.75H, the temperature and density are constant, in space due to vertical mixing of all these quantities. At the thermocline layer, at around $0.75H<z<0.9H$, the temperature profile increases and

reaches a stable behaviour, while the convective heat transfer is minimum. The mixing layer grows within the transitional layer. In the transitional layer the convection is characterised by narrow plumes in the form of domes of rising horizontal surfaces balanced by larger regions of descending motion.

The extent of thermal mixing achieved by the natural convection in the respective layers and the level of stratification obtained over the heating period is shown in Fig 5.12 based on the MIX number of Anderson, described in chapter 2. From this plot the level of mixing achieved over the heating time can be obtained. Mixing is seen to be high at the early times and linearly decreases with time. At τ=1.6$\times$ 10^{-4}, the charging process lead to 26% of mixing or 74% stratification. At a later time of τ=3.43$\times$ 10^{-4}, 11% mixed volume and 89% stratification is obtained.

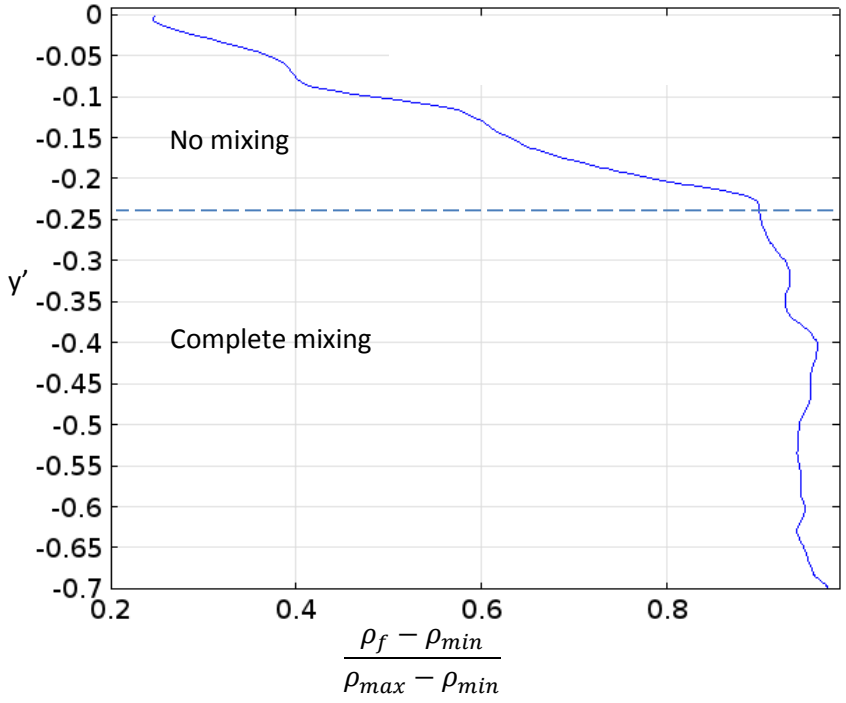

FIGURE 5.11: Normalised density profiles showing regions of no mixing and complete mixing. ρ_{min} is the minimum possible value of the final potential energy (which occurs when there is no mixing) and P_{max} is the maximum possible value of the final potential energy(which occurs when there is complete mixing) and E=0 lies between 1 respectively.

5.6 Effect of the lower heating surface

To further illustrate the influence of the impact of an absorber plate as applied in the present configuration, Fig 5.13 and Fig 5.14, show the transient temperatures along

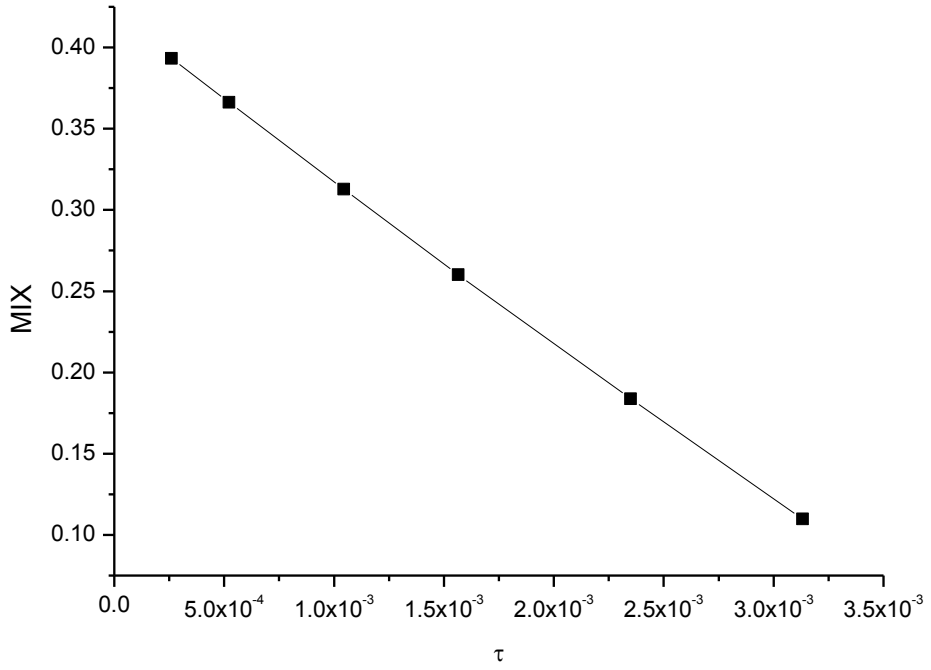

FIGURE 5.12: MIX number vs time

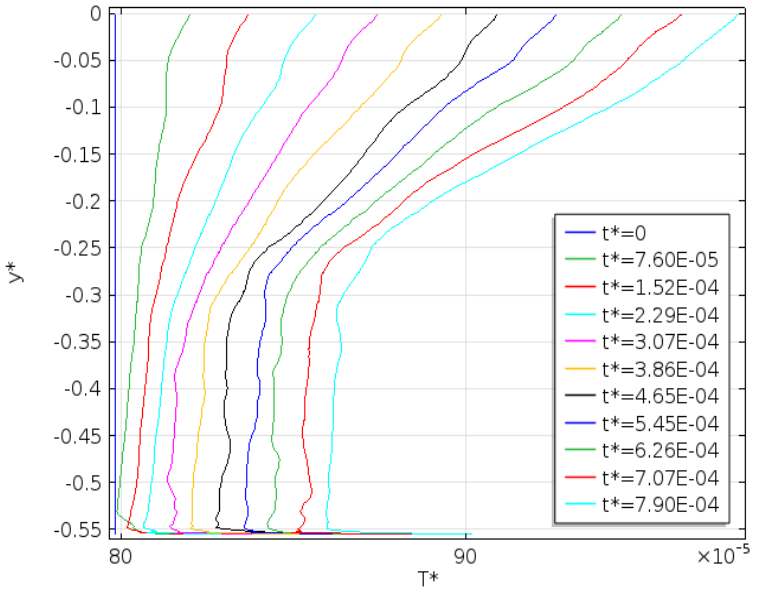

FIGURE 5.13: Temperature profiles at various time intervals for enclosure with lower absorber plate (dx=2.5×10^{-3}).

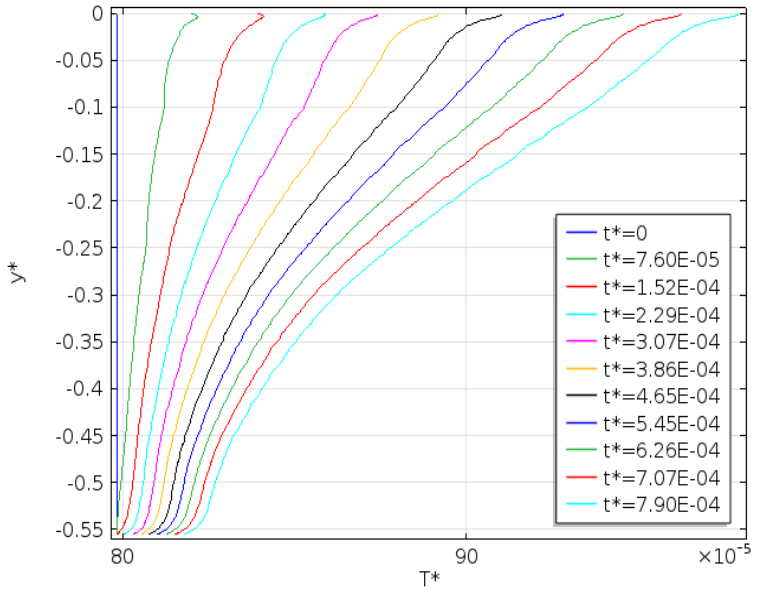

FIGURE 5.14: Temperature profiles at various time intervals for enclosure for without lower absorber plate (dx=2.5×10^{-3}).

the fluid depth for a) an enclosure with a lower absorber plate and b) an enclosure without a lower absorber plate, respectively. It can be seen from Fig 5.13 that at early times τ=0.86×10^{-4} nearly isothermal temperatures are obtained within the fluid domain. However above τ=3.86×10^{-4} times, stable temperature gradients at the upper part of the fluid domain and a non-linear temperature distribution is obtained where the temperature of the upper fluid column exceeds the lower boundary temperatures and the distinct temperature regions are clearly indicated in the domain. Fig 5.14 shows the transient heating in an identical fluid domain in which there is no lower heating from a absorber plate. Temperatures in Fig 5.14 at identical times as those of Fig 5.13 show much higher fluid temperatures in the fluid domain and low fluid temperatures at the bottom region. A direct comparison between the two profiles reveal that higher temperatures are obtained for case 1 compared to case 2. Thus, increases in fluid average temperature of greater than 10% can be obtained in an enclosure with the lower absorber receiver.

Fig 5.15 shows the transient boundary layer temperatures for the lower absorber plate thickness (dx) over the range $5\times\ 10^{-3}$ to $1\times\ 10^{-1}$. The plate heat capacitance is the same for all thicknesses considered. The plot shows that the boundary temperature, shortly after the initiation of the surface radiation, started to fluctuate indicating the

onset of convective instability which is seen to be larger at smaller plate thickness. It can be seen that the fluid temperature decreased with increasing plate thickness resulting in a delay to the onset of convective instability. This is due to the fact that as the plate thickness increases, more of the heat is absorbed and therefore takes a longer time to reach high temperature. Employing an absorber plate thickness of $5\times\ 10^{-3}$ results in a 25% increase in the average fluid temperature, whereas using a $1\times\ 10^{-1}$ thick absorber plate yielded only a 2% increase in the average temperature. On the other hand, Fig 5.16 indicates that the variation in lower plate thickness does not have a direct influence on the surface layer temperature; thus it can be inferred here that stability and temperature of the surface layer is unaffected by the presence of the lower plate.

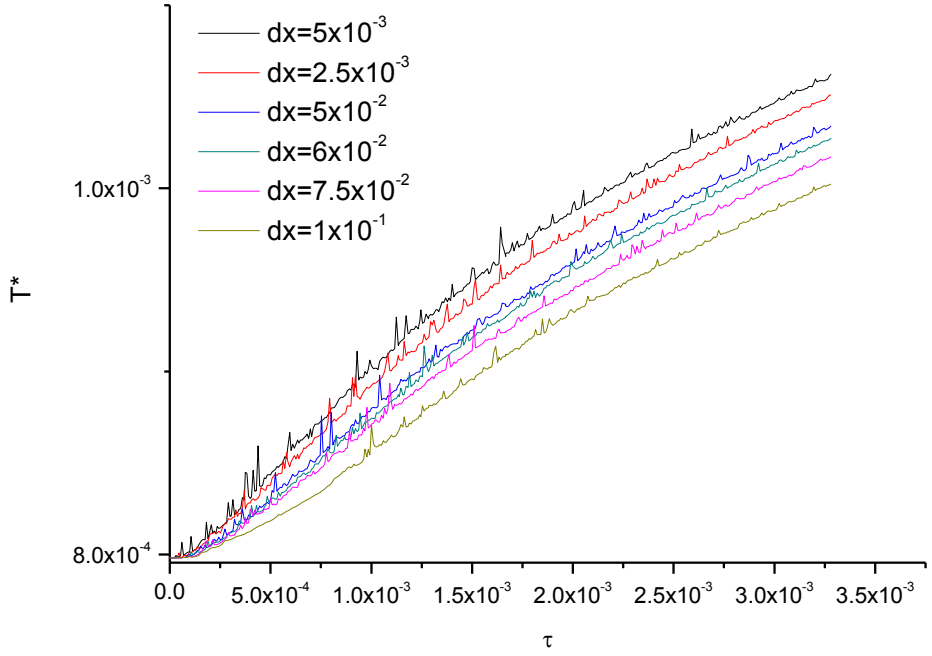

FIGURE 5.15: Effect of the lower surface absorber thickness on heat transfer from the lower surface.

In Fig 5.17 the time average of the Nusselt number (Nu) in the transitional regime displays an approximately linear decrease with increasing lower plate thickness. As Nu and velocity are driven by the presence of thermal plumes, it is inferred here that the intensity and strength of the occurring thermal plumes also decrease with plate thickness. This is consistent with observations for surface temperature in the height and number of occurring plumes. This is due to the fact that with increasing thickness, heating time increases and results in delayed heating of the lower fluid.

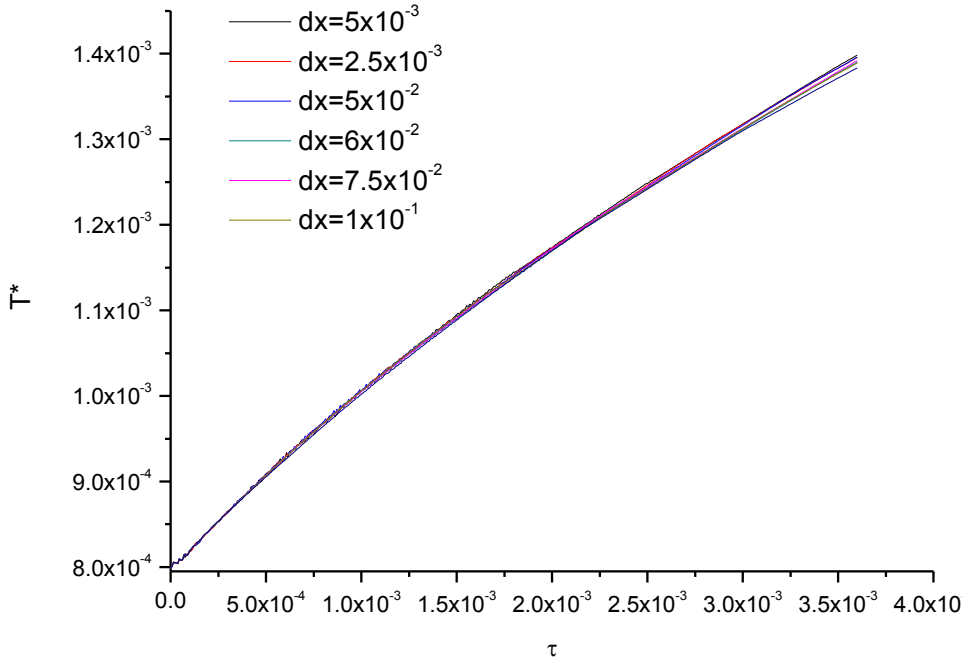

FIGURE 5.16: Surface layer temperature for different lower surface absorber thickness.

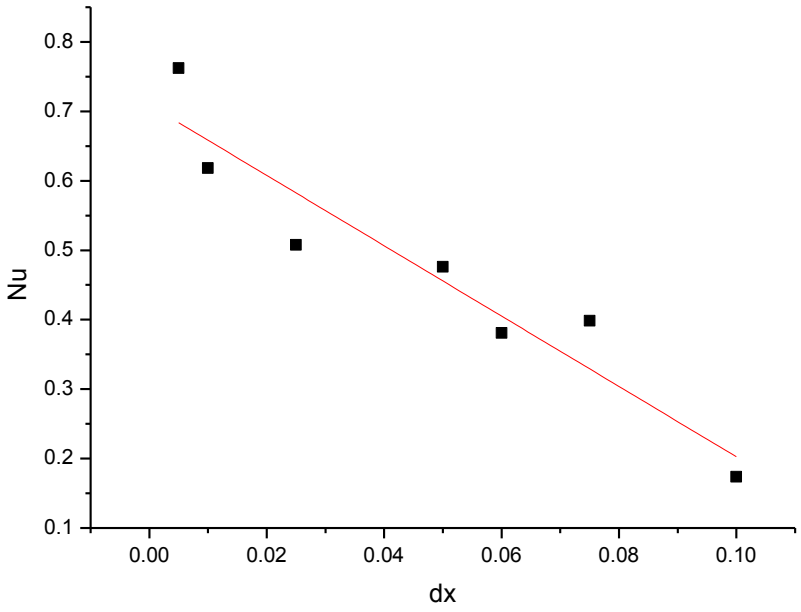

FIGURE 5.17: Effect of the lower surface absorber thickness (dx) on heat transfer from the lower surface.

5.7 Spectral analysis

Fig 5.8 shows the power spectrum corresponding to the early to middle transition stage. The present results were post processed with Matlab version 2013 software [129]. Two significant peaks in the frequency spectrum are identified at f_1=0.5Hz and f_2=0.48Hz. Other frequencies are visible within the power spectrum; their amplitudes are one order smaller than the amplitude of the two main frequencies however. In the middle to late transition stage (Fig 5.7 c), several peaks in the frequency spectrum may be identified, however peaks with significant amplitudes are seen at f=1.014, 1.044, and 1.114Hz. The interaction between the different frequency modes is non-harmonic, thereby indicating characteristics of chaotic flows. At the quasi steady state, the spectrum exhibits spectra reduced peaks.

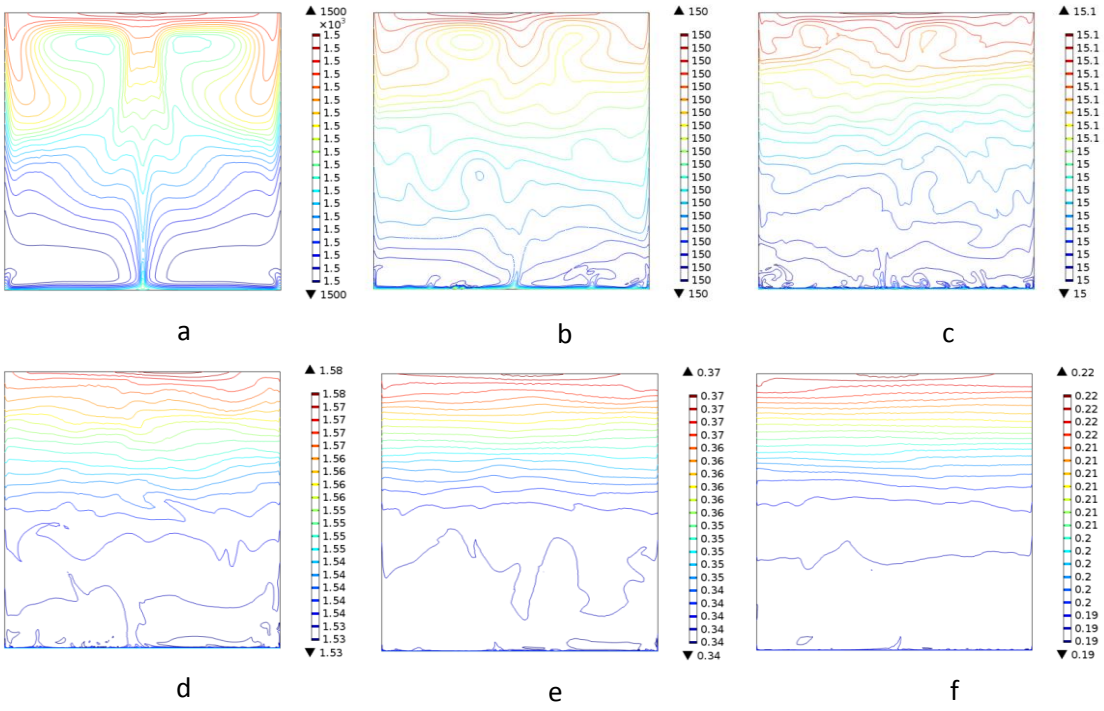

FIGURE 5.18: Isotherms at different flux Rayleigh numbers (a) Ra=6.08× 10^7 , (b) Ra=6.08×10^8, (c) Ra=6.08×10^9, (d) Ra=6.336×10^{10}, (e) Ra=3.77×10^{11} and (f) Ra=8.99×10^{11} .

Fig 5.20 shows the normalised density profiles measured at the end of the simulation for Ra=6.08× 10^7 , Ra=6.08×10^8, Ra=6.08×10^9, Ra=6.336×10^{10}, Ra=3.77×10^{11}. When Ra is greater than 6.08×10^9 near complete mixing was found. However at the other extreme, when Ra, was less than 6.08×10^7, a lack of adequate mixing led to a non

linear decrease in the stratified zone and linearly decreasing mixing efficiencies in the mixing layer. Convective regimes between these extremes produced moderate mixing and intermediate density profiles. In general, the mixing efficiency is found to increase with increasing Rayleigh number. The plot also shows that the homogeneity and completeness of mixing increases with increasing Ra. Fig 5.21 also shows the MIX number defined in Chapter 2 during the heating process at the respective Rayleigh number(Ra). At each of the respective Ra it is clearly seen that the MIX number decreases with heating time. Thus stratification is seen to be promoted at later heating times which is consistent with observations form isotherms and streamlines.

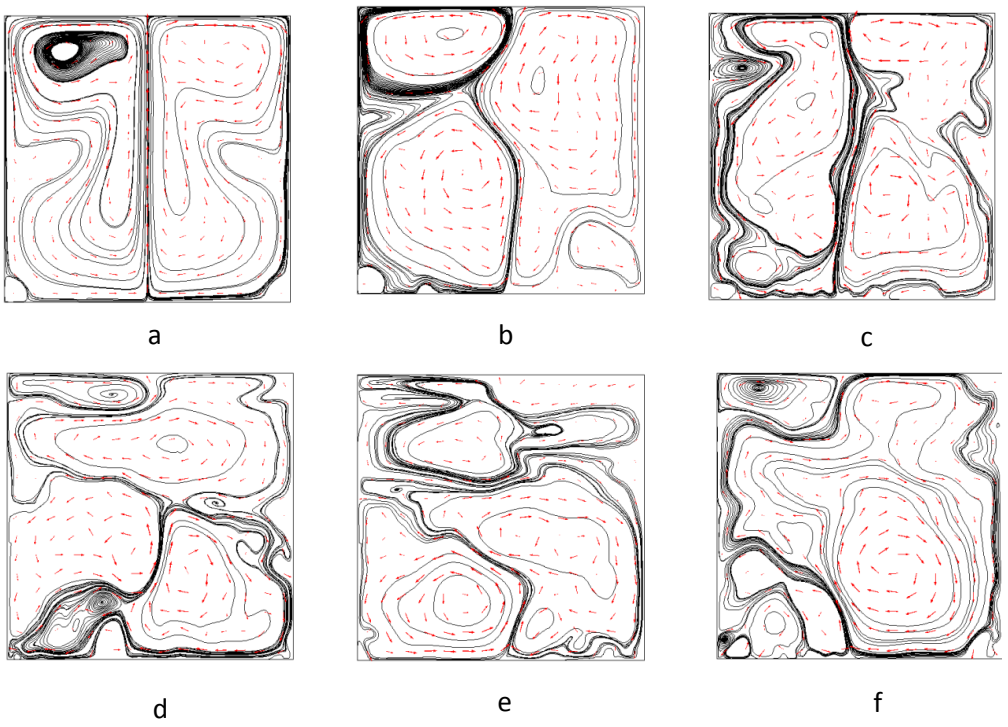

FIGURE 5.19: Streamlines for a) Ra=6.08× 10^7 , (b) Ra=6.08×10^8, (c) Ra=6.08×10^9, (d) Ra=6.336×10^{10}, (e) Ra=3.77×10^{11} and (f) Ra=8.99×10^{11}

5.8 Effect of aspect ratio

This section presents the temperature and flow fields for the domain containing a fixed volume of KNO_3-$NaNO_3$ salt at height to width ratios (H/D) of 0.5, 1, and 2 corresponding to dimensionless height 1, 2, and 4 respectively. The dimensionless height is defined as the product of the attenuation coefficient and the fluid depth (Γ=Hα).

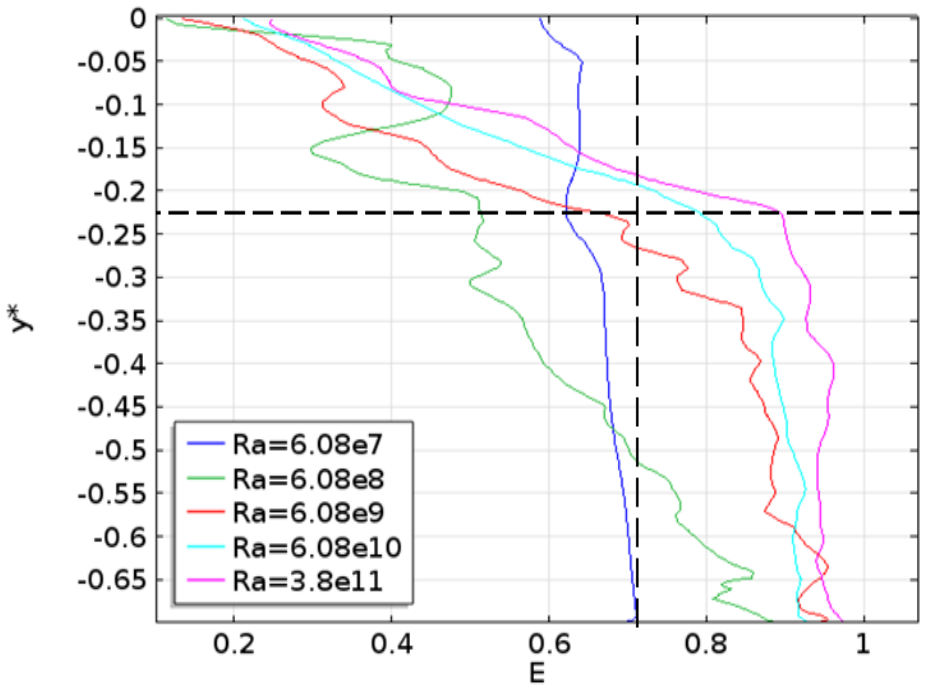

FIGURE 5.20: Normalised density profiles in domain for various Ra.

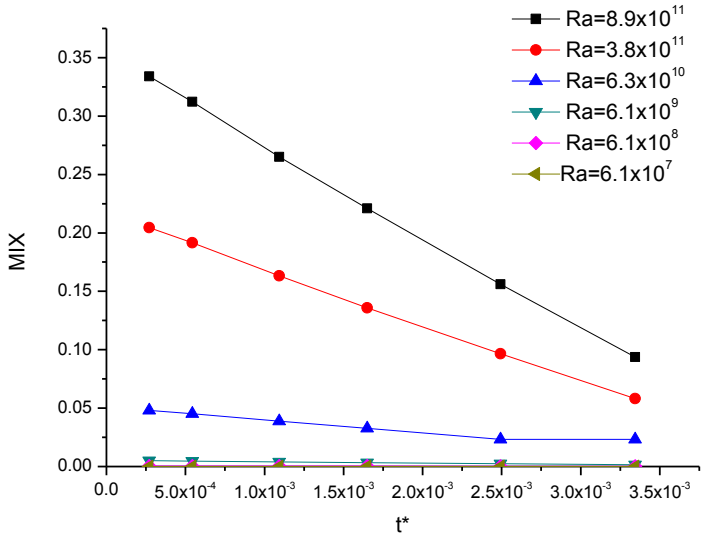

FIGURE 5.21: Transient MIX number at various Ra.

However, in the present study the dimensionless height will be considered as the dimensionless height, owing to the optical thickness variation being obtained by only varying the fluid depth with the attenuation coefficient remaining constant. Fig 5.22, Fig 5.23 and Fig 5.24 show isotherms and flow velocity streamlines at dimensionless time steps (τ) in a fixed volume of molten salt for cavity showing different stages of flow development are shown for dimensionless heights (Γ=αH) 1, 2 and 4. In Fig 5.22 a, b and c, demonstrate thermal features at selected times during the initial stage, transitional stage and quasi-steady stage.

At Γ=1 (H/D = 0.5), at $\tau = 3.03\times10^{-5}$ (Fig 5.22a (i)) temperature contours established by absorption of solar radiation and a horizontal thermal boundary layer develop above the lower surface as evident by the isotherms. At $\tau = 7.71\times10^{-4}$ (Fig 5.22b(i)), complex temperature contours arising from the interaction of the direct absorption of the solar radiation phenomenon and the thermo natural convection developed at lower absorber surface. At a time, τ= 4.12×10^{-3} (Fig 5.22c(i)), when the quasi steady stage is reached a nonlinear temperature profile is obtained where a stratified top layer and a convicting lower stage can be clearly seen. Corresponding streamlines (Fig 5.22a (ii)) show stable circulation cells with induced flows of low velocities which do not contribute to the heat transfer. At t=000 (Fig Fig 5.23b(ii))), increased fluid movement is evident as illustrated by the presence of the thermal plumes and the burification of circulation cells and the occurrence of eddies at the lower left and right wall. In Fig 5.23c(ii), as the establishment of a stable surface layer and convection lower fluid leads to stronger fluid flows in the lower fluid column compared to the top fluid where the fluid flow become diminished at later times in the quasi steady state stage.

At Γ= 2 (Fig 5.23a,b,c) the isotherms and streamlines show similar thermal driving mechanisms and fluid flow transitions as occurred for Γ = 1. Flow feature transitions show: i) an initial stage (Fig 5.23a), ii) a transitional stage (Fig 5.23b) and iii) a quasi-steady stage (Fig 5.23c). Significant differences between the two aspect ratios can be seen from the layout of the thermal and flow features as well as their magnitudes and the time scales at which these transitions occur. In early stage ($\tau = 3.03\times10^{-5}$), the isotherms and streamlines indicate the evolution of vortices in the top fluid column. At Fig 5.23b (ii) ($\tau = 7.71\times10^{-4}$), it is apparent that the top fluid becomes stratified, while the lower fluid is mixing due to induced convection. Streamline indicate no flow in the top fluid and significant convective flows evident from the developed circulation cells. At τ= 4.12×10^{-3} (Fig 5.23c(iii)) the enclosure becomes fully stratified which is evident from the nearly parallel isotherms. Streamlines at this time indicate no bulk fluid movement. For Γ= 4 (Fig 5.24a), as a high proportion of the incident radiation is absorbed directly by the salt volume resulting in a further reduction in the amount of transmitted radiation at the lower absorber surface boundary layer, observed at the

other lower aspect ratios is reduced at $\tau = 3.03\times10^{-5}$. At $\tau = 7.71\times10^{-4}$ (Fig 5.24b)(i)) and $\tau = 4.12\times10^{-3}$ (Fig 5.24c (i)); the isotherms have become monotonic (Fig 5.24c) and nearly parallel temperature contours illustrating that the heat transfer is primarily due to conduction. Streamlines show weak flows in the steady flow solution and at $\tau = 4.12\times10^{-3}$c fluid circulation of lower intensity compared with those observed at $\Gamma = 1$ & 2 is evident in the lower fluid column in Fig 5.24b(ii). In Figure $\tau = 4.12\times10^{-3}$c(iii) streamlines become broken illustrating no flow occurs at this time.

Fig 5.25 illustrates the effect of the changing dimensionless height on the velocity and mixing. It can be seen that the velocity and the mixing decreases with increasing domain height. This is consistent with observations from Fig 5.22, Fig 5.23 and Fig 5.24, where stratification is observed to be promoted at higher optical depths.

The effect of the dimensionless depth on the strength of circulation is presented in Fig 5.26. These plots indicate the stages of the flow development and give an indication of the approximate time of occurrence. The volumetric flow rate is normalised by κH At $\Gamma = 1$, the average volumetric flow gradually increases at the early stage ($\tau = 0.006$) to a flow rate of 0.029 which then drops slightly to τ=0.001. The flow rate then sharply increases immediately after the dip to approximately 0.06 at $\tau = 0.001$. The initial dip signifies the start of the transition stage. In the transitional stage, the occurrences of thermal plumes which introduce vertical velocities, explained in section 5.3, results in fluid velocities with strong irregular fluctuations. The high fluid velocities soon drop off as the quasi-steady state is reached. In the quasi-steady stage, fluid velocities are reduced and the volumetric flow rate oscillates about a mean flow rate of 0.008, with regular fluctuation. At $\Gamma = 2$, identical volumetric flow rate trends are observed. However they occurs at lower magnitudes and at different times than at $\Gamma = 1$. The volumetric flow also gradually increases from the quiescent state to 0.022 and dips slightly and then increases sharply to 0.02, in a similar manner to the flow rate at $\Gamma = 1$. In the transitional stage, strong irregular fluctuations of lower intensity are clearly seen from Fig 5.26 of lower strength than the fluctuations attained at Γ=1. After a quasi-steady state is reached, the average flow rate oscillates about a stable mean value of 0.03 with reduced amplitude. At $\Gamma = 4$, a very low value of $\bar{Q}$ for the full length of time indicates the absence of bulk fluid movement at this configuration. The strength of fluid circulation (volumetric flow) rate decreases as Γ increase from 1 and 2 and is insignificant at 4. The decrease in circulation strength coincides with the disappearance in number of circulation cells as observed from the streamlines with increasing Γ.

The time history for the heat transfer from the lower surface at the point 0.25H, 0.95H is shown in Fig 5.27. A sharp increase in the heat transfer to a maximum at the early stages is seen (Fig 5.27) at all depths. At $\Gamma = 1$ and 2 the change from the initial stage

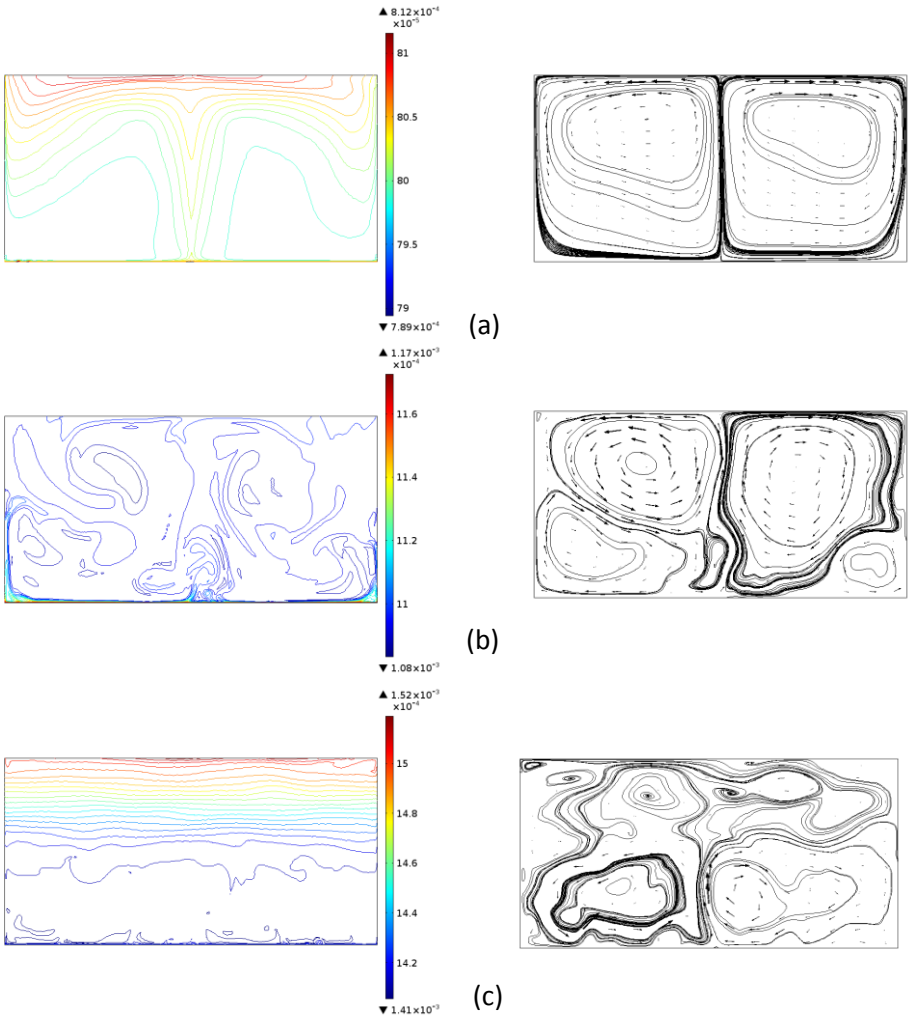

FIGURE 5.22: Temperature (left) and velocity (right) contours for Γ=1 (a) $\tau = 3.03\times10^{-5}$ (b)$\tau = 7.71\times10^{-4}$ (c) $\tau = 4.12\times10^{-3}$.

to the transitional stage corresponding approximately to the presence of the first dip in the plots of the volumetric rate can easily be seen. The high heat transfer rates in the transition stage correspond to the occurrence of thermal plumes and high volumetric flow rates in Fig 5.26. This plot is consistent with the important role of the thermal plumes in mixing in radiation induced convection problems. This is followed by a quasi-steady state where the rate of heat transfer oscillates about a stable mean value. The average rate of heat transfer is seen to decrease at $\Gamma = 2$. For the higher aspect ratio, $\Gamma = 4$ the heat transfer rate remains constant and low after the sharp spike in the heat transfer at the early stage. When the dimensionless height (Γ=2)decreases to the lower height

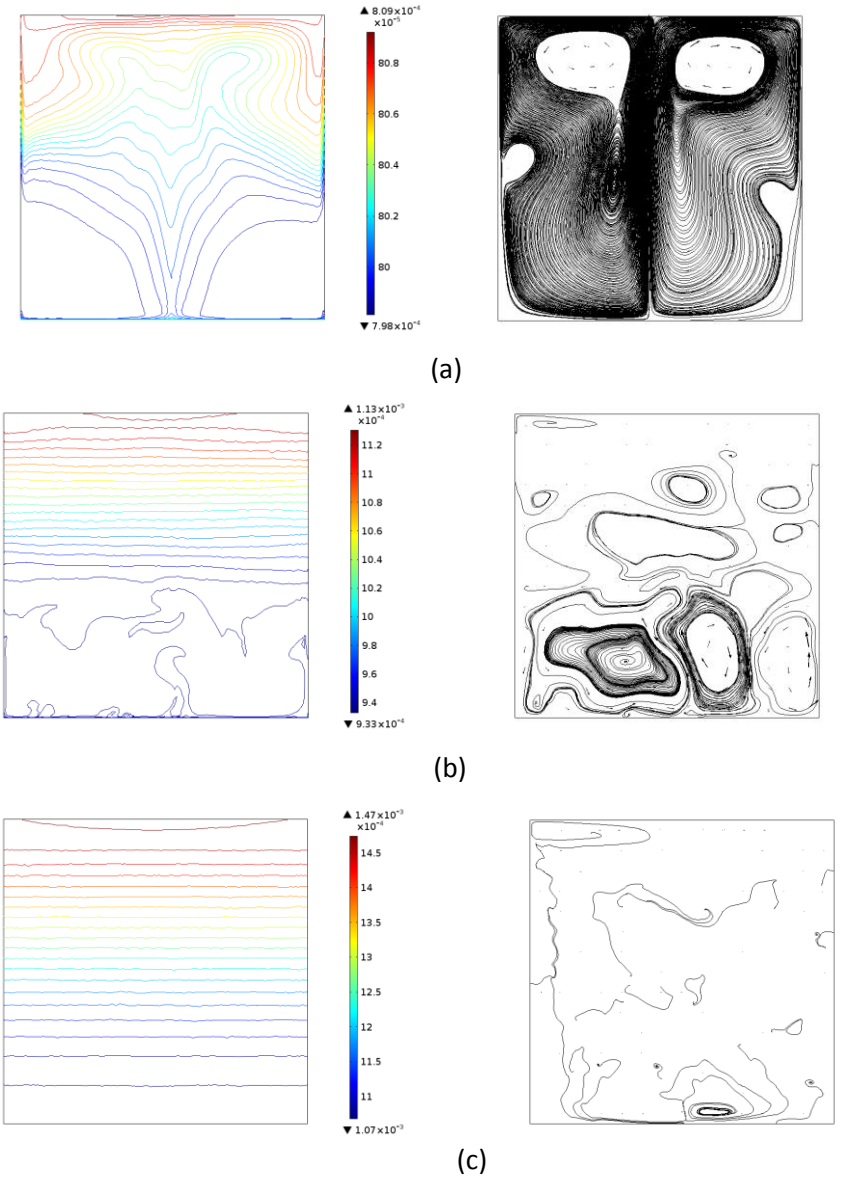

FIGURE 5.23: Temperature (left) and velocity (right) contours for Γ=2: $\tau = 3.03\times10^{-5}$ (b)$\tau = 7.71\times10^{-4}$ (c) $\tau = 4.12\times10^{-3}$

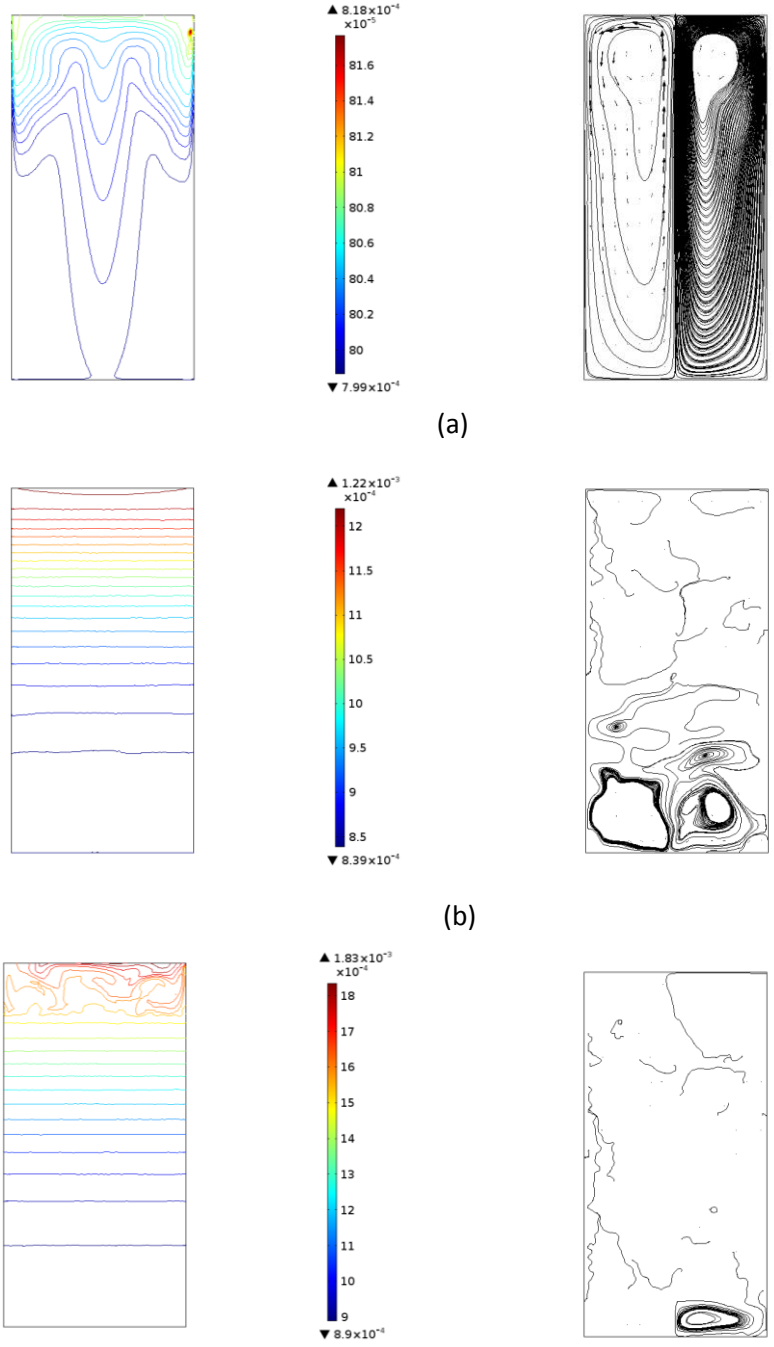

FIGURE 5.24: Temperature (left) and velocity (right) contours for Γ=4: $\tau = 3.03\times10^{-5}$ (b)$\tau = 7.71\times10^{-4}$ (c) $\tau = 4.12\times10^{-3}$

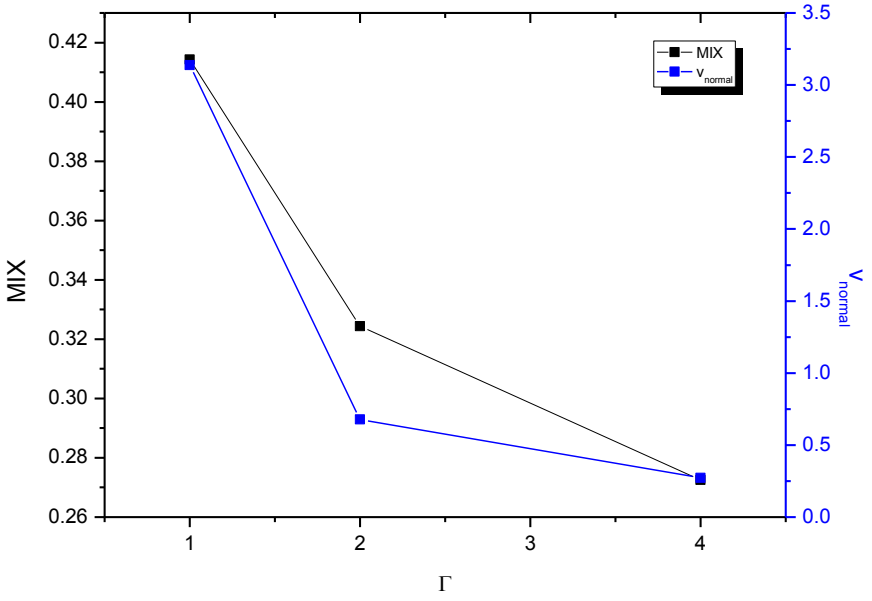

FIGURE 5.25: Max MIX number vs dimensionless depths (left), Max velocity vs dimensionless depths (right)

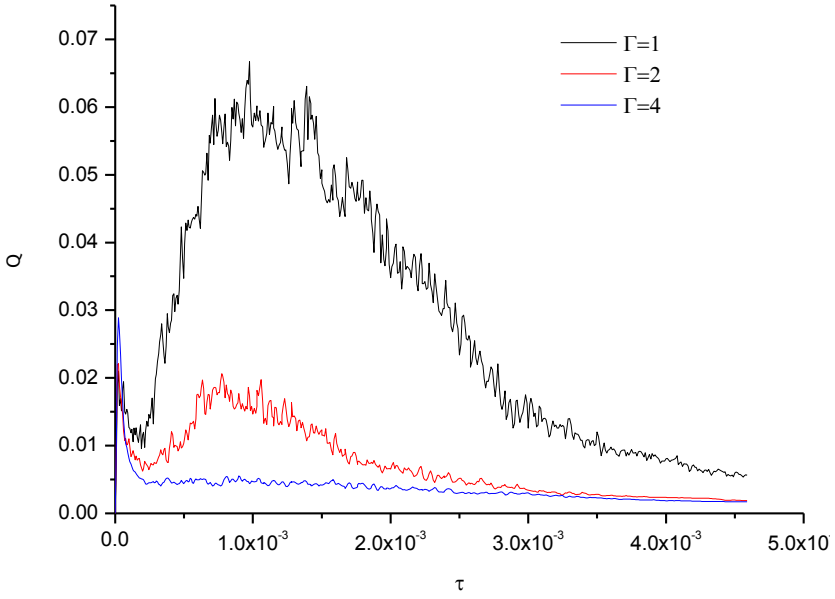

FIGURE 5.26: Time series of volumetric flow rate for Γ=1, 2 and 4

of 1, heat transfer is increased by 55% whereas at Γ=4 heat transfer is decreased by 30%. The plots reveal features that are consistent with those presented in the isotherms and streamline shown Fig 5.22, Fig 5.23 and Fig 5.24. The driving mechanisms for heat transfer here can easily be matched with the major fluid developments and features identified from the averaged flow rate in Fig 5.26

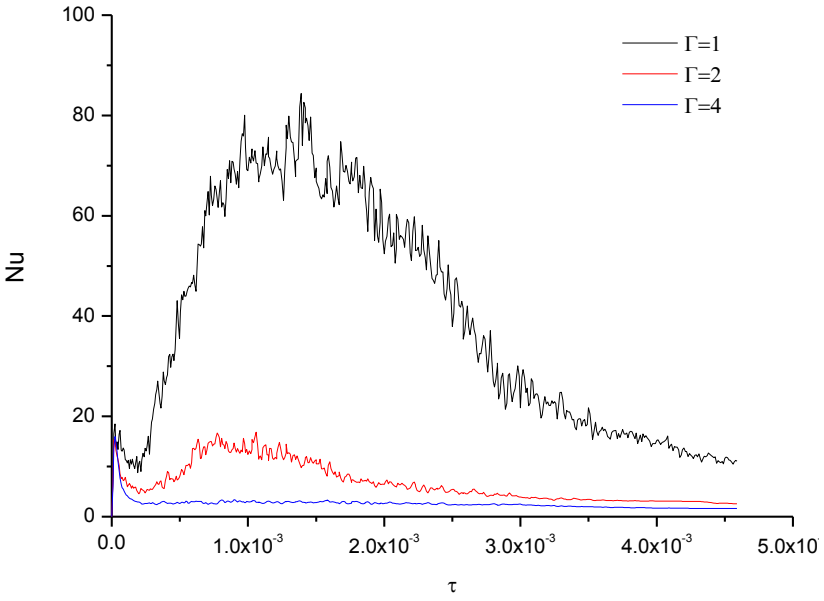

FIGURE 5.27: Time series of the heat transfer rate for Γ=1, 2 and 4

Fig 5.28 shows the heat transfer in the cavity for Γ= 1, 2 and 4 for 10^7 <Ra<10^{11}. Heat transfer by conduction dominates the flow at low Rayleigh numbers (Ra<10^7) for all three aspect ratios. Convection starts just before Ra less 10^8 for Γ=1, Ra 10^8 for Γ=2 and at Ra>10^9 for Γ= 4. The Nusselt number is highest in the shallow domain, Γ =1 and lowest at Γ =4. At Ra=10^{10} the heat transfer is lower by 65% for Γ=2 than that for Γ=1 and it is higher by a factor of 1.38 for Γ=2 than that for at Γ=4. The decrease in heat transfer from the lower surface with increase in dimensionless height (Γ) is consistent with findings in Fig 5.26 and Fig 5.27 as well as those obtained from surface temperature and velocity plots of Fig 5.22, Fig 5.23 and Fig 5.24 respectively.

Fig 5.29 shows the influence of the dimensionless height (Γ) on the critical time for the onset of instability for, Ra=8.99×10^{11}, Ra=6.33×10^{10}, Ra=3.768×10^{11} and Ra=8.99×10^{11}, respectively. The critical time t_b at which convective instability evolves can be obtained from equation 5.10. At each Rayleigh number, the critical time for onset is seen to

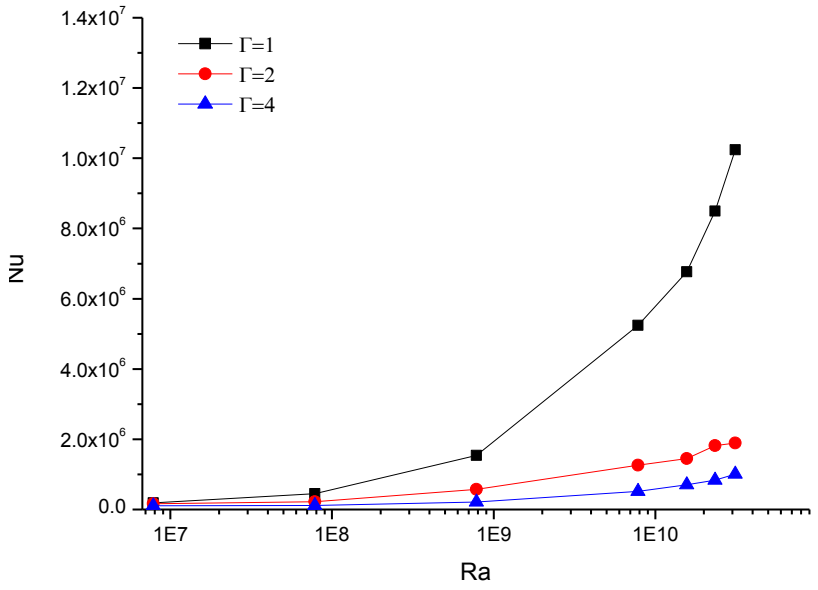

FIGURE 5.28: Nusselt number versus the Rayleigh number at different dimensionless depths

increase with increasing optical depth. However this effect is also seen to decrease with increasing Ra.

$$t_b \approx \frac{H^2}{\kappa}\left(\frac{Ra_c}{Ra}\right) \tag{5.10}$$

Of practical significance is the estimation of the performance of the thermal capture and quantification on the amount of heat accumulated within the a thermal energy store. The capture energy efficiency metric (see chapter 2) is defined by the ratio of the collected thermal energy to the total incident energy given in equation 5.11 defined for stationary receivers undergoing transient heating used [4].

$$\epsilon_{rec} = \frac{ThermalEnergyStored}{ThermalIncidentEnergy} = \frac{mc_p\Delta T}{CIA_{rec}t_{exp}} \tag{5.11}$$

where, m is the mass of the fluid that is the exposure time to solar radiation and A_{rec} is the surface area of the receiver. In Table 5.1 degree of thermal stratification is quantified by evaluation of the MIX number, the non-dimensional exergy of the enclosure and the capture efficiency. As expected the stratification is highest at Γ=4 and lowest at Γ=1. The increase in aspect ratio from 1 to 4 results in a 34% increase in thermal

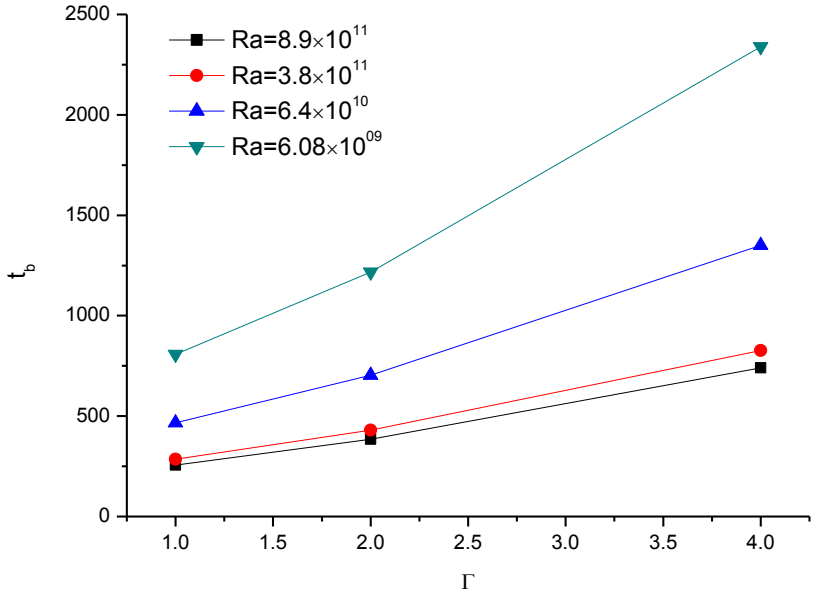

FIGURE 5.29: The critical time (t_b) vs dimensionless depth at different Ra.

stratification. In the opposite direction, mixing within the enclosure is increased by the same magnitude. The non-dimensional exergy is found to be highest at Γ=1, where the most mixing is observed to take place. Its values is observed to decrease as Γ increases, reaching its lowest value at Γ=4, where the rate of mixing becomes considerably diminished.

TABLE 5.1: Calculated MIX, non dimensionless and capture efficiency for Γ=1,2 and 4 respectively.

Γ	MIX	exergy	η
1	0.4142	0.522	0.45
2	0.32431	0.411	0.31
4	0.2725	0.219	23.5

5.9 Three Dimensional simulation

Two dimensional (2D) simulations are used to understand the physical mechanisms in many three dimensional configurations as two dimensional numerical simulations are substantially less CPU intensive than three dimensional simulations [130–132].

Three dimensional numerical simulations of radiation induced natural convection in a high temperature molten salt filled cylindrical enclosure with height to diameter ratio, H/D=1 and absorbing concentrated solar radiation are presented in this section. At the onset of charging, concentrated radiation of 700X is directly deposited into the molten salt, thereby heating it in the process. As previously stated, the salt within the enclosure is considered to be heated by two contributions: firstly, by direct absorption of the incident solar radiation and secondly a lower absorber plate heated from the full absorption of any radiation transmitted to the lower surface, which develops large adverse temperature gradients to influence convective heat transfer. The model accounts for the depth dependent attenuation of the incident non uniform concentrated flux is based on a solar weighted average attenuation coefficient as described in section 2.4 (equation 2.2). Temperature fields and flow field are obtained from solving the three dimensional energy, mass and momentum equations. The boundary conditions imposed in the three dimensional simulations the same as those described previously in the two dimensional simulations (section 5.2): i.e molten salt is confined by rigid adiabatic walls and a rigid black wall of finite thickness and heat capacitance. The top surface is considered to be open and adiabatic. Due to the substantial computational costs, the three dimensional simulations use computational domains, meshing could not be run to extra fine element sizes.

Fig 5.30- Fig 5.32 presents transient three dimensional temperature and corresponding velocity field for various times, τ=2.27×10^{-5}, 6.14×10^{-4} and τ=1.05×10^{-2}. Temperature isocontours, velocity, isocontours and vector presented show important driving and flow features within the enclosure. Also, from the plots The effect of confinement in cylindrical geometries on internally generated natural convection is apparent. At the time of writing this thesis, investigation found in existing literature, on the effects of lateral confinement on internally heated natural convection, with linear and nonlinear temperature stratification have been found in geometries.

In Fig 5.30, the early surface heating of the top fluid along the radial direction and downwards is evident. The corresponding velocity (Fig 5.30b) reveals the tangential fluid velocities generated just below the lower surface and downwards along the vertical cylinder walls. These heat transfer and flow phenomena are observed in the two dimensional study. During this time, a thermal boundary layer forms above the lower heated plate owing to the absorption of residual flux radiation at the lower plate. Fig 5.31 a and b, shows the temperature and velocity fields at 6.14×10^{-4}. It can be seen that the mixing induced from the lower boundary heating significantly influences the temperature field within the enclosure. At this stage, the interaction between the stabilisation and destabilising forces results in almost isothermal temperatures. Fig 5.31 b shows interaction between the stabilisation effect from the top heating and the destabilising

force from the lower surface results in a complex flow. Fig 5.31 b also shows increased fluid velocities emanating from the lower plate which is seen to dominate the tangential velocities seen at earlier heating times. The mixing and fluid velocities are driven by the thermal plumes and boundary layers formed along the cylinder walls as can be seen in Fig 5.31 a. Fig 5.32 b (τ=1.05×10^{-2}), a non-linear is established. The existence of two distinct layers: a surface layer and mixing similar to that in the two dimensional simulations is observed (Hattori 2015). The velocity plots show drastically reduced flows, which indicate mixing and natural convective heat transfer are insignificant at this time. The thermal and flow features found in the three dimensional simulation are identical to that observed two dimensional simulation.

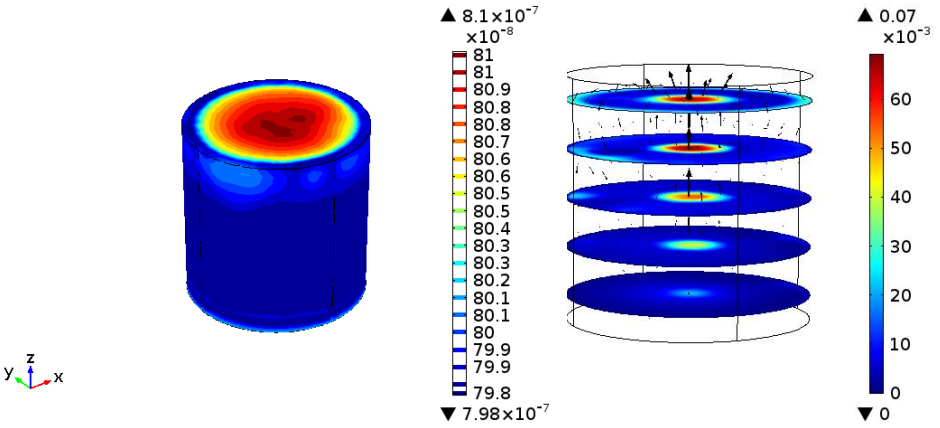

FIGURE 5.30: Temperature (left) and velocity field (right) at τ=2.71×10^{-5}

5.10 Three dimensional features of the surface and boundary layer

Based on the two dimensional simulation, the driving mechanism and flow features for the surface layer and the boundary layer are described. In the two dimensional simulations the stratified top layer was characterised by no bulk fluid flow, however tangential fluid velocities induced by surface heating at the salt/air interface are observed just below the surface. The existence of the flow and this structure are observed in the

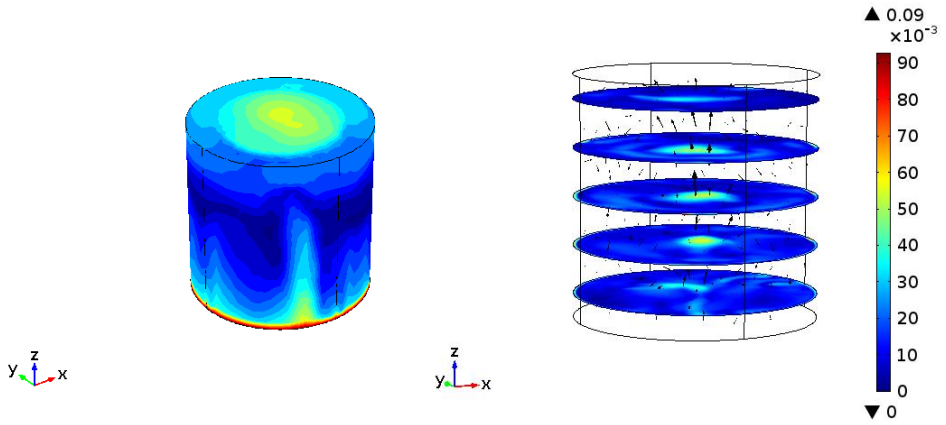

FIGURE 5.31: Temperature (left) and velocity field (right) isosurface at 6.14×10^{-4}

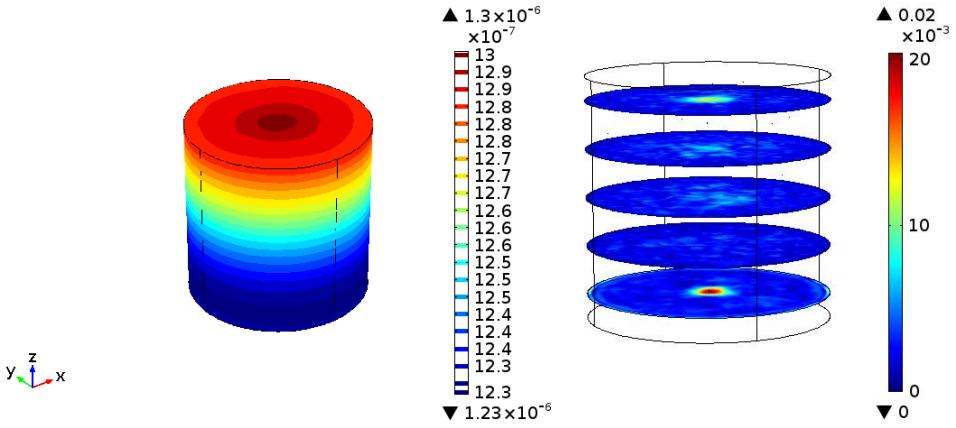

FIGURE 5.32: Temperature (left) and velocity field (right) isosurface at τ=1.05×10^{-2}

three dimensional simulation. However, the temperature and tangential velocity within the top surface in the three dimensional simulation are lower than those on the two dimensional simulation. The induced vortex in the top layer is also seen to be reduced in the three dimensional simulation. In addition, the three dimensional structure of the longitudinal rolls cannot be described by the two dimensional simulation.

Fig 5.33-Fig 5.38 a and b show the time average temperature isosurface and velocity streamlines and vectors for the three stages of flow development: the early flow, transitional, and quasi steady state identified earlier in the two dimensional models. The driving mechanisms and flow features of the respective flow regimes are fully described in previous sections. However it can clearly be seen that in the three dimensional simulations. Fig 5.33 show the 3 dimensional temperature isocontour and velocity streamlines and vectors observed at the early stage. The early heating of the top fluid along with the development of the thermal boundary layer is evident. Streamlines show longitudinal rolls where the fluid circulation initiated moves along the top surface, then the side walls and subsequently returned to the top layer without reaching the lower surface. The low velocities indicate that heat transfer in the early stage is predominantly by conduction. This effect could not be captured and fully described in the two dimensional simulation. Fig 5.34 to Fig 5.37 show the temperature isocontours and corresponding streamlines in the transitional regime. the presented times are shown for times with the early transitional(Fig 5.35b), middle transitional and (Fig 5.36) late transitional regimes (Fig 5.37) as identified in the two dimension simulation. Fig 5.34 shows the formation of thermal plumes in the boundary layer, while in the top fluid column, the convection cells formed in identical regions to those observed in the two dimensional simulation can be observed. Streamlines show low fluid velocities at the lower surface, while eddies can be seen to form at the lower part of the cylinder walls. Fig 5.35 shows the occurrence of thermal plumes which extend vertically upwards into the fluid. Convection cells formed at the top become reduced at this stage. Streamlines show a fully developed unsteady complex flow. Mixing can be seen to be intense at this time. In Fig 5.36, in the late transitional regimes, establishment of the 2 layers: surface and boundary layer are seen. At these times the temperature contours emanating from the direct absorption are observed to progress towards the lower surface. The mixing layer is at the same time observed to decrease as well as the height of the thermal plumes. Mixing is then confined to the lower fluid column as was shown in the two dimensional simulations. It is apparent from the temperature and velocity plots the the heat transfer in the transitional stage is primarily by convection. The two dimensional simulations flow was seen to be plume dominated with plumes having a mushroom like form. However, in the three dimensional simulations thermal plumes when viewed from the three dimensional structure is seen as sheet like plumes, generally observed as elongated boundary layers stretching

upwards generally characterised by high absolute values of temperature, velocity (vertical) local heat flux and vertical vortices. Lastly in at the quasi steady state, stabilisation temperature contours occupy most of the cylinder, and the mixing layer becomes really reduced. Thermal plumes also become reduced and are restricted to the boundary layer. In general, the two dimensional and three dimensional simulations appear to have identical driving mechanism and flow features, the isothermal and velocity contours reveal different structures.

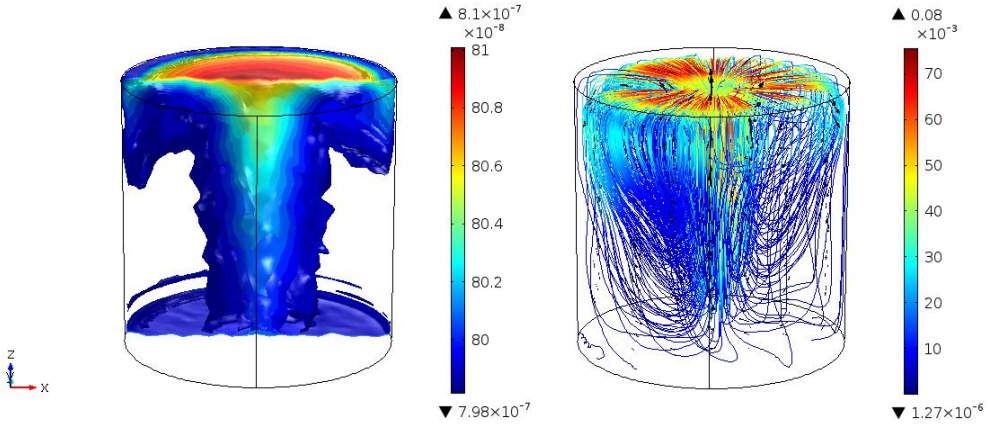

FIGURE 5.33: Temperature (left) and velocity (right) field isosurface at τ=2.71×10^{-5}

5.11 Comparisons with two dimensional (2D) simulation

In this section, results for the two dimensional (2D)model presented in section 5.3 and three dimensional (3D) model from the current numerical simulations are compared. The differences and similarities between the two dimensional (2D) and three dimensional (3D)models are studied for the flux Rayleigh number Ra=3.8×10^{11} (I=1000Wm^{-2}) and presented in the form of isotherms, isosurfaces, streamlines surface and line plots. Fig 5.39, shows the non-linear temperature profile in the quasi-steady flow regime as obtained from the two and three dimensional simulations. For each case, the two dimensional and three dimensional results show similar temperature distributions, i.e the

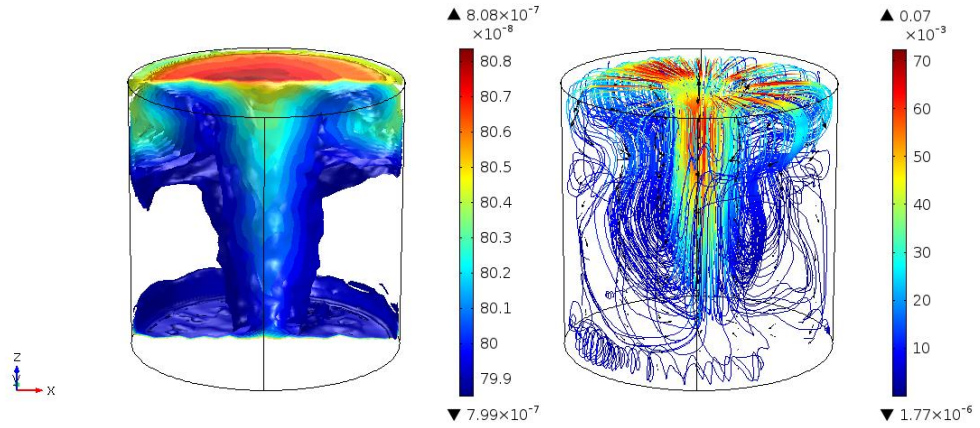

FIGURE 5.34: Temperature isosurface (left) and velocity streamlines (right) at τ=9.04×10^{-5}

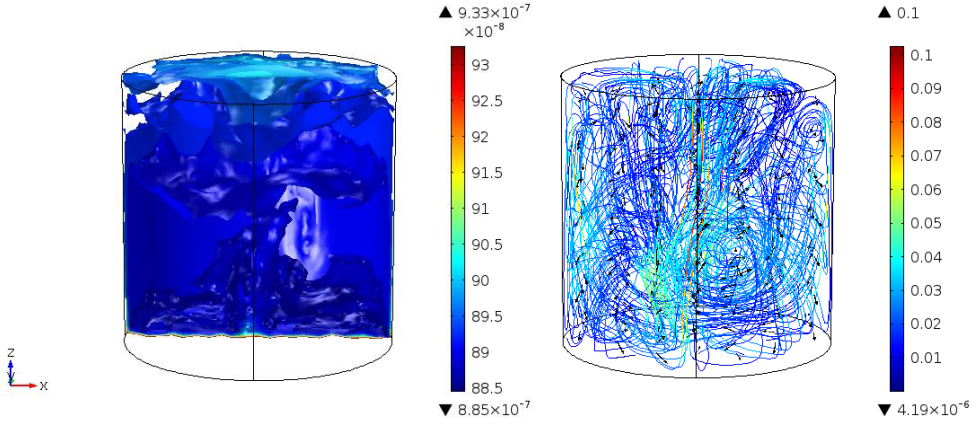

FIGURE 5.35: Temperature isosurface (left) and velocity streamlines (right) at τ=9.1×10^{-4}

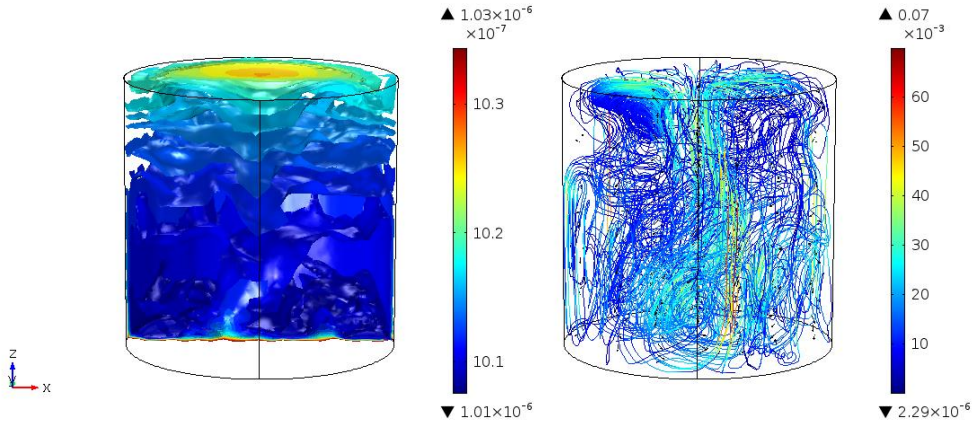

FIGURE 5.36: Temperature isosurface (left) and velocity streamlines (right) at τ=3.528×10^{-3}

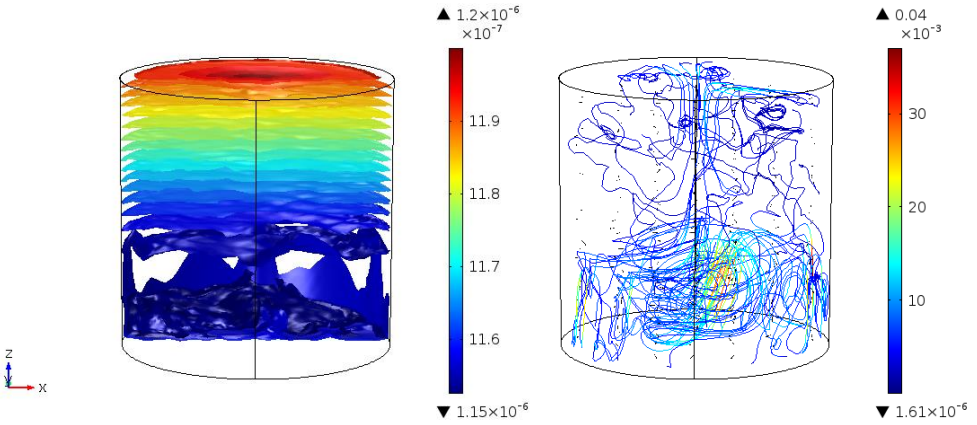

FIGURE 5.37: Temperature isosurface (left) and velocity streamlines (right) at τ=7.565×10^{-3}

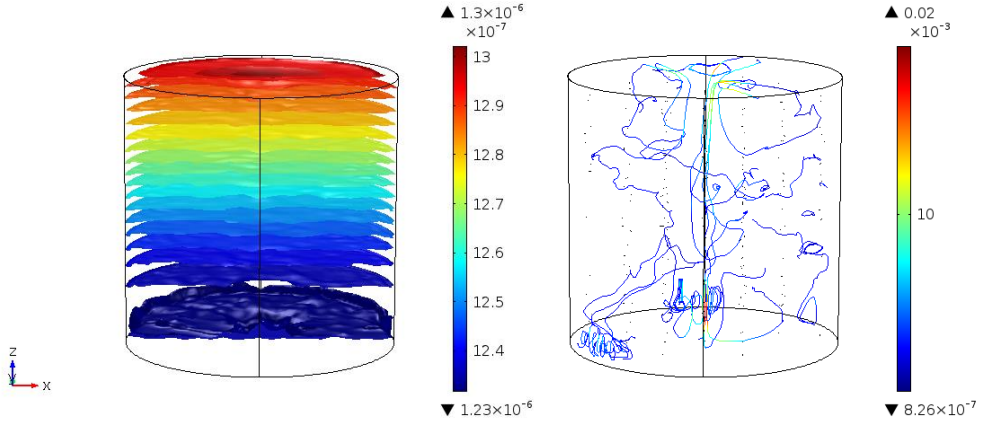

FIGURE 5.38: Temperature isosurface (left) and velocity streamlines (right) at τ=1.05×10^{-2}

surface plots and contours of temperature the existence of the surface and convection (mixing) layers is evident in both cases.

Fig 5.40, Fig 5.41, and Fig 5.42 compare the predicted time histories of the temperature, velocity and heat transfer obtained for the two dimensional and three dimensional at the point(0,-0.98H) and (0,0,-0.98H) respectively. From Fig 5.40 it can be seen that both temperatures have a similar profile, showing good agreement between the two dimensional and three dimensional simulations. However the differences observed between the three dimensional and two dimensional simulations may be attributed to the geometry. Fig 5.41 shows the time series, of the velocity for the three and two dimensional simulations. Both simulations confirm the initial (conduction), transitional (convective) and a quasi-steady stages of flow development. It is clear from the plots that the two and three dimensional simulations exhibit similar flow features; however the basic flow characteristics of the respective flows differ. The difference in the average velocity is more than 10%. This implies that although the two dimensional indicates important flow features it falls short of predicting the flow in a cylinder. It can be seen from the difference between them might be due to the absence of the azimuthal orientation in the two dimensional simulation. In the three dimensional model it can also be seen that the flow in the convecting layer does not enclose the entire fluid. Fig 5.42 shows

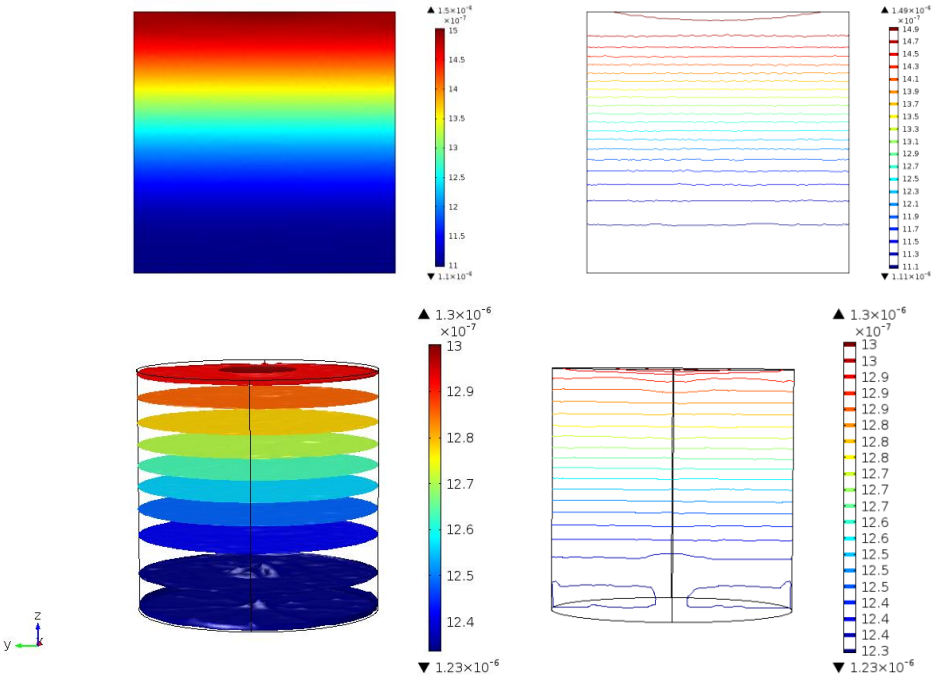

FIGURE 5.39: Surface plot, isotherms and isocontours showing temperature fields obtained from two and three dimensional simulations

the time series of the calculated heat transfer coefficient (Nusselt number), where the heat transfer coefficient is calculated from (equation 5.10). Both plots confirm the three stages of flow development. However, in Fig 5.42, it apparent the the results of the heat transfer coefficient calculated based on the 2 dimensional simulation are lower that that calculated based on the three dimensional simulation.

Direct comparison between the two and three dimensional simulations have revealed that the two dimensional simulation is able to capture the major features of the heat and flow features, including the basic features of the flow instabilities, and thus can be used to extract additional flow details with confidence for the DATES. However, the nature of the two dimensional model would not allow a full resolution of the details of the three dimensional convective instability. It is also noteworthy that the calculated flow and heat transfer rates from the three dimensional simulation fluctuate at smaller amplitudes than those calculated from the two dimensional simulation at both transitional and quasi-steady stages. This is because the quantities from the three dimensional simulation are averaged over the transverse direction, whereas those from the two dimensional simulation are representative of the values on a single sectional plane summary

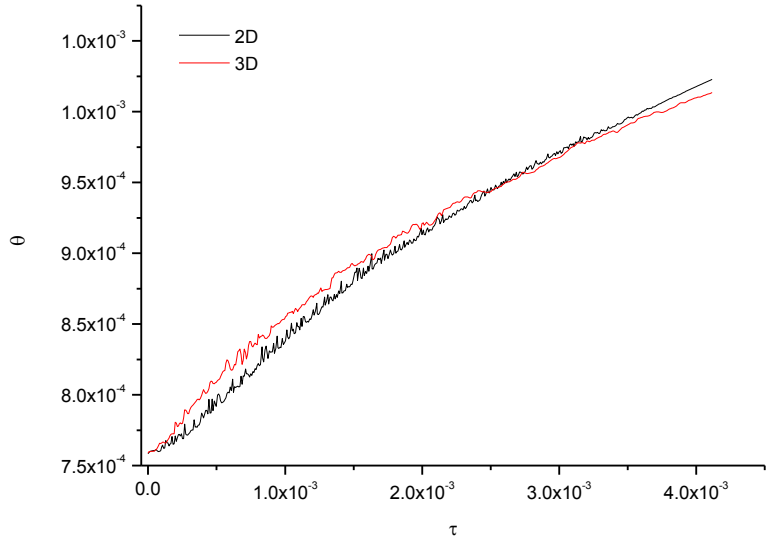

FIGURE 5.40: Plot showing comparison between two and three dimensional model time series of temperature in the boundary layer to the point(0,-0.98H) and (0,0,-0.98H)

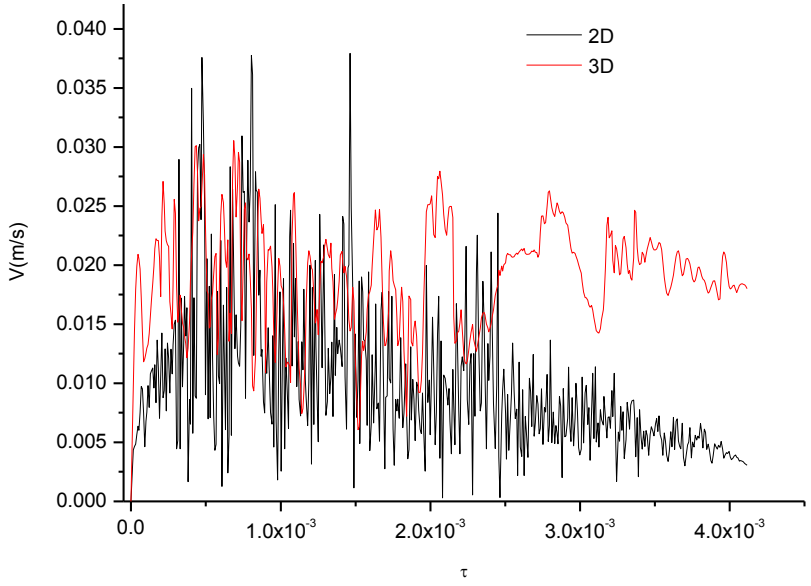

FIGURE 5.41: Plot showing comparison between two and three dimensional model time series of the velocity in the boundary layer to the point (0,-0.98H)

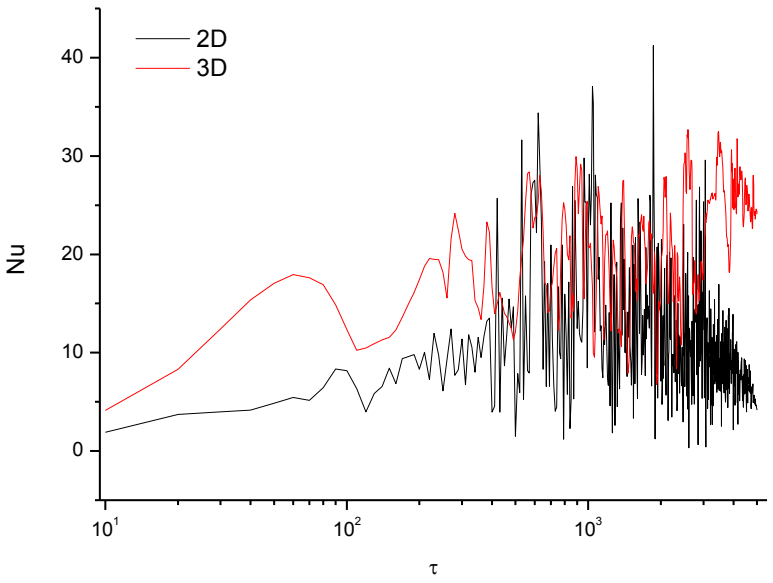

FIGURE 5.42: Comparison of Time series of the heat transfer coefficient at (0,-0.98H) and (0,0,-0.98H)in the two and three dimensional cases

- Two dimensional simulations clearly fails to capture the three dimensionality in real flow.
- Two dimensional simulations are not capable of accounting for three dimensional effects resulting from boundary conditions.
- Studies show the significant quantitative differences exist between two dimensional and three dimensional simulations, therefore two dimensional simulations should be only used for qualitative studies.
- Reported differences are attributed to inherent three dimensional nature of flows and the geometrical inconsistency of simplifying a cylinder to a cartesian three dimensional plane.

Two dimensional numerical model developed and simulations of the transient heat transfer and fluid flow in an enclosure of unit aspect ratio filled with molten binary KNO_3NANO_3 salt, directly absorbing concentrated solar radiation has been been presented in this chapter.

The numerical domain consisting of an open, adiabatic top surface, rigid and adiabatic vertical, and a rigid black boundary of finite thickness is directly heated by non uniform

concentrated solar radiation at the top surface. The molten salt enclosed in the domain captures, converts and stores harvested solar thermal energy incident in the domain. The sole function of the bottom wall is to collect all radiation transmitted radiation to the lower surface as useful energy, which will heat up the plate and induce natural convection. This will in turn provide the isothermalisation required in maximising the storage capacity without damaging the storage medium, which can typically sustain temperatures up to 600^oC quantification of the degree of thermal. The developed numerical model accounts for the depth dependent nonlinear volumetric absorption of directly deposited solar radiation based on weighted average values for the solar radiation and the salts attenuation coefficient. The governing equations for the numerical simulations have been carried out using commercial COMSOL Multiphysics software.

Numerical simulations were conducted for a charging period of 3 hours used in conjunction with a solar system. Two dimensional numerical results revealed a nonlinear temperature profile consisting of a hot stratified fluid layer lying above a cooler mixing layer. The observed nonlinear temperature was found to occur due to the absorption of radiation within the fluid body being a stabilising force, and the thermal instability at the lower surface being a destablising force. In the top fluid layer Maragoni convection is observed in the region below the top surface, however no bulk flow of fluid is observed. In this layer heat is transferred primarily by conduction On the other hand, in the lower fluid layer, where convective heat transfer was observed to dominate, the observed flow regimes are classified into 3 distinct regimes: (1) an initial stage (conduction regime) (2) a transitional stage (evolution of instabilities and onset of convection) and (3) quasi steady state (convective flow). A frequency domain study conducted showed the flow regime in the lower region has a fundamental frequency of 0.5Hz. Model parametric calculations were also carried out to determine the effect of the absorber plate thickness, flux Rayleigh number and the aspect ratio on the heat transfer, fluid flow, and the thermal performance. The effective heat transfer mechanism was observed to destroy the symmetry of the system that relates clock wise and counters clockwise flows state that without volumetric absorption exists for all values of Rayleigh number.

The two dimensional framework was successfully extended to three dimensional simulations. The three dimensional simulations were showed similar features to those found in the two dimensional simulations. However the three dimensional results revealed three dimensionality dependence of the observed heat transfer and fluid flow phenomena.

Chapter 6

Transient natural convection induced by the absorption of radiation based on a discretised waveband attenuation model

The use of direct capture, conversion and storage solar thermal technologies based on the direct volumetric absorption of solar energy for power generation has recently gained much attention. Development of realistic prediction tools capable of accurately modelling the local rate of solar radiation absorbed at various fluid depths is critical to providing greater understanding of the physical processes. Therefore such a model, will aid design, avoiding costly system over design and can keep the cost of such technologies to a minimum to make them economically competitive [64].

Absorption of spectral solar radiation in high temperature molten salts over wavelengths relevant to solar applications are not completely understood. Models predicting the absorption of solar radiation in high temperature fluid layers over wavelengths relevant to solar energy application are not available.

Researchers have developed numerical models to investigate natural convection induced by the volumetric absorption of radiation within fluids layers in various enclosures. Amongst these include: rectangular enclosures [65, 99–101], 2 and 3D triangular enclosures [83–86, 88–90], parallelepiped [91, 92] and in a cube [97, 98].

In spite these models giving insights and understanding of the physical processes encountered in the respective geometries, the models have relied on accounting for the depth dependent absorption of solar radiation within fluid depths using a single value,

solar weighted, absorption coefficient and a Total Solar Intensity (TSI) value. The major drawback of applying single bulk values for the absorption coefficient as obtained from equation 2.2 (chapter 2) is that they are characteristic of the visible part of the spectrum, where the salt is mostly transparent to radiation. As such the models fail to account for the effects of the longer wavelengths [65]

More numerical models found in literature have accounted for the spectral volumetric absorption of solar radiation in fluid depths, using spectral band models [66, 67]. In spectral band models, an average extinction coefficient k_j and an energy component, B_j over each wavelength band are employed to estimate the spectral depth dependent absorption of solar radiation in fluid layers. Lenert and Wang [4] used a two band model to in a numerical study on "Optimisation of Nano fluid volumetric receivers for solar thermal energy conversion". Webb and Viskanta [68] studied the absorption of solar radiation and heat transfer in a directly irradiated thin, falling molten salt film based on a two and three band attenuation models. Their results showed the sensitivity of their calculations to absorption coefficient band models where the two band model was found to give higher system performance compared with the three band model [68]. Hattori et al. [66] used a three band attenuation model to study the unsteady natural convection induced by absorption of solar radiation, with relevance to littoral waters. Wu et al. [67], studied the volumetric heat release inside a heat transfer fluid based on a six band attenuation spectral model. The study made comparisons between results of a six band spectral model with those of a twenty band solar spectrum model and results were said to be in good agreement [67]. Decrepencies exists between conclusions of the study of Wu et al. [67] and findingd of Webb and Viskanta [68]. The latter which reports considerable differences between a 2 and 3 band model, which is expected to depend on the resolution of the spectral band. Estimating spectral radiation and wavelength attenuation coefficient of a fluid by bands has been found to lead to errors however. Gueymard [69] discusses the drawbacks of the band models with regards to solar intensity distribution and shows the limitations of employing band models over his parametrised models spectra transmittance models, the standard reference considered in this chapter. According to Gueymard [69] using a small number of wavelengths in the band model limits the accuracy of the modelled attenuation, particularly, in spectral bands where strong absorption exists.

The purpose of this chapter is to apply Computational Fluid dynamic model, based on Finite Element Methods to develop a realistic model, which accounts for the spectral absorption of solar radiation in a high temperature molten salt filled in an enclosure of unit aspect ratio. As the current model considers the spectral nature of solar radiation, the solar radiation data is described by a standard condition for the spectral irradiation data, ASTM G173-03 Reference Spectra Derived from Simple Model of the Atmospheric

Radiative transfer of Sunshine (SMARTS v. 2.9.2) [69]. While the wavelength attenuation coefficients for the high temperature salts (KNO_3-$NaNO_3$) are accounted for by experimentally determined values measured using a Elmer Perkins EPP2000-UVN-spectrophotometer from StellarNet [133] over the wavelength range 380-1087nm. Experimental attenuation coefficients obtained in this study are compared with transmission measurements of Passerini [29] made in the visible wavelengths and a good agreement was found. Thermophysical properties of the salt are taken for temperature dependent properties given in Table 3.3. The geometry considered in the present model is similar to that considered in the previous chapter (chapter 5). However, the boundary and initial conditions are now described based on the spectral properties of the attenuation coefficient and solar radiation distribution.

Section 6.1 of this chapter presents the numerical formulation governing equations, numerical method and validation. Section 6.2 presents results and discussion for the spectral volumetric heating of a unit aspect ratio enclosure based on the solar spectrum at Air Mass AM1.5D. A spectral analysis of flow properties is also presented. Section 6.3 presents the results for the circulation rate and heat transfer in the enclosure at AM1.5D. Section 6.4 presents results for an analysis of the mixing and thermal stratifications for AM1.5D. Section 6.5 presents the evaluation of heat and flow features under variable Air Mass, Section 6.6 presents a comparative study is presented for a solar average weighted value and the current spectral dependent model. The chapter concludes with presentation of three dimensional simulation of the present problem for Air Mass 1.5D in section 6.7.

6.1 Numerical formulation

Under consideration is an enclosure of aspect ratio, H/D=1, filled with a high temperature fluid at an initial temperature, T_0=250^o C and in a quiescent state. The fluid is bounded by vertical rigid, adiabatic walls, a lower rigid black wall of finite thickness (dx), and an adiabatic top stress free boundary. The domain represents a fixed volume of commercially available binary mixture of Na and K nitrate salts (KNO_3-$NaNO_3$) used as a heat transfer fluid/storage medium, presently used in existing and demonstration solar plants around the world. At t=0, a non-uniform concentrated beam at 700X is incident over a fixed area (diameter,d= 0.2m) at the domain's top surface which is thereafter maintained. Owing to the spectral nature of the radiation and absorption coefficient, the incident radiation within the fluid depth is selectively absorbed in a non uniform manner. Assuming an optically smooth surface, the reflection, transmission

and refraction of incident solar rays can be predicted from Fresnel's equation of classical electromagnetic theory [67]. From equation 6.1 [64], the penetrating flux solar flux distribution just below the molten salt interface, neglecting scattering, directional dependence and accounting for reflection losses and optical losses at the top is estimated by:

$$I(z) = \sum_{i=1}^{n} \eta C(1 - r_a) I_\lambda e^{-\alpha_\lambda y} \tag{6.1}$$

where n is the discrete wavelength bands characterised by I_λ and α_λ: the solar intensity and absorption coefficient of the salt at respective wavelengths which can be found in Appendix A. The local rate of absorption of spectral flux, and the subsequent spectral volumetric heat generation is given by 6.2 [64]

$$S' = -\alpha\lambda \frac{dI(z)}{dz} \tag{6.2}$$

For the absorber plate, at the lower surface, which is perfectly insulated from the external surroundings, the non-absorbed portion of the transmitted radiation to the lower surface, which is subsequently collected as heat by the absorber plate is estimated by equation 6.3

$$I_b = \alpha[1 - \rho_a(\gamma)] I_0 e^{-\alpha_\lambda H} \tag{6.3}$$

The transient temperature and flow field in the cavity is obtained by solving the coupled mass, momentum and energy equations while accounting for the source term. The source term is obtained as the sum of the direct absorption heating and the heating from the lower surface.

$$\nabla \cdot \overrightarrow{V} = 0 \tag{6.4}$$

$$\rho \frac{\partial(\overrightarrow{V})}{\partial t} + \rho(\overrightarrow{V} \cdot \nabla)\overrightarrow{V}) = -RaPr\nabla p + RaPr\nabla^2 \overrightarrow{V} + PrRaT \tag{6.5}$$

$$\rho C_p \left(\frac{\partial T}{\partial t} + \nabla . \overrightarrow{V} T \right) = \nabla \cdot (k \cdot \nabla T) + S \tag{6.6}$$

where $\overrightarrow{V}$ is the velocity vector consisting of the velocity components u v and w. T is the spatial temperature in the domain from the resulting heating, P is the pressure and S is the spectral volumetric heating source term defined in equation 3.4.

The boundary and initial conditions are similar to the boundary conditions considered in the previous formulation and simulation except for the fact that the solar radiation (SMARTS model v 9.2) and attenuation coefficients are now described for the spectral properties. The solar spectrum is generated based on the SMARTS2. Clear skies are assumed and the zenith angle (z), and hence the Air Mass is considered to be the only variant that affects the direct spectral. As previously presented earlier in section 3.4.1, where the temperature of the lower plate due to residual flux absorption heating was derived, the perturbation temperature can then be obtained from equation 6.7:

$$\Delta T = \frac{\alpha I_b e^{-\alpha H}}{\kappa \rho C_p} \left(\frac{\kappa t}{\pi} \right)^{0.5} \tag{6.7}$$

The derived systems of unsteady state nonlinear partial differential equations (PDEs) from the present numerical formulation are solved using commercial finite element software COMSOL Multiphysics version 4.4 [120]. The numerical model utilised the conjugate heat transfer interface which includes radiation in participating media interface. Fluid discretisation was carried out using second-order elements for the velocity and linear elements for the pressure field (P_2+P_1). A fully implicit time-stepping method using backward differential formulations (BDF) solver was employed [120]. As the numerical result should be independent of the mesh element size, the check of the mesh sensitivity has been conducted. Fig 6.2 shows the mesh sensitivity a representative simulation where the aspect ratio, H/D=1, a spectral solar radiation distribution at Airmass 1.5D, concentrated at 700x and wavelength dependent attenuation whose data is given in appendix A. The difference in the solution max velocity at different mesh element sizes and the solution at the finest mesh converged at N=5 equivalent to an element size of 20mm, above which the solution for the maximum velocity remained constant. Following the results obtained in this study, a mesh size of 20mm is chosen mesh giving a total of 5842 mesh elements, because the relative error for this mesh was found within 0.2%. Fig 6.1shows a schematic of the numerical domain and mesh. In the numerical model, a convergence criterion of 1 $\times 10^{-6}$ was imposed on the residuals of all the governing equations to ensure convergence. The present numerical model was also checked for accuracy against the published numerical solution of the experimental study of Coates and Patterson [104] on the unsteady natural convection in a cavity with non-uniform absorption of radiation [104]. Results of the present simulation satisfactorily agree with

those reported in Coates and Patterson [104] with errors of less than 5%. Full details of the validation study please refer to chapter 4.

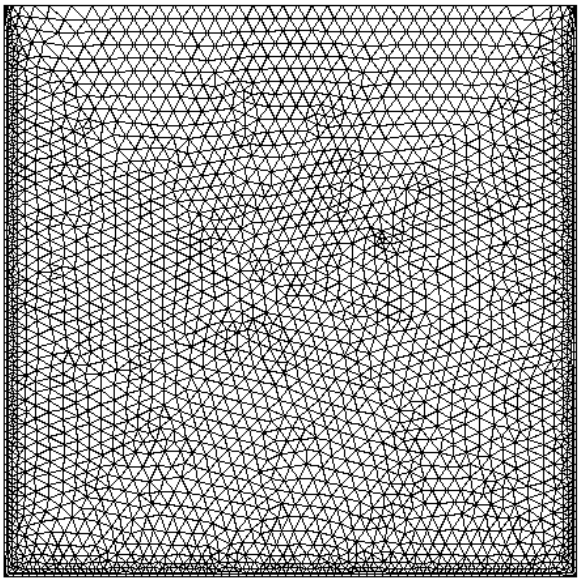

FIGURE 6.1: Computational domain and mesh.

6.2 Results and discussion

Numerical results for the transient temperature field resulting from the volumetric heating of a high temperature salt within an enclosure (H/D=1) at Air Mass 1.5D are presented in Fig 6.3 a-d. Fig 6.3a shows the temperature profile at a time (τ=2.21×10^{-5}) representing the early stage where the solar radiation has been initiated. From the figure it is seen that the downward travelling radiation heats the fluid body during its absorption in an non uniform manner. The fluid is heated along the top surface and in a region below it. At the lower surface, the transmitted flux heats the absorber plate and subsequently develops a thermal boundary layer. Fig 6.3b, shows the temperature profile at a later heating time, τ=9.09×10^{-5}, when thermal plumes begin to emerge from within the lower boundary layer, while the top heated surface layer progressed downward into the fluid. In Fig 6.3c (τ=3.57×10^{-4}) thermal plumes are seen to increase in height and extend into the fluid volume, confined to below mid depth of the fluid height. At the top a hot stratified layer is seen. Fig 6.3d (τ=3.124×10^{-3}), reveals a nonlinear temperature profile where a hotter fluid layer lies above cooler fluid depth thermal, similar to that

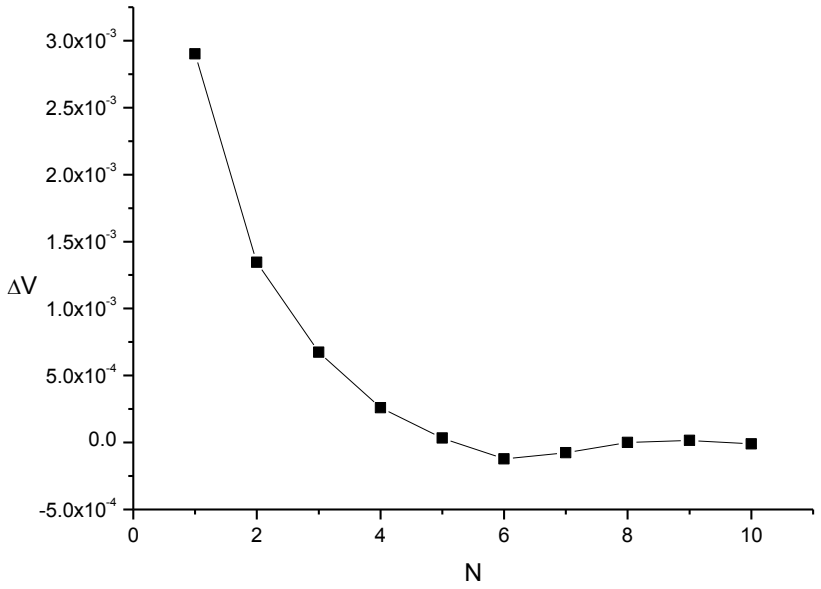

FIGURE 6.2: Mesh refinement test results.

observed in chapter 5 . A significant effect of the non linear temperature stratification is that it confines the mixing mechanisms length in a region below the hot stable surface layer. According to Hattori et al. [91] the mixing confinement height has a typical height equal to the attenuation length of radiation in relatively deep waters with the penetration length scale of plume determining the lower mixed layer thickness [91].

6.2.1 Features of transient natural convection in the thermal boundary layer flow

In Fig 6.4 to Fig 6.7 the temperature and velocity contours for heating times in the range $2.27\times10^{-5} \leqslant \tau \leqslant 3.92\times10^{-3}$ due the direct absorption of spectral radiation based on the solar spectrum Air Mass 1.5D in high temperature molten KNO_3-$NaNO_3$ are shown. All figures presented by isotherms are shown in non-dimensional form. Fig 6.4 a-i covers times from the early heating to the mid heating times, while Fig 6.7 covers heating times form the mid heating to the late heating times Fig 6.4a, at $\tau = 2.27\times10^{-5}$, the temperature contours shows the non uniform volumetric heating of the fluid body. The temperatures encountered in the fluid body are attributed to absorption of the radiation of the long wavelengths in the infra red range of the spectrum where this fluid is considered to be effectively opaque to radiation and from the short wavelengths. The

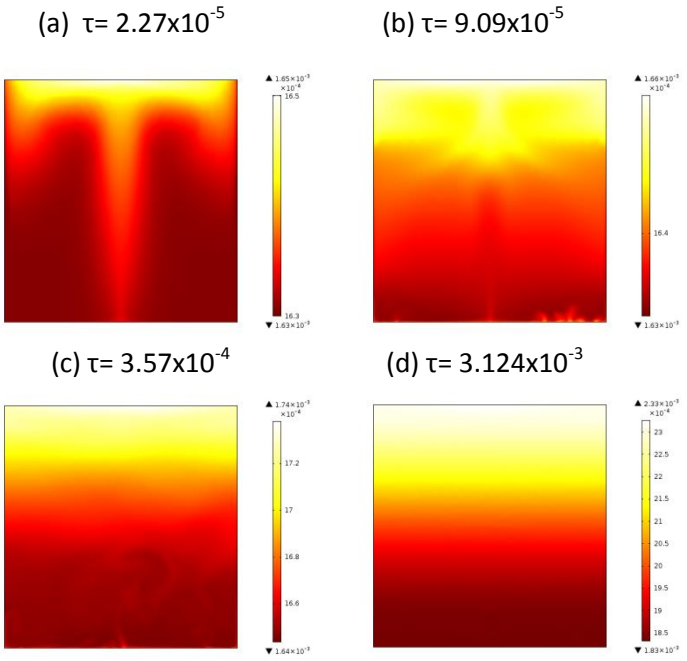

FIGURE 6.3: Surface plots showing the transient temperature within the domain at time :a)τ=2.21×10^{-5}, b) τ=9.09×10^{-5}, c) τ=3.57×10^{-4}, d)τ=3.124×10^{-3}.

figure illustrates the surface heating along the top surface and a non-uniform downward heating. Isotherms show that a thin thermal boundary forms above the lower boundary, which is subsequently developed at the lower corners of the vertical walls owing to end wall effects. The nearly parallel temperature contours with the boundary layer illustrates that the heat transfer is primarily due to conduction in the boundary layer. The thermal boundary layer developed is heated by a contributions of the heat from the lower surface and the absorption of radiation.

At τ =8.33×10^{-5}(Fig 6.4b), the continued heating shows (i) thermal structure developed in the top fluid layer below the top surface and (ii) the emergence of thermal plumes from within the thermal boundary layer. Isotherms are observed to expand toward the lower surface, transferring heat within the fluid body mainly by conduction. However the thermal features observed at the top surface indicate convective heat transfer within the region. The presence of thermal plumes mark instability, which occur, whenever temperature gradients within the boundary layer exceeds some critical value, thereby satisfying the stability criterion for free convection and hence introducing a Rayleigh Bernard instability. The stability criterion for free convection and time of occurrence are important to this class of problem and have been discussed extensively elsewhere [80]. At τ=8.33×10^{-5}(Fig 6.4b), stabilising temperature contours are seen to extend to

the lower surface, while thermal plumes continue to develop. At $\tau = 1.59\times10^{-4}$(Fig 6.4c) interaction between the temperature contours from the volumetric absorption and the thermal plumes can be seen. Recalling that the absorption of solar radiation is a stabilising force and is responsible for the top heating source, while the thermal instability in the lower fluid column is a destabilising force. From Fig 6.4a, b and c, it can be seen that the stabilising force dominates the destabilising force. At the later heating times, $\tau = 2.35\times10^{-4}$ to $\tau = 3.8\times10^{-4}$, a mixing layer developing in the lower fluid column is clearly seen. This is owing to the destabilising force dominating due to increased heating of the lower fluid from the absorber plate. With increasing time the mixing depth is seen to increase in height thereby the stabilising temperature contours are pushed back towards the top surface. Isotherms indicate convective heat transfer within the mixing depth and rising plumes are seen to extend into the mixing layer.

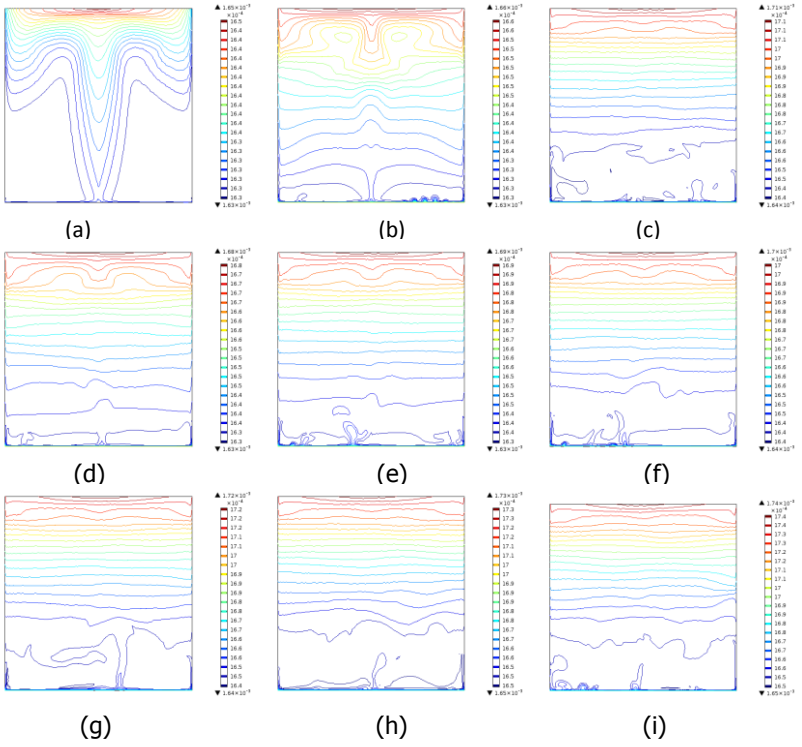

FIGURE 6.4: Transient evolution of the fluid inside the enclosure.Temperature contours :a) $\tau = 2.27\times10^{-5}$, b)τ =8.33×10^{-5}, c)$\tau = 1.59\times10^{-4}$ d) $\tau = 2.35\times10^{-4}$ e) $\tau = 2.81\times10^{-4}$ f)$\tau = 3.91\times10^{-4}$ g) $\tau = 3.42\times10^{-4}$ h) $\tau = 3.57\times10^{-4}$, i)$\tau = 3.8\times10^{-4}$ AM1.5D, H/D=1.

The process is further illustrated in Fig 6.5 a-i, where the corresponding velocity contours and vectors for heating times $2.77\times10^{-5} \leqslant \tau \leqslant 3.8\times10^{-4}$ are presented. In Fig 6.5a, during the boundary layer development, no bulk fluid movement is observed within the

domain, however tangential fluid flows confined to the region just below the top surface and along the vertical wall due to the end wall effects can be seen. At the boundary layer no bulk flow is observed; this confirms that heat transfer within this stage is purely conductive. At Fig 6.5b (τ= 3.8×10^{-4}) and Fig 6.5c shows the existence of two vortices in the top fluid column as seen in Fig 6.4b and c. In these transients, low fluid velocities can be seen for the boundary layer region. Flow transition from τ= 2.27×10^{-5} to τ= 3.8×10^{-4},(Fig 6.5d-i),shows a developing unsteady irregular and complex flow confined to the lower fluid region which corresponds to the development of the mixing layer. The flow is characterised by a combination of thermal plumes, circulation cells and the boundary layer flows found to be irregular in occurrence. An important feature seen in this flow is the occurrence of the intrusion flow at the interface between the competing vertical stabilising and the destabilising effects, which is a major contribution to the flow and temperature field. The boundary layer flows do not enclose the entire flow but is seen to discharge fluid from the boundary layer into the core of the fluid in the mixing layer.

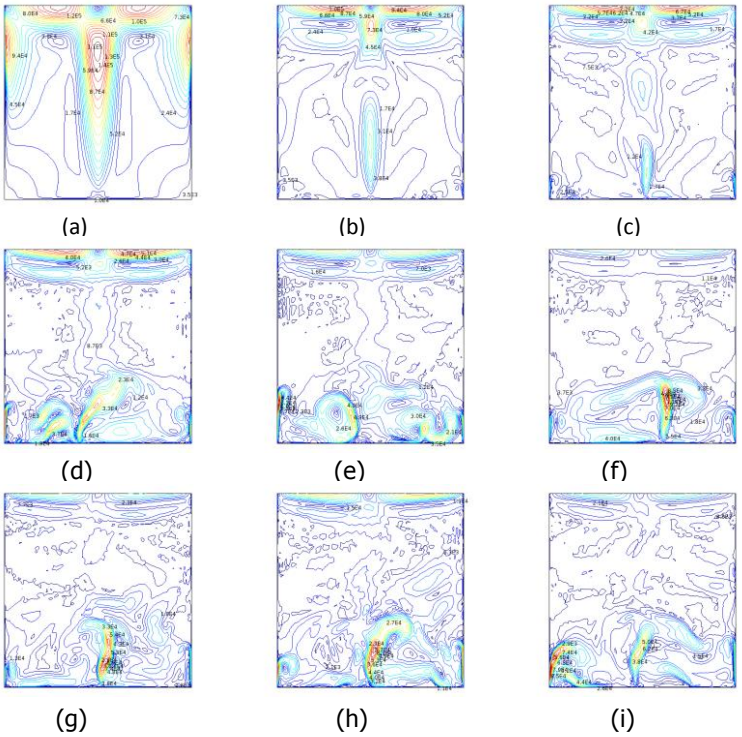

FIGURE 6.5: Evolution of the fluid flow within the enclosure:velocity contours :a) τ= 2.27×10^{-5}, b) τ =8.33×10^{-5}, c) τ= 1.59×10^{-4} d) τ= 2.35×10^{-4} e) τ= 2.81×10^{-4} f) τ= 3.91×10^{-4} g) τ= 3.42×10^{-4} h) τ= 3.57×10^{-4}, i) τ= 3.8×10^{-4}. AM1.5D, H/D=1.

Fig 6.6 a-i show temperature contours for dimensionless times $\tau = 6.86\times10^{-4}$ to $\tau = 3.92\times10^{-3}$. Fig 6.6a,b and c how continued development of the surface layer and the mixing layer, there a fully developed unsteady complex flow is seen at $\tau = 3.92\times10^{-3}$(Fig 6.6c). During these heating times the thermal plumes remain active in the mixing process. For $\tau = 1.62\times10^{-3}$, $\tau = 2.17\times10^{-3}$ and $\tau = 2.33\times10^{-3}$, as the flow begins to reach the quasi steady state, thermal plumes become reduced, while the stabilising thermal contours advance towards the lower surface. Thus reduction in the mixing layer is observed. At $\tau = 2.73\times10^{-3}$ and $\tau = 3.12\times10^{-3}$ further reduction in the mixing depth can be seen while a greater depth is covered by stabilisation contours. Finally at $\tau = 3.92\times10^{-3}$ the mixing depth is completely reduced and stabilisation contours completely fill the domain. Thus it can be seen from the time presented that, the lower column of the domain goes from a purely convective stage to a predominantly conductive heat transfer regime as illustrated by the nearly parallel isotherms.

Fig 6.7 a-i shows the corresponding velocity contours for $\tau = 6.86\times10^{-4}$ to $\tau = 3.92\times10^{-3}$. In Fig 6.7 a,b and c the unsteady complex flow is still observed and is seen to be confined in the mixing layer which is seen to be approximately 0.5H. The strength of the flow increases up to $\tau = 1.46\times10^{-3}$, after which is seen to decrease. Fig 6.7 d to i reveal that increased heating times, the mixing depth, thermal plumes and convective heat transfer are drastically diminished. At $\tau = 3.92\times10^{-3}$ no bulk flow is observed, and the flow becomes reduced to the boundary layer region as seen in Fig 6.7i. This is consistent with observations for the temperature contours at the corresponding time (Fig 6.6i). Flow solutions observed here are very different from typical flows obtained in conventional Rayleigh Bernard convection. Flow solutions also show that competing stabilisation effects of flow stratification established by the absorption of solar radiation and the destabilising effect of natural convection from the lower surface heating destroys the symmetry of the system. The flow transitions observed reveal an initial stage, a transitional regime and a quasi steady regime (Fig 6.7).

6.2.2 Spectral analysis

In this section, spectral analysis is applied to investigate the flow properties of the lower boundary fluid flow within the fluid domain. Fig 6.8 presents the time history of the velocities at a point 0.25H, 0.95H, above the lower surface in linear scales (Fig 6.8a) and the logarithmic scale (Fig 6.8b) . The plots (Fig 6.8a and b) reveal the existence of the three stages: initial, transitional and quasi steady regimes that can easily be matched with temperature and velocity contours shown in Fig 6.4 to Fig 6.7. In the early flow stage the velocity increases smoothly between τ=0 and $\tau = 2.77\times10^{-5}$ which is clearly shown by the the logarithmic scale plot of (Fig 6.8b). Flow at this stage is generally

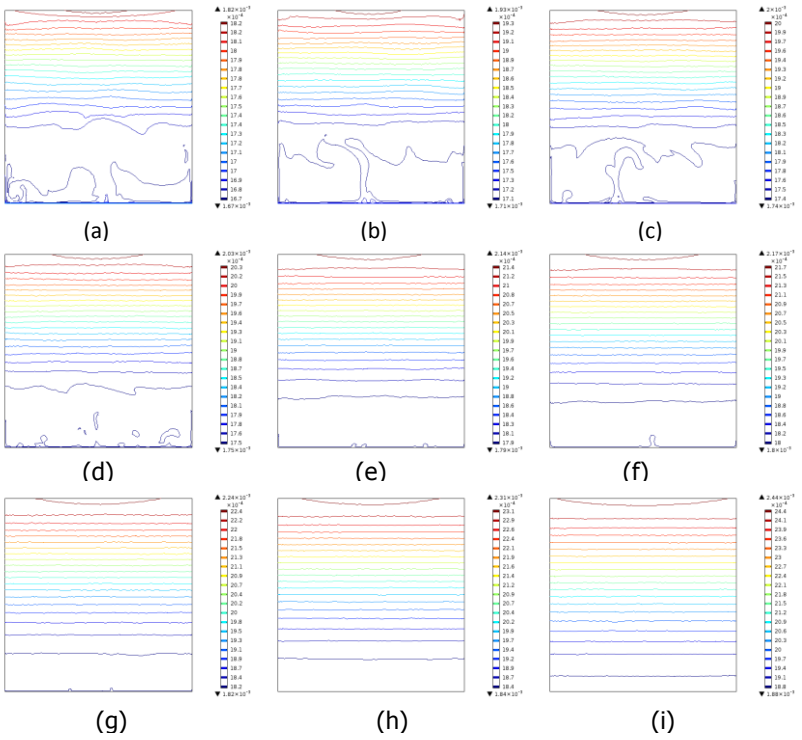

FIGURE 6.6: Surface plots showing the transient temperature within the domain at time :a) τ= 6.86×10^{-4} b) τ= 1.15×10^{-3} c) τ= 1.46×10^{-3} d) τ= 1.62×10^{-3} e) τ= 2.17×10^{-3} f) τ=2.33×10^{-3} g) τ= 2.73×10^{-3} h) τ= 3.12×10^{-3} i) τ= 3.92×10^{-3}.

characterised by low flow velocities. In the transitional stage which occurs between $8.33\times10^{-5} \leqslant \tau \leqslant 2.73\times10^{-3}$, velocities are characterised by sharp and irregularly fluctuating velocities. Similarly,the transitional regime exhibits the early, middle and late transitional stages described in chapter 5. The variation in the flow velocity fluctuation at this stage coincides with the occurrence and disappearance of thermal plumes at the respective heating times. The transitions identified here are identical to those obtained for the solar weighted average model, however the occurrence times magnitudes and frequency of oscillation, are observed to be reduced. The quasi steady stage is reached at $\tau > 2.73\times10^{-3}$.

Fig 6.9a shows the spectrum of the velocity time series in the early to middle transition stage (τ=1.67 × 10^{-4} to τ=1.58 × 10^{-3}). A dominant frequency, f$_1$ =0.34Hz is evident with amplitude 1.4× 10^{-4}, with a second frequency peak is seen at f$_2$=0.36Hz, with amplitude 3.2× $^{-4}$. In the middle to the late stage (Fig 6.9b), the dominant frequency has increased to f=0.5648Hz, with other lower amplitude and frequency modes observed between 0.7309$\leqslant$ f $\leqslant$ 0.9833Hz. In the quasi steady stage, the dominant frequency has

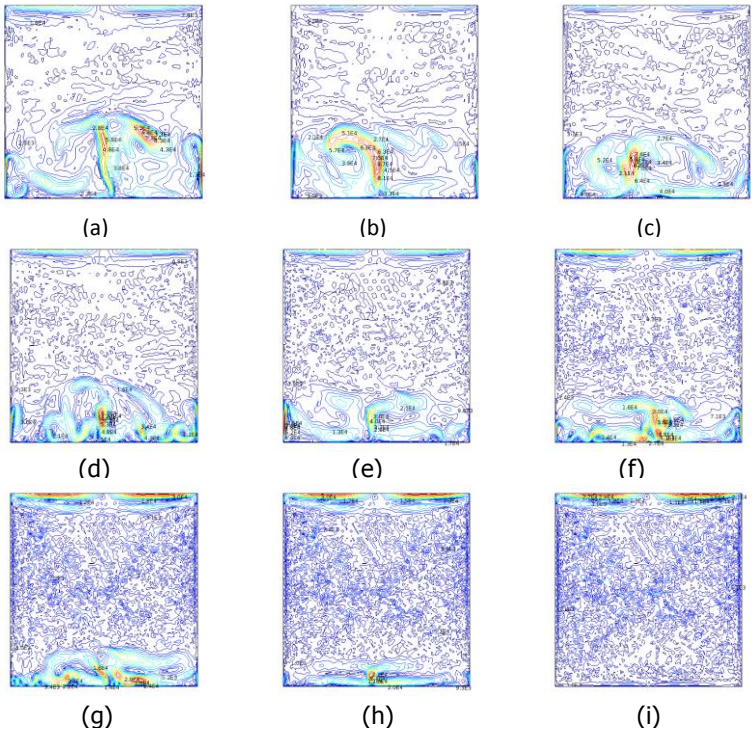

FIGURE 6.7: Evolution of the fluid flow within the enclosure:velocity contours : a) τ= 6.86×10^{-4} b) τ= 1.15×10^{-3} c) τ= 1.46×10^{-3} d) τ= 1.62×10^{-3} e) τ= 2.17×10^{-3} f) τ=2.33×10^{-3} g) τ= 2.73×10^{-3} h) τ= 3.12×10^{-3} i) τ= 3.92×10^{-3}.

moved towards the high end of the spectrum to 1.189Hz with reduced amplitude to 1.647×10^{-5}.

The time varying velocity components, u,v at x=0,0.9H in the enclosure is presented in Fig 6.10 a&b. It can be seen that the velocity components are very close to zero, under the present heating conditions. Both velocities exhibit, the early, transitional and quasi steady state regimes. It can also be seen that the major contribution of the flow is to the vertical component of the velocity.

6.2.3 Spectral variation with fluid depth

Fluid velocities induced within the enclosure following the direct absorption of concentrated solar radiation has been illustrated in figures 6.5 and 6.6 respectively. Similarly, the results presented in the section are post processed with Matlab version 2013 software [129]. The local flows paths developed at different depths are dependent on the downward spectral attenuation and as such has a major influence on the temperature

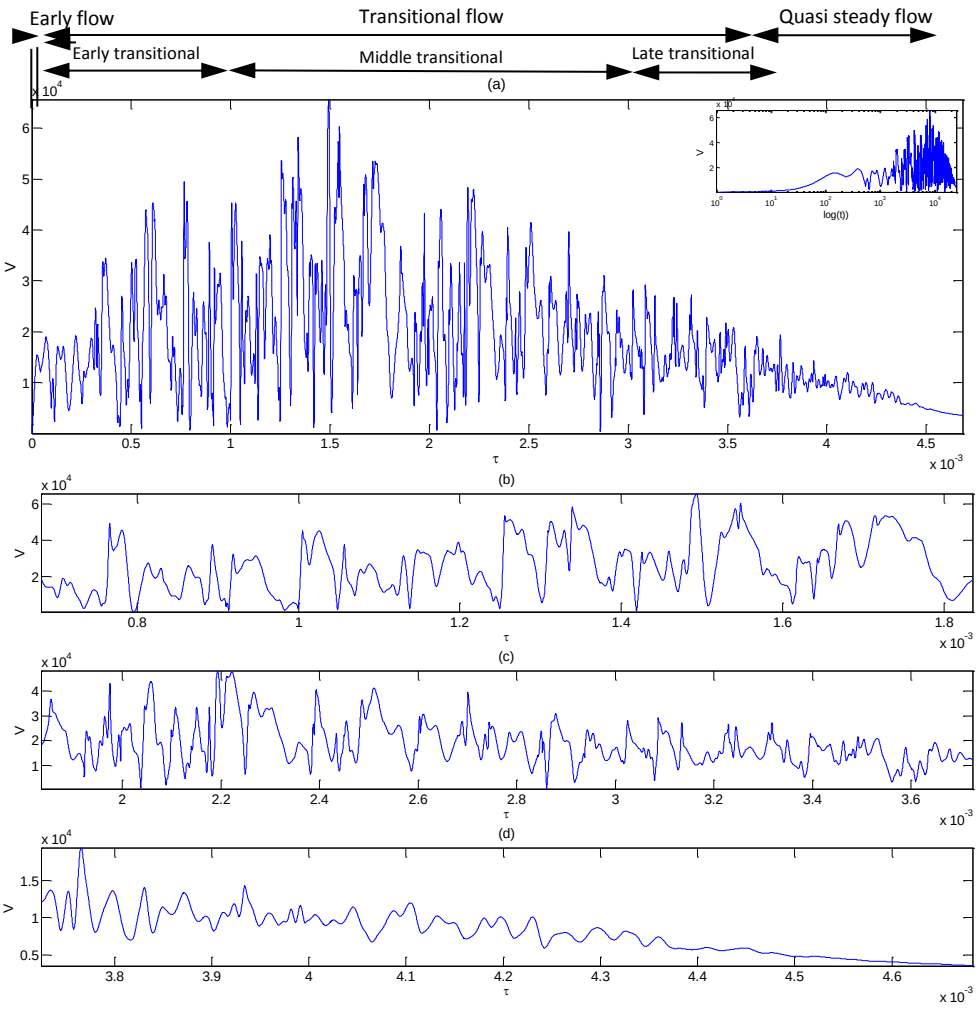

FIGURE 6.8: Time series of velocity at a position (0,H), and the spectra of different sections of the time series for Ra=8.3×10^{11}. (a) Time series with linear scale (b) early transitional (c) Middle transitional (d) Late transitional stages.

profile. Fig 6.11, shows the time series for various vertical depths taken at a horizontal position, mid way along the lower boundary. Flows at the respective fluid depths experience the early, transitional and quasi steady state stages flows. However, the magnitude of the flows fluctuations and duration of occurrence of the transitional regime are seen to decrease with increasing depth. The plots agree with observations form temperature contours which showed no bulk fluid flows at the top fluid column.

Of primary interest here is to investigate the spectral variation on flow properties with local depth at a given horizontal position. Fig 6.12 shows the corresponding spectra for the time series of the vertical velocity for the respective location. It is clear in these figures that, the power of fluctuation varies with the depth and that the major frequency of the vertical velocity is different at each depths.

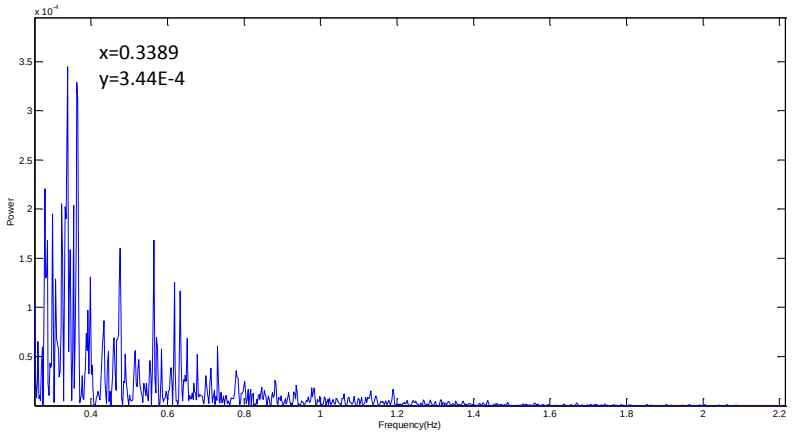

FIGURE 6.9: (a) Spectra in the transition regime.

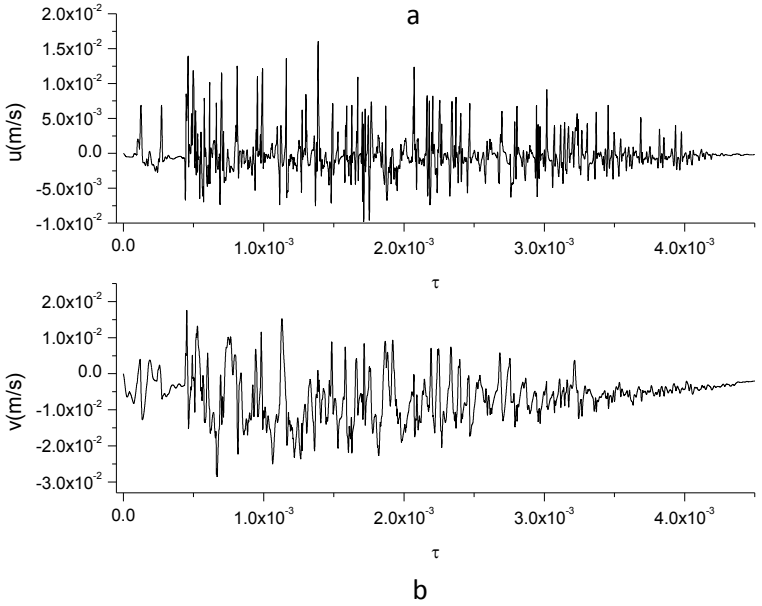

FIGURE 6.10: Time histories of u and v velocity components at the at x=0, 0.9H.

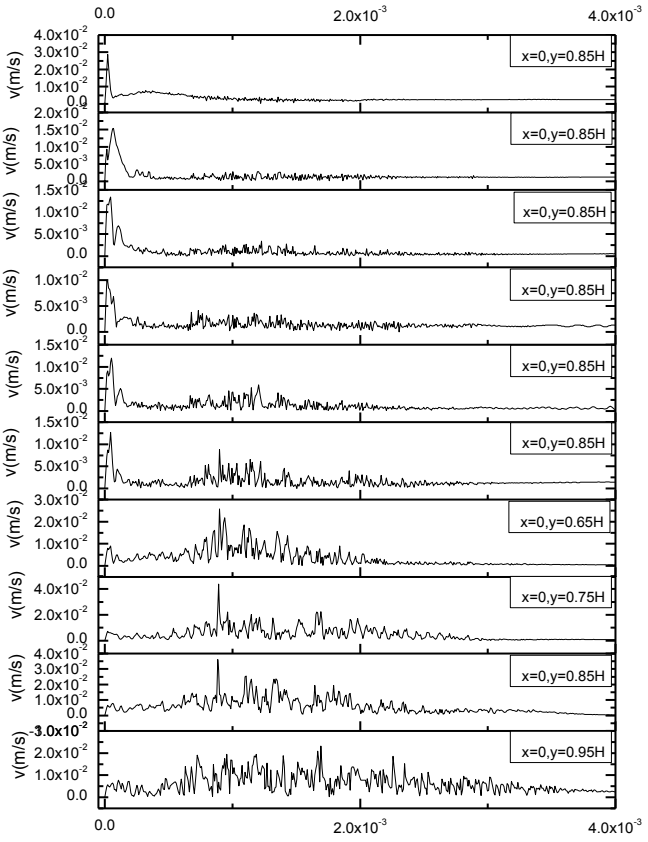

FIGURE 6.11: Time histories of temperatures at selected locations along different depths from the top surface

6.3 Heat transfer from the lower surface and the average volumetric flow rate.

Time histories of the averaged volumetric flow rate and the heat transfer rate integrated over a point L/4, -0.98H obtained by integration of both quantities over the enclosure depth are presented in Fig 6.9 and Fig 6.10 respectively. The volumetric flow rate and the heat transfer rate are presented in dimensionless for by normalising the corresponding dimensioned quantities with κ and h respectively. In Fig 6.13, the volumetric flow rate increases sharply in the early stage to a peak flow rate of 0.022 at (τ = 0.0009). The flow rate then dips to 0.0055 and is followed by an increase to approximately 0.006 at τ =0.006 to the transitional stage where the flow rate is characterised by strong and irregular fluctuations. In the transitional stage, the flow rate is characterised by strong and irregular fluctuations. The initial dip signifies the start of the transition stage which

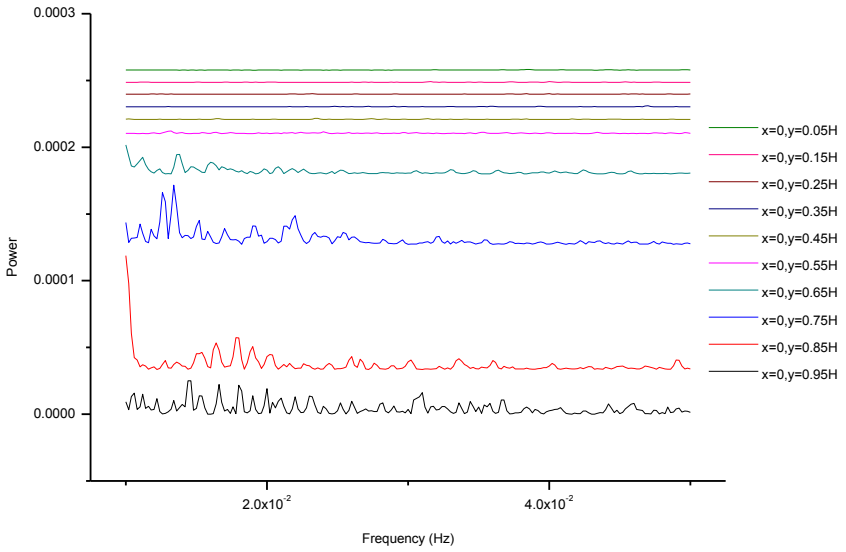

FIGURE 6.12: Spectra for the time series of the vertical velocity at selected locations along different depths from the top surface

coincides with the occurrence of thermal plumes. At τ =0.006, the quasi-steady stage is reached, where the volumetric flow rate oscillates about a mean flow rate, with more regular fluctuation ofreduced amplitude.

Fig 6.14 presents the time history of the heat transfer from the lower surface. The heat transfer shows similar features to those identified form the volumetric flow rate plot (Fig 6.13). The plot reveals a sharp increase in the heat transfer to a maximum at the early stages. The value then decreases into a region of sharp irregular occurring fluctuations of varying amplitudes. The high heat transfer rate shown by the spike in Fig 6.14 corresponds to high volumetric flow rate observed in Fig 6.13. Both spikes however, coincides with the change from the initial stage to the transitional stage when thermal instability is introduced. Both plots confirm the three stages of flow development, driving mechanisms and the approximate time of their occurrence.

Fig 6.15 shows a cross correlation function plot between the heat transfer coefficient (Nu) and the transient velocity components, u,v at x=0.25H, 0.9H for AM1.5D and H/D=1. Fig 6.15a shows the a negative value of -0.8 which indicates a weak correlation between the horizontal velocity component and the convective heat transfer. On the other hand Fig 6.15b show a peak positive correlation value of 0.04, thus indicating a positive correlation between the convective heat transfer and the vertical velocity,

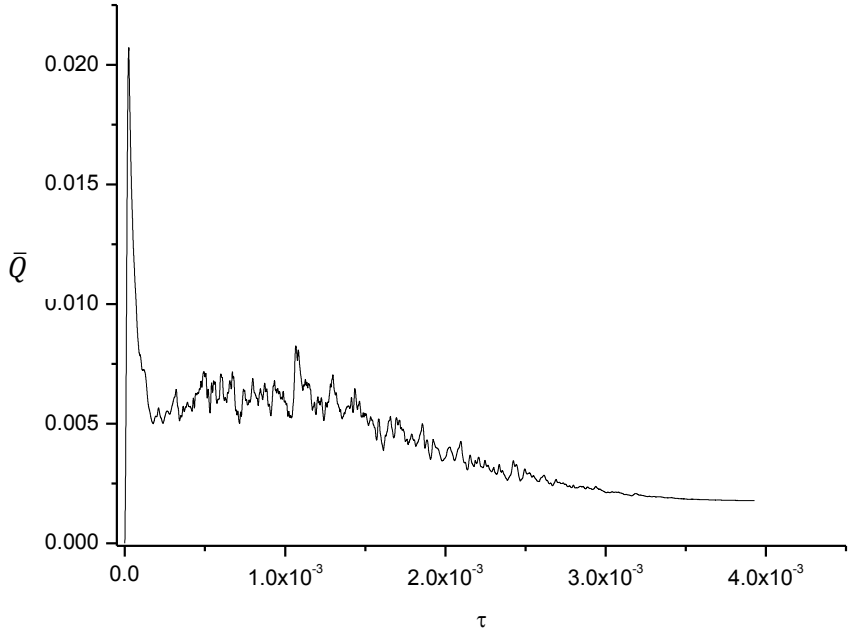

FIGURE 6.13: Time series of integrated flow rate at 0.25H, 0.98H

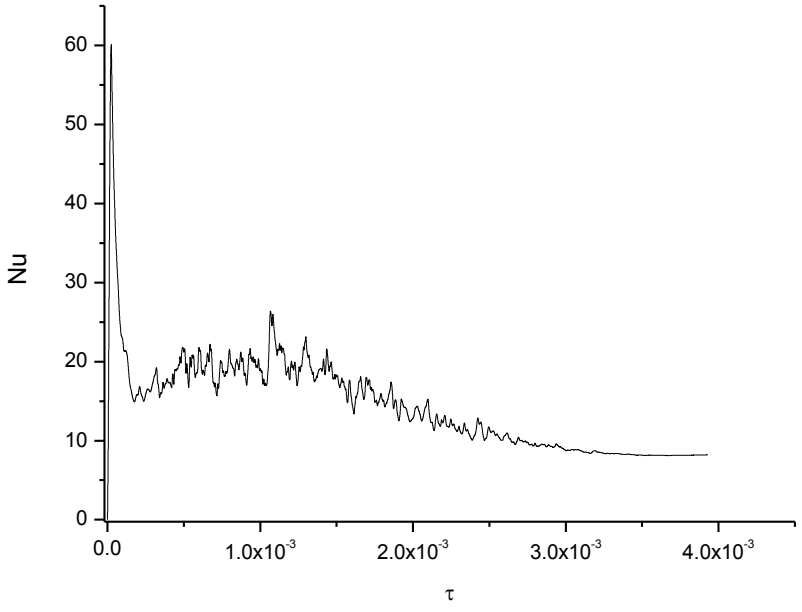

FIGURE 6.14: Time series of integrated heat transfer rate at the point (0.25H, -0.98H

which is an expected result as the convective heat transfer is dependent on the vertical velocities driven by thermal plumes. [134].

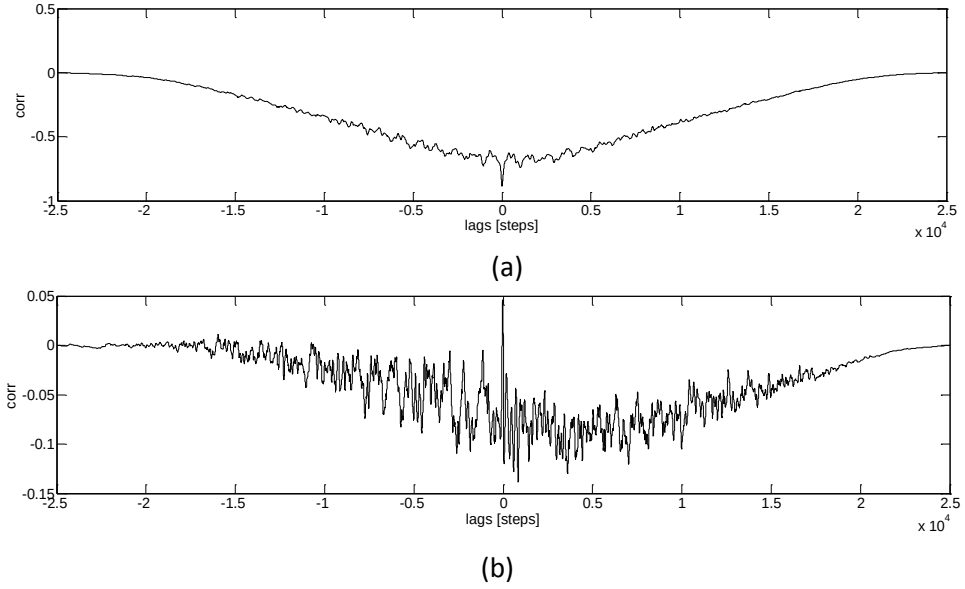

FIGURE 6.15: Cross correlation function plot between the heat transfer coeffienct (Nu) and the transient velocity components, u,v at x=0.25H, 0.9H for AM1.5D and H/D=1.

6.4 Mixing and stratification

In this section the MIX number defined by Davidson et al. [112] is used to estimate the level of fluid mixing and stratification in the thermal energy store.

Fig 6.16 shows the transient MIX number against the dimensionless heating times τ=5$\times$ 10^{-4} to τ=3.5$\times$ 10^{-3}. The time represents the period on the transitional stage, when mixing takes place. From Fig 6.16, it can be seen that as heating progressed, the MIX number linearly decreases. At τ=3.5$\times$ 10^{-3} a 40% decrease in the mixing was obtained. As the MIX number tends towards zero, stratification is promoted at later heating times (MIX=1 indicates full mixing, while MIX=0 indicated full stratification). The figure is in good agreement with earlier observations, where mixing in the lower fluid column decreased, while stratification increased. The major weakness of the current method is that it does not show what time mixing was most severe during the charging period [111]. A plot of the time averaged Nu number against the time averaged MIX number is shown in Fig 6.17. The plot shows a linear increase in the heat transfer with increasing MIX number, thus indicating increased heat transfer with increasing level of mixing in the enclosure.

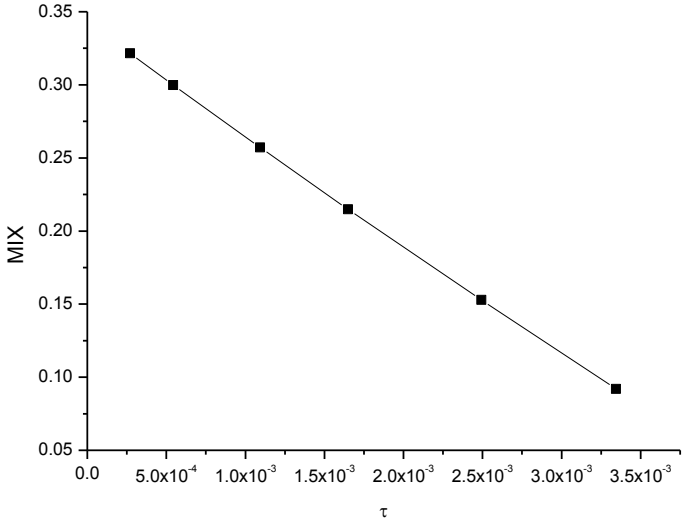

FIGURE 6.16: Transient MIX number

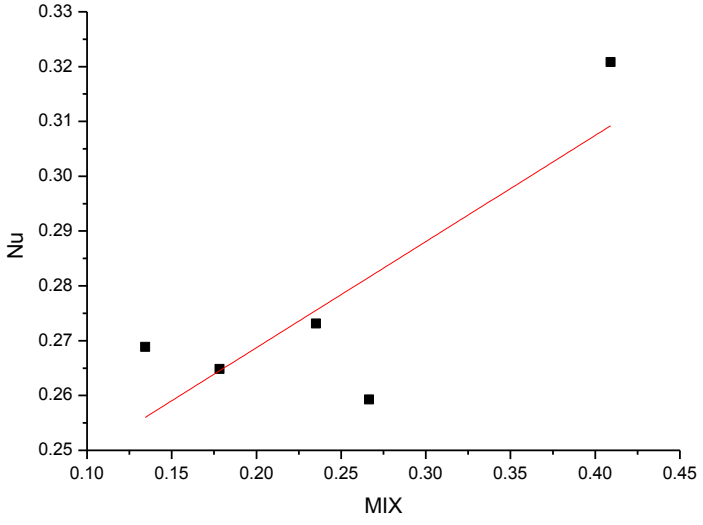

FIGURE 6.17: Heat transfer coefficient (Nu) vs MIX number

6.5 Evaluation of Thermal and flow features under variable Air Mass

This section investigates the heat and fluid flow features due to the volumetric absorption of the spectral irradiation distribution under variable Air Mass. The relationship of Direct Normal Intensity, zenith angle and Air Mass were presented in chapter 2.

The spectral irradiation data obtained from Reference Spectra Derived from a Simple Model of the Atmospheric Radiative transfer of Sunshine (SMARTS v. 2.9.2) (NREL) at Air Mass AM1.5D was presented in Fig 2.11. Fig 6.19 present solar irradiation distribution for Air Mass; AM1, AM1.5D, AM2, AM3, AM4, and AM5, as obtained with the SMARTS model. The influence of variable Air Mass(AM) on the UV, Vis and IR components of DNI is presented in Fig 6.19. In this figure, it can be seen from the figure that as the Air Mass increases, the UV and Visible radiation components decrease and the radiation shifts to higher wavelengths. This therefore translates to reduced intensity associated with increasing Air Mass. Fig 6.20 shows the Direct Normal Intensity (DNI) versus zenith angle and Air Mass. It can be seen that DNI decrease with Air Mass and zenith angle.

Fig 6.21 shows the spectral power density at Air Mass AM1, AM1.5D, AM2, AM3, AM4, and AM5, evaluated based on spectral irradiation distribution obtained SMARTS v. 2.9.2 (NREL) model and the spectral attenuation coefficient of molten KNO_3-$NaNO_3$ salts. In the present study, the UV component (9%) and infra red radiation above 1087um was not used due to lack of data on attenuation coefficients. The region accounts for over half of the solar spectrum as 55% of the spectrum lies in the 400-800 um range , while the infra-red wavelength covers 27% lies in the region covered. Thus it is believed here to be a good representation of the solar spectrum in the present study to demonstrate the functionality of the model. Dronting [57] in a study on optical properties of high temperature molten molten KNO_3-$NaNO_3$ and molten KNO_3-$NaNO_2$ $NaNO_3$ cut off part of the Infra-red spectrum beyond 25μm and ,400nm in the UV was not used due to lack of data on the absorption coefficient at high temperature at the respective wavelengths [57]; the same method has been followed here. The attenuation coefficient is considered to remain the same at all Air Mass values as the current application is considered from a fixed focal point application. From Fig 6.21, it can be seen that the spectral power density shifts towards the longer wavelengths with increasing Air Mass. As the visible component of the radiation decreasing higher Air Mass (AM), the amount of radiation transmitted and absorbed at the lower surface will be decreased. Thus, its is expected that the thermal plumes, mixing and convective heat transfer should decrease with increasing Air Mass, this leading in a decrease in the destablising effect from the

lower plate heating. On the other hand, it is expected that the stabilisation would be promoted with increasing Air Mass.

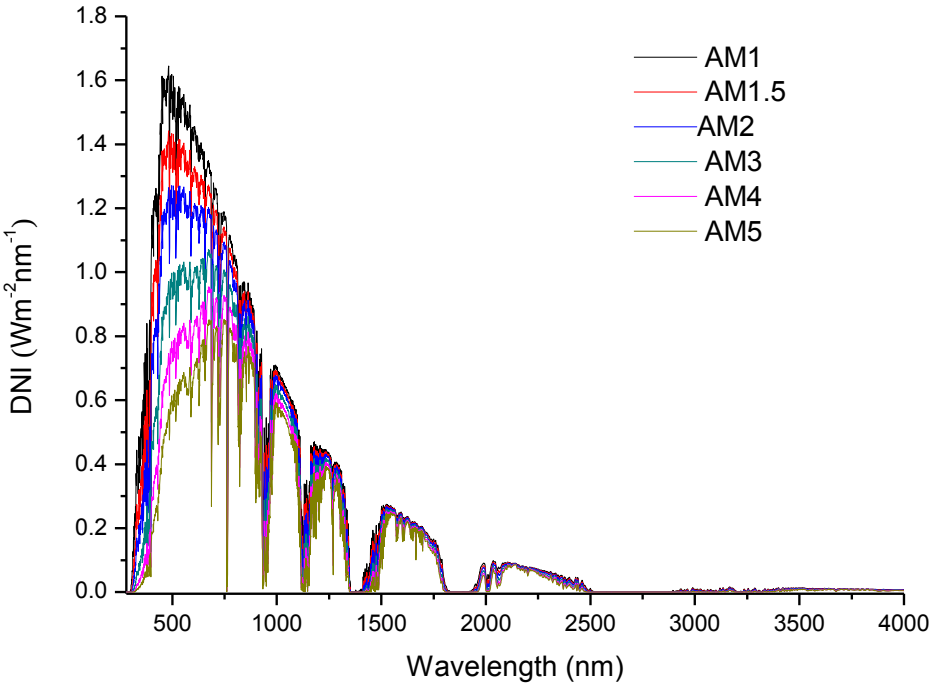

FIGURE 6.18: ASTM G173-03 Reference Spectra Derived from SMARTS v. 2.9.2 t Air Mass (AM1-5)

Fig 6.22 and Fig 6.23 shows time averages for the temperature contours and the streamlines for AM1(Fig 6.22a), AM1.5 (Fig 6.22b), AM2 (Fig 6.22c), AM3 (Fig 6.23a), AM4 (Fig 6.23b), AM5 (Fig 6.23c), in the transitional regimes. Modest variations in the thermal and flow field can be seen by comparisons between the various plots. Temperature contours show an increasing surface layer temperatures as AirMass increases for AM1 to AM5, by 1%, 21%, 31% 41% and 5% respectively (Fig 6.22 and Fig 6.23. The increase in surface layer temperatures are attributed to the fact that as the Air Mass increase to higher values, the visible component of the incident radiation decreases , while the IR radiation increases. This results in reduction in the amount of heating, while directly impacts the subsequent mixing and convective heat transfer from the lower absorber plate. Since longer wavelength are absorbed within mainly the fluid depth to which is opaque, it results in the higher temperatures in this layer. Similarly, from the streamlines, the increasing Air Mass (AM1 to AM5) shows considerable differences in the circulations cell observed in the lower mixing layer, however plots for the velocity, volumetric flow

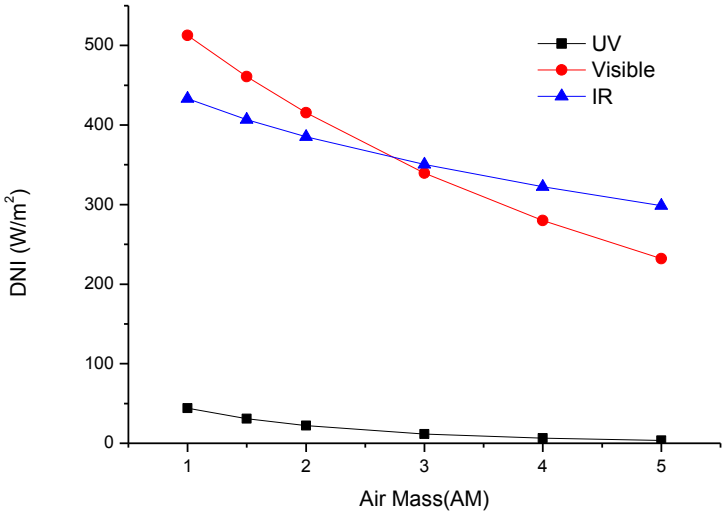

FIGURE 6.19: Variation of UV, Vis and Ir components of solar radiation with increasing Air Mass

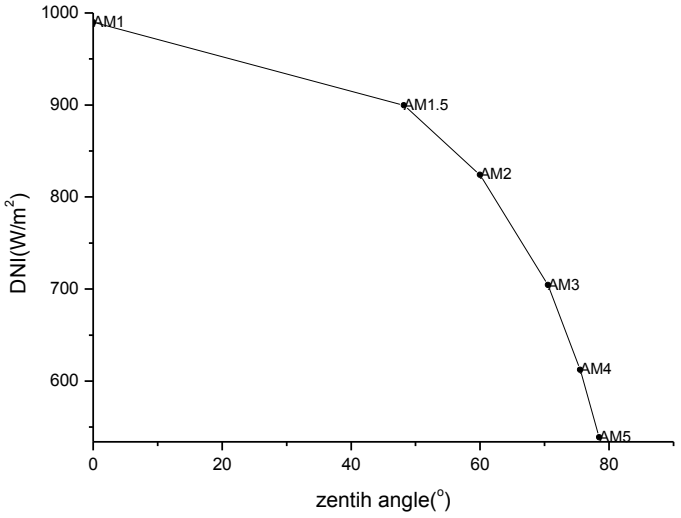

FIGURE 6.20: Direct intensity versus zenith angle and Air Mass.

rate and heat transfer from the lower will give clear revelation of the effects of varying Air Mass (AM).

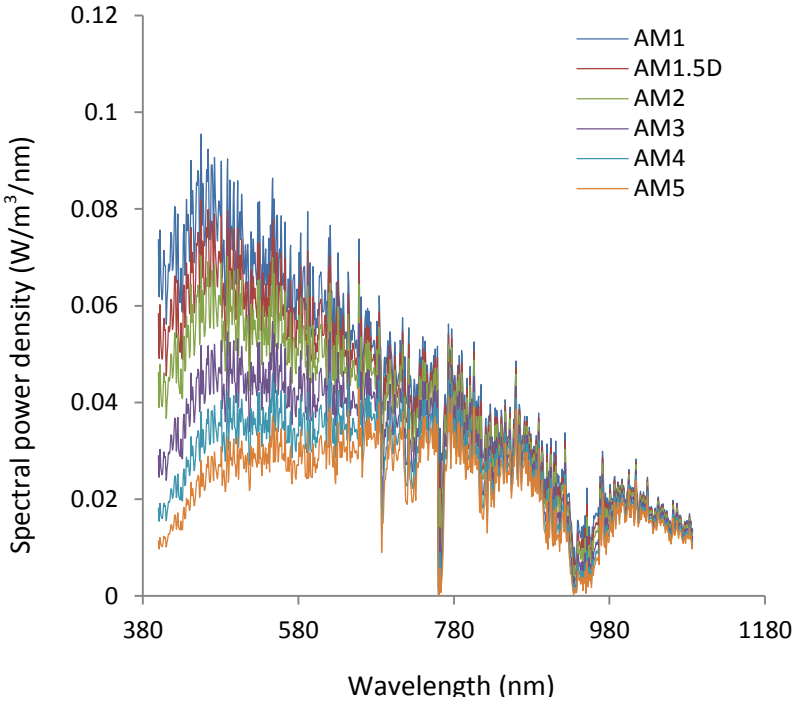

FIGURE 6.21: Spectral power density at Air Mass AM1 , AM1.5, AM2, AM3, AM4 , AM5

Fig 6.24 presents a plot of the stratification parameter, defined as the ratio of the time averaged temperature difference in the mixing depth and the difference of the time average temperature difference in the surface layer. The stratification parameter, as previously defined by Abib and Jularia [135], can be considered as the dimensionless temperature at the interface. It can be seen that the stratification parameter monotonically increases with increasing Air Mass which gives a clear indication of increment in the stratification obtained with increasing Air Mass increases from AM1 to AM5.

Fig 6.25 shows the variation of the average velocity with AirMass. It is clearly seen that as the Air Mass increases to higher values, the average volumetric flow rate/velocity monotonically decrease. From this plots it can be seen that as the component of the visible radiation decreases, the heating of the lower plate decreases. As such the occurrence of thermal plumes which initiate and drive the fluid velocities decreases. The volumetric flow rate decreases by approximately 40% as the Air Mass increases from AM1 to AM5.

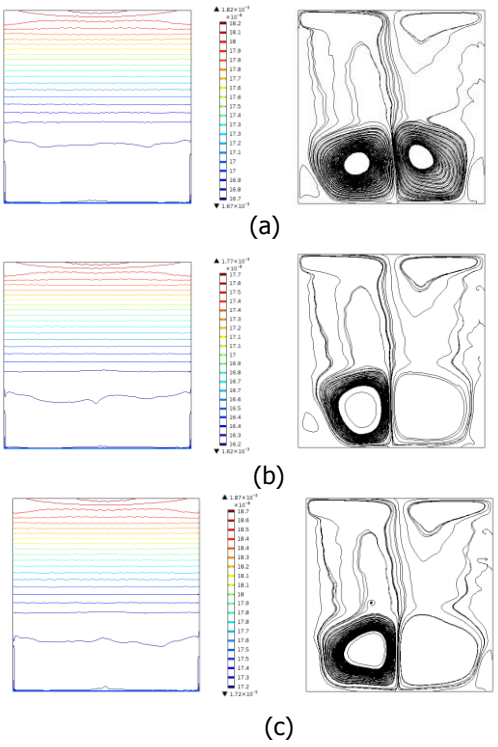

FIGURE 6.22: Time average of isotherms (left) and streamlines (right) for different Air Mass (a) AM1 , (b) AM1.5 and (c) AM2

Fig 6.26 shows the plot of the dependence of the critical time for the onset of instability at the lower surface against Air Mass. As expected, the critical time for onset of instability increases monotonically with Air Mass (AM). This is due to the increased heating time required for the temperature gradients to satisfy the instability criterion. For example the time for onset of instability to occur increases by 29% from AM1 to AM5

Fig 6.27 shows the effect of variable Air Mass on the MIX number. From the plot it can be seen that the MIX number decreases with heating time with Air Mass. For all Air Mass (AM1, 1.5, 2, 3, 4, 5), the MIX number decreases by approximately 40% from τ=2.71$\times$ 10^{-4} to τ=3.4$\times$ 10^{-3}. At τ=3.4$\times$ 10^{-3} the MIX number indicates that stratification increases approximately by 1%, 1.6%, 3.2%, 4.6% and 6% for AM1, 1.5, 2, 3,4, 5 respectively. The decrease in the MIX number is owing to the reduction in the visible radiation component, which promotes stratification.

The variation in the maximum local heat transfer with increasing Air Mass is presented in Fig 6.28. As expected, the figure shows a decrease in the convective heat transfer with increasing Air Mass. Approximately, a 23% drop in the heat transfer occurs for AM5

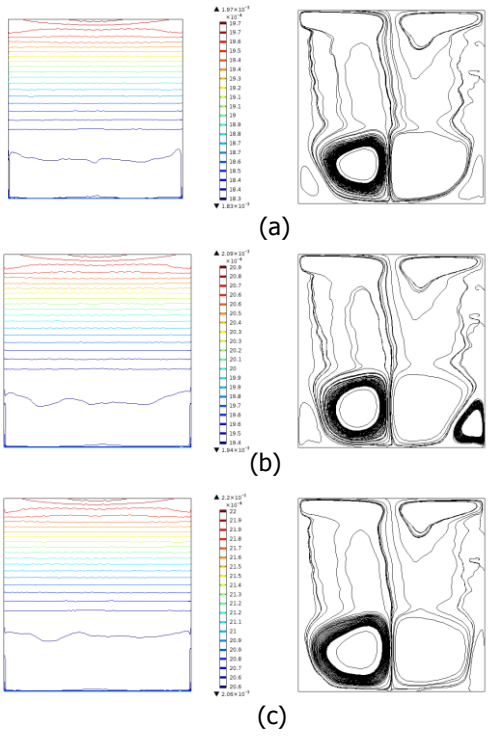

FIGURE 6.23: Time average of isotherms (left) and streamlines (right) for different Air Mass (a)AM3, (b) AM4 ,and (c) AM5

in comparison with AM1. This results coincides with the earlier finding of decreasing mixing and velocities with increasing Air Mass owing to the reduction in the visible radiation, component.

Table 6.1, presents the non dimensionless exergy (ξ) and the capture efficiency (η) at the various Air Mass studied. It can be seen that the highest exergy is obtained at the lowest AirMass , while the highest capture efficiency is obtained at the highest AirMass (AM5).The high dimensionless exergy value seen at the low AirMass(AM1) is attributed to the higher mixing and flow velocities encountered. Thus the entropy generated at the lower AirMass is higher, increasing the entropy generation and lowering the capture efficiency in accordance to the second law. The capture efficiency is seen to increase with increasing AirMass with stratification being promoted at high AirMass due to the increase in the IR radiation component. From this result, the effect of variable spectra on the thermal and flow behaviour in a volumetrically heated enclosure can be established. Thus as expected, the non dimensional exergy deceased with increasing AirMass, while the efficiency increases with increasing AirMass. Thus all these suggest that with the

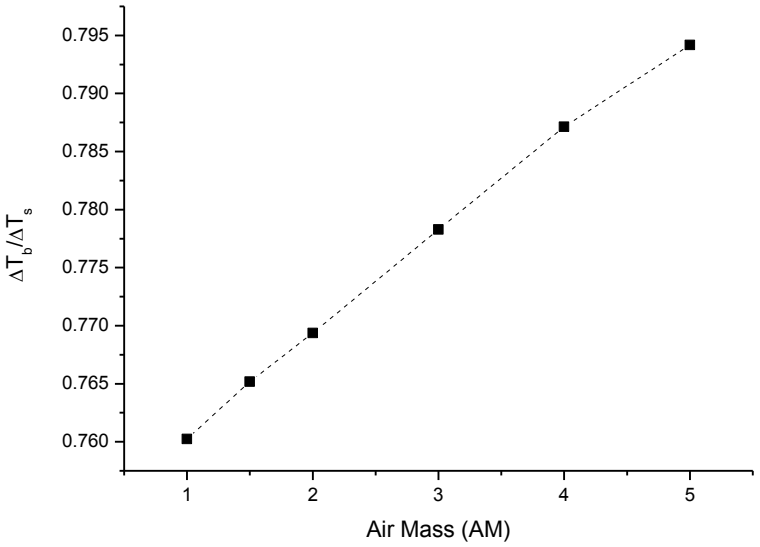

FIGURE 6.24: Stratification parameter vs Air Mass

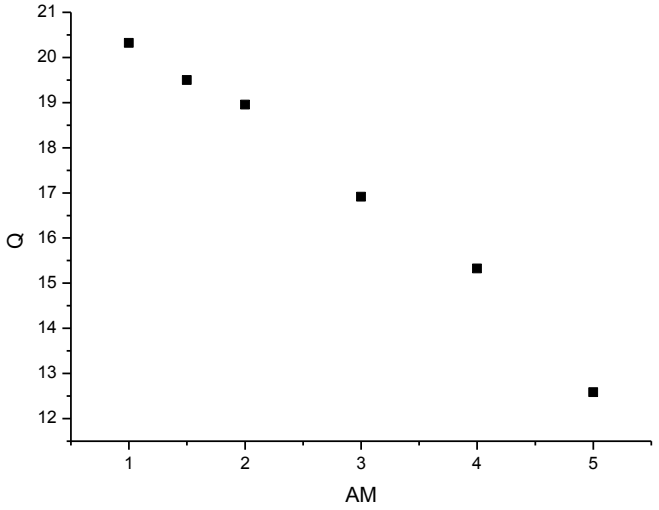

FIGURE 6.25: Maximum Volumetric flow rate at Air Mass AM1, AM1.5, AM2, AM3, AM4, AM5

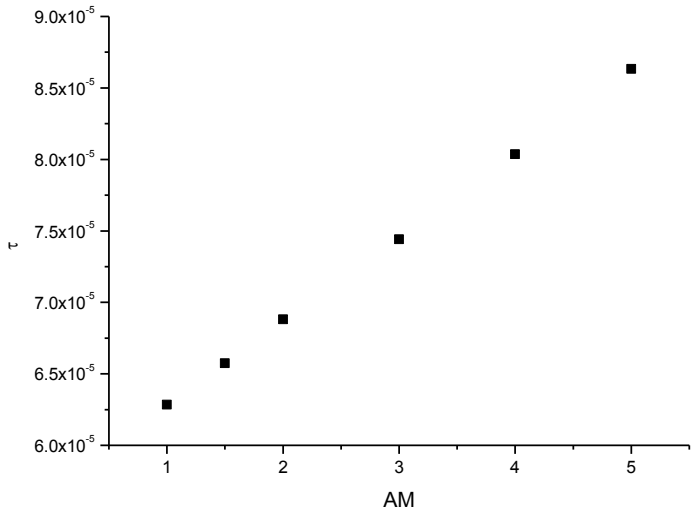

FIGURE 6.26: Effect of the increasing Air Mass on The critical time for the onset of instability

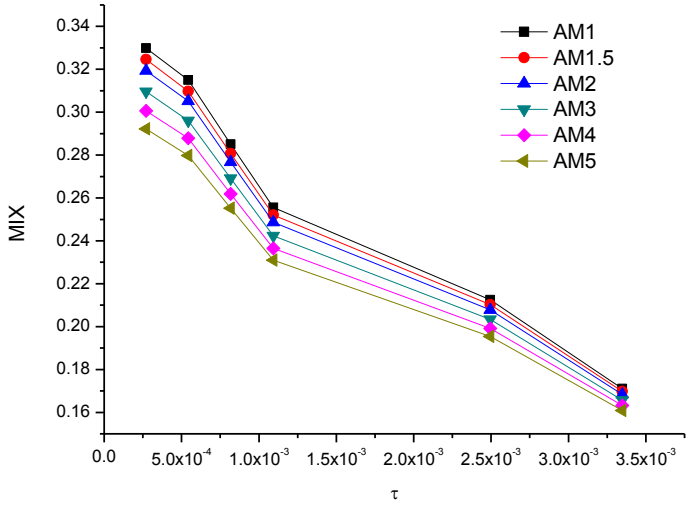

FIGURE 6.27: Mix numbers for transient heating in fluid domain of unit aspect ratio.

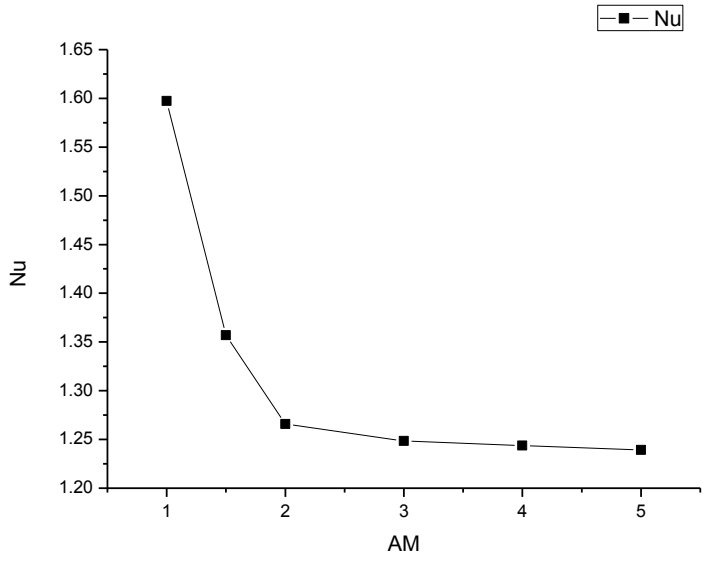

FIGURE 6.28: Plot showing the heat transfer variation with Air Mass.

current numerical tool, it is possible to propose and evaluate a direct absorption thermal energy storage system for different regions as represented by various spectra.

TABLE 6.1: MIX numbers and capture efficiencies at different instants for Air Mass of 1,1.5,2,3,4 and 5.

quantity	1	1.5	2	3	4	5
ϵ	0.402	0.393	0.384	0.375	0.371	0.366
η	0.476	0.481	0.487	0.4935	0.497	0.501

6.6 Comparison solar weighted average model and spectral dependent model

In this section, a comparison between numerical results obtained for the single average weighted model and those obtained from the spectral dependent model developed in the present study. Comparison is based on a DNI of 700W/m^2 over the wavelengths covered in this chapter. This is equivalent to 15.5kW/m^2 incident power. Table 6.2 presents calculated values of output quantities: average temperature, maximum velocity, dimensionless heat transfer coefficient, critical onset time Mix number and non dimensional

exergy number for the solar weighted average value model and the spectral model. The comparisons in the output variables showed significant differences. From the table is can be seen that all output quantities presented were between $\sim$ 10 and 20 % higher in the solar weighted absorption compared with the spectral model output variables. The results obtained here are in agreement with works of authors Cengel and Ozişik [65] and Webb and Viskanta [68] regarding application of single weighted attenuation coefficients.

TABLE 6.2: Comparison of computed numerical results for solar weighted model and a spectral model.

Output quantities	Solar weighted model	spectral model	% diff
Max Temp (K)	0.01856	0.001444288	11.68
Max Vel(m/s)	0.08029	0.077	24.76
Average heat transfer coefficient(Nu)	70.65	60.49273	17.75
critical time(t_b)	0.8	0.7	12.5
MIX	0.385	0.32	15.8
Frequency	0.3696	0.3389	8.31

6.7 Three dimensional simulations

Three dimensional simulations of natural convection in high temperature molten salt driven by the direct absorption of concentrated solar radiation based on spectral attenuation coefficients and spectral irradiation data defined at the solar spectrum for Air Mass 1.5D is presented. The cylindrical geometry which has a height to diameter ratio (H/D=1) consists of a rigid wall and lower absorber plate which confines the high temperature KNO_3-$NaNO_3$ molten salts similar to the two dimensional simulations. The top of the enclosure is open and considered to be adiabatic. At the onset of heating, 15.5kW/m^2 concentrated solar flux based on a standard reference (SMARTS scheme) is incident at the top surface and deposited in the molten salt volume. As flows occurring in the physical system are three-dimensional. The natural convection flows in enclosed cavities in the previous section is assumed a two dimensional behaviour. Thus this section considers three dimensional simulations to compare with the two dimensional simulations and evaluate the heat transfer and flow three dimensionality dependencies. The three dimensional mass, momentum and energy equations have been solved to obtained temperature and velocity fields. Normalisation is carried out using scaling presented previously in section 6.2. The nonlinear partial differential equations were solved using Computational Fluid Dynamics (CFD)Finite Element Method package COMSOL, with Backward Differential Formula (BDF) with implicit time stepping scheme(COMSOL). Initial and boundary conditions remain the same as described previously. Discretisation

is done based on P_2+P_1 schemes for the velocity and the pressure. Owing to high computational and time cost a mesh refinement was not conducted. However, a COMSOL predefined mesh 5mm tetrahedral mesh made up of having 234322 elements is selected which conforms to validation mesh element size.

Fig 6.29-Fig 6.32 shows the 3 dimensional surface temperature and velocity for dimensionless times τ=3.79×10^{-5},7.59×10^{-5},1.57×10^{-3} and 9.47×10^{-3} owing to spectral volumetric heating. In Fig 6.29a at τ=3.79×10^{-5}, the top fluid is heated radially along the top surface and down the side walls. At the lower surface, the boundary layer heating is apparent. Fig 6.29b, fluid velocities are observed long beam profile and at along the top side wall. No significant fluid velocity is found in the lower layer. In Fig 6.30a (τ=7.59×10^{-5}), the top heating can be seen to extend towards the lower surface, while at the same time the bottom heating is seen to extend upwards. Fig 6.30b, it can be seen that the increased lower fluid heating generates fluid velocities in that region. At a later heating time, τ=1.57×10^{-3} (Fig 6.31a and b), top heating and lower surface heating phenomena interact, resulting in more uniform fluid temperatures within the domain. This is owing to the mixing taking place which is confirmed by the velocity profile as shown in Fig 6.31b. Fig 6.32(τ=9.47×10^{-3}), shows a stable nonlinear temperature profile as obtained in the two dimensional stimulations. The corresponding velocity profile at this time shows no fluid flows as the flow velocities become drastically reduced.

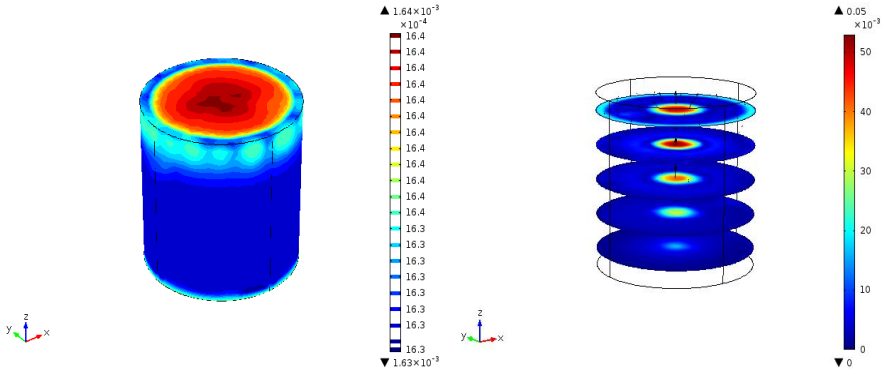

FIGURE 6.29: Three dimensional temperature and velocity fields at τ=3.79×10^{-5} .

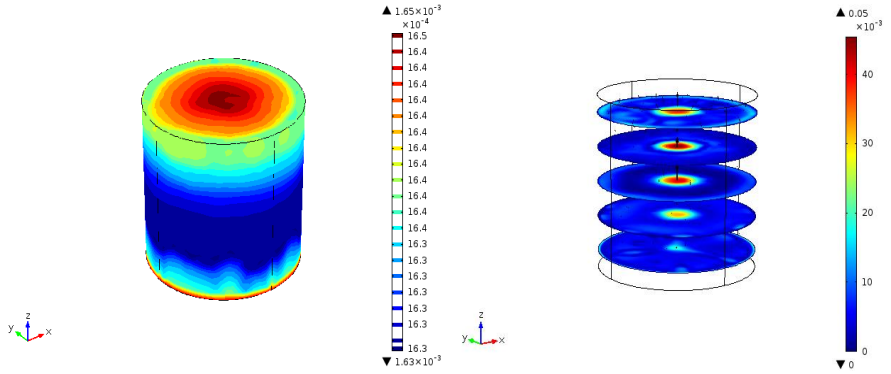

FIGURE 6.30: Three dimensional temperature and velocity fields at 7.59×10^{-5}.

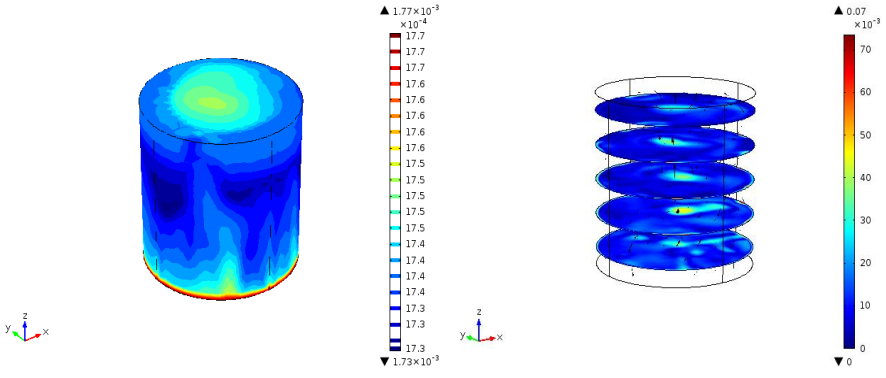

FIGURE 6.31: Three dimensional temperature and velocity fields at 1.57×10^{-3}

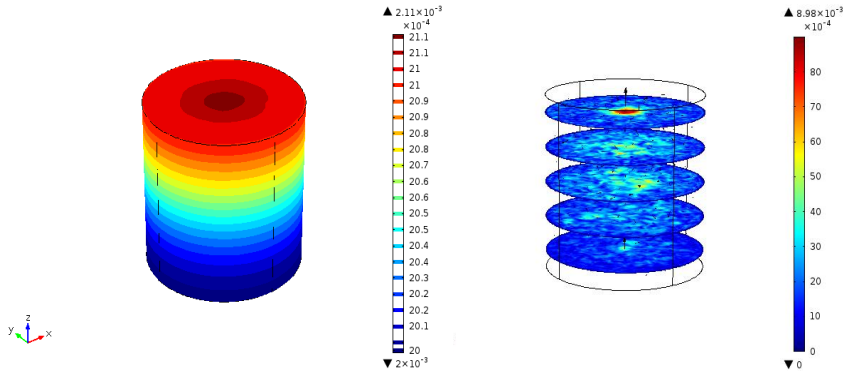

FIGURE 6.32: Three dimensional temperature and velocity fields at 9.47×10^{-3}

In the two dimensional simulations no bulk fluid movements occurred within the stable surface layer, other than the tangential fluid velocities along the radial direction and side walls. Similar features have been exhibited by the three dimensional surface layer. Based on the two dimensional simulation of section 6.2, three flow stages were identified: early, transitional and quasi steady stages. Fig 6.33-Fig 6.38 present three dimensional thermal and flow features in the early, transitional (early, middle and late) and quasi steady stages corresponding to the two dimensional simulations (section 6.2).

Initial stage τ <3.79×10^{-5}

Fig 6.33 shows the temperature isocontours and streamline and velocity vector at τ=2.27×10^{-5}, a time during the early flow. Fig 6.33a, shows radial heating along the opm surface, while at the lower surface the thermal boundary layer is clearly shown.

Streamlines indicate no bulk flow at the within the domain and at lower surface, except at the top surface where flow initiated along the top surface is observed. A similar phenomena was observed in the two dimensional simulation. Heat transfer at this stage is primarily by conduction which is confirmed by the low fluid velocities observed. Generally, the heat transfer mechanism and flow structures seen at this stage are consistent with observations in two dimensional simulations. However, the time of occurrence and

the attained temperatures differ from those obtained from the two dimensional simulations.

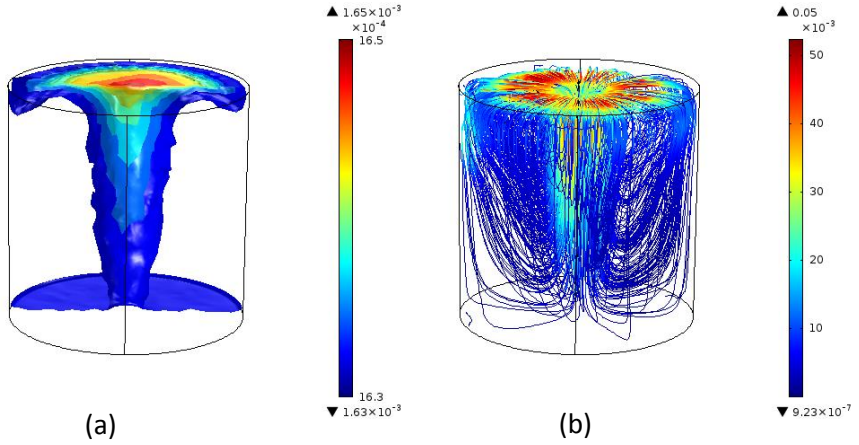

FIGURE 6.33: Temperature iso-surface(a) and corresponding streamlines(b) at τ=2.27×10^{-5}, showing the early flow stage .

Transitional stage (3.79×10^{-5} < τ <6.73×10^{-3})

Fig 6.34 shows the isocontours and streamlines for a later heating time(τ=6.07×10^{-5}, where thermal plumes are observed to grow out on the boundary layer. This has been previously shown to marks the onset of thermal instability and also shows the stability conditions criteria for instability has been satisfied [80, 118]. Fig 6.31b show the formation of eddies at the the end walls at the lower surface. Modifications in the streamlines can be observed in the fluid column which indicate the introduction of flow in the lower boundary. In the two dimensional simulations, the transitional regime was divided into early, middle and late transitional stages, distinguished by their magnitude of amplitudes and frequencies.

Fig 6.35-Fig 6.37 shows the temperature isocontours and streamlines for τ=1.17×10^{-3}, τ=4.10×10^{-3} and τ=6.73×10^{-3}, illustrating heat and flow structures in the early, middle and late transitional stage. The fluctuations correspond to the occurrence of plumes development. Streamlines reveal a complex unsteady flow in Fig 6.32b and Fig 6.33b. As the transitional flow attains the late transitional stage, flow becomes confined to the lower layer as the surface layer becomes established.

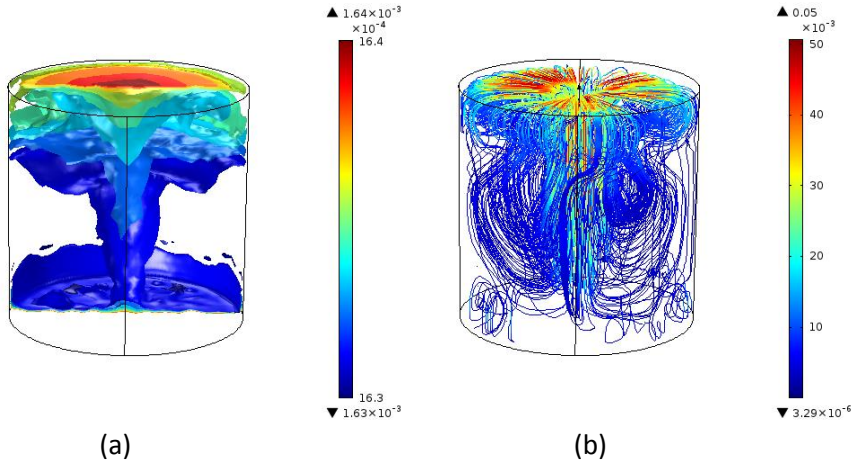

FIGURE 6.34: Temperature iso-surface(a) and corresponding streamlines(b) at τ=6.07×10^{-5}, showing the onset of thermal instability .

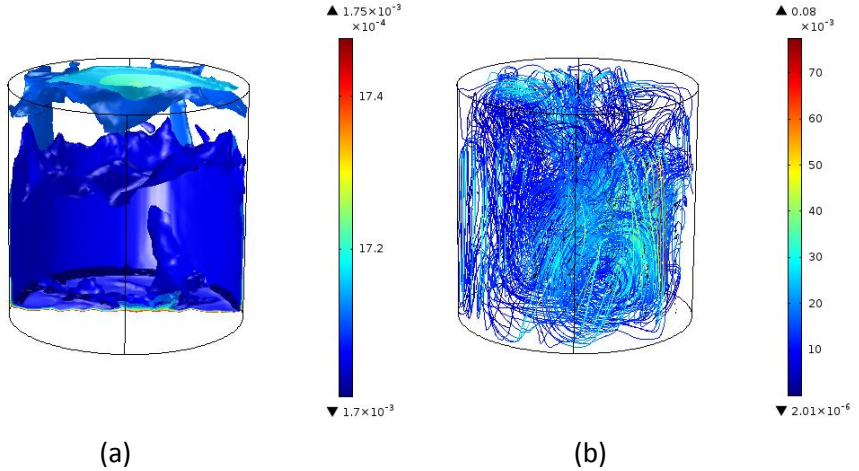

FIGURE 6.35: Temperature iso-surface(a) and corresponding streamlines(b) at τ=1.17×10^{-3}, showing the early transition stage.

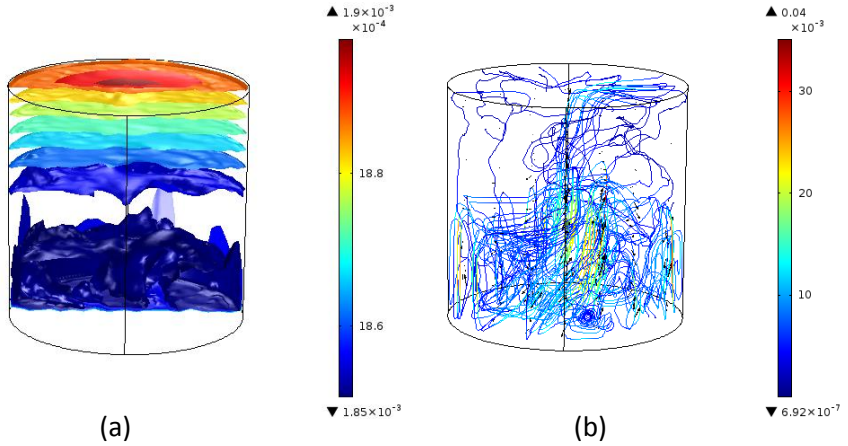

FIGURE 6.36: Temperature iso-surface(a) and corresponding streamlines(b) at τ=4.10×10^{-3}, showing the onset of middle transition stage.

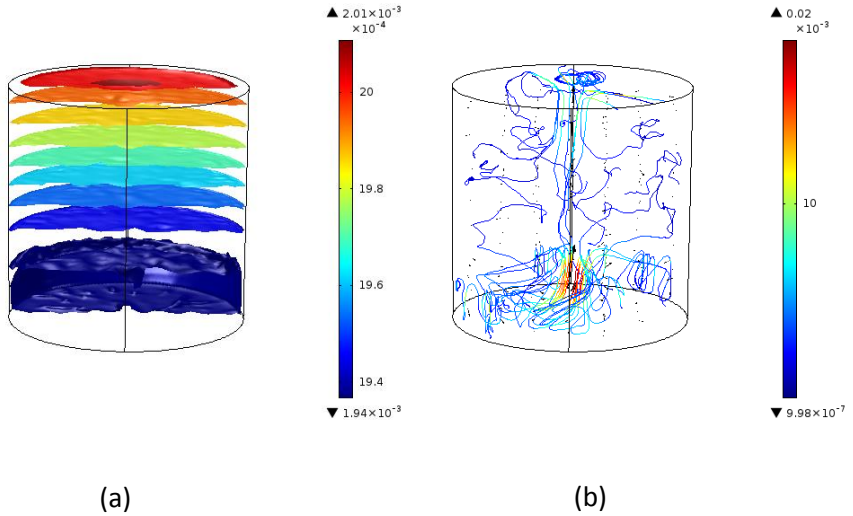

FIGURE 6.37: Temperature iso-surface(a) and corresponding streamlines(b) at τ=6.73×10^{-3}, showing the late transition stage .

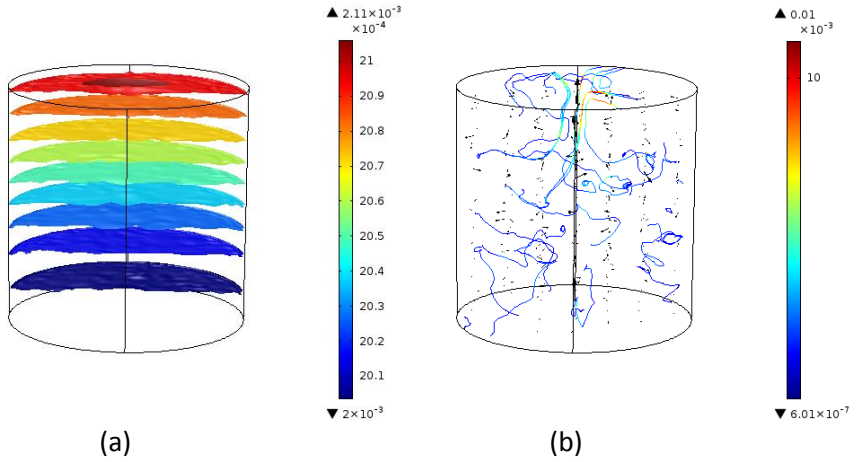

FIGURE 6.38: Temperature iso-surface(a) and corresponding streamlines(b) at τ=6.73×10^{-3}, showing the late transition stage.

Quasi steady state $\tau > 6.73\times10^{-3}$;

As the flow in the lower fluid column approaches the quasi steady state (Fig 6.38), flow velocity decreases in to oscillations of regular and constant amplitudes. It can be seen here that the as the surface layer and mixing layer become fully established, thermal plume become smaller and reduced. The continued heating sees the surface layer advancing towards the lower surface resulting in the mixing layer being pushed back. At this stage the stabilising forces overcome the destabilising forces. Fig 6.35 a, b and c show the time series of the u, v and w components of the velocity. at the point (0,0,-0.98H). The x and y velocity components are significant. The y component can rise up to 0.02, which cannot be accounted for with the two dimensional model as presented earlier.

In this chapter, a two dimensional spectral dependent radiation induced natural convection in a molten salt (binary KNO_3-$NaNO_3$) filled enclosure which accommodates an absorber plate at the lower surface was numerically simulated. The wavelength dependent absorption of radiation has been based on a standard reference parametrised spectral irradiation data (SMARTS model) and spectral attenuation coefficients described over the range of wavelengths relevant to solar energy. The resulting temperature profile is characterised by a nonlinear temperature profile where a stratified hot top fluid layer

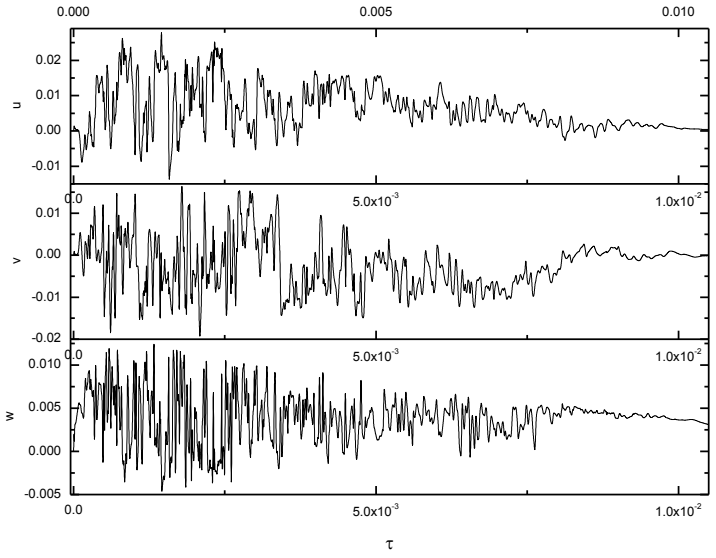

FIGURE 6.39: Time series of the velocity components (a) x velocity component (b) y velocity component and (c) z velocity component.

lay above a cooler fluid layer. As observed in the previous weighted model described in chapter 5, there is no bulk fluid flow observed the top fluid layer. Maragoni convection was however observed in the region just below the heated top fluid surface. In the lower convention layer, flow regimes are characterised by an initial stage where heat is primarily transferred by conduction (2) a transitional stage where natural convection is the prevalent heat transfer mechanism and (3) a quasi-steady regime. The vertical fluid velocity in the lower fluid layer was found to have a fundamental frequency of 0.48Hz. Parametric investigation of the effects of the variable Air Mass showed significant effects on the heat transfer, flow velocity and structures, quantity of mixing, stratification, critical time for onset of convection and the thermal performance. A direct comparison between a solar weighed model and the discretised spectral model shows approximately 10 to 25% higher values in the measured output quantities in the weighted model compared with the spectral model.

The three dimensional simulation carried out. Comparisons of the three and two dimensional results reveals a significant influence of dimensionality on the heat transfer and flow. Despite the two dimensional and three dimensional simulation appearing to have identical driving mechanism and flow features, the isothermal and velocity contours reveal different structures. The driving mechanisms and flow structures can be seen to

have three dimensionality dependence and were found to have a higher maximum heat transfer rate and flow velocities when compared to equivalent two dimensional domains. The two dimensional simulations were able to capture the major features of the heat and flow features, including the basic features of the flow instabilities, they are suitable for extracting flow details with confidence. The two dimensional simulation are only suitable for extracting general flow details and were not adequate for full resolution of the details in the real flow as it failed to capture the three dimensionality of the flow.

Chapter 7

Thermoconvection in an inclined enclosure by the absorption of non uniform solar radiation

In this chapter, the effect of inclination angles on the unsteady radiation induced natural convection in an inclined 2 dimensional volumetrically heated square enclosure filled with molten KNO_3-$NaNO_3$ salt directly absorbing concentrated solar radiation is presented. The inclined enclosure is subjected to a solar radiative heating from a top surface whose optical axis and central axis is inclined to the gravity vector, but remains perpendicular to the top surface. Heating of the enclosure is studied for the particular case in which the molten salt is heated by two heat contributions: internal heat is generated by direct absorption of the incident solar radiation and secondly a lower boundary heated surface from the absorption of transmitted radiation to this surface; the relative influence of each mechanism is dependent on the amount of radiation penetrating the entire depth. The local depth dependent absorption of penetrative solar radiation is based on the spectral distribution of the incident radiation and attenuation coefficient.

Heat transfer and fluid flows in inclined enclosures which attract attention, owing to their significance in industry and nature (heat exchangers, solar collectors and nuclear reactors)[79]. In applications, such as crank thermosyphon type heat exchangers inclination was found to enhance performance [136]. A differentially heated cavity with idealised isothermal or isoflux boundary conditions have formed fundamental studies to understand the heat transfer and fluid flow interactions within an enclosure. For various contexts and several boundary conditions experimental and numerical studies conducted in simple, regular and inclined two dimensional (rectangular and square) geometries have investigated the effect of angles on: stability of fluid layers, several flow

types, instabilities in heat transfer and their corresponding interactions by a suitable choice of the values of the external parameters [136–141]. The class of problems dealing with the unsteady heat transfer and flow structures owing to absorption of radiation in fluid layer have been found in literature for various geometries. Amongst these include; triangular enclosures, rectangular enclosures and parallelepipeds. Boundary conditions found in these problems are transient and complex and their temperature profiles are nonlinear [91]. However, compared to a large body of literature available for the classical Rayleigh-Bernard convection, the study of nonlinear temperature stratification is limited in spite of the many important applications. In particular, literature on heat transfer (natural convection) and fluid flow in inclined enclosures, in which the primary driving phenomenon is the volumetric absorption of radiation is found to be lacking. Further, at the time of writing this thesis, to the best of the author's knowledge, none of the existing literature for radiation on the driving mechanisms and flow features, in enclosures subject to concentrated solar radiative heating have incorporated the effect of angles on stability of fluid layers, and nonlinear temperature stratification and fluid flow structures. However as radiation induced buoyancy flows are complex, due to the essential coupling between the radiation with flow and transport, it is expected that the thermal and flow features will be quite different from those found in an inclined differentially heated cavity.

Thus the present study concerns the investigation of the effects of inclination angles on thermal and flow structures in an inclined enclosure, representative of a thermal store, where the primary driving force in the volumetric absorption of solar radiation. The depth dependent volumetric absorption of the concentrated solar radiation is accounted for based on spectral distribution of solar radiation and the attenuation coefficients over wavelengths relevant to solar energy applications. The study also investigates the effects of inclination angles on thermal and flow structures under variable spectra; results are presented in the form of isotherms and streamlines. The study is aimed at giving new insights and greater understanding to the flow and heat transfer behaviour in an inclined enclosure under the present heating phenomena and configuration which finds relevance in a proposed solar thermal energy storage application. The study also seeks to develop results against which further works can be benchmarked and validated against. The outline of this chapter is as follows: section 7.1 presents the numerical formulation and governing equations; section 7.2 presents the results and discussion; section 7.3 presents the effect of inclination angle on stratification and mixing and Section 7.4 presents effects of inclination angle on thermo convection under variable Air Mass.

7.1 Mathematical formulation and governing equations

A two dimensional inclined enclosure with H/D=1, shown in Fig 7.1 has been considered in this chapter. The domain vertical boundaries inclined at an angle denoted by ϕ to the gravity vector are rigid and adiabatic, while the top wall is an open stress free boundary. The lower boundary is rigid plate of finite thickness (dx), and of known absorption characteristics, i.e black surface. The bottom surface is considered to be a transient temperature heated surface. High temperature molten KNO_3-$NaNO_3$ salt, initially at a temperature T_0 and at rest is enclosed within the domain walls. At the dimensionless time t=0, a non-uniform concentrated radiation flux is initiated and thereafter maintained over fixed area on the top surface (Fig 7.1). The radiation is directly deposited into the fluid which is considered to heat up the enclosed molten salt volumetrically by contributions: the directly absorbed radiation within the fluid body and lower surface absorber plate heated from the absorption of transmitted/residual flux incident at its surface The spectral irradiation is described based on the Air Mass (AM) 1.5D (SMARTS model [69]). The temperature and flow fields within the enclosure (Fig 7.1) are obtained by solving the two dimensional incompressible Navier-Stokes, continuity and energy equations shown in equations (7.1)- (7.4) [142].

$$\nabla \cdot \overrightarrow{V} = 0 \tag{7.1}$$

$$\rho \frac{\partial(\overrightarrow{V})}{\partial t} + \rho(\overrightarrow{V} \cdot \nabla) \cdot \overrightarrow{V} = -\nabla p + \nabla.\mu(\nabla V) + g_x \beta \sin\theta \Delta T \tag{7.2}$$

$$\rho \frac{\partial(\overrightarrow{V})}{\partial t} + \rho(\overrightarrow{V} \cdot \nabla) \cdot \overrightarrow{V} = -\nabla p + \nabla.\mu(\nabla V) + g_z \beta \cos\theta \Delta T \tag{7.3}$$

$$\rho Cp\left(\frac{\partial T}{\partial t} + \nabla.VT\right) = \nabla.(k.\nabla T) + S \tag{7.4}$$

where S is the source term (volumetric heating) obtained from the RTE and g_x and g_y=0, but the driving force term in the y direction is due to buoyancy. ϕ is the inclination angle measured in the anti-clockwise direction with respect to the vertical.

The applied boundary condition include: Side walls are all rigid, non-slip and adiabatic, with velocity components and normal temperature gradients being zero, (u=v=w=dT/dn=0). The fluid depth is bounded by a stress free (du/dy=v=dw/dy=0) and adiabatic top at y=0 (dT/dy=0). The lower boundary is rigid wall with no slip (u=v=w=0) and of

finite thickness and thermal conductivity, where the transmitted flux to this surface is absorbed and heats the lower fluid . The boundary condition for the temperature on the lower boundary is given by T=T_0+ΔT, where ΔT is as given in equation (6.7). The flux Rayleigh number (equation 7.5) is defined by Dou et al.[143].

$$Ra = \frac{\rho^2 C_p g \beta q (L \sin\theta)^4}{\mu k^2} \tag{7.5}$$

For a free-rigid configuration with constant temperatures on the horizontal boundaries and a linear temperature profile across the depth of the fluid layer, Ra =1106.5 [143]. According to Dou et al.[143], the critical Rayleigh number for the onset of Rayleigh Bernard instability in the inclined bottom boundary layer can be approximated by equation (7.6).

$$Ra_c = Ra_c(0^o)/\cos\theta \tag{7.6}$$

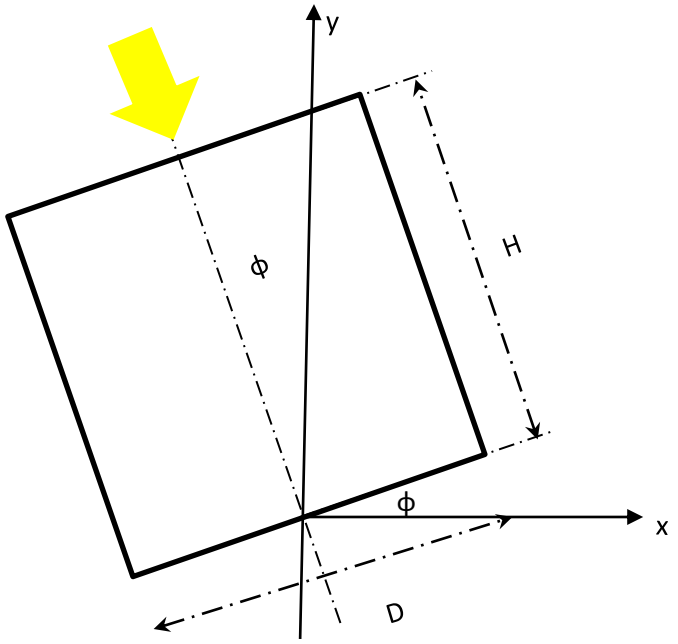

FIGURE 7.1: Geometry of the problem H/D=1.

7.1.1 Numerical implementation

The derived, time dependent system of nonlinear partial differential equations (PDEs) obtained from the numerical formulation above are solved using COMSOL Multiphysics

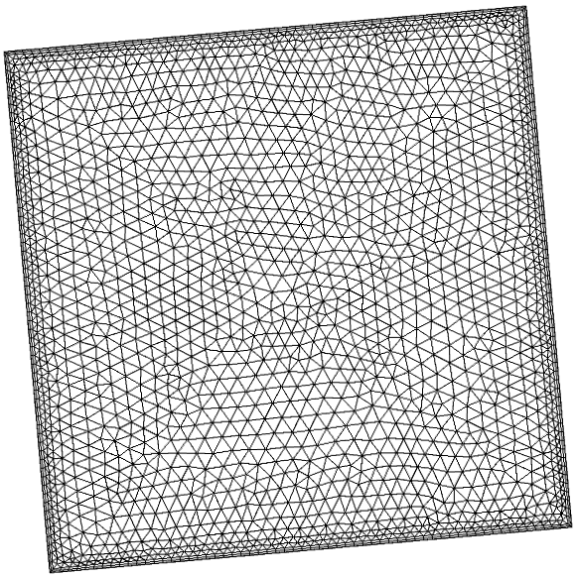

FIGURE 7.2: Computational mesh.

software [120], a commercially available Finite Element Method (FEM) package. The two dimensional domain is discretised into a unstructured mesh composed of triangular cells shown in Fig **??** . Second-order elements for the velocity field and linear elements for the pressure field, (P_2+P_1) discretisation is used [120].

To define the size of a mesh to ensure the independence of computational results and gives a good compromise between accuracy and CPU cost, mesh refinement tests were performed. The mesh convergence test plot for two-dimensional simulations with aspect ratio, H/D=1, inclination angle ϕ=5^o a salt volume of 2 m^3, spectral attenuation coefficient given in Appendix A and spectral solar radiation at Air Mass 1.5D. It can be seen from Fig 7.3 that as the mesh was refined from a coarse mesh to a fine mesh, seen by the increasing value of the refinement ratio (N), the difference in the solutions at the respective mesh element sizes converged at N=5. The mesh element size of 30mm was the selected giving 6084 domain elements and was considered sufficient for the accurate simulation. A mesh of 30mm gives an error in the average temperature of 0.31% compared solution at the finest mesh element size considered. The convergence criteria for the residuals of continuity equation, velocity components and energy equation were 10^{-5}. The solutions were obtained once the convergence criteria were satisfied. We also carried out some numerical simulations to check the validation of the numerical scheme.

The comparison of the natural convection in a triangular enclosure subject to solar radiation representative of a reservoir side arm studied by Lei and Patterson [83, 84] is used. Numerical results obtained from COMSOL are compared with the results of Lei and Patterson [83, 84] for the same for different Rayleigh numbers. From Fig 4.26,a very good agreement exist between the two results. Although the current geometry and conditions differ considerably from the radiatively heated triangular cavity, agreement with the Lei and Patterson [83, 84] problem lends some confidence in the ability of the code to model the strongly coupled flows. Full description of the validation study is presented in section 4.5.

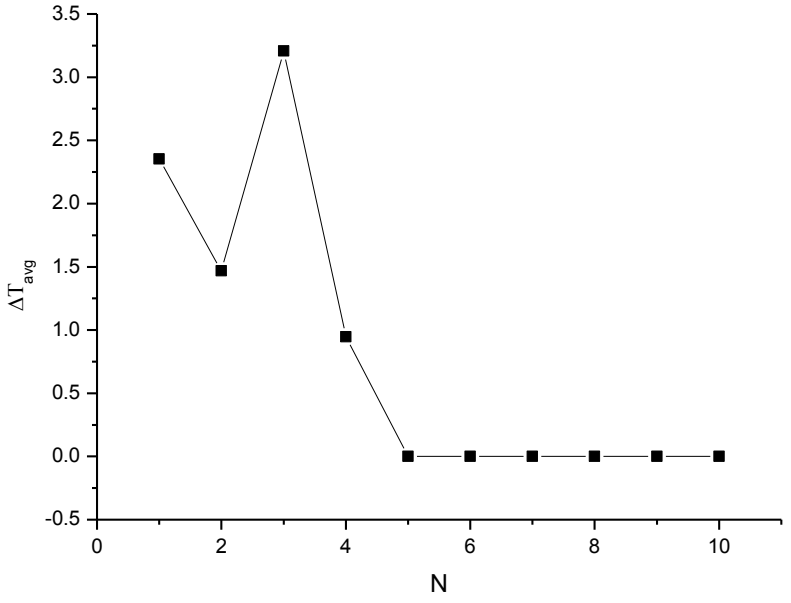

FIGURE 7.3: Geometry of the problem H/D=1.

7.2 Results and discussion

Fig 7.4 and Fig 7.5 presents the two dimensional temperature and velocity fields for spectral volumetric heating in a 2D square enclosure at angles of inclination, ϕ =0^o, 5^o, 15^o, 30^o, 45^o and 60^o at time, t= 1400s for Air Mass 1.5D. The selected time illustrates the effect on the heat transfer and flow structures at a time during the transitional stage when rising plumes, mixing and convective heat is most significant. Temperature and velocity fields are shown in Fig 7.4a which contains the temperature (Fig 7.4(i)) and velocity (Fig 7.4 (ii)) contours for an enclosure directly irradiated from the top

at inclination angle ϕ=0^o (t=1400s); this is the enclosure configuration presented in chapter 6. For brevity, nonlinear temperature profiles the heat transfer and flow regimes are briefly discussed here. The nonlinear temperature profile is characterised by a hot stable stratification surface layer on top of a cooler convective mixing layer consisting of a boundary layer and thermal plumes. The fairly parallel isotherms observed in the top layer indicate a predominantly conductive heat transfer in the stable surface layer, while velocity contours show a unsteady flow with a complex and irregular structure, owing to the irregular occurrence of the rising plumes. An important consequence of such a nonlinear temperature stratification is the limitation of the mixing driven by rising thermal plumes with the penetration length scale of the plumes determining the lower mixed layer thickness. Thus thermal plumes and boundary layers formed along the lower right and left vertical walls are confined within the lower fluid layer. Fig 7.4a shows the temperature (Fig 7.4b (i))and velocity (Fig 7.4b(ii)) surface plots of the domain for an inclination angle ϕ=5^o. Fig 7.4b(i) shows that the stratification layer formed in the top right region is much stronger that the stratification attained in the top left region to the straight line a-a splits the cavity into a left region and a right region, hence more heat flux will be accumulated in the top right region. Height of thermal plumes seen in the lower right region of the enclosure is greater than those on the lower left corner. In Fig 7.4b(ii), an irregular flow phenomena observed in the surface plots indicate that the flow of the fluid is stable. The intensity of flow instability in the left region is much stronger than that in the right region. The location of the instabilities accord well with the location of high velocities. In contrast to the case at 0^o, velocity contours show an increased enclosure circulation with increased vertical boundary layers and thermal plumes than those seen at 0^o. Thus the central core fluid is now being heated by convection. The thermal plumes are seen to be larger and have higher velocity than as observed at 0^o. Velocity contours illustrate a fully developed unsteady flow with a complex and irregular structure. At ϕ=15^o (Fig 7.4 c(i)), thermal plume intensity is reduced in the lower fluid region and the temperature profile in the top column shows a more uniform distribution and is at a higher temperature than in Fig 7.4a(i). In Fig 7.4c (ii), the generated flow is confined to a much smaller domain depth and the intensity of flow is lower compared with the case at ϕ=5^o. Similar to Fig 7.4c (ii), the intensity of flow in the left region is much stronger than that in the right region.

As the inclination angles increases ϕ=30^o (Fig 7.5a), 45^o (Fig 7.5b) and 60^o (Fig 7.4c), it is easy to observe that (1) stratification increases (2) surface layer temperature increases (3) thermal plumes are diminished (4) the intensity of flow instability in the lower region decreases (5) tangential surface flow velocities increase and (6) the velocities induced at the top left are much higher than that in the right region below the top surface. Inclination angles have a profound influence on the temperature and flow transitions

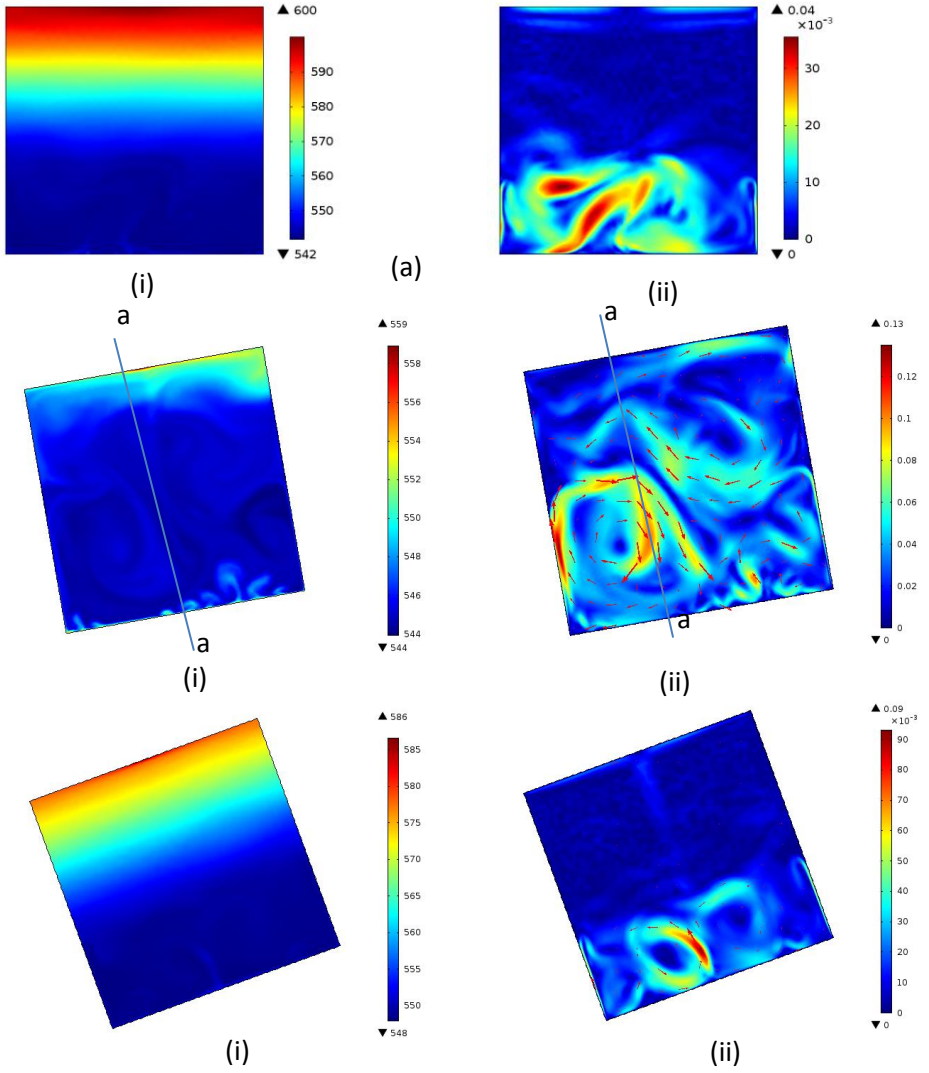

FIGURE 7.4: Surface plots of temperature(left) and velocity (right at inclination angles (a) ϕ= 0^o (b)ϕ= 5^o and (c) ϕ= 15^o.

housed by the enclosure, as seen by the increasing stratification and reducing mixing and thermal plumes with increasing inclination angle from 5^o to 60^o. Results observed in the present study are different from those obtained from results of Beacamonte et al. [144] that made an experimental and numerical study on the effect of tilt angles on thermal efficiency and stratification in a solar water heater. Their results showed that the angle of inclination has a significant effect on the temperatures and thermal stratification in an enclosure. When the angle of the inclined plate increased, greater temperatures and thermal stratification were achieved. A stratification index ((ST=C_1e-C_2 β/EN)) which has an exponential dependence of the tilt angle was proposed [144, 145].

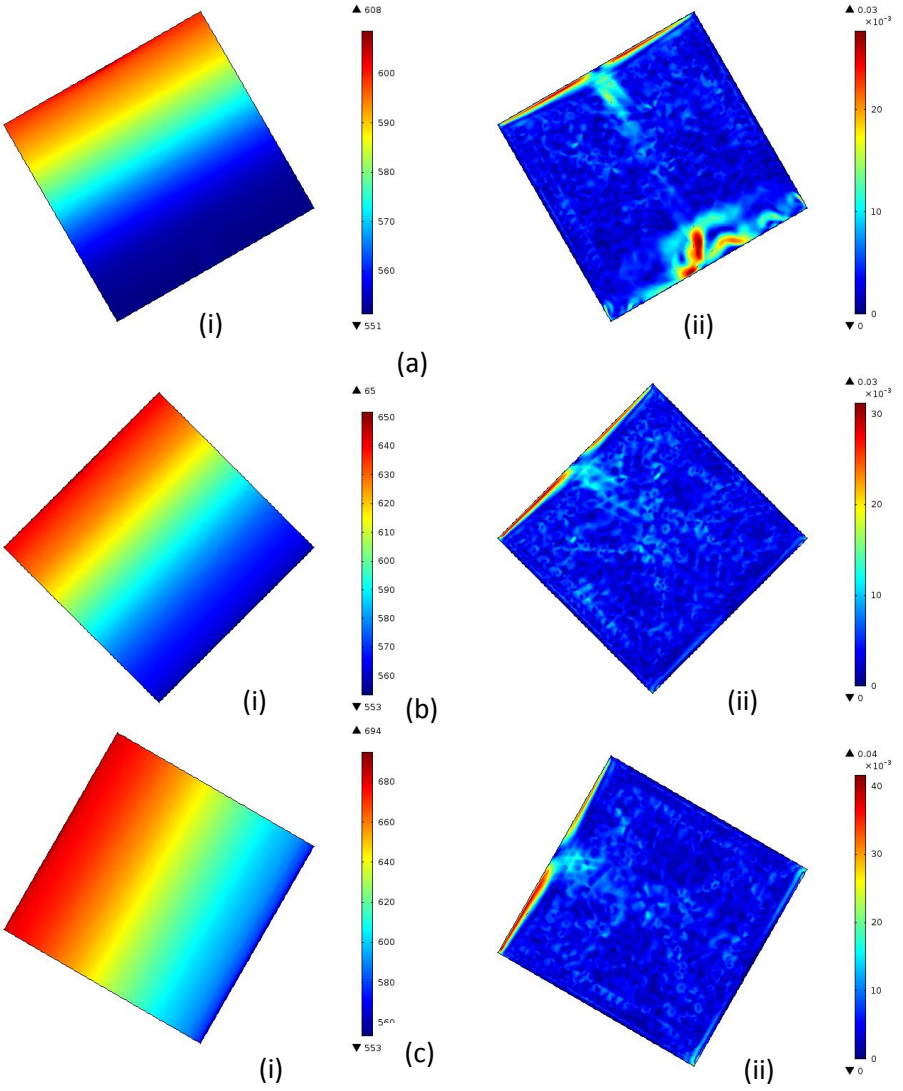

FIGURE 7.5: Surface plots of temperature (left) and velocity (right) at inclination angles (a) ϕ= 30^o (b) ϕ= 45^o and (c) ϕ= 60^o.

The time series of the temperature at location x=0.5H, y=0.95H, that is at half the width location and in a region above the lower heating surface is shown in Fig 7.6 for inclination angles, ϕ= 5^o, 15^o, 30^o, 45^o and 60^o. The plots show the initial flow stage to the early transitional regime. The figure reveals that, at the start up the temperature displayed an oscillatory behaviour shortly after the initiation for all inclination angles. Inclination angle ϕ= 5^o has the duration with the longest fluctuations, while the shortest fluctuation time is obtained at ϕ= 60^o. This effect is in agreement with observations from the temperature and velocity contours found in Fig 7.4 and Fig 7.5. From Fig 7.6 it can be clearly seen that surface temperature increases with increasing inclination, attaining a maximum at ϕ= 60^o and a minimum at ϕ=5^o. As a result of the higher level of mixing and convective heat transfer associated with the inclination angle ϕ=5^o, almost homogenised temperatures are obtained. One of the significant effects of inclination angles on the thermal and flow structures is the delay in the initiation time of the start of the onset of convective instability which is seen to increase with increasing inclination angle.

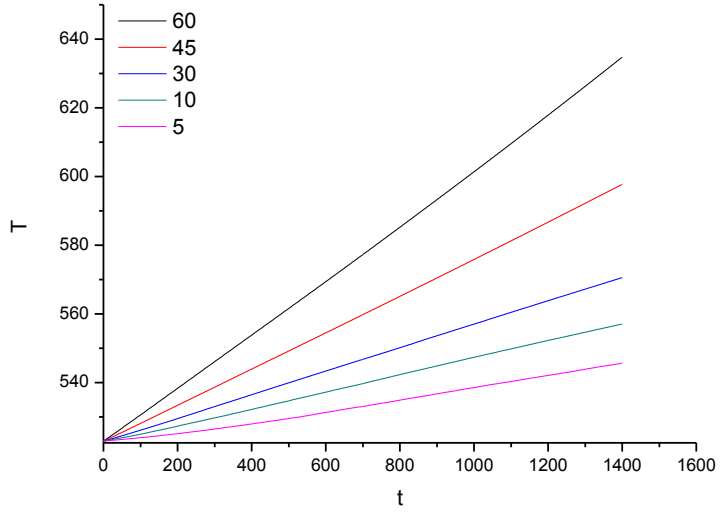

FIGURE 7.6: Surface temperature and velocity plots for ϕ= 0^o 5^o 15^o 30^o 45^o 60^o.

Fig 7.7 shows the time histories for the maximum velocity at an identical point as in Fig 7.6 for inclinations angles 0< ϕ < 60^o. This plot exhibits identical trends as those seen in the the temperature plot presented in Fig 7.6. For all inclinations the initial flow rises sharply to a maximum velocity and then drops to a velocity characterised by irregular flow fluctuations. The sharp spike corresponds to the introduction of thermal

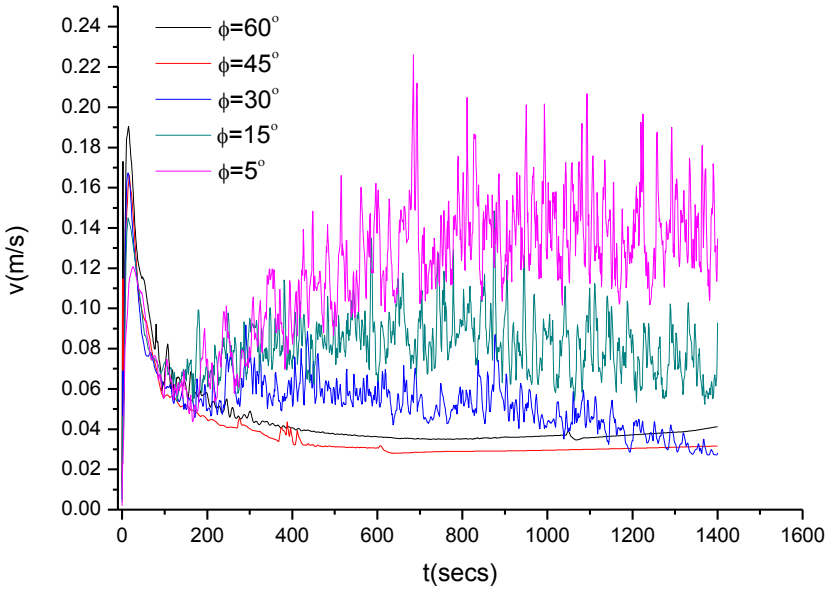

FIGURE 7.7: Time series of velocity with inclination angle (ϕ).

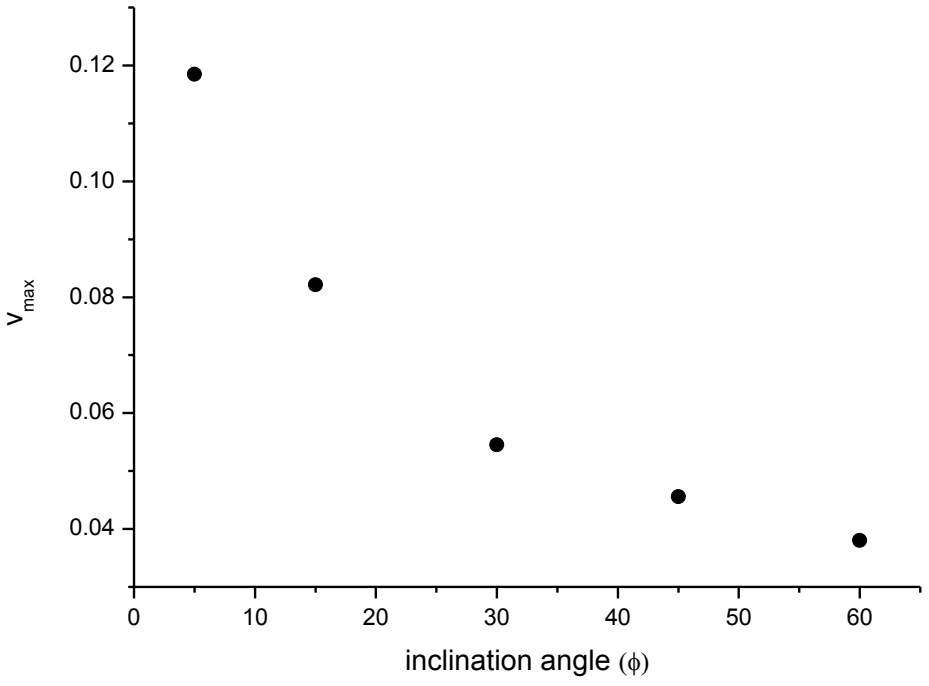

FIGURE 7.8: Maximum velocity variation with inclination angle (ϕ).

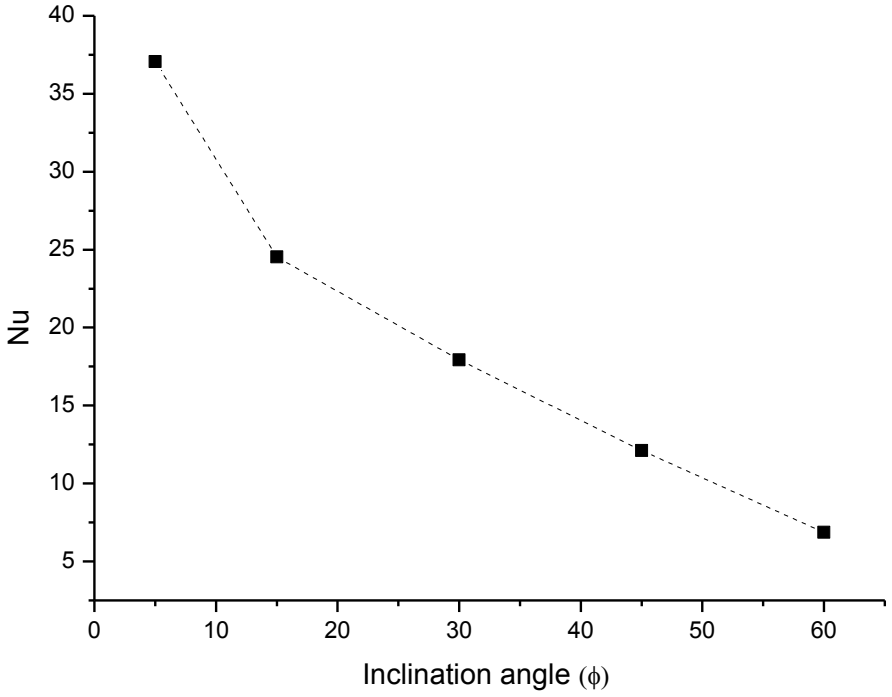

FIGURE 7.9: Heat transfer coefficient (Nu) variation with inclination angle ϕ.

instabilities, while the irregular flow velocity fluctuations which corresponds to the occurrence of rising plumes encountered in the the transitional regimes. It can clearly be seen that, as the inclination angle increases from 5^o to 60^o. A maximum velocity of 0.03m/s is attained at 5^o, while a minimum is found to occur at ϕ =60^o. At $\phi = 45^o$ and 60^o plot shows that after 400s the flow regimes changes from the transitional stage to the quasi steady state regime, indicating that stratification is promoted at higher inclination angles. The features observed here i.e. the driving mechanisms for heat transfer and flow regimes over the inclination angle range $0< \phi < 60^o$, are consistent and can easily be matched with the major fluid developments and features identified from the temperature and velocity contours (Fig 7.4 and Fig 7.5). Fig 7.8, shows the variation of the maximum velocity with inclination angle; the maximum velocity is also observed to decrease with increasing inclination angle.

The effect of inclination angles on the dimensionless heat transfer, Nu from the lower surface at the point x=0.5H, y=0.95H, is shown in Fig 7.9. The Nusselt number is seen to decrease monotonically from a maximum value Nu=37.5 at 5^o to Nu=8 at 60^o. Thus as the enclosure is inclined the heat transfer mechanism in the lower column varies from a pure natural convection boundary layer flow in the transitional regime from 5^o to a pure conductive regime at 60^o. This is owing to the fact that as the enclosure is inclined, the buoyancy driving force for the natural convection in the boundary layers will reduce

as given in equations (7.1) and (7.3), where the buoyancy term varies with $\cos(\phi)$. Thus the overall reduction in Nu observed from Fig 7.9 is associated with the $\cos(\phi)$ reduction in the driving force for the natural convection in boundary layer flows.

7.3 Inclination angle and mixing

Fig 7.10 shows the effect of the inclination on the MIX number for inclination angles 5^o, 15^o, 30^o, 45^o and 60^o. At all inclination angles presented, the MIX number shows a monotonic decrease with increased heating times, due to the stabilising force dominating the destabilising force and stratification being promoted at higher heating times. The figure also shows a decrease in the MIX number as inclination angles go from 0^o to 60^o, with the highest level of mixing obtained at 5^o and the lowest level of mixing seen at ϕ=60^o. This clearly indicates that vertical stratification is promoted with higher inclination angles up to 60^o. This phenomenon is clearly exhibited from the temperature and velocity contours shown in Fig 7.4 and Fig 7.5 respectively. An increase in inclination angle $\phi > 30^o$ results in a significant reduction in the existence of thermal plumes, which are the important mechanisms in mixing [91]. The thermal plumes occurrence and the level of mixing variation with increasing inclination angles is consistent with features observed in Fig 7.4 and Fig 7.5 and clearly indicate the dependency of the respective parameters on the gravity vector which varies with inclination angles.

7.4 Effect of inclination on capture efficiency

Fig 7.11 presents results of the effects of increasing inclination angles on the capture efficiency (see Chapter 2 for definition), used to estimate the fraction of incoming energy retained by a receiver during the heating process [19, 32, 40]. As it can be seen in Fig 7.11, the efficiency rises from a minimum efficiency 0.125 at a 5^o and attains a maximum efficiency of 0.65 at 60^o. The drop at lower in the efficiency at lower inclination angles of 5^o and 15^o is due to the generation of entropy associated with the mixing and convective heat transfer, which lowers thermal efficiency. The increasing capture efficiencies with inclination angles above 5^o is solely due to the promotion of thermal stratification observed at higher inclination angles. The results obtained for higher capture efficiency at higher stratification levels is consistent with theories of Dincer and Rosen [13] where thermal efficiencies can be enhanced with increased thermal stratification.

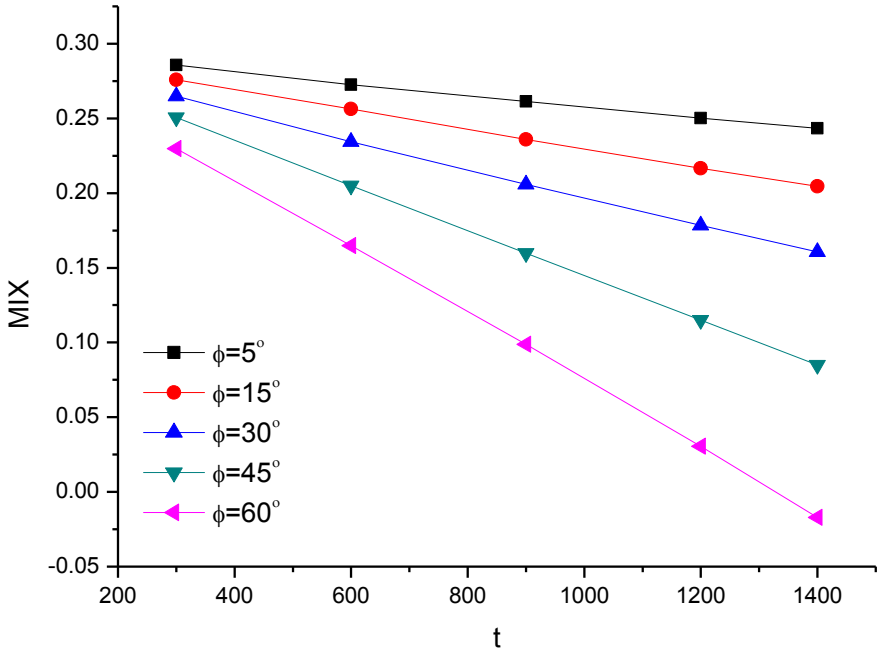

FIGURE 7.10: Transient MIX number at various inclination angle (ϕ).

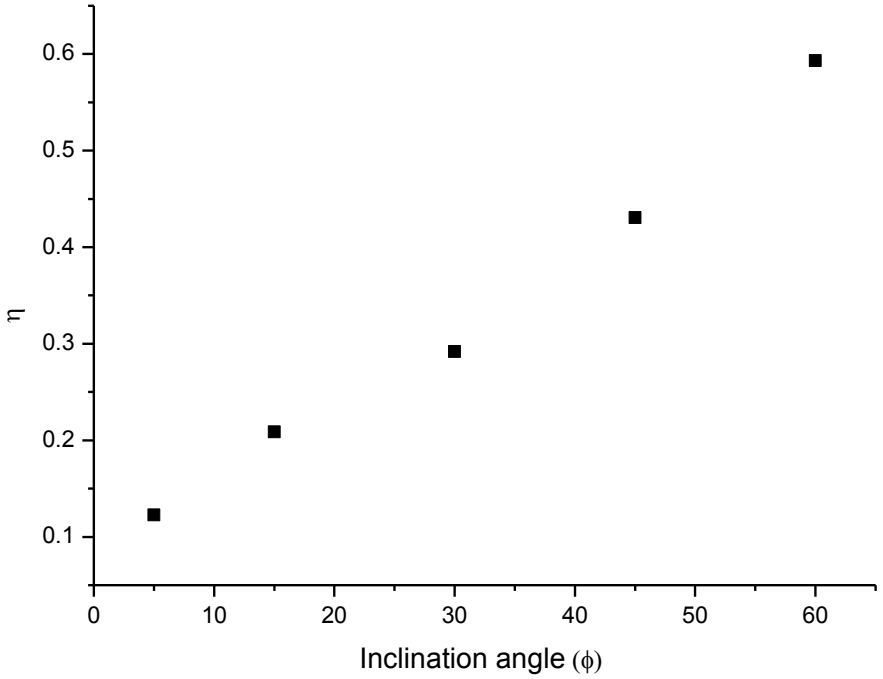

FIGURE 7.11: Effect of inclination angle (ϕ) on capture efficiency.

7.5 Effect of inclination angles on volumetric heating in an enclosure under variable Air Mass.

In this section, time averaged temperature and velocity contours in the range t= 200s to 1000s at inclination angle $0^o < \phi < 60^o$ for solar spectrum; Air Mass 1 (Fig 7.12), 3 (Fig 7.14) and 5 are presented (Fig 7.16). For all Air Mass values, the effect of the gravity vector results in higher surface temperature and promotion of stratification, with increasing inclination angles. On the other hand convective heat transfer and mixing are found to decrease with increasing Air Mass. As the reduction in the overall solar intensity and variation in spectral distribution with increasing Air Mass is expected to have an influence on the heat and flow features in the enclosure. Visual inspection of temperature and velocity vectors AM1.5 (Fig 7.12) AM3 (Fig 7.14) and AM5 (Fig 7.16), shows modest variations in the temperature and flow fields obtained for the respective solar spectra. Direct comparison of these figures reveals decreasing temperatures in the top and lower fluid column with increasing Air Mass. This trend occurs as a result of the decreasing solar intensity at higher Air Mass. In particular, the visible radiation component decreases and the radiation shifting to higher wavelengths results in decreases lower surface temperatures, convective heat transfer and mixing at higher Air Mass. Thus it can be seen that for the shift to higher wavelengths at higher Air Mass, there is a reduction in the frequency in the occurrence of thermal plumes, which in turn results in low mixing as illustrated from temperature contours. As expected, stratification is promoted at higher Air Mass.

Fig 7.18 shows the dependence of the critical time τ_b on inclination angles at different Air Mass. The critical time is defined in equation 5.10 and obtained from the time series of the perturbation temperature at the lower surface. It can be clearly seen that the minimum critical time for the onset of thermal instability is attained at ϕ=0^o, which increases monotonically with inclination angle and attains a maximum at ϕ=60^o. It can also be seen here that the critical time for the onset of instability increases with Air Mass. The former is due to the velocity which is dependent on the gravity component which is in turn a function of the inclination angle.

Table 7.1, 7.2 and 7.3 presents calculated values for the average weighted heat transfer coefficient, the exergy MIX number and capture efficiency for Air Mass 1.5, 3 and 5 and angles of inclination $0< \phi < 60^o$ respectively. From Table 7.1 it can be seen, as expected, that heat transfer increases at ϕ=5^o which then decrease with increasing Air Mass number and attains a minimum value at ϕ=60^o. The MIX number (exergy) follows an identical trend of attaining a maximum and minimum value at ϕ=5^o and ϕ=60^o respectively. The capture efficiency is seen to attain a minimum at ϕ=5^o and

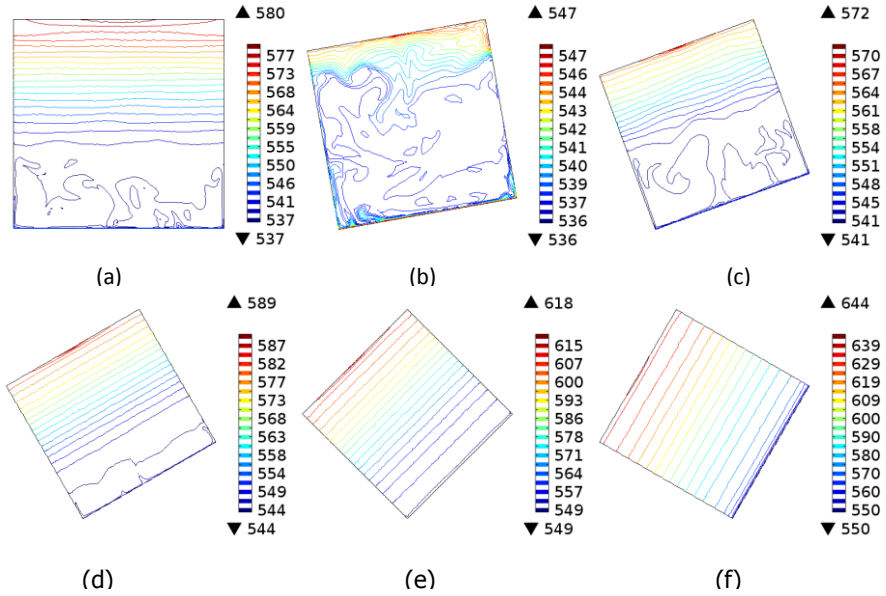

FIGURE 7.12: Temperature contours showing temperature field at AM1.5D for inclination angles (a) ϕ=0^o (b) ϕ=5^o (c) ϕ=15^o (d) ϕ=30^o e) ϕ=45^o f) ϕ=60^o.

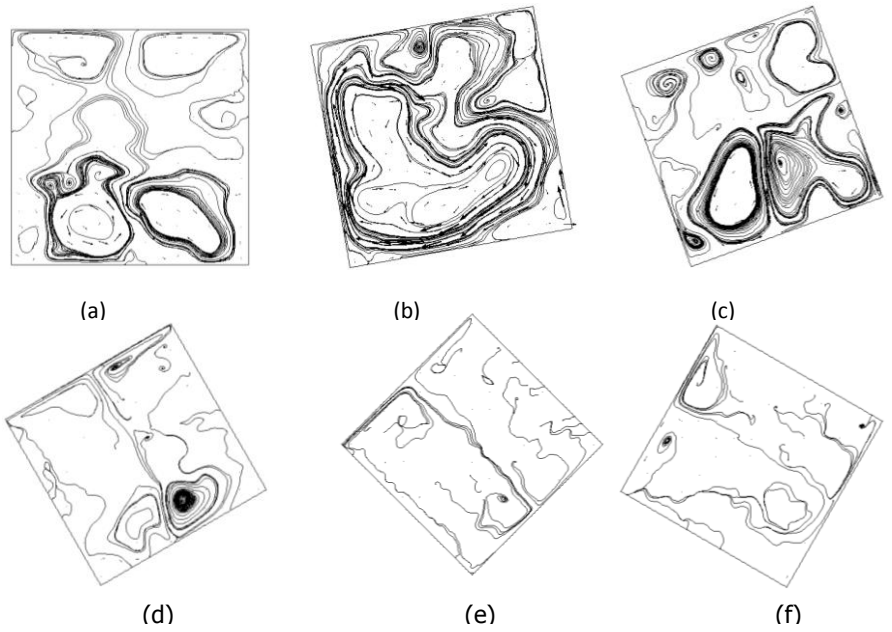

FIGURE 7.13: Streamlines and velocity vectors showing velocity field at AM1.5D for inclination angles (a) ϕ=0^o (b) ϕ=5^o (c) ϕ=15^o (d) ϕ=30^o e) ϕ=45^o f) ϕ=60^o.

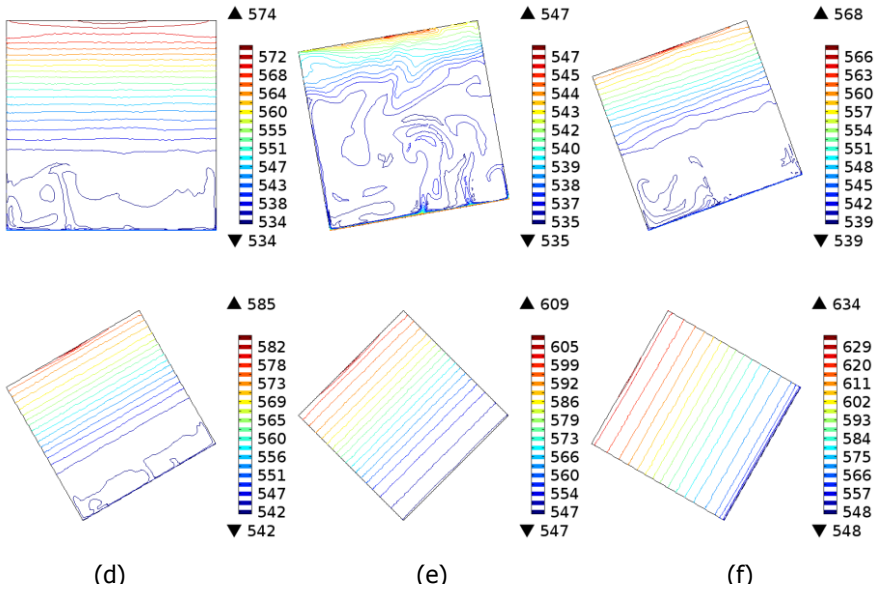

FIGURE 7.14: Temperature contours showing temperature field at AM3 for inclination angles over the range (a) ϕ=0^o (b) ϕ=5^o (c) ϕ=15^o (d) ϕ=30^o e) ϕ=45^o f) ϕ=60^o.

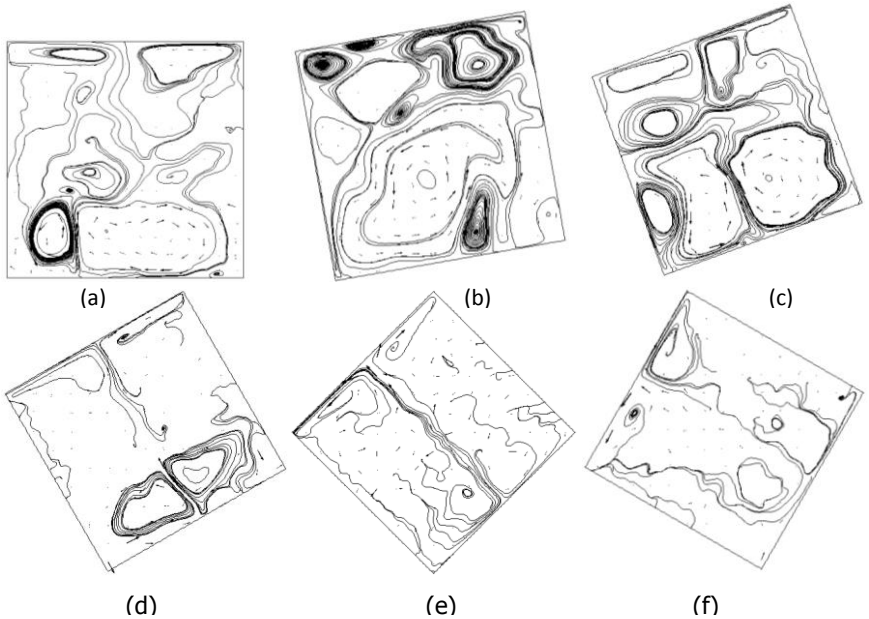

FIGURE 7.15: Streamlines and velocity vectors showing velocity field at AM3 for inclination angles over the range (a) ϕ=0^o (b) ϕ=5^o (c) ϕ=15^o (d) ϕ=30^o e) ϕ=45^o f) ϕ=60^o.

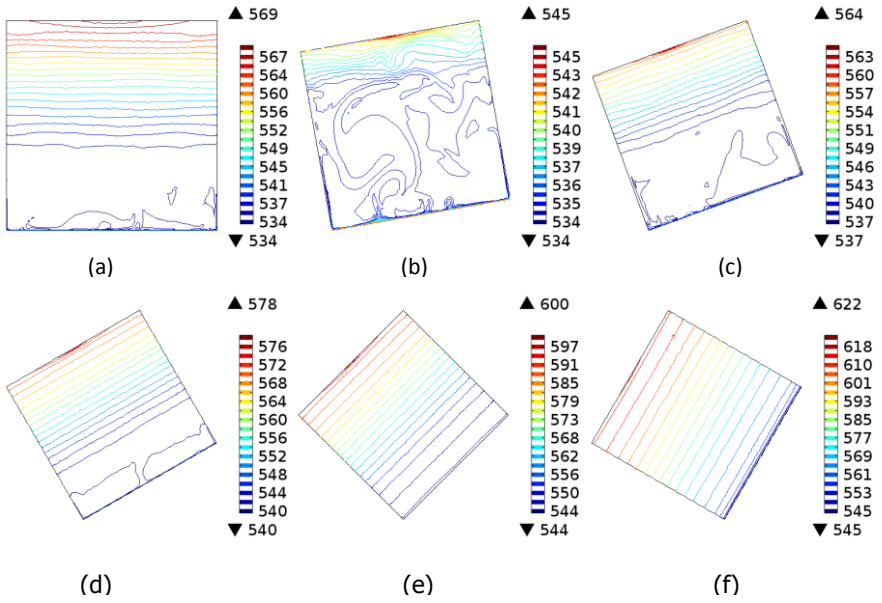

FIGURE 7.16: Temperature contours showing temperature field at AM5 for inclination angles over the range (a) ϕ=0^o (b)ϕ=5^o (c) ϕ=15^o (d) ϕ=30^o e) ϕ=45^o f) ϕ=60^o.

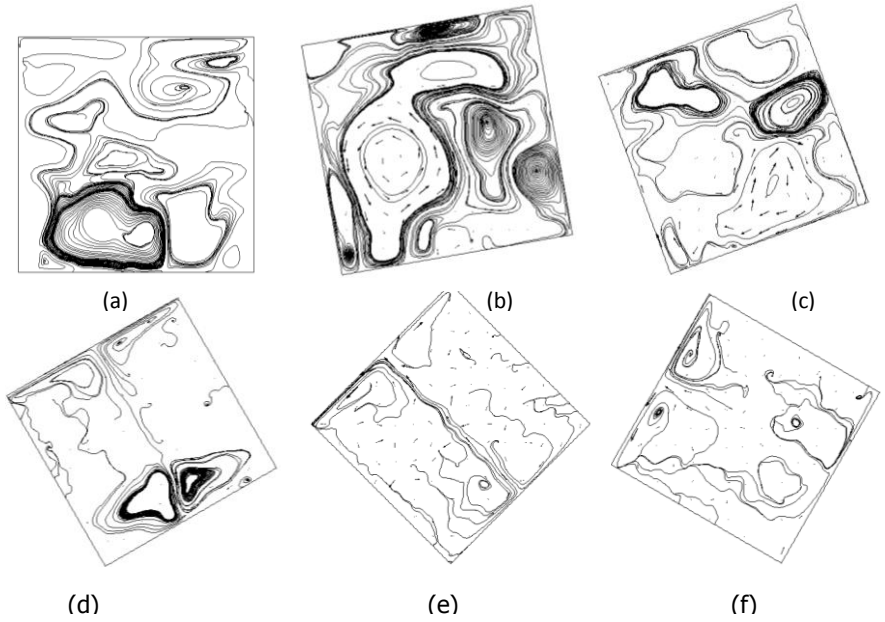

FIGURE 7.17: Temperature and velocity vectors showing temperature and velocity field at AM5 for inclination angles over the range (a) ϕ=0^o (b) ϕ=5^o (c) ϕ=15^o (d) ϕ=30^o e) ϕ=45^o f) ϕ=60^o.

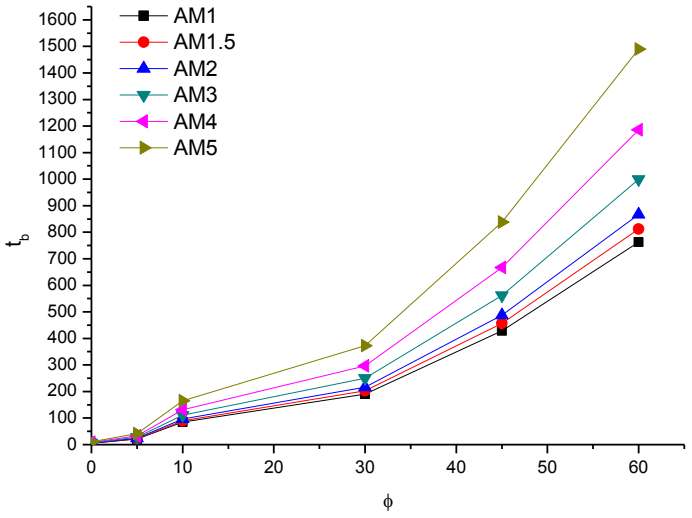

FIGURE 7.18: Plot of critical time (t_b) variation with inclination angle (ϕ) and Air Mass.

afterwards increases monotonically to attain a maximum at ϕ=60^o. Thus the increase in thermal efficiency with increase in inclination angle is due to the gravity vector influencing thermal stratification at higher inclination angles. Dincer and Rosen [13] stated that the thermal efficiency of a sensible heat thermal energy storage systems increases with thermal stratification. The present results are in good agreement with the statements of Dincer and Rosen [13]. This is also the case for AM3 (Table 7.2) and AM 5 (Table 7.3) respectively. The direct comparison of the values of Table 7.1, 7.2 and 7.3 reveal that the energy and exergy decreases with increasing Air Mass (AM1.5 to AM5) even though stratification is promoted at higher Air Mass. This is due to the higher temperatures obtained from the lower fluid heating from the absorber plate. For Air Mass 1.5, increase on the angle of inclination from 0^o, caused the heat transfer to increases by 28% at 5^o and 22% at 15^o. Beyond this point an increase in the angle results in a 15%, 22% and 24% decrease in the average heat transfer, attaining a local minimum at 45^o. At AM3 and AM5 similar trends are seen with heat transfer with increasing inclination angles. Table 7.2 and 7.3 show the respective increments and reduction with the associated inclination angles. The combination of the decrease in gravity component along the heating direction and the reduction in the amount of radiation transmitted to the lower surface promotes the stabilisation force owing to the direct absorption suppresses the destabilising effect from the lower heated surface. The flow attained at inclination

angle to 60^o results in an decrease in the heat transfer. The heat transfer is also found to decrease with increasing Air Mass and is in good agreement with the observations from the isotherms and streamlines shown in Fig 7.12 AM3 Fig 7.14 and AM5 Fig 7.16 respectively.

TABLE 7.1: Calculated values of Nu, MIX (exergy) and Capture efficiency at Air Mass 1

ϕ	Nu	ξ	η
5	37.05	0.52	0.12
15	24.52	0.43	0.21
30	17.92	0.40	0.29
45	17.12	0.37	0.4306
60	6.87	0.17	0.59

TABLE 7.2: Calculated values of the energy exergy and heat transfer at Air Mass 3

ϕ	Nu	ξ	η
5	36.05	0.49	0.20
15	18.33	0.35	0.22
30	17.43	0.29	0.27
45	13.65	0.28	0.39
60	6.94	0.25	0.57

TABLE 7.3: Calculated values of the energy exergy and heat transfer at Air Mass 5

ϕ	Nu	ξ	η
5	34.08	0.49	0.23
15	21.16	0.38	0.24
30	12.32	0.33	0.28
45	11.65	0.31	0.39
60	5.22	0.31	0.58

In this chapter two dimensional simulations on the heat transfer and fluid flow in an inclined enclosure (H/D=1), directly illuminated by non-uniform concentrated radiation is presented for inclination angles 5^o 15^o 30^o 45^o and 60^o respectively. The model accounts for the spectral volumetric absorption of solar radiation using the standard reference SMARTS model for the solar radiation and empirical wavelength dependent models. Temperature fields within the enclosures were found to have a nonlinear profile.The heat transfer and flow structures were found to change when the enclosure is inclined. Stratification was found to be promoted with increasing inclination angle and

increasing Air Mass. This translated into lower MIX number, reduced natural convection, increase in the critical time for onset of convective instability and increase in thermal performance with increasing inclination angle and Air Mass.

Chapter 8

Conclusion

8.1 Concluding remarks

Effective design of thermal storage systems requires an extensive knowledge of the interaction of the heat transfer and fluid flow within a store. The current study considers virtual prototyping of complex phenomena of heat transfer and fluid flow during charging in an enclosure filled with high temperature molten salt directly irradiated by concentrated solar radiation, is carried out using computational fluid dynamics. Understanding the transient response of the heat transfer and fluid dynamics in this system is of greatest importance in aiding the design of a thermal store for a small scale (circa 5kWe) Concentrated Solar Power (CSP) System.

Thus, in this thesis numerical models have been developed using commercially available FEM software (COMSOL) and has been employed to investigate the heat transfer and fluid flow within an enclosure driven primarily but concentrated radiation. Special attention has been given to the depth dependent absorption of solar radiation by considering the spectral behaviour of solar radiation based on (a) a weighted attenuation model and (b) the spectral dependence of the attenuation coefficient based on the solar spectrum. The validity of the developed numerical tools has been presented based on a number of test cases by comparison of numerical results with established analytical and experimental results in published literature. This conceptual distinction allows the two models to be analysed and compared. The transient nature of the boundary conditions is considered in contrast to the isoflux /isothermal boundary condition commonly used in typical problems.

The main contributions of this thesis to the study of the transient heat transfer and fluid dynamics phenomena in a cavity enclosure have been presented in chapter 5, chapter 6 and chapter 7 and are highlighted hereafter.

- Chapter 3 presents the geometry, mathematical formulation and governing equations. Numerical discretisation and implementation using FEM, COMSOL, the applied boundary and initials conditions were presented.

- In Chapter 4, the validity of the numerical tool has been verified and validated by comparing published analytical and experimental results with corresponding numerical results in four test cases. The post-processing procedure followed in the assessment of the numerical solutions, in order to quantify errors and uncertainties, has been also presented. This post-processing procedure implemented in COMSOL, is based on the generalised Richardson extrapolations for h-refinement studies.

- Chapter 5: A numerical model predicting the transient volumetric heating in a high temperature KNO_3-$NaNO_3$ filled enclosure. The model accounts for the depth dependent absorption of incident solar radiation based on a single weighted absorption coefficient commonly used in many models. Two dimensional heat transfer and fluid flow is assumed and the model is solved for the transient temperature and fluid flow fields. The temperature in the enclosure is shown to be increased by the geometry which includes a lower absorber plate above that of a corresponding enclosure without a lower absorber. Temperature, velocity and heat transfer from the lower surface decrease with increasing absorber thickness. The flow structures and transitions as well as the corresponding heat transfer revealed an early conductive regime, a convective transitional regime and a quasi-steady regime. A fundamental flow frequency of 0.5Hz was obtained for the enclosures for an incident solar radiation of $1000\mathrm{Wm}^{-2}$ concentrated at 700X. The effect of flux Rayleigh number ($10^7 \leqslant \mathrm{Ra} \leqslant 10^{11}$) and the aspect ratio (H/D), 0.5,1,2 of the heat transfer and fluid mechanisms were considered. Results obtained show the convection dominates the thermal transport at aspect ratios of H/D =0.5 and H/D=1. When H/D=2, the heat transfer is primarily dominated by conduction with convection being less significant. Under this condition there is little bulk fluid movement. The average volumetric flow rate and heat transfer seen to be highest at H/D =0.5 and lowest at H/D =2; this is also confirmed by heat transfer and fluid regimes for all aspect ratios. Results also reveal that the critical time for the onset of thermal instability was also found to increase with H/D and decrease with increasing Ra. Three dimensional simulations were also obtained. Results reveal that the heat transfer and fluid flow; vortex plumes and streamlines show three dimensional behaviours.

- Volumetric absorption of radiation in a fluid layer behaves differently owing the wavelength dependence of the attenuation coefficient of most fluids. In Chapter 6,

a numerical model based on a standard solar spectrum reference, SMARTS model and a wavelength absorption coefficient was proposed to predict the temperature and flow field within an enclosure subjected to concentrated radiation from the top. Time dependent mass momentum and energy equations are solved using a Finite Element Method, with a Backward Differential Formula (BDF) with implicit time stepping.

Based on the proposed model, heat transfer and flow structures were investigated under varying Airmass; $1 \leqslant AM \leqslant 5$, which showed that the resulting temperature and velocity profile were affected by varying Airmass. For each AirMass, heat transfer and flow regimes exhibit: (1) an initial conductive regime, (2) a transitional stage where natural convection is dominant and (3) a quasi-steady state regime. Increment of the AirMass (AM) from AM1 to AM5 resulted in approximately 23%, 40% and 25% decrease in the heat transfer, volumetric flow rate and MIX number. While stratification time for onset of instability increased by 6% and 28% respectively. A spectral band dependence investigation of the model was conducted by comparing the with a single weighted attenuation model under identical conditions showed output quantities presented are between 10-30 % higher in the solar weighted absorption compared with the spectral model output variables. Three dimensional behaviours were investigations of the driving mechanisms and flow structures were conducted based on three dimensional simulations. On the basis of the the results obtained in this chapter with the current numerical tool, it is possible to propose and evaluate a direct absorption thermal energy storage system for different regions as represented by various spectra and zenith angles.

- Chapter 7: The parametrised attenuation model, which was successfully used in chapter 6 has been successfully extended to inclined enclosures. Two dimensional numerical simulation of radiation induced natural convection in a unit aspect ratio enclosures was conducted. Spectral solar radiation based on the SMARTS model incident at the top surface which was inclined at different angles to the gravity vector is absorbed based on wavelength dependent absorption coefficients. The heat transfer and flow structure is changed when the cavity is inclined. The effect of AirMass: 1.5, 3 and 5 on heat and flow transport was reported. Increasing the inclination angle from ϕ=5^o to ϕ=60^o resulted in 29% decrease in the lower fluid temperature, 78% decrease in the heat transfer, maximum velocity flow rate is for to decrease by 67% and 40% drop in the MIX number. Stratification was observed to increase with inclination, where the largest stratification obtained at ϕ=60^o. In the same line, for the respective AirMass 1, 3 and 5 similar trends with increasing inclination angle. Comparison of the isotherms and streamlines reveal stratification to be promoted with increasing AirMass and increase the critical time for

onset for convection and thermal efficiency. On the other hand the heat transfer, flow rate MIX number and non dimensionless exergy decreased with increasing AirMass. In spite of the achievements of the present model, further numerical and experimental studies will be required for optimisation of inclination angle.

8.2 Future works

This theses presents numerical models that simulate the radiation induced natural convection in an enclosure of aspect ratio H/D=1, which has been implemented in COMSOL. A number of limitations and problems have to be addressed to advance the proposed numerical model developed in this thesis for adequate prediction, design and optimisation of the direct absorption thermal storage system and related technologies. These limitations and problems suggest a variety of research directions that need to be investigated which would require further research works. Regarding numerical modelling:

- The spectral range should be extended to include the UV radiation (280-380nm) and infra-red radiation above 1100nm. Ray tracing for the volumetric absorption of solar radiation based on wavelength, would go a long way in improving current models.
- Addition of scattering data is required to investigate the directional heating effects.
- Implementation and assessment of different numerical methods DNS, LES, SPH etc, should be carried out in order to choose an appropriate modelisation of these phenomena should also be considered.
- Numerical simulation using Smooth Particle Hydrodynamics (SPH) combined with experimental tests might be used as reliable tools for a clear understanding of physical phenomena effects.
- New unsteady prediction models for their use in long-term simulations of solar energy systems are expected to be developed. Current prediction models do not take into account the daily variation of the solar radiation and as such not capable of modelling the transient heating over a day, week, month or year.
- Other high temperature molten salts suitable for the direct absorption of solar radiation for high temperature application should be considered.

- Following this research line, innovative concepts and future designs might be the object of future works such as a combined sensible and latent heat thermal energy storage.

8.3 Contributions

Solar weighted average model

With respect to other models published in literature, the present model (solar weighed average model is the first general numerical formulation of natural convection in a cylindrical enclosure driven by concentrated solar radiation. It is also the first formulation which solves the mass momentum and energy equation considering a non Boussinesq approximation as well as the temperature dependent thermophysical properties of fluid. The formulation in this thesis is discretised and solved based on a Finite Element Method (FEM) which used a Backward Differential Formula (BDF), with implicit time stepping coupled with a refined mesh. The three dimensional model presented is a first numerical model belonging to this class problem presented in a cylindrical geometry.

Parametrised standard reference (SMARTS) based model

This thesis presents a numerical model which allows the prediction of absorption of solar ration based on the spectral distribution of solar irradiation using SMARTS model and considers the wavelength dependence of attenuation coefficients based on empirical data. The current model provides a new approach, prediction model and information regarding thermal and flow fields in enclosures owing to volumetric absorption spectral solar radiation and varying AirMass Demonstrated significant differences in single weighted model and multi band models and illustrated that spectral properties are critical to efficiency. The developed a framework was successfully extended to three dimensional simulations.

Inclined cavity direct absorption model

Developed a physical model to explain the local heat transfer characteristics and flow in an inclined enclosure where the primary driving force in the absorption of concentrated solar radiation. Analysis of the heat transfer and fluid flow in a directly irradiated

inclined enclosure filled with high temperature molten salt under concentrated condition based on the SMARTS model and wavelength attenuation coefficients is presented. Models are simulated to determine the effect of angle inclination and AirMass (AM).

Appendix A

Spectral absorption and radiation data for Airmass 1-5

Wavelength (nm)	Abs coff (cm^{-1})	AM1 (Wm^{-2})	AM1.5 (Wm^{-2})	AM2 (Wm^{-2})	AM3 (Wm^{-2})	AM4 (Wm^{-2})	AM5 (Wm^{-2})
400.09	1.16E-02	1.084	0.859	0.6804	0.4267	0.2673	0.1672
401	1.70E-02	1.115	0.8854	0.7028	0.4426	0.2784	0.1749
402.37	1.28E-02	1.178	0.9375	0.7458	0.4717	0.298	0.188
403.29	1.48E-02	1.121	0.8938	0.7125	0.4525	0.2871	0.1818
404.2	1.61E-02	1.106	0.8832	0.7053	0.4495	0.2862	0.1819
405.11	1.59E-02	1.108	0.8862	0.7089	0.4534	0.2896	0.1847
406.03	1.46E-02	1.091	0.8748	0.7012	0.4503	0.2889	0.185
407.4	1.48E-02	1.075	0.8636	0.6937	0.4474	0.2882	0.1853
408.31	1.48E-02	1.119	0.9005	0.7243	0.4684	0.3026	0.1952
409.22	1.65E-02	1.2	0.9671	0.7792	0.5057	0.3278	0.2122
410.14	1.65E-02	1.05	0.8475	0.6841	0.4456	0.2899	0.1883
411.05	1.72E-02	1.139	0.9209	0.7447	0.4868	0.3178	0.2072
412.42	1.63E-02	1.224	0.9919	0.8037	0.5274	0.3457	0.2263
413.33	1.52E-02	1.196	0.9706	0.7874	0.5181	0.3405	0.2234
414.24	1.52E-02	1.212	0.9856	0.8011	0.529	0.3489	0.2298
415.16	1.56E-02	1.217	0.9909	0.8069	0.5347	0.354	0.234
416.07	1.44E-02	1.239	1.011	0.825	0.5489	0.3647	0.242
417.44	1.52E-02	1.211	0.9896	0.8085	0.5395	0.3595	0.2393
418.35	1.51E-02	1.191	0.9744	0.7973	0.5336	0.3567	0.2381
419.26	1.29E-02	1.208	0.99	0.8114	0.5447	0.3653	0.2446
420.17	1.37E-02	1.204	0.9887	0.8114	0.5463	0.3674	0.2468
421.08	1.09E-02	1.262	1.037	0.8527	0.576	0.3886	0.2618
422	1.28E-02	1.201	0.9888	0.8141	0.5515	0.3732	0.2522
423.36	1.55E-02	1.175	0.9687	0.7987	0.5427	0.3683	0.2497
424.28	1.47E-02	1.245	1.028	0.8485	0.578	0.3934	0.2674
425.19	1.37E-02	1.244	1.029	0.8507	0.5815	0.397	0.2707
426.1	1.63E-02	1.212	1.004	0.8319	0.5707	0.391	0.2676
427.01	1.62E-02	1.191	0.988	0.8196	0.5636	0.3872	0.2656
428.38	1.31E-02	1.162	0.9652	0.8015	0.5525	0.3805	0.2616
429.29	1.41E-02	1.101	0.9163	0.7623	0.5274	0.3645	0.2515
430.2	1.22E-02	0.9646	0.8038	0.6696	0.4646	0.3219	0.2228
431.11	1.30E-02	0.9581	0.7991	0.6664	0.4632	0.3216	0.223
432.02	1.20E-02	1.238	1.034	0.8639	0.6025	0.4198	0.2921
433.39	1.30E-02	1.246	1.042	0.872	0.6098	0.426	0.2972
434.3	1.47E-02	1.159	0.9706	0.8127	0.5696	0.3988	0.2788
435.21	1.44E-02	1.212	1.016	0.8519	0.5982	0.4196	0.294
436.12	1.25E-02	1.367	1.148	0.9634	0.6787	0.4776	0.3357
437.03	1.59E-02	1.348	1.134	0.9537	0.6741	0.4759	0.3356
438.39	1.06E-02	1.229	1.035	0.8715	0.6177	0.4373	0.3092
439.3	1.76E-02	1.274	1.074	0.9043	0.6414	0.4544	0.3216
440.21	1.59E-02	1.316	1.11	0.9364	0.6661	0.4733	0.3359

441.12	1.33E-02	1.364	1.153	0.9741	0.6951	0.4954	0.3527
442.03	1.25E-02	1.465	1.239	1.048	0.7496	0.5356	0.3821
443.4	1.59E-02	1.43	1.21	1.024	0.7333	0.5245	0.3747
444.3	1.40E-02	1.462	1.239	1.05	0.7538	0.5406	0.3872
445.21	1.65E-02	1.433	1.215	1.03	0.7407	0.5319	0.3815
446.12	1.84E-02	1.367	1.161	0.9865	0.7114	0.5125	0.3687
447.03	1.53E-02	1.478	1.258	1.07	0.7739	0.5592	0.4035
448.4	1.61E-02	1.505	1.281	1.09	0.7893	0.5709	0.4124
449.3	1.35E-02	1.511	1.288	1.098	0.7979	0.5792	0.4199
450.21	1.57E-02	1.554	1.327	1.133	0.825	0.6004	0.4364
451.12	1.39E-02	1.613	1.379	1.178	0.8601	0.6272	0.4568
452.03	1.44E-02	1.556	1.331	1.139	0.8329	0.6086	0.4442
453.39	1.68E-02	1.464	1.254	1.074	0.7874	0.5766	0.4217
454.3	1.32E-02	1.529	1.311	1.124	0.8264	0.6067	0.4449
455.21	1.58E-02	1.541	1.322	1.135	0.8354	0.6144	0.4513
456.12	1.85E-02	1.579	1.356	1.165	0.8595	0.6334	0.4663
457.03	1.47E-02	1.607	1.382	1.188	0.878	0.6483	0.4781
458.39	1.63E-02	1.555	1.338	1.151	0.8515	0.6294	0.4647
459.3	1.69E-02	1.548	1.333	1.148	0.8512	0.6305	0.4664
460.2	1.64E-02	1.554	1.34	1.155	0.8571	0.6357	0.471
461.11	1.63E-02	1.592	1.373	1.184	0.8809	0.6546	0.4859
462.02	1.25E-02	1.604	1.386	1.197	0.8921	0.6645	0.4944
463.38	1.22E-02	1.595	1.379	1.191	0.8891	0.663	0.4938
464.29	1.21E-02	1.569	1.357	1.174	0.8786	0.6567	0.4904
465.19	1.61E-02	1.549	1.342	1.162	0.872	0.6535	0.4892
466.1	1.80E-02	1.564	1.357	1.177	0.8847	0.6645	0.4985
467.01	1.80E-02	1.538	1.335	1.158	0.8713	0.6549	0.4918
468.37	1.10E-02	1.558	1.353	1.175	0.8854	0.6666	0.5014
469.27	1.48E-02	1.568	1.363	1.184	0.8937	0.6739	0.5076
470.18	1.46E-02	1.52	1.322	1.149	0.8681	0.6553	0.4941
471.09	1.43E-02	1.519	1.322	1.15	0.8702	0.6579	0.4968
472.45	1.49E-02	1.603	1.395	1.214	0.9198	0.6961	0.5262
473.35	1.34E-02	1.584	1.38	1.202	0.9112	0.6904	0.5225
474.26	1.67E-02	1.589	1.385	1.206	0.9146	0.6931	0.5247
475.17	1.59E-02	1.606	1.399	1.219	0.9245	0.7007	0.5305
476.07	1.71E-02	1.562	1.36	1.185	0.8983	0.6806	0.5151
477.43	1.55E-02	1.569	1.367	1.191	0.9033	0.6846	0.5184
478.34	1.55E-02	1.613	1.407	1.227	0.9327	0.7084	0.5375
479.24	1.79E-02	1.604	1.401	1.223	0.9319	0.7097	0.5399
480.15	1.59E-02	1.607	1.405	1.228	0.9386	0.7166	0.5467
481.05	1.53E-02	1.637	1.433	1.255	0.9614	0.7361	0.5631
482.41	1.96E-02	1.645	1.442	1.264	0.9713	0.7457	0.572
483.32	1.69E-02	1.625	1.426	1.252	0.9643	0.7422	0.5707

484.22	2.00E-02	1.592	1.399	1.229	0.948	0.7309	0.563
485.13	1.53E-02	1.517	1.334	1.173	0.9065	0.7	0.5401
486.03	2.10E-02	1.326	1.167	1.027	0.7955	0.6155	0.4758
487.39	1.62E-02	1.39	1.225	1.079	0.837	0.6488	0.5025
488.29	8.02E-03	1.527	1.346	1.186	0.9209	0.7145	0.5539
489.2	1.25E-02	1.534	1.352	1.192	0.9264	0.7193	0.5581
490.1	1.64E-02	1.614	1.424	1.257	0.9783	0.7611	0.5915
491.01	1.36E-02	1.587	1.401	1.238	0.9653	0.7523	0.5858
492.36	1.24E-02	1.499	1.325	1.171	0.9146	0.7137	0.5565
493.27	1.01E-02	1.55	1.371	1.212	0.9475	0.7403	0.5779
494.17	2.07E-02	1.566	1.386	1.226	0.9597	0.7507	0.5867
495.07	1.54E-02	1.581	1.4	1.239	0.9709	0.7603	0.5949
496.43	1.29E-02	1.591	1.41	1.249	0.9793	0.7676	0.6012
497.33	1.34E-02	1.618	1.434	1.271	0.9978	0.783	0.614
498.24	1.37E-02	1.543	1.369	1.214	0.954	0.7495	0.5884
499.14	1.79E-02	1.565	1.388	1.231	0.9689	0.7618	0.5985
500.04	1.93E-02	1.522	1.35	1.198	0.9431	0.742	0.5833
501.4	1.34E-02	1.496	1.328	1.178	0.9277	0.7301	0.5742
502.3	1.73E-02	1.478	1.312	1.164	0.9156	0.7201	0.5661
503.2	1.68E-02	1.543	1.368	1.213	0.954	0.7498	0.5891
504.11	1.22E-02	1.512	1.337	1.183	0.9255	0.724	0.5662
505.91	1.59E-02	1.561	1.385	1.228	0.9667	0.7605	0.5981
506.82	1.13E-02	1.613	1.431	1.27	1	0.7874	0.6196
507.27	1.46E-02	1.536	1.364	1.211	0.9544	0.7521	0.5926
508.17	1.50E-02	1.487	1.322	1.175	0.9285	0.7334	0.5792
509.07	1.20E-02	1.528	1.36	1.21	0.9579	0.7581	0.5998
510.43	1.78E-02	1.519	1.353	1.205	0.9558	0.7578	0.6005
511.33	1.72E-02	1.559	1.39	1.239	0.9846	0.782	0.6209
512.23	1.70E-02	1.577	1.407	1.255	0.9985	0.7943	0.6315
513.13	1.60E-02	1.494	1.333	1.19	0.9483	0.7553	0.6013
514.03	1.50E-02	1.484	1.325	1.184	0.9443	0.7531	0.6003
515.39	1.75E-02	1.47	1.313	1.174	0.9372	0.7481	0.5969
516.29	1.81E-02	1.468	1.312	1.173	0.9372	0.7487	0.5978
517.19	1.82E-02	1.304	1.167	1.044	0.835	0.6677	0.5338
518.09	1.51E-02	1.373	1.228	1.099	0.8799	0.7042	0.5634
519.44	1.05E-02	1.441	1.29	1.154	0.9246	0.7404	0.5927
520.34	1.42E-02	1.494	1.338	1.198	0.9597	0.7689	0.6159
521.24	1.39E-02	1.509	1.352	1.21	0.9705	0.7779	0.6235
522.15	1.98E-02	1.512	1.354	1.213	0.9729	0.7802	0.6255
523.05	1.42E-02	1.487	1.332	1.193	0.9578	0.7686	0.6167
524.4	1.43E-02	1.542	1.382	1.238	0.9936	0.7974	0.6398
525.3	1.55E-02	1.563	1.4	1.254	1.006	0.8073	0.6476
526.2	1.43E-02	1.495	1.339	1.2	0.963	0.7729	0.6203

527.1	1.58E-02	1.411	1.264	1.132	0.9081	0.7285	0.5845
528	1.51E-02	1.494	1.338	1.198	0.9612	0.771	0.6186
529.35	1.38E-02	1.576	1.411	1.264	1.014	0.8129	0.6521
530.25	1.69E-02	1.555	1.393	1.248	1.001	0.8032	0.6446
531.15	1.29E-02	1.58	1.415	1.268	1.018	0.8171	0.6561
532.05	1.58E-02	1.527	1.368	1.226	0.9849	0.7912	0.6357
533.4	1.57E-02	1.483	1.33	1.192	0.9582	0.7704	0.6195
534.3	1.74E-02	1.527	1.37	1.229	0.9889	0.7958	0.6406
535.2	1.36E-02	1.56	1.4	1.257	1.012	0.8158	0.6574
536.1	1.77E-02	1.575	1.414	1.27	1.024	0.8255	0.6659
537	1.41E-02	1.513	1.359	1.221	0.9857	0.7959	0.6427
538.34	1.60E-02	1.54	1.384	1.244	1.006	0.8128	0.6571
539.24	1.64E-02	1.529	1.375	1.236	0.9999	0.8089	0.6545
540.14	1.49E-02	1.467	1.319	1.186	0.9597	0.7765	0.6284
541.04	1.62E-02	1.48	1.33	1.195	0.9661	0.7808	0.6313
542.39	9.64E-03	1.528	1.374	1.235	0.9979	0.8066	0.6523
543.29	1.16E-02	1.511	1.36	1.224	0.9917	0.8035	0.6512
544.19	1.64E-02	1.54	1.385	1.246	1.009	0.8167	0.6614
545.09	1.28E-02	1.535	1.382	1.243	1.007	0.816	0.6614
546.43	1.27E-02	1.544	1.389	1.249	1.01	0.8175	0.6618
547.33	1.48E-02	1.542	1.388	1.249	1.012	0.8197	0.6646
548.23	1.30E-02	1.523	1.372	1.235	1.002	0.8126	0.6596
549.13	1.62E-02	1.529	1.377	1.241	1.008	0.8185	0.6652
550.02	1.55E-02	1.548	1.396	1.258	1.023	0.8315	0.6764
551.37	9.45E-03	1.53	1.38	1.245	1.013	0.8242	0.6712
552.27	1.23E-02	1.542	1.391	1.255	1.022	0.832	0.678
553.17	1.65E-02	1.515	1.367	1.234	1.005	0.8185	0.6673
554.06	1.52E-02	1.552	1.401	1.264	1.03	0.8393	0.6844
555.41	1.64E-02	1.556	1.404	1.267	1.032	0.8415	0.6863
556.31	1.31E-02	1.537	1.387	1.252	1.02	0.8314	0.6782
557.2	1.17E-02	1.491	1.345	1.214	0.9893	0.8065	0.658
558.1	1.45E-02	1.481	1.336	1.206	0.9821	0.8004	0.6528
559	1.51E-02	1.455	1.313	1.184	0.9641	0.7854	0.6404
560.34	1.33E-02	1.475	1.331	1.201	0.978	0.797	0.6501
561.24	1.61E-02	1.496	1.35	1.218	0.9925	0.809	0.66
562.14	1.25E-02	1.488	1.342	1.211	0.9862	0.8036	0.6555
563.03	1.10E-02	1.531	1.381	1.246	1.014	0.826	0.6735
564.38	1.33E-02	1.492	1.345	1.213	0.9871	0.8038	0.6552
565.27	1.78E-02	1.481	1.335	1.204	0.9793	0.7972	0.6497
566.17	1.52E-02	1.461	1.317	1.187	0.9654	0.7857	0.6401
567.06	1.33E-02	1.49	1.343	1.21	0.9837	0.8001	0.6514
568.41	1.61E-02	1.482	1.334	1.2	0.9729	0.7893	0.6411
569.3	1.24E-02	1.455	1.305	1.172	0.9445	0.7622	0.616

570.2	1.55E-02	1.454	1.306	1.173	0.9469	0.7652	0.6192
571.09	1.53E-02	1.444	1.298	1.168	0.9447	0.765	0.6202
572.44	1.31E-02	1.485	1.332	1.196	0.9643	0.7783	0.629
573.33	1.47E-02	1.502	1.348	1.21	0.9751	0.7868	0.6356
574.23	1.70E-02	1.499	1.345	1.207	0.9721	0.7839	0.633
575.12	1.38E-02	1.473	1.321	1.185	0.9534	0.768	0.6195
576.02	1.12E-02	1.46	1.31	1.175	0.9457	0.762	0.6148
577.36	1.13E-02	1.476	1.324	1.188	0.9574	0.7721	0.6234
578.26	1.13E-02	1.452	1.305	1.172	0.9464	0.7648	0.6189
579.15	1.47E-02	1.456	1.31	1.179	0.9549	0.7743	0.6287
580.04	1.14E-02	1.479	1.334	1.203	0.9791	0.7976	0.6506
581.39	1.45E-02	1.483	1.34	1.211	0.989	0.8085	0.6618
582.28	1.32E-02	1.509	1.365	1.236	1.013	0.8308	0.6823
583.17	1.23E-02	1.511	1.369	1.241	1.02	0.8393	0.6913
584.07	9.97E-03	1.523	1.382	1.253	1.032	0.8509	0.7022
585.41	1.29E-02	1.485	1.348	1.224	1.009	0.8331	0.6883
586.3	1.41E-02	1.455	1.321	1.199	0.9888	0.8162	0.6745
587.2	1.17E-02	1.489	1.35	1.224	1.008	0.83	0.6846
588.09	1.79E-02	1.462	1.32	1.192	0.9733	0.7959	0.6519
589.43	1.48E-02	1.313	1.174	1.05	0.8423	0.6777	0.547
590.32	1.02E-02	1.372	1.228	1.1	0.8844	0.7124	0.5752
591.22	1.20E-02	1.442	1.297	1.168	0.9484	0.7715	0.6288
592.11	1.59E-02	1.431	1.285	1.154	0.9328	0.7556	0.6134
593	1.22E-02	1.446	1.303	1.175	0.9572	0.7812	0.6388
594.34	1.28E-02	1.44	1.297	1.169	0.9505	0.7749	0.6331
595.23	1.17E-02	1.412	1.268	1.14	0.9222	0.7476	0.6073
596.13	1.23E-02	1.453	1.313	1.188	0.9732	0.7987	0.6568
597.02	1.11E-02	1.441	1.302	1.176	0.961	0.7866	0.6449
598.36	1.70E-02	1.434	1.299	1.176	0.9657	0.7942	0.6544
599.25	1.44E-02	1.435	1.301	1.18	0.9715	0.801	0.6616
600.14	9.57E-03	1.434	1.303	1.184	0.9786	0.8098	0.6711
601.04	1.42E-02	1.42	1.292	1.176	0.9742	0.8082	0.6714
602.37	1.60E-02	1.41	1.283	1.168	0.9679	0.8032	0.6676
603.27	1.75E-02	1.432	1.304	1.187	0.9853	0.8186	0.6812
604.16	1.12E-02	1.455	1.325	1.207	1.002	0.8328	0.6933
605.05	1.56E-02	1.447	1.319	1.202	0.9991	0.8314	0.693
606.39	1.27E-02	1.442	1.316	1.2	1	0.8342	0.6968
607.28	1.71E-02	1.456	1.33	1.215	1.015	0.8488	0.7106
608.17	1.28E-02	1.44	1.317	1.204	1.008	0.8444	0.7083
609.06	1.15E-02	1.442	1.32	1.208	1.013	0.8495	0.7136
610.4	1.58E-02	1.43	1.31	1.199	1.006	0.8452	0.7107
611.29	1.19E-02	1.438	1.318	1.208	1.014	0.853	0.7181
612.18	1.13E-02	1.433	1.314	1.204	1.013	0.852	0.7178

613.07	1.35E-02	1.415	1.297	1.19	1.001	0.8427	0.7104
614.4	1.02E-02	1.395	1.28	1.174	0.9891	0.8339	0.7038
615.3	1.17E-02	1.425	1.308	1.201	1.014	0.8557	0.7232
616.19	1.25E-02	1.378	1.266	1.163	0.9823	0.8303	0.7025
617.08	1.53E-02	1.375	1.264	1.161	0.9817	0.8305	0.7032
618.41	1.19E-02	1.427	1.312	1.206	1.02	0.8635	0.7316
619.3	1.34E-02	1.412	1.299	1.195	1.011	0.8559	0.7254
620.19	1.23E-02	1.421	1.307	1.201	1.016	0.86	0.7287
621.08	1.14E-02	1.422	1.306	1.2	1.013	0.8557	0.7237
622.42	1.35E-02	1.4	1.282	1.174	0.9845	0.8268	0.6954
623.31	1.48E-02	1.373	1.253	1.144	0.9542	0.7969	0.6667
624.19	1.04E-02	1.352	1.237	1.131	0.9469	0.7936	0.6661
625.08	1.32E-02	1.356	1.243	1.139	0.9582	0.8066	0.6799
626.42	1.20E-02	1.378	1.264	1.159	0.9759	0.8223	0.6936
627.31	1.21E-02	1.398	1.281	1.173	0.9858	0.8288	0.6977
628.2	1.34E-02	1.346	1.211	1.09	0.8831	0.7163	0.5819
629.08	1.40E-02	1.38	1.258	1.146	0.9522	0.7919	0.6595
630.42	9.51E-03	1.351	1.231	1.121	0.9314	0.7743	0.6444
631.31	1.18E-02	1.37	1.257	1.153	0.97	0.8169	0.6885
632.2	7.18E-03	1.354	1.243	1.142	0.9648	0.8154	0.6898
633.08	1.38E-02	1.392	1.283	1.182	1.005	0.8548	0.7275
634.42	1.24E-02	1.375	1.27	1.173	1.002	0.8557	0.7313
635.3	1.42E-02	1.395	1.29	1.193	1.021	0.8737	0.7483
636.19	1.11E-02	1.374	1.272	1.177	1.009	0.8656	0.7427
637.08	8.40E-03	1.394	1.292	1.197	1.027	0.8821	0.7579
638.41	8.99E-03	1.405	1.304	1.209	1.041	0.8964	0.7723
639.3	8.99E-03	1.389	1.29	1.198	1.033	0.8916	0.7696
640.19	1.47E-02	1.375	1.279	1.189	1.028	0.8886	0.7688
641.08	9.97E-03	1.374	1.278	1.19	1.03	0.8922	0.7731
642.41	1.27E-02	1.367	1.273	1.185	1.028	0.8921	0.7742
643.29	1.27E-02	1.385	1.29	1.202	1.043	0.9051	0.7858
644.18	1.87E-02	1.38	1.286	1.199	1.042	0.9058	0.7877
645.07	1.48E-02	1.384	1.29	1.202	1.044	0.9071	0.7883
646.4	1.53E-02	1.357	1.262	1.174	1.016	0.8798	0.7622
647.29	1.14E-02	1.352	1.251	1.159	0.9936	0.8528	0.7323
648.17	1.70E-02	1.356	1.254	1.16	0.996	0.8564	0.7375
649.06	8.63E-03	1.331	1.231	1.139	0.9763	0.838	0.7198
650.39	1.34E-02	1.323	1.232	1.148	0.9964	0.8658	0.7528
651.27	1.11E-02	1.378	1.285	1.199	1.043	0.9079	0.7907
652.16	1.08E-02	1.337	1.238	1.146	0.9857	0.8493	0.733
653.05	1.21E-02	1.361	1.269	1.184	1.031	0.8991	0.7842
654.38	1.30E-02	1.344	1.255	1.171	1.021	0.8909	0.7774
655.26	1.27E-02	1.302	1.211	1.126	0.9761	0.8468	0.7353

656.15	1.03E-02	1.148	1.071	0.9989	0.8696	0.7574	0.66
657.03	1.13E-02	1.178	1.099	1.025	0.8931	0.7785	0.6789
658.36	1.18E-02	1.316	1.23	1.149	1.004	0.8782	0.7684
659.25	1.26E-02	1.321	1.235	1.154	1.009	0.8819	0.7713
660.13	7.16E-03	1.321	1.233	1.151	1.003	0.8749	0.7633
661.02	9.79E-03	1.322	1.23	1.145	0.9918	0.8599	0.7463
662.35	1.26E-02	1.321	1.225	1.135	0.9765	0.8408	0.7251
663.23	8.66E-03	1.298	1.207	1.121	0.9685	0.8374	0.725
664.12	8.48E-03	1.318	1.231	1.149	1.002	0.874	0.7632
665	1.03E-02	1.321	1.237	1.158	1.016	0.8916	0.7827
666.33	9.00E-03	1.325	1.244	1.167	1.029	0.9064	0.799
667.21	9.33E-03	1.326	1.246	1.172	1.036	0.9163	0.8102
668.1	9.75E-03	1.326	1.249	1.176	1.042	0.9236	0.8186
669.42	1.14E-02	1.347	1.269	1.196	1.061	0.9419	0.8359
670.31	1.01E-02	1.341	1.264	1.192	1.059	0.9411	0.8361
671.19	1.29E-02	1.341	1.264	1.193	1.061	0.9434	0.8388
672.07	1.05E-02	1.329	1.254	1.183	1.053	0.9374	0.8341
673.4	8.40E-03	1.349	1.273	1.202	1.071	0.9539	0.8495
674.28	1.02E-02	1.344	1.269	1.198	1.069	0.9526	0.849
675.17	1.10E-02	1.332	1.258	1.188	1.06	0.9459	0.8437
676.05	1.24E-02	1.341	1.267	1.197	1.069	0.9541	0.8515
677.38	1.05E-02	1.327	1.254	1.185	1.059	0.9458	0.8445
678.26	7.03E-03	1.33	1.258	1.189	1.063	0.9494	0.8481
679.14	9.80E-03	1.309	1.238	1.17	1.047	0.9356	0.8362
680.03	1.34E-02	1.319	1.248	1.181	1.056	0.945	0.8451
681.35	1.06E-02	1.311	1.241	1.174	1.051	0.9407	0.8417
682.23	9.40E-03	1.31	1.24	1.174	1.051	0.9413	0.8427
683.12	1.23E-02	1.308	1.238	1.172	1.05	0.941	0.8428
684	8.21E-03	1.302	1.233	1.167	1.046	0.9373	0.8396
685.32	1.08E-02	1.313	1.244	1.178	1.057	0.948	0.8499
686.2	1.22E-02	1.306	1.237	1.171	1.05	0.9417	0.8439
687.09	7.57E-03	1.048	0.8841	0.7455	0.5301	0.3767	0.2676
688.41	9.84E-03	1.138	1.006	0.8895	0.6949	0.5426	0.4235
689.29	1.36E-02	1.14	1.009	0.8936	0.7004	0.5488	0.4298
690.17	8.38E-03	1.167	1.049	0.9432	0.7621	0.6155	0.4969
691.05	1.27E-02	1.197	1.093	0.9991	0.8343	0.6963	0.581
692.38	1.13E-02	1.216	1.125	1.041	0.8913	0.7632	0.6534
693.26	7.32E-03	1.209	1.117	1.032	0.8826	0.7557	0.6475
694.14	9.72E-03	1.201	1.108	1.024	0.8791	0.758	0.6555
695.02	1.05E-02	1.23	1.147	1.071	0.938	0.8238	0.7249
696.34	1.16E-02	1.232	1.149	1.073	0.9412	0.8282	0.7301
697.22	1.09E-02	1.279	1.21	1.145	1.025	0.9173	0.8212
698.1	7.18E-03	1.26	1.192	1.127	1.009	0.903	0.8083

699.43	1.50E-02	1.249	1.17	1.097	0.968	0.8556	0.757
700.31	1.21E-02	1.234	1.156	1.084	0.9561	0.8445	0.7469
701.19	1.05E-02	1.227	1.147	1.073	0.9402	0.8253	0.7251
702.07	7.91E-03	1.229	1.153	1.082	0.9542	0.8424	0.7442
703.39	1.23E-02	1.232	1.155	1.085	0.9582	0.8482	0.752
704.27	1.11E-02	1.261	1.189	1.122	1	0.8923	0.7968
705.15	1.03E-02	1.263	1.191	1.124	1.002	0.8939	0.7978
706.03	4.93E-03	1.258	1.189	1.124	1.006	0.8998	0.805
707.35	5.71E-03	1.258	1.19	1.126	1.009	0.9041	0.8101
708.23	1.06E-02	1.261	1.193	1.129	1.011	0.9059	0.8115
709.11	1.17E-02	1.257	1.193	1.132	1.021	0.9196	0.8283
710.43	7.98E-03	1.26	1.195	1.132	1.017	0.914	0.8208
711.31	1.17E-02	1.257	1.193	1.132	1.019	0.9177	0.8261
712.19	9.94E-03	1.25	1.188	1.129	1.02	0.9213	0.8317
713.06	1.13E-02	1.241	1.178	1.118	1.007	0.9073	0.817
714.38	8.16E-03	1.245	1.182	1.123	1.013	0.9135	0.8237
715.26	1.29E-02	1.213	1.148	1.087	0.9743	0.8739	0.7839
716.14	9.68E-03	1.216	1.149	1.087	0.9736	0.8725	0.782
717.02	9.48E-03	1.121	1.02	0.9308	0.7818	0.6617	0.5629
718.34	1.40E-02	1.045	0.9409	0.8536	0.7129	0.6021	0.5118
719.22	5.69E-03	0.9675	0.8648	0.7814	0.6488	0.5451	0.4609
720.09	1.14E-02	1.016	0.9076	0.8176	0.6734	0.5609	0.4701
721.41	1.08E-02	1.078	0.9882	0.9105	0.78	0.6723	0.5815
722.29	9.33E-03	1.186	1.116	1.05	0.9318	0.8276	0.7355
723.17	7.78E-03	1.13	1.047	0.9739	0.8487	0.7432	0.6523
724.04	1.03E-02	1.047	0.9527	0.8731	0.7415	0.6346	0.5455
725.36	8.96E-03	1.04	0.9408	0.8575	0.7222	0.6144	0.5257
726.24	1.25E-02	1.081	0.9833	0.8987	0.7584	0.6458	0.5532
727.12	1.06E-02	1.083	0.9926	0.9152	0.7859	0.6798	0.5904
728.43	8.53E-03	1.04	0.9403	0.8559	0.7188	0.6103	0.5215
729.31	1.09E-02	1.054	0.9677	0.8929	0.7683	0.6663	0.5804
730.19	1.15E-02	1.112	1.024	0.9455	0.8103	0.6983	0.6043
731.06	1.10E-02	1.074	0.9826	0.9031	0.77	0.6616	0.571
732.38	1.32E-02	1.123	1.043	0.9711	0.8475	0.7438	0.655
733.26	8.61E-03	1.164	1.096	1.033	0.9192	0.8192	0.7308
734.13	6.31E-03	1.185	1.12	1.059	0.9485	0.8505	0.7631
735.01	1.16E-02	1.164	1.098	1.037	0.9258	0.8275	0.7404
736.32	7.76E-03	1.162	1.097	1.036	0.9243	0.8249	0.7365
737.2	9.68E-03	1.168	1.102	1.041	0.9286	0.8296	0.7417
738.08	1.12E-02	1.171	1.114	1.06	0.9604	0.8702	0.7884
739.39	1.35E-02	1.149	1.093	1.04	0.9423	0.8546	0.7753
740.27	1.18E-02	1.174	1.12	1.068	0.9726	0.8856	0.8063
741.14	1.15E-02	1.16	1.108	1.059	0.9665	0.8822	0.805

742.02	1.07E-02	1.158	1.108	1.061	0.9713	0.8891	0.8134
743.33	8.96E-03	1.187	1.137	1.088	0.9975	0.914	0.8369
744.21	1.20E-02	1.182	1.133	1.086	0.9973	0.9154	0.8396
745.08	1.29E-02	1.182	1.133	1.087	0.9998	0.9191	0.8444
746.39	8.43E-03	1.187	1.139	1.092	1.005	0.9239	0.849
747.27	8.82E-03	1.19	1.142	1.095	1.008	0.9274	0.8526
748.14	1.02E-02	1.187	1.14	1.094	1.007	0.9265	0.8521
749.02	1.26E-02	1.174	1.127	1.082	0.9961	0.9169	0.8435
750.33	1.30E-02	1.173	1.126	1.081	0.9962	0.9173	0.8441
751.21	9.06E-03	1.162	1.115	1.071	0.9867	0.9088	0.8364
752.08	8.93E-03	1.167	1.12	1.076	0.9917	0.9137	0.8413
753.39	9.45E-03	1.173	1.126	1.082	0.9975	0.9194	0.8468
754.27	9.48E-03	1.176	1.129	1.085	1	0.9221	0.8494
755.14	5.99E-03	1.169	1.123	1.079	0.995	0.9173	0.8451
756.01	1.41E-02	1.169	1.123	1.079	0.9954	0.918	0.846
757.33	6.03E-03	1.171	1.125	1.081	0.9973	0.9198	0.8478
758.2	7.23E-03	1.157	1.111	1.068	0.9851	0.9084	0.8372
759.07	4.17E-03	1.142	1.092	1.044	0.9547	0.8722	0.7963
760.38	7.01E-03	0.4219	0.2453	0.1425	0.04812	0.01623	0.005469
761.26	7.94E-03	0.294	0.1429	0.06941	0.01639	0.003863	0.00091
762.13	5.21E-03	0.7803	0.6233	0.4977	0.3174	0.2023	0.1288
763	5.54E-03	0.5343	0.35	0.2291	0.09818	0.04204	0.01799
764.31	1.09E-02	0.6693	0.492	0.3615	0.1952	0.1053	0.05676
765.19	1.04E-02	0.7816	0.6241	0.4982	0.3175	0.2021	0.1286
766.06	9.71E-03	0.8603	0.7359	0.6292	0.4601	0.3362	0.2455
767.37	7.00E-03	0.994	0.8988	0.8124	0.6638	0.5421	0.4423
768.24	1.06E-02	1.079	1.014	0.9529	0.8414	0.7426	0.6549
769.11	2.41E-03	1.087	1.03	0.9766	0.8774	0.7879	0.707
770.42	9.43E-03	1.107	1.06	1.014	0.9283	0.8494	0.7767
771.29	9.80E-03	1.109	1.066	1.024	0.9456	0.8724	0.8044
772.17	1.05E-02	1.109	1.068	1.027	0.951	0.8799	0.8135
773.04	1.49E-02	1.117	1.075	1.035	0.9589	0.8879	0.8217
774.35	8.14E-03	1.111	1.07	1.031	0.9555	0.8854	0.8199
775.22	7.82E-03	1.103	1.062	1.023	0.9492	0.8801	0.8155
776.09	9.40E-03	1.116	1.075	1.036	0.9615	0.8918	0.8267
777.4	7.12E-03	1.101	1.061	1.023	0.9494	0.8808	0.8168
778.27	1.06E-02	1.095	1.055	1.017	0.9441	0.876	0.8123
779.14	9.72E-03	1.096	1.056	1.018	0.9453	0.8773	0.8137
780.01	8.04E-03	1.09	1.051	1.013	0.9407	0.8734	0.8103
781.32	1.16E-02	1.091	1.052	1.014	0.9423	0.8751	0.8121
782.19	8.30E-03	1.098	1.059	1.021	0.9488	0.8814	0.8182
783.06	5.80E-03	1.079	1.041	1.003	0.933	0.867	0.8052
784.36	7.41E-03	1.084	1.046	1.009	0.9383	0.8723	0.8105

785.23	9.42E-03	1.077	1.039	1.001	0.931	0.865	0.8033
786.1	5.56E-03	1.089	1.05	1.013	0.941	0.8739	0.8112
787.41	9.29E-03	1.077	1.035	0.9937	0.9165	0.845	0.7788
788.28	1.19E-02	1.067	1.023	0.9809	0.9016	0.8287	0.7616
789.15	9.35E-03	1.068	1.023	0.9806	0.9013	0.8288	0.7623
790.02	8.76E-03	1.051	0.9999	0.9526	0.8664	0.7894	0.7201
791.32	9.78E-03	1.05	1.005	0.9634	0.8856	0.8149	0.7501
792.19	1.01E-02	1.041	0.9978	0.9569	0.8812	0.8123	0.7491
793.06	9.89E-03	1.026	0.9823	0.9415	0.8662	0.7979	0.7352
794.37	6.02E-03	1.032	0.9957	0.9603	0.8931	0.8302	0.7713
795.24	1.03E-02	1.053	1.014	0.9762	0.9054	0.8396	0.7783
796.11	1.27E-02	1.035	0.9876	0.9433	0.862	0.7884	0.7215
797.41	1.10E-02	1.036	0.9892	0.9446	0.8621	0.7872	0.719
798.28	1.07E-02	1.053	1.014	0.9756	0.9037	0.8369	0.7748
799.15	7.41E-03	1.05	1.008	0.969	0.8953	0.8275	0.7648
800.02	1.24E-02	1.035	0.9923	0.9517	0.8764	0.8076	0.7442
801.32	1.34E-02	1.035	0.9905	0.9484	0.8703	0.799	0.7338
802.19	1.26E-02	1.032	0.9878	0.946	0.868	0.7965	0.7309
803.06	1.02E-02	1.026	0.981	0.9386	0.8597	0.7874	0.721
804.36	1.07E-02	1.026	0.9821	0.9406	0.8632	0.7922	0.7269
805.23	9.69E-03	1.019	0.9779	0.9388	0.8656	0.798	0.7355
806.09	7.39E-03	1.041	1.003	0.967	0.8984	0.8344	0.7746
807.4	1.20E-02	1.03	0.992	0.9553	0.8862	0.8221	0.7624
808.26	1.25E-02	1.03	0.9929	0.9566	0.8881	0.8241	0.7644
809.13	1.30E-02	1.016	0.9762	0.9378	0.8656	0.7988	0.7369
810	9.47E-03	1.012	0.9696	0.9296	0.855	0.7869	0.7243
811.3	5.43E-03	1.019	0.9734	0.9293	0.848	0.7768	0.7134
812.17	8.81E-03	1	0.949	0.9009	0.8131	0.7349	0.6646
813.03	1.20E-02	0.9867	0.9316	0.8812	0.7919	0.7144	0.6462
814.34	1.01E-02	0.9042	0.8309	0.7687	0.6665	0.5844	0.5158
815.2	1.29E-02	0.898	0.8257	0.7645	0.6649	0.5852	0.5188
816.07	7.45E-03	0.8429	0.7703	0.711	0.6153	0.5384	0.4737
817.37	9.54E-03	0.8531	0.7832	0.725	0.629	0.5504	0.4838
818.24	5.75E-03	0.8293	0.7566	0.6964	0.5986	0.5199	0.4541
819.1	1.24E-02	0.8948	0.8362	0.7848	0.6956	0.6191	0.552
820.4	7.95E-03	0.8559	0.7916	0.7371	0.6461	0.5708	0.5066
821.27	1.07E-02	0.9572	0.912	0.8701	0.7942	0.7264	0.6652
822.13	9.09E-03	0.9375	0.8883	0.8441	0.7655	0.6964	0.6344
823	1.21E-02	0.7053	0.6258	0.5611	0.4631	0.3889	0.3295
824.3	8.24E-03	0.9242	0.8674	0.8168	0.7289	0.6535	0.5874
825.16	6.18E-03	0.9442	0.8976	0.8557	0.7817	0.7163	0.6575
826.03	9.30E-03	0.9212	0.8678	0.8209	0.7397	0.6693	0.6068
827.33	1.06E-02	0.9583	0.9116	0.8692	0.7937	0.7267	0.6663

828.19	7.25E-03	0.8514	0.7852	0.7293	0.6363	0.5594	0.4937
829.06	3.10E-03	0.9134	0.8622	0.8171	0.7386	0.6705	0.6099
830.35	8.33E-03	0.9059	0.8523	0.8058	0.7262	0.6583	0.5986
831.22	1.23E-02	0.9074	0.8551	0.809	0.7293	0.6605	0.5996
832.08	7.03E-03	0.887	0.8312	0.783	0.7005	0.6302	0.5686
833.38	1.03E-02	0.9224	0.8783	0.8372	0.7627	0.6964	0.6367
834.25	3.95E-03	0.9027	0.8513	0.8051	0.7244	0.6556	0.5956
835.11	1.37E-02	0.9644	0.9269	0.8905	0.8233	0.7637	0.7101
836.41	5.12E-03	0.9401	0.8927	0.8488	0.7699	0.7005	0.6387
837.27	5.88E-03	0.9667	0.9295	0.8937	0.8268	0.7667	0.7121
838.13	9.69E-03	0.9443	0.9031	0.8642	0.792	0.7277	0.6708
839	1.71E-02	0.9511	0.9153	0.8811	0.8166	0.7568	0.7012
840.29	7.42E-03	0.9703	0.935	0.9011	0.8372	0.7776	0.7222
841.16	8.89E-03	0.9597	0.9229	0.8877	0.8216	0.7605	0.7038
842.02	8.75E-03	0.9573	0.9235	0.8912	0.8299	0.7727	0.7192
843.32	9.13E-03	0.952	0.9216	0.8922	0.8363	0.7836	0.734
844.18	4.38E-03	0.9415	0.9098	0.8793	0.8215	0.7675	0.7168
845.04	7.42E-03	0.9697	0.9395	0.9102	0.8542	0.8013	0.7512
846.34	1.63E-03	0.9649	0.9354	0.9067	0.8519	0.8002	0.7512
847.2	3.17E-03	0.9456	0.9176	0.8905	0.8383	0.7888	0.7418
848.06	7.11E-03	0.9419	0.9128	0.8846	0.8306	0.7796	0.7313
849.36	6.43E-03	0.9154	0.8871	0.8596	0.8072	0.7578	0.711
850.22	1.01E-02	0.8768	0.85	0.8239	0.774	0.7269	0.6822
851.08	6.00E-03	0.9307	0.9008	0.8719	0.8168	0.7648	0.7159
852.38	9.16E-03	0.9233	0.8943	0.8663	0.8128	0.7625	0.7149
853.24	1.29E-02	0.8871	0.8604	0.8346	0.7851	0.7382	0.6937
854.1	6.12E-03	0.7675	0.7436	0.7203	0.676	0.6343	0.5948
855.39	9.09E-03	0.8412	0.8164	0.7922	0.7459	0.702	0.6603
856.25	1.12E-02	0.9203	0.8926	0.8657	0.8142	0.7655	0.7193
857.12	6.97E-03	0.9395	0.9122	0.8856	0.8346	0.7862	0.7401
858.41	8.75E-03	0.9334	0.9058	0.8791	0.8278	0.7792	0.733
859.27	1.39E-02	0.9333	0.9065	0.8804	0.8302	0.7825	0.7372
860.13	7.76E-03	0.9345	0.9081	0.8824	0.8329	0.7858	0.7409
861.42	5.93E-03	0.9297	0.9034	0.8777	0.8283	0.7814	0.7366
862.28	1.02E-02	0.9441	0.9176	0.8918	0.8421	0.7948	0.7497
863.15	9.40E-03	0.9665	0.9394	0.913	0.8623	0.8139	0.7678
864.01	6.06E-03	0.9182	0.8926	0.8676	0.8196	0.7738	0.7302
865.3	4.35E-03	0.9101	0.8849	0.8603	0.813	0.7679	0.7248
866.16	4.31E-03	0.8184	0.7958	0.7737	0.7313	0.6908	0.6521
867.02	7.17E-03	0.8542	0.8306	0.8077	0.7635	0.7213	0.6811
868.31	5.63E-03	0.9295	0.904	0.8791	0.8312	0.7855	0.7418
869.17	4.85E-03	0.9103	0.8854	0.8611	0.8143	0.7697	0.7271
870.03	1.00E-02	0.9363	0.9107	0.8859	0.8379	0.7922	0.7485

871.32	1.09E-02	0.9237	0.8985	0.874	0.8268	0.7817	0.7386
872.18	9.01E-03	0.9204	0.8955	0.8711	0.8243	0.7795	0.7368
873.04	8.68E-03	0.9186	0.8938	0.8696	0.8229	0.7784	0.7358
874.33	3.64E-03	0.9078	0.8833	0.8595	0.8135	0.7695	0.7275
875.19	6.82E-03	0.8896	0.8656	0.8422	0.7971	0.7541	0.7129
876.05	1.28E-02	0.8991	0.8748	0.8511	0.8055	0.762	0.7203
877.34	1.28E-02	0.9081	0.8838	0.86	0.8141	0.7704	0.7285
878.19	1.45E-02	0.9185	0.8936	0.8694	0.8227	0.7782	0.7356
879.05	8.60E-03	0.9043	0.88	0.8563	0.8105	0.7668	0.725
880.34	5.24E-03	0.8851	0.8613	0.8381	0.7934	0.7508	0.71
881.2	6.51E-03	0.8729	0.8488	0.8254	0.7803	0.7374	0.6965
882.06	6.60E-03	0.8923	0.8674	0.8433	0.7968	0.7526	0.7104
883.35	1.01E-02	0.8942	0.87	0.8465	0.8011	0.7579	0.7166
884.2	9.35E-03	0.8905	0.8663	0.8426	0.7971	0.7537	0.7123
885.06	1.25E-02	0.8974	0.873	0.8492	0.8034	0.7596	0.7179
886.35	3.98E-03	0.8588	0.8333	0.8083	0.7606	0.7157	0.6737
887.21	8.26E-03	0.8654	0.8414	0.818	0.7731	0.7304	0.6898
888.07	6.28E-03	0.8803	0.8545	0.8296	0.7824	0.738	0.6959
889.35	1.14E-02	0.8869	0.8633	0.8403	0.796	0.7536	0.7131
890.21	1.00E-02	0.8835	0.8574	0.8322	0.784	0.7386	0.6956
891.07	1.30E-02	0.8801	0.8555	0.8316	0.7857	0.7422	0.7007
892.35	1.99E-03	0.8594	0.8325	0.8061	0.756	0.7093	0.6658
893.21	5.85E-03	0.8397	0.8085	0.7792	0.7256	0.6771	0.6326
894.07	8.65E-03	0.8224	0.7838	0.7483	0.6849	0.6292	0.5796
895.35	8.06E-03	0.7929	0.7453	0.7025	0.6283	0.5655	0.5114
896.21	8.17E-03	0.7563	0.7042	0.6603	0.5871	0.5261	0.4735
897.07	9.13E-03	0.6737	0.6113	0.5614	0.4827	0.4207	0.3694
898.35	1.03E-02	0.7206	0.6636	0.616	0.5376	0.4734	0.419
899.21	7.28E-03	0.5789	0.5126	0.4619	0.3851	0.3266	0.2796
900.06	4.06E-03	0.7243	0.6759	0.6348	0.5651	0.506	0.4543
901.35	5.67E-03	0.6046	0.5371	0.4842	0.4034	0.3422	0.2933
902.2	1.03E-02	0.6705	0.6203	0.5779	0.5062	0.4459	0.3937
903.06	6.93E-03	0.6891	0.6298	0.5805	0.4997	0.434	0.3788
904.34	5.58E-03	0.8171	0.779	0.7441	0.6814	0.6256	0.5751
905.2	7.80E-03	0.7967	0.7544	0.7168	0.6514	0.5949	0.5447
906.05	1.00E-02	0.7522	0.7078	0.6694	0.6038	0.5476	0.4981
907.34	7.96E-03	0.6458	0.5846	0.5349	0.4553	0.3919	0.3394
908.19	1.30E-02	0.6545	0.5949	0.547	0.4714	0.4117	0.3621
909.05	6.93E-03	0.6911	0.64	0.5968	0.5245	0.4644	0.4127
910.33	7.11E-03	0.6416	0.574	0.5202	0.4374	0.3741	0.3231
911.19	4.12E-03	0.6667	0.6071	0.5597	0.4864	0.4297	0.3831
912.04	1.13E-02	0.6886	0.633	0.5865	0.5104	0.4486	0.3965
913.32	8.82E-03	0.6526	0.5831	0.5279	0.4429	0.3782	0.3262

914.18	3.59E-03	0.6423	0.5768	0.525	0.4447	0.3832	0.3333
915.03	4.10E-03	0.6904	0.6247	0.5692	0.4801	0.4107	0.3548
916.31	7.18E-03	0.5974	0.5312	0.4803	0.4028	0.344	0.2967
917.17	1.24E-02	0.7207	0.6655	0.6175	0.5374	0.4723	0.4179
918.02	1.03E-02	0.6125	0.545	0.4921	0.411	0.3493	0.2997
919.3	7.65E-03	0.7274	0.6758	0.6313	0.5568	0.495	0.442
920.15	7.22E-03	0.7216	0.6787	0.6426	0.5823	0.5316	0.4869
921.01	1.21E-02	0.7449	0.7051	0.6688	0.6048	0.5493	0.5004
922.29	1.01E-02	0.6878	0.6361	0.5924	0.5212	0.4639	0.4157
923.14	9.90E-03	0.719	0.681	0.6468	0.5868	0.5349	0.4888
924	8.21E-03	0.7049	0.6525	0.6065	0.5292	0.466	0.4132
925.28	5.26E-03	0.6912	0.6385	0.5936	0.5192	0.4586	0.4074
926.13	1.08E-02	0.6976	0.6456	0.5996	0.5217	0.4578	0.4042
927.41	8.33E-03	0.7604	0.7174	0.677	0.6036	0.5392	0.483
928.26	7.94E-03	0.6177	0.5417	0.4806	0.3872	0.3183	0.2649
929.11	1.41E-02	0.5803	0.4986	0.4343	0.3391	0.2715	0.2208
930.39	1.16E-02	0.4728	0.3983	0.3343	0.2441	0.1827	0.1386
931.24	9.84E-03	0.4451	0.3765	0.3177	0.2319	0.1719	0.1283
932.52	6.99E-03	0.3481	0.2776	0.2214	0.1451	0.0969	0.06544
933.37	7.94E-03	0.305	0.2291	0.1763	0.1087	0.06876	0.04406
934.23	7.07E-03	0.2047	0.1329	0.08893	0.04173	0.0202	0.009929
935.08	9.68E-03	0.2987	0.2317	0.1836	0.1186	0.07781	0.05139
936.36	7.98E-03	0.2113	0.1493	0.1097	0.06185	0.03586	0.0211
937.21	1.16E-02	0.224	0.1519	0.1107	0.06218	0.03622	0.0215
938.06	1.12E-02	0.265	0.185	0.138	0.08073	0.04867	0.02977
939.34	7.26E-03	0.445	0.3652	0.3081	0.2247	0.1662	0.1239
940.19	1.06E-02	0.5136	0.4349	0.376	0.2871	0.2222	0.1731
941.04	9.36E-03	0.4156	0.3343	0.2768	0.1957	0.1411	0.1028
942.31	1.12E-02	0.46	0.3833	0.3248	0.2376	0.1758	0.1307
943.16	6.47E-03	0.3304	0.2569	0.2081	0.1406	0.09662	0.06699
944.02	5.85E-03	0.3273	0.2664	0.2246	0.1641	0.1217	0.09082
945.29	7.87E-03	0.4197	0.3438	0.287	0.2067	0.1518	0.1126
946.14	8.14E-03	0.247	0.1814	0.1386	0.08462	0.05308	0.03375
947.42	7.60E-03	0.4267	0.347	0.2864	0.202	0.1457	0.1062
948.27	7.43E-03	0.3239	0.256	0.2096	0.1465	0.1051	0.07626
949.12	1.01E-02	0.5455	0.4583	0.3908	0.2914	0.2219	0.1712
950.39	1.19E-02	0.2036	0.1372	0.09751	0.05344	0.03095	0.01848
951.24	4.09E-03	0.5278	0.4503	0.3863	0.2899	0.2205	0.1689
952.09	8.67E-03	0.3275	0.2503	0.1978	0.13	0.08853	0.06152
953.37	9.94E-03	0.393	0.3179	0.2621	0.1851	0.1341	0.09845
954.22	8.82E-03	0.4486	0.3838	0.3286	0.2467	0.1878	0.144
955.06	1.02E-02	0.3964	0.3208	0.2658	0.1893	0.1385	0.1029
956.34	8.77E-03	0.3752	0.3086	0.2633	0.2036	0.1638	0.1343

957.19	1.16E-02	0.3325	0.2516	0.1974	0.1289	0.08782	0.06133
958.04	1.07E-02	0.4819	0.4289	0.3827	0.311	0.2558	0.2114
959.31	8.67E-03	0.4114	0.3473	0.2957	0.2221	0.1707	0.1328
960.16	6.36E-03	0.4575	0.389	0.3314	0.249	0.1918	0.1498
961.01	8.57E-03	0.4959	0.4317	0.3787	0.2995	0.2414	0.1965
962.28	6.55E-03	0.4727	0.4092	0.3577	0.2824	0.2279	0.1861
963.13	8.33E-03	0.5274	0.4674	0.4181	0.3432	0.2866	0.2416
964.4	7.10E-03	0.4874	0.4297	0.3814	0.3095	0.2563	0.2144
965.25	8.82E-03	0.52	0.4653	0.4171	0.3417	0.2835	0.2366
966.09	7.10E-03	0.5312	0.4664	0.4158	0.3394	0.2824	0.2375
967.37	1.10E-02	0.5304	0.4649	0.4135	0.3354	0.277	0.2312
968.21	5.45E-03	0.6471	0.6084	0.5756	0.5202	0.4733	0.432
969.06	8.33E-03	0.6782	0.6367	0.599	0.5329	0.4766	0.4277
970.33	1.18E-02	0.6334	0.5868	0.5476	0.4831	0.4304	0.3855
971.18	3.77E-03	0.6971	0.6652	0.6362	0.5843	0.5384	0.4969
972.03	4.55E-03	0.6723	0.6377	0.6069	0.5523	0.5042	0.461
973.3	8.92E-03	0.613	0.5619	0.5191	0.4495	0.3935	0.3466
974.14	9.26E-03	0.587	0.5344	0.4917	0.4243	0.3716	0.328
975.41	6.33E-03	0.5979	0.5522	0.5141	0.4509	0.3987	0.3541
976.26	1.12E-02	0.5818	0.5278	0.483	0.4104	0.3525	0.3047
977.11	8.44E-03	0.6343	0.5938	0.5599	0.5038	0.4575	0.4174
978.38	8.28E-03	0.6142	0.5671	0.5277	0.4634	0.4112	0.367
979.22	1.15E-02	0.6337	0.5919	0.5557	0.4942	0.4426	0.3978
980.07	7.74E-03	0.6028	0.5579	0.5208	0.4603	0.4109	0.3687
981.34	7.43E-03	0.6922	0.6619	0.6338	0.5832	0.538	0.4972
982.18	9.93E-03	0.6716	0.6361	0.6044	0.5493	0.5023	0.4612
983.03	8.97E-03	0.651	0.6114	0.5768	0.5181	0.4691	0.4268
984.3	1.07E-02	0.7029	0.6796	0.6574	0.6158	0.5774	0.5417
985.14	1.20E-02	0.6687	0.6331	0.6007	0.5437	0.4946	0.4515
986.41	6.94E-03	0.7092	0.6901	0.6715	0.6361	0.6025	0.5706
987.25	6.34E-03	0.7014	0.6784	0.6557	0.6133	0.5766	0.5436
988.1	1.36E-02	0.7006	0.6772	0.6547	0.6132	0.577	0.5451
989.37	8.51E-03	0.7035	0.6872	0.6713	0.6406	0.6111	0.5826
990.21	8.45E-03	0.6954	0.6732	0.6509	0.6093	0.5732	0.5404
991.06	7.19E-03	0.7064	0.6896	0.6733	0.6417	0.6115	0.5825
992.32	8.70E-03	0.7099	0.6935	0.6775	0.6466	0.6169	0.5883
993.17	1.22E-02	0.7004	0.6799	0.6598	0.622	0.5882	0.5576
994.01	7.80E-03	0.7091	0.6933	0.6778	0.6479	0.619	0.5912
995.28	1.00E-02	0.7074	0.6923	0.6775	0.6487	0.621	0.5941
996.12	6.62E-03	0.7053	0.6895	0.6741	0.6444	0.6157	0.5881
997.39	8.09E-03	0.7059	0.6905	0.6754	0.6462	0.6181	0.5909
998.23	7.58E-03	0.703	0.6874	0.6722	0.6427	0.6143	0.5869
999.07	8.21E-03	0.7002	0.6849	0.67	0.641	0.613	0.586

1000.34	1.23E-02	0.6968	0.6806	0.6647	0.6341	0.6048	0.5767
1001.18	1.05E-02	0.7039	0.6887	0.6738	0.645	0.6171	0.5902
1002.03	1.07E-02	0.691	0.6714	0.6527	0.6169	0.5832	0.5512
1003.29	8.21E-03	0.6919	0.6768	0.6619	0.6332	0.6056	0.5789
1004.13	7.81E-03	0.6767	0.6607	0.6451	0.6151	0.5863	0.5587
1005.4	4.00E-03	0.6497	0.636	0.6226	0.5965	0.5712	0.5467
1006.24	1.01E-02	0.6763	0.6612	0.6465	0.6181	0.5908	0.5645
1007.08	7.14E-03	0.69	0.6751	0.6606	0.6322	0.6049	0.5785
1008.35	1.02E-02	0.6875	0.6719	0.6566	0.6271	0.5989	0.5717
1009.19	7.26E-03	0.6852	0.6687	0.6526	0.6218	0.5925	0.5644
1010.03	7.26E-03	0.683	0.6661	0.6497	0.6183	0.5884	0.56
1011.29	7.32E-03	0.6866	0.672	0.6576	0.6298	0.6029	0.5769
1012.13	1.28E-02	0.6819	0.6665	0.6515	0.6225	0.5948	0.5681
1013.4	9.02E-03	0.6847	0.6704	0.6564	0.6292	0.6028	0.5773
1014.24	3.48E-03	0.6799	0.6658	0.6519	0.6248	0.5987	0.5734
1015.08	7.44E-03	0.6757	0.6615	0.6476	0.6205	0.5944	0.5692
1016.34	8.20E-03	0.6728	0.6586	0.6447	0.6177	0.5916	0.5663
1017.18	1.29E-02	0.6748	0.6604	0.6463	0.6189	0.5925	0.5669
1018.02	1.17E-02	0.6716	0.6578	0.6443	0.618	0.5926	0.5679
1019.29	1.03E-02	0.6597	0.6445	0.6296	0.601	0.5735	0.5471
1020.13	7.21E-03	0.6685	0.6546	0.6409	0.6144	0.5888	0.5639
1021.39	1.03E-02	0.6672	0.6536	0.6403	0.6144	0.5893	0.565
1022.23	7.83E-03	0.6629	0.6489	0.6351	0.6083	0.5824	0.5574
1023.07	8.62E-03	0.6702	0.6558	0.6418	0.6146	0.5885	0.5632
1024.33	7.14E-03	0.664	0.648	0.6325	0.6027	0.5743	0.5471
1025.17	9.65E-03	0.669	0.6553	0.6419	0.6158	0.5906	0.5661
1026.01	7.96E-03	0.6668	0.6527	0.639	0.6123	0.5864	0.5614
1027.27	1.06E-02	0.6652	0.6513	0.6376	0.6112	0.5857	0.5609
1028.11	7.41E-03	0.664	0.65	0.6363	0.6097	0.584	0.5592
1029.37	4.67E-03	0.6564	0.6425	0.6288	0.6022	0.5766	0.5517
1030.21	1.00E-02	0.6601	0.6467	0.6335	0.6079	0.5831	0.559
1031.05	1.09E-02	0.6579	0.6443	0.6309	0.605	0.58	0.5557
1032.3	1.00E-02	0.6557	0.6424	0.6293	0.6038	0.5792	0.5552
1033.14	1.01E-02	0.6459	0.6328	0.6199	0.5948	0.5705	0.5469
1034.4	9.52E-03	0.6459	0.6329	0.6201	0.5951	0.5709	0.5474
1035.66	1.02E-02	0.648	0.6349	0.6221	0.5971	0.5728	0.5493
1036.08	1.45E-02	0.6517	0.6383	0.6252	0.5998	0.5751	0.5512
1037.34	1.24E-02	0.6408	0.6277	0.6148	0.5898	0.5655	0.542
1038.18	1.14E-02	0.6439	0.6308	0.6179	0.5927	0.5684	0.5448
1039.01	9.71E-03	0.6437	0.6305	0.6175	0.5922	0.5677	0.544
1040.27	1.25E-02	0.6412	0.628	0.6151	0.5898	0.5654	0.5417
1041.11	1.24E-02	0.6441	0.6307	0.6176	0.592	0.5673	0.5434
1042.37	8.00E-03	0.6397	0.6264	0.6134	0.588	0.5635	0.5397

1043.2	7.00E-03	0.6378	0.6245	0.6115	0.5861	0.5616	0.5378
1044.04	9.71E-03	0.6402	0.6268	0.6137	0.588	0.5633	0.5393
1045.3	9.00E-03	0.6317	0.6184	0.6054	0.58	0.5554	0.5316
1046.13	1.00E-02	0.625	0.6117	0.5987	0.5734	0.549	0.5253
1047.39	8.25E-03	0.6308	0.6173	0.6041	0.5784	0.5535	0.5295
1048.23	9.28E-03	0.6345	0.6208	0.6074	0.5813	0.5562	0.5318
1049.06	8.08E-03	0.6321	0.6182	0.6046	0.5782	0.5527	0.528
1050.32	1.01E-02	0.6293	0.6153	0.6016	0.575	0.5493	0.5245
1051.16	9.38E-03	0.6291	0.615	0.6013	0.5747	0.549	0.5242
1052.41	1.24E-02	0.6266	0.6125	0.5986	0.5717	0.5458	0.5208
1053.25	1.01E-02	0.622	0.6078	0.5939	0.5669	0.5409	0.5159
1054.08	9.38E-03	0.6238	0.6094	0.5953	0.568	0.5417	0.5164
1055.34	1.16E-02	0.6246	0.61	0.5956	0.5679	0.5412	0.5156
1056.17	1.16E-02	0.6229	0.608	0.5935	0.5654	0.5384	0.5124
1057.01	1.53E-02	0.6213	0.6063	0.5916	0.5632	0.536	0.5098
1058.26	1.16E-02	0.6064	0.5916	0.577	0.549	0.5221	0.4962
1059.1	1.62E-02	0.6075	0.5924	0.5776	0.549	0.5216	0.4954
1060.35	1.35E-02	0.6068	0.5915	0.5767	0.5479	0.5204	0.494
1061.19	1.17E-02	0.6063	0.591	0.5759	0.547	0.5193	0.4927
1062.02	6.45E-03	0.6099	0.5942	0.5789	0.5493	0.521	0.494
1063.27	1.06E-02	0.6042	0.5884	0.573	0.5434	0.5151	0.488
1064.11	1.17E-02	0.6112	0.5954	0.5799	0.55	0.5215	0.4942
1065.36	1.00E-02	0.6078	0.5915	0.5755	0.5448	0.5155	0.4876
1066.2	8.79E-03	0.5951	0.5796	0.5645	0.5353	0.5074	0.4807
1067.03	6.74E-03	0.6033	0.5872	0.5717	0.5419	0.5134	0.4862
1068.28	8.99E-03	0.5906	0.5746	0.5591	0.5291	0.5006	0.4734
1069.12	1.11E-02	0.572	0.5568	0.5421	0.5138	0.4868	0.4611
1070.37	9.20E-03	0.5921	0.576	0.5603	0.5303	0.5019	0.4749
1071.2	9.30E-03	0.5992	0.5844	0.57	0.5422	0.5156	0.49
1072.03	9.52E-03	0.594	0.5782	0.5628	0.5333	0.5054	0.4787
1073.29	1.16E-02	0.5853	0.5698	0.5549	0.5263	0.4991	0.4731
1074.12	1.38E-02	0.5978	0.5839	0.5704	0.5441	0.5188	0.4945
1075.37	1.28E-02	0.5747	0.5565	0.539	0.5065	0.4774	0.4513
1076.2	1.29E-02	0.5978	0.5837	0.5699	0.5432	0.5177	0.4932
1077.04	1.07E-02	0.5911	0.5743	0.5581	0.5279	0.5	0.4743
1078.28	1.31E-02	0.5813	0.5638	0.547	0.5151	0.4861	0.4595
1079.12	1.08E-02	0.5873	0.5742	0.5615	0.5367	0.5129	0.49
1080.37	1.00E-02	0.5823	0.5656	0.5498	0.5202	0.4926	0.4666
1081.2	9.88E-03	0.5667	0.5483	0.5308	0.4982	0.4686	0.4418
1082.03	1.13E-02	0.57	0.5557	0.5418	0.5153	0.49	0.466
1083.28	7.69E-03	0.5704	0.5571	0.5442	0.5194	0.4957	0.473
1084.11	1.00E-02	0.5675	0.5476	0.529	0.4953	0.4649	0.4371
1085.36	1.01E-02	0.5829	0.5669	0.5516	0.5226	0.4955	0.4699
1086.19	1.25E-02	0.5438	0.5201	0.4993	0.4632	0.4318	0.4036
1087.02	1.14E-02	0.5523	0.5349	0.5184	0.4874	0.459	0.4332

Bibliography

[1] A. Kribus, Y. Gray, M. Grijnevich, G. Mittelman, S. Mey-Cloutier, and C. Caliot. The promise abd challenge of volumetric recievers. *Solar energy*, 110(110):463–481, September 2014. URL http://link.aip.org/link/?RSI/69/1236/1.

[2] L. F. Cabeza, C. Sole, A. Castell, E. Oro, and A. Gil. Review of solar thermal storage techniques and associated heat transfer technologies. *Proceedings of the Ieee*, 100(2):525–538, 2012. ISSN 0018-9219. doi: 10.1109/jproc.2011.2157883. URL <GotoISI>://WOS:000299429700018. Times Cited: 0.

[3] R. I. Dunn, P. J. Hearps, and M. N. Wright. Molten-salt power towers: Newly commercial concentrating solar storage. *Proceedings of the Ieee*, 100(2):504–515, 2012. ISSN 0018-9219. doi: 10.1109/JPROC.2011.2163739. Cited References Count:36—880TG—IEEE-INST ELECTRICAL ELECTRONICS ENGINEERS INC—445 HOES LANE, PISCATAWAY, NJ 08855-4141 USA—Dunn, Rebecca I.—Hearps, Patrick J.—Wright, Matthew N.—ISI Document Delivery No.:880TG.

[4] A. Lenert and E. N. Wang. Optimization of nanofluid volumetric receivers for solar thermal energy conversion. *Solar Energy*, 86(1):253–265, 2012. ISSN 0038-092X. doi: 10.1016/j.solener.2011.09.029. URL http://www.sciencedirect.com/science/article/pii/S0038092X11003550.

[5] N. Boerema, G. Morrison, R. Taylor, and G. Rosengarten. Liquid sodium versus hitec as a heat transfer fluid in solar thermal central receiver systems. *Solar Energy*, 86(9):2293–2305, 2012. ISSN 0038-092X. doi: 10.1016/j.solener.2012.05.001. URL <GotoISI>://WOS:000309079800007. Boerema, Nicholas Morrison, Graham Taylor, Robert Rosengarten, Gary.

[6] J. Hinkley, B. Curtin, J. Hayward, R. Wonhas, A.and Boyd, C. Grima, A. Tadros, R. Hall, K. Naicker, and A. Mikhail. Concentrating solar power–drivers and opportunities for cost-competitive electricity. *Clayton South: CSIRO*, 2011.

[7] R. Pitz-Paal, A. Amin, M.O. Bettzuge, P. Eames, G. Flamant, F. Fabrizi, J. Holmes, A. Kribus, van der L. H., F. Lopez, C.and Garcia Novo, P. Papagiannakopoulos, E. Pihl, P. Smith, and H. Wagner. Concentrating solar power in europe, the middle east and north africa: A review of development issues and potential to 2050. *Journal of Solar Energy Engineering-Transactions of the Asme*, 134(2), 2012. ISSN 0199-6231. doi: 02450110.1115/1.4006390. URL <GotoISI>://WOS:000302579400014. Times Cited: 0.

[8] M. A. Al-Nimr, B. Khuwaileh, and M. Alata. A novel integrated direct absorption self-storage solar collector. *International journal of green energy*, 8(6):618–630, 2011.

[9] R. A. Taylor, P. E. Phelan, R. J. Adrian, A. Gunawan, and T. P. Otanicar. Characterization of light-induced, volumetric steam generation in nanofluids. *International Journal of Thermal Sciences*, 56(0):1–11, 2012. ISSN 1290-0729. doi: 10.1016/j.ijthermalsci.2012.01.012. URL http://www.sciencedirect.com/science/article/pii/S1290072912000269.

[10] A. Ghobeity and A. Mitsos. Optimal design and operation of a solar energy receiver and storage. *Journal of Solar Energy Engineering-Transactions of the Asme*, 134 (3), 2012. ISSN 0199-6231. doi: 10.1115/1.4006402. URL <GotoISI>://WOS:000306141800005. Ghobeity, Amin Mitsos, Alexander.

[11] J. Rawlins and M. Ashcroft. Small-scale concentrated solar power: A review of current activity and potential to accelerate deployment. Report, Carbon Trust,UK, 2013.

[12] M. Wells and T. O'Donovan. Modular solar collector with storage. Report, UK Astronomy Technology Centre and Heriot-Watt University, 2013.

[13] I. Dincer and M. Rosen. *Thermal energy storage: systems and applications*. John Wiley and Sons, 2006. ISBN 0471495735.

[14] K. Heinloth and P. Freund. *Energy technologies, Renewable energy*, book section 4.1 Solar, pages 242–279. Landolt-Bornstein.,Numerical data and functional relationships in science and technology., Group VIII,, Advanced materials and technologies. Springer, Verlag, 2006.

[15] M. Thirugnanasambandam, S. Iniyan, and R. Goic. A review of solar thermal technologies. *Renewable and Sustainable Energy Reviews*, 14(1):312–322, 2010. ISSN 1364-0321. doi: 10.1016/j.rser.2009.07.014. Cited References

Count:185—512VJ—PERGAMON-ELSEVIER SCIENCE LTD—THE BOULEVARD, LANGFORD LANE, KIDLINGTON, OXFORD OX5 1GB, ENGLAND—Thirugnanasambandam, Mirunalini—Iniyan, S.—Goic, Ranko—ISI Document Delivery No.:512VJ.

[16] M. Becker, K. H. Funken, and Raumfahrt Deutsche Forschungsanstalt fur Luft- und. *Solar thermal energy utilization : German studies on technology and application*. Springer, Berlin ; London, 1991. ISBN 3540532684. v.4 Final reports 1988 (Manfred) At head of title: Deutsche Forschungsanstalt fur Luft- und Raumfahrt E.V. (DLR).

[17] C. K. Ho and B. D Iverson. Review of high-temperature central receiver designs for concentrating solar power. *Renewable and Sustainable Energy Reviews*, 29: 835–846, 2014. ISSN 1364-0321.

[18] D. Barlev, R. Vidu, and P. Stroeve. Innovation in concentrated solar power. *Solar Energy Materials and Solar Cells*, 95(10):2703–2725, 2011. ISSN 0927-0248. doi: 10.1016/j.solmat.2011.05.020. Cited References Count:108—ELSEVIER SCIENCE BV—PO BOX 211, 1000 AE AMSTERDAM, NETHERLANDS—ISI Document Delivery No.:807XM.

[19] D. Codd. *Concentrated solar power on Demand*. Thesis, 2011.

[20] J. A. Duffie and W. A. Beckman. *Solar engineering of thermal processes*, volume 3. Wiley New York etc., 1980.

[21] S. K Osman and B. S Yilbas. Solar absorption heating in horizontal channel: Influence of absorbing plate location on thermal performance. *Energy Conversion and Management*, 74:140–148, 2013. ISSN 0196-8904.

[22] O. K. Siddiqui and B. S. Yilbas. Thermal characteristics of a volumetric solar absorption system. *International Journal of Energy Research*, 38(5):581–591, 2014.

[23] G. Hadi, N. George, M. Amy Marie, L. James, Y. Selcuk, M. Nenad, and C. Gang. Solar steam generation by heat localization. *Nature communications*, 5, 2014.

[24] A. L. Avila-Marin. Volumetric receivers in solar thermal power plants with central receiver system technology: A review. *Solar Energy*, 85(5):891–910, 2011. ISSN 0038-092X. doi: 10.1016/j.solener.2011.02.002. URL <GotoISI>://WOS:000290644000019. Times Cited: 0.

[25] M. S. Bohn. Experimental investigation of the direct absorption receiver concept. *Energy*, 12(3-4), 1987. ISSN 0360-5442. doi: 10.1016/0360-5442(87)90081-8. URL <GotoISI>://WOS:A1987H714300008. Times Cited: 3.

[26] M. S. Bohn and K. Y. Wang. Experiments and analysis on the molten salt direct absorption receiver concept. *Journal of solar energy engineering*, 110(1):45–51, 1988. ISSN 0199-6231.

[27] M. S. Bohn and H. J. Green. Heat-transfer in molten-salt direct absorption receivers. *Solar Energy*, 42(1):57–66, 1989. ISSN 0038-092X. doi: 10.1016/0038-092x(89)90130-8. URL <GotoISI>://WOS:A1989T164500007. BOHN, MS GREEN, HJ.

[28] G. Jorgensen, P. Schissel, and R. Burrows. Optical-properties of high-temperature materials for direct absorption receivers. *Solar Energy Materials*, 14(3-5), 1986. ISSN 0165-1633. doi: 10.1016/0165-1633(86)90061-4. URL <GotoISI>://WOS:A1986E640900020. Times Cited: 1.

[29] S. Passerini. *Optical and Chemical Properties of Molten Salts Mixtures for Use in High Temperature Power Systemsystems*. Thesis, 2010.

[30] Council European Academies Science Advisory. *Concentrating solar power : its potential contribution to a sustainable energy future*. EASAC policy report. EASAC Secretariat, Halle (Saale), 2011. ISBN 9783804729445 (pbk.). ill. ; 30 cm. "November 2011"–Cover. Includes bibliographical references (p. 47-50).

[31] J. T. Van Lew, P. W. Li, C. L. Chan, W. Karaki, and J. Stephens. Analysis of heat storage and delivery of a thermocline tank having solid filler material. *Journal of Solar Energy Engineering-Transactions of the Asme*, 133(2), 2011. ISSN 0199-6231. doi: 10.1115/1.4003685. URL <GotoISI>://WOS:000289487500003. Van Lew, Jon T. Li, Peiwen Chan, Cho Lik Karaki, Wafaa Stephens, Jake.

[32] A. H. Slocum, D. S. Codd, J. Buongiorno, C. Forsberg, T. McKrell, J. C. Nave, C. N. Papanicolas, A. Ghobeity, C. J. Noone, S. Passerini, F. Rojas, and A. Mitsos. Concentrated solar power on demand. *Solar Energy*, 85(7):1519–1529, 2011. ISSN 0038-092X. doi: 10.1016/j.solener.2011.04.010. Cited References Count:46—PERGAMON-ELSEVIER SCIENCE LTD—THE BOULEVARD, LANGFORD LANE, KIDLINGTON, OXFORD OX5 1GB, ENGLAND—Slocum, Alexander H.—Codd, Daniel S.—Buongiorno, Jacopo—Forsberg, Charles—McKrell, Thomas—Nave, Jean-Christophe—Papanicolas, Costas N.—Ghobeity, Amin—Noone, Corey J.—Passerini, Stefano—Rojas, Folkers—Mitsos, Alexander—ISI Document Delivery No.:788LD.

[33] H. Hasuike, Y. Yoshizawa, A. Suzuki, and Y. Tamaura. Study on design of molten salt solar receivers for beam-down solar concentrator. *Solar Energy*, 80 (10):1255–1262, 2006. ISSN 0038-092X. doi: 10.1016/j.solener.2006.03.002|10.

1016/j.solener.2006.03.002. Cited References Count:6—PERGAMON-ELSEVIER SCIENCE LTD—THE BOULEVARD, LANGFORD LANE, KIDLINGTON, OXFORD OX5 1GB, ENGLAND—Hasuike, Hiroshi—Yoshizawa, Yoshio—Suzuki, Akio—Tamaura, Yutaka—ISI Document Delivery No.:112GH.

[34] P. W. Li, J. Van Lew, W. Karaki, C. Chan, J. Stephens, and Q. W. Wang. Generalized charts of energy storage effectiveness for thermocline heat storage tank design and calibration. *Solar Energy*, 85(9):2130–2143, 2011. ISSN 0038-092X. doi: 10.1016/j.solener.2011.05.022. URL <GotoISI>://WOS:000295233600041. Li, Peiwen Van Lew, Jon Karaki, Wafaa Chan, Cholik Stephens, Jake Wang, Qiuwang.

[35] R. Gabbrielli and C. Zamparelli. Optimal design of a molten salt thermal storage tank for parabolic trough solar power plants. *Journal of Solar Energy Engineering-Transactions of the Asme*, 131(4), 2009. ISSN 0199-6231. doi: 10.1115/1.3197585. URL <GotoISI>://WOS:000271021000002. Gabbrielli, R. Zamparelli, C.

[36] Z. Yang and S. V. Garimella. Thermal analysis of solar thermal energy storage in a molten-salt thermocline. *Solar Energy*, 84(6):974–985, 2010. ISSN 0038-092X. doi: 10.1016/j.solener.2010.03.007. URL <GotoISI>://WOS:000278235200011. Yang, Zhen Garimella, Suresh V.

[37] C. Mira-Hernández, S. M. Flueckiger, and S. V. Garimella. Comparative analysis of single-and dual-media thermocline tanks for thermal energy storage in concentrating solar power plants. *Journal of Solar Energy Engineering*, 137(3):031012, 2015.

[38] S. Flueckiger, Z. Yang, and S. V. Garimella. An integrated thermal and mechanical investigation of molten-salt thermocline energy storage. *Applied Energy*, 88(6): 2098–2105, 2011. ISSN 0306-2619. doi: 10.1016/j.apenergy.2010.12.031. URL <GotoISI>://WOS:000288406000012. Flueckiger, Scott Yang, Zhen Garimella, Suresh V.

[39] S. M. Flueckiger and S. V. Garimella. Second-law analysis of molten-salt thermal energy storage in thermoclines. *Solar Energy*, 86(5):1621–1631, 2012. ISSN 0038-092X. doi: 10.1016/j.solener.2012.02.028. URL <GotoISI>://WOS:000303304900050. Flueckiger, Scott M. Garimella, Suresh V.

[40] D. S. Codd and A. H. Slocum. Direct absorption volumetric molten salt receiver with integral storage. *ASME Conference Proceedings*, 2011(54686):511–521, 2011. URL http://dx.doi.org/10.1115/ES2011-54175.

[41] J. Van Berkel, C. C. M. Rindt, and A. A. Van Steenhoven. Thermocline dynamics in a thermally stratified store. *International journal of heat and mass transfer*, 45 (2):343–356, 2002.

[42] Y. H. Zurigat, P. R. Liche, and A. J Ghajar. Influence of inlet geometry on mixing in thermocline thermal energy storage. *International Journal of Heat and Mass Transfer*, 34(1):115–125, 1991.

[43] S. M. Flueckiger, Z. Yang, and S. V. Garimella. Review of molten-salt thermocline tank modeling for solar thermal energy storage. *Heat Transfer Engineering*, 34(10): 787–800, 2013.

[44] A. Pizzolato, F. Donato, V. Verda, and M. Santarelli. Cfd-based reduced model for the simulation of thermocline thermal energy storage systems. *Applied Thermal Engineering*, 76:391–399, 2015.

[45] Z. S. Chang, X. Li, C. Xu, C. Chang, and Z. F. Wang. The design and numerical study of a 2mwh molten salt thermocline tank. *Energy Procedia*, 69:779–789, 2015.

[46] R.J. Copeland and J. Green. *Raft thermocline thermal storage*, pages Medium: X; Size: Pages: 1801–1805. 1983. ISBN CONF-830812-; Journal ID: CODEN: PIECD United StatesJournal ID: CODEN: PIECDWed Feb 06 20:51:25 EST 2008EDB-84-021723English.

[47] A. Ghobeity, C. J. Noone, C. N. Papanicolas, and A. Mitsos. Optimal time-invariant operation of a power and water cogeneration solar-thermal plant. *Solar Energy*, 85(9):2295–2320, 2011. ISSN 0038-092X. doi: 10.1016/j.solener.2011.06.023. URL http://www.sciencedirect.com/science/article/pii/S0038092X11002350.

[48] G. J. Janz. *Molten salts handbook / by George J. Janz.* Academic P., 1967., 1967. URL http://search.ebscohost.com/login.aspx?direct=true&db=cat00289a&AN=hwu.125690&site=eds-live. Riccarton - Standard loan 546.34 JAN Accession Number: hwu.125690; Publication Type: Book; Language: English.

[49] R. Serrano-López, J. Fradera, and S. Cuesta-López. Molten salts database for energy applications. *Chemical Engineering and Processing: Process Intensification*, 73:87–102, 2013.

[50] S. M. Sohal, A. M. Ebner, P. Sabharwall, and P. Sharpe. Engineering database of liquid salt thermophysical and thermochemical properties. Report, Idaho National Laboratory, 2010.

[51] LLC. Coastal Chemical Co. Hitec heat transfer salt technical bulletin, coastal chemical co., llc.

[52] A. Sharma, V.V. Tyagi, C.R. Chen, and D. Buddhi. Review on thermal energy storage with phase change materials and applications. *Renewable and Sustainable Energy Reviews*, 13(2):318 – 345, 2009. ISSN 1364-0321. doi: http://dx.doi.org/10.1016/j.rser.2007.10.005. URL http://www.sciencedirect.com/science/article/pii/S1364032107001402.

[53] N. Pfleger, T. Bauer, C. Martin, M. Eck, and A. Wörner. Thermal energy storage – overview and specific insight into nitrate salts for sensible and latent heat storage. *Beilstein Journal of Nanotechnology*, 6:1487–1497, 2015. ISSN 2190-4286. doi: 10.3762/bjnano.6.154.

[54] Q. Peng, X. Wei, J. Ding, J. Yang, and X. Yang. High temperature thermal stability of molten salt materials. *International Journal of Energy Research*, 32 (12):1164–1174, 2008. ISSN 1099-114X.

[55] Q. Peng, J. Ding, X. Wei, J. Yang, and X. Yang. The preparation and properties of multi component molten salts. *Applied Energy*, 87(9):2812–2817, 2010. ISSN 0306-2619.

[56] R. I. Olivares. The thermal stability of molten nitrite/nitrates salt for solar thermal energy storage in different atmospheres. *Solar Energy*, 86(9):2576–2583, 2012. ISSN 0038-092X. doi: 10.1016/j.solener.2012.05.025. URL <GotoISI>://WOS:000309079800031. Olivares, Rene I.

[57] W. D. Drotning. Optical properties of solar absorbing oxide particles suspended in a molten salt heat transfer fluid. *Solar Energy*, 20(4), 1978. ISSN 0038-092X. doi: 10.1016/0038-092x(78)90123-8. URL <GotoISI>://WOS:A1978EW74000003. Times Cited: 14.

[58] M. Corcione. *Natural Convection in Nanofluids*, book section Chapter 10, pages 277–319. CRC Press, 2013.

[59] J. C. Gomez, N.and S. Calvet, Anne K., and G. C. Glatzmaier. Ca (no3)2 nano3 kno3 molten salt mixtures for direct thermal energy storage systems in parabolic trough plants. *Journal of Solar Energy Engineering*, 135(2):021016, 2013. ISSN 0199-6231.

[60] D. Mantha, T. Wang, and R. G. Reddy. Thermodynamic modeling of eutectic point in the lino3-nano3-kno3 ternary system. *Journal of phase equilibria and diffusion*, 33(2):110–114, 2012.

[61] D. Mantha, T. Wang, and R. G. Reddy. Thermodynamic modeling of eutectic point in the lino 3–nano 3–kno 3–nano 2 quaternary system. *Solar Energy Materials and Solar Cells*, 118:18–21, 2013.

[62] T. Wang, D. Mantha, and R. G. Reddy. *High Thermal Energy Storage Density LiNO3-NaNO3-KNO3-KNO2 Quaternary Molten Salts for Parabolic Trough Solar Power Generation*, pages 73–84. John Wiley and Sons, Inc., 2012. ISBN 9781118365038. doi: 10.1002/9781118365038.ch10. URL http://dx.doi.org/10.1002/9781118365038.ch10.

[63] T. P. Otanicar, P. E. Phelan, and J. S. Golden. Optical properties of liquids for direct absorption solar thermal energy systems. *Solar Energy*, 83(7):969–977, 2009. ISSN 0038-092X. doi: 10.1016/j.solener.2008.12.009. URL http://www.sciencedirect.com/science/article/pii/S0038092X08003496.

[64] R. Viskanta and J. S. Toor. Absorption of solar radiation in ponds. *Solar Energy*, 21(1):17–25, 1978. ISSN 0038-092X.

[65] Y. A. Cengel and M. N. Ozişik. Solar radiation absorption in solar ponds. *Solar Energy*, 33(6):581–591, 1984. ISSN 0038-092X.

[66] T. Hattori, J. C. Patterson, and C. Lei. Study of unsteady natural convection induced by absorption of radiation based on a three-waveband attenuation model. In *Journal of Physics: Conference Series*, volume 530, page 012036. IOP Publishing. ISBN 1742-6596.

[67] W. Hongbo, T. Runsheng, L. Zhimin, and Z. Hao. A mathematical procedure to estimate solar absorptance of shallow water ponds. *Energy Conversion and Management*, 50(7):1828–1833, 2009. ISSN 0196-8904.

[68] B. W. Webb and R. Viskanta. Analysis of heat transfer and solar radiation absorption in an irradiated thin, falling molten salt film. *Journal of solar energy engineering*, 107(2):113–119, 1985.

[69] C. A. Gueymard, D. Myers, and K. Emery. Proposed reference irradiance spectra for solar energy systems testing. *Solar energy*, 73(6):443–467, 2002. ISSN 0038-092X.

[70] C. A. Gueymard. The sun's total and spectral irradiance for solar energy applications and solar radiation models. *Solar energy*, 76(4):423–453, 2004. ISSN 0038-092X.

[71] D. R. Myers and C. A. Gueymard. Description and availability of the smarts spectral model for photovoltaic applications. In *Optical Science and Technology,*

the SPIE 49th Annual Meeting, pages 56–67. International Society for Optics and Photonics, 2004.

[72] C. Gueymard. *SMARTS2: a simple model of the atmospheric radiative transfer of sunshine: algorithms and performance assessment*. Florida Solar Energy Center Cocoa, FL, 1995.

[73] D. R. Myers. Solar radiation modeling and measurements for renewable energy applications: data and model quality. *Energy*, 30(9):1517–1531, 2005.

[74] C. A. Gueymard. Direct solar transmittance and irradiance predictions with broadband models. part i: detailed theoretical performance assessment. *Solar Energy*, 74(5):355–379, 2003.

[75] C. A. Gueymard. Direct solar transmittance and irradiance predictions with broadband models. part ii: validation with high-quality measurements. *Solar Energy*, 74(5):381–395, 2003.

[76] AM NREL. 1.5 gobal solar spectrum derived from smarts v. 2.9. 2.

[77] D. T. Reindl, W. A. Beckman, and J. W. Mitchell. Transient natural convection in enclosures with application to solar thermal storage tanks. *Journal of solar energy engineering*, 114(3):175–181, 1992.

[78] F. P. Incropera and D. P DeWitt. *Fundamentals of heat and mass transfer*. John Wiley and Sons, 4th edition, 1996.

[79] S. Ostrach. Natural convection in enclosures. *Journal of Heat Transfer*, 110(4b): 1175–1190, 1988. ISSN 0022-1481.

[80] P. G. Drazin and W. Reid. *Hydrodynamic stability*. Cambridge university press, 2004. ISBN 0521525411.

[81] R. Viskanta. Radiation induced buoyancy-driven flow in rectangular enclosures experiment and analysis. *J. Heat Trans.-T. ASME*, 109:427–433, 1987.

[82] B. W. Webb and R. Viskanta. Analysis of radiation-induced natural convection in rectangular enclosures. *Journal of Thermophysics and Heat Transfer*, 1(2): 146–153, 1987. ISSN 0887-8722.

[83] C. Lei and J. C. Patterson. Natural convection in a reservoir sidearm subject to solar radiation: a two-dimensional simulation. *Numerical Heat Transfer: Part A: Applications*, 42(1-2):13–32, 2002. ISSN 1040-7782.

[84] C. Lei and J. C. Patterson. Natural convection in a reservoir sidearm subject to solar radiation: experimental observations. *Experiments in Fluids*, 32(5):590–599, 2002. ISSN 0723-4864.

[85] C. W. Lei and J. C. Patterson. Unsteady natural convection in a triangular enclosure induced by absorption of radiation. *Journal of Fluid Mechanics*, 460, 2002. ISSN 0022-1120. doi: 10.1017/s0022112002008091. URL <GotoISI>://WOS:000176602500009. Times Cited: 40.

[86] J. C. Lei, C.and Patterson. A direct stability analysis of a radiation-induced natural convection boundary layer in a shallow wedge. *Journal of Fluid Mechanics*, 480:161–184, 2003. ISSN 1469-7645.

[87] J. C Lei, C.and Patterson. Unsteady natural convection in a triangular enclosure induced by surface cooling. *International Journal of Heat and Fluid Flow*, 26(2): 307–321, 2005.

[88] Y. Mao, C. Lei, and J. C. Patterson. Unsteady natural convection in a triangular enclosure induced by absorption of radiation - a revisit by improved scaling analysis. *Journal of Fluid Mechanics*, 622, 2009. ISSN 0022-1120. doi: 10.1017/s0022112008005077. URL <GotoISI>://WOS:000264384800005. Times Cited: 7.

[89] Y. Mao, C. Lei, and J. C. Patterson. Characteristics of instability of radiation-induced natural convection in shallow littoral waters. *International Journal of Thermal Sciences*, 49(1):170–181, 2010. ISSN 1290-0729. doi: http://dx.doi.org/10.1016/j.ijthermalsci.2009.07.004. URL http://www.sciencedirect.com/science/article/pii/S1290072909001549.

[90] C. Lei and J. C. Patterson. A direct three-dimensional simulation of radiation-induced natural convection in a shallow wedge. *International Journal of Heat and Mass Transfer*, 46:161–184, 2003. ISSN 1183–1197.

[91] T. Hattori, J. C Patterson, and C. Lei. Mixing in internally heated natural convection flow and scaling for a quasi-steady boundary layer. *Journal of Fluid Mechanics*, 763:352–368, 2015.

[92] T. Hattori, J. C. Patterson, and C. Lei. Scaling and direct stability analyses of natural convection induced by absorption of solar radiation in a parallelepiped cavity. *International Journal of Thermal Sciences*, 88:19–32, 2015. ISSN 1290-0729.

[93] R. W. Walden and G. Ahlers. Non-boussinesq and penetrative convection in a cylindrical cell. *Journal of Fluid Mechanics*, 109:89–114, 1981.

[94] M. Moroni and A. Cenedese. Penetrative convection in stratified fluids: velocity and temperature measurements. *Nonlinear processes in Geophysics*, 13(3):353–363, 2006.

[95] R. Krishnamurti. Convection induced by selective absorption of radiation: A laboratory model of conditional instability. *Dynamics of Atmosphere and Oceans*, 27(3-5), 1997.

[96] A. A. Hill. Penetrative convection induced by the absorption of radiation with a nonlinear internal heat source. *Dynamics of Atmosphere and Oceans*, 38(3-5): 57–67, 2004.

[97] A. J. Harfash. Three dimensional simulation of radiation induced convection. *Applied Mathematics and Computation*, 227:92–101, 2014. ISSN 0096-3003. doi: http://dx.doi.org/10.1016/j.amc.2013.11.007. URL http://www.sciencedirect.com/science/article/pii/S0096300313011673.

[98] A. J. Harfash. Three dimensional simulations and stability analysis for convection induced by absorption of radiation. *International Journal of Numerical Methods for Heat and Fluid Flow*, 25(4):810–824, 2015. ISSN 0961-5539.

[99] S.O. Onyegegbu. Solar radiation induced natural convection in stagnant water layers. *Energy Conversion and Management*, 30(2):91–100, 1990. ISSN 0196-8904. doi: 10.1016/0196-8904(90)90018-T. Cited References Count:0—DK239—PERGAMON-ELSEVIER SCIENCE LTD—THE BOULEVARD, LANGFORD LANE, KIDLINGTON, OXFORD, ENGLAND OX5 1GB—ONYEGEGBU, SO—ISI Document Delivery No.:DK239.

[100] D. E. Farrow and J. C. Patterson. On the stability of the near shore waters of a lake when subject to solar heating. *International journal of heat and mass transfer*, 36(1):89–100, 1993. ISSN 0017-9310.

[101] Y. G. Verevochkin and S. A. Startsev. Numerical simulation of convection and heat transfer in water absorbing solar radiation. *Journal of Fluid Mechanics*, 421: 293–305, 2000. ISSN 1469-7645.

[102] H. Salmun. Convection patterns in a triangular domain. *International Journal of Heat and Mass Transfer*, 38(2):351–362, 1995.

[103] M. J. Coates and J. C. Patterson. Numerical simulations of the natural convection in a cavity with nonuniform internal sources. *International journal of heat and fluid flow*, 15(3):218–225, 1994.

[104] M. J. Coates and J. C. Patterson. Unsteady natural convection in a cavity with non-uniform absorption of radiation. *Journal of Fluid Mechanics*, 256:133–161, 1993.

[105] H. Cui, F. Xu, and S. C. Saha. A three-dimensional simulation of transient natural convection in a triangular cavity. *International Journal of Heat and Mass Transfer*, 85:1012 – 1022, 2015. ISSN 0017-9310. doi: http://dx.doi.org/10.1016/j.ijheatmasstransfer.2015.02.055. URL http://www.sciencedirect.com/science/article/pii/S0017931015002185.

[106] Joel H Ferziger and Milovan Peric. *Computational methods for fluid dynamics*. Springer Science & Business Media, 2012.

[107] Rainald Löhner. *Applied computational fluid dynamics techniques: an introduction based on finite element methods*. John Wiley & Sons, 2008.

[108] Perez. *Unsteady laminar convection in cylindrical domains: numerical studies and application to solar water storage tanks*. Universitat Politècnica de Catalunya, 2007.

[109] S. Ievers and W. Lin. Numerical simulation of three-dimensional flow dynamics in a hot water storage tank. *Applied Energy*, 86(12):2604–2614, 2009.

[110] Y. M. Han, R. Z. Wang, and Y. J. Dai. Thermal stratification within the water tank. *Renewable and Sustainable Energy Reviews*, 13(5):1014–1026, 2009.

[111] M. Y. Haller, E. Yazdanshenas, E. Andersen, C. Bales, W. Streicher, and S. Furbo. A method to determine stratification efficiency of thermal energy storage processes independently from storage heat losses. *Solar Energy*, 84(6):997–1007, 2010. ISSN 0038-092X.

[112] J. H. Davidson, D. A. Adams, and J. A. Miller. A coefficient to characterize mixing in solar water storage tanks. *Journal of Solar Energy Engineering*, 116(2):94–99, 1994. ISSN 0199-6231.

[113] G. G. Ilis, M. Mobedi, and B. Sunden. Effect of aspect ratio on entropy generation in a rectangular cavity with differentially heated vertical walls. *International Communications in Heat and Mass Transfer*, 35(6):696–703, 2008. ISSN 0735-1933.

[114] M. Magherbi, H. Abbassi, and A. Ben Brahim. Entropy generation at the onset of natural convection. *International journal of Heat and Mass transfer*, 46(18): 3441–3450, 2003. ISSN 0017-9310.

[115] H. F. Oztop and K. Al-Salem. A review on entropy generation in natural and mixed convection heat transfer for energy systems. *Renewable and Sustainable Energy Reviews*, 16(1):911–920, 2012.

[116] T. Basak, A. K. Singh, and R. Anandalakshmi. Analysis of entropy generation during conjugate natural convection within a square cavity with various location of wall thickness. *Industrial and Engineering Chemistry Research*, 53(9):3702–3722, 2014. ISSN 0888-5885.

[117] V. Khullar, H. Tyagi, N. Hordy, T. P. Otanicar, Y. Hewakuruppu, P. Modi, and R. A Taylor. Harvesting solar thermal energy through nanofluid-based volumetric absorption systems. *International Journal of Heat and Mass Transfer*, 77:377–384, 2014. ISSN 0017-9310.

[118] S. Chandrasekhar. *Hydrodynamic and hydromagnetic stability*, volume 196. Clarendon Press Oxford, 1970.

[119] N. M. Ozisik. *Boundary value problems of heat conduction*. International Textbook Company, 1968.

[120] COMSOL user's guide. Introduction to comsol multiphysics, 2010.

[121] P. J. Roache. Quantification of uncertainty in computational fluid dynamics. *Annual Review of Fluid Mechanics*, 29(1):123–160, 1997. ISSN 0066-4189.

[122] Procedure for estimation and reporting of uncertainty due to discretization in cfd.

[123] C. J. Roy and W. L. Oberkampf. A comprehensive framework for verification, validation, and uncertainty quantification in scientific computing. *Computer Methods in Applied Mechanics and Engineering*, 200(25–28):2131–2144, 2011. ISSN 0045-7825. doi: http://dx.doi.org/10.1016/j.cma.2011.03.016. URL http://www.sciencedirect.com/science/article/pii/S0045782511001290.

[124] F. Stern, R. V. Wilson, H. W. Coleman, and E. G. Paterson. Comprehensive approach to verification and validation of cfd simulations—part 1: methodology and procedures. *Journal of fluids engineering*, 123(4):793–802, 2001.

[125] W. L. Oberkampf, T. G. Trucano, and C. Hirsch. Verification, validation, and predictive capability in computational engineering and physics. *Applied Mechanics Reviews*, 57(5):345–384, 2004.

[126] J. T. Beard, L. U. Lilleleht, F. L. Huckstep, W. B. May, and F. A. Iachetta. Design and operational influences on thermal performance of "solaris" solar collector. *Journal for Engineering for Power*, 100(4):497–502, 1978. ISSN 0742-4795.

[127] R. S. Kaluri, S. Dattarajan, and S. Ganapathisubbu. Numerical simulations of direct absorption of solar radiation by a liquid, 2012.

[128] A. Cramer, S. Landgraf, E. Beyer, and G. Gerbeth. Marangoni convection in molten salts. *Experiments in Fluids*, 50(2):479–490, 2011. ISSN 0723-4864. doi: 10.1007/s00348-010-0951-8. URL http://dx.doi.org/10.1007/s00348-010-0951-8.

[129] MATLAB. *User's Guide (R2013a)*. The MathWorks Inc., Natick, Massachusetts, 2013.

[130] F. X. Trias, M. Soria, A. Oliva, and C. D. Pérez-Segarra. Direct numerical simulations of two-and three-dimensional turbulent natural convection flows in a differentially heated cavity of aspect ratio 4. *Journal of Fluid Mechanics*, 586:259–293, 2007.

[131] M. Soria, F. X. Trias, C. D. Pérez-Segarra, and A. Oliva. Direct numerical simulation of a three-dimensional natural-convection flow in a differentially heated cavity of aspect ratio 4. *Numerical Heat Transfer, Part A: Applications*, 45(7):649–673, 2004.

[132] B. Zamora and A.S. Kaiser. 3d effects in numerical simulations of convective flows in cubical open cavities. *International Journal of Thermal Sciences*, 77: 172 – 185, 2014. ISSN 1290-0729. doi: http://dx.doi.org/10.1016/j.ijthermalsci.2013.11.004. URL http://www.sciencedirect.com/science/article/pii/S129007291300272X.

[133] Shelton CT USA) PerkinElmer, Inc. Perkinelmer lambda 1050 uv/vis/nir spectrometer (perkinelmer, inc., shelton, ct, usa).

[134] J. S. Bendat and A. G. Piersol. *Random data: analysis and measurement procedures*, volume 729. John Wiley & Sons, 2011.

[135] A. H. Abib and Y. Jaluria. Penetrative convection in a partially open enclosure. *ASME-PUBLICATIONS-HTD*, 198:73–73, 1992.

[136] R. Delgado-Buscalioni and E. C. del Arco. Flow and heat transfer regimes in inclined differentially heated cavities. *International Journal of heat and mass transfer*, 44(10):1947–1962, 2001. ISSN 0017-9310.

[137] F. J. Hamady, J. R. Lloyd, H. Q. Yang, and K. T. Yang. Study of local natural convection heat transfer in an inclined enclosure. *International Journal of Heat and Mass Transfer*, 32(9):1697–1708, 1989. ISSN 0017-9310.

[138] O. Hiroyuki, Y. Kazumitsu, S. Hayatoshi, and S. W Churchill. Natural circulation in an inclined rectangular channel heated on one side and cooled on the opposing side. *International Journal of Heat and Mass Transfer*, 17(10):1209–1217, 1974. ISSN 0017-9310.

[139] H. Ozoe, H. Sayama, and S. W. Churchill. Natural convection in an inclined rectangular channel at various aspect ratios and angles—experimental measurements. *International Journal of Heat and Mass Transfer*, 18(12):1425–1431, 1975. ISSN 0017-9310.

[140] J. Rasoul and P. Prinos. Natural convection in an inclined enclosure. *International Journal of Numerical Methods for Heat and Fluid Flow*, 7(5):438–478, 1997. ISSN 0961-5539.

[141] V. Kurian, M. N Varma, and A. Kannan. Numerical studies on laminar natural convection inside inclined cylinders of unity aspect ratio. *International Journal of Heat and Mass Transfer*, 52(3):822–838, 2009. ISSN 0017-9310.

[142] S. W. Armfield, N. Williamson, W. Lin, and M. P. Kirkpatrick. Nusselt number scaling in an inclined differentially heated square cavity. 2014.

[143] H. Dou and C. Jiang, G.and Lei. Numerical simulation and stability study of natural convection in an inclined rectangular cavity. *Mathematical Problems in Engineering*, 2013, 2013. ISSN 1024-123X.

[144] J. Bracamonte, J. Parada, J. Dimas, and M. Baritto. Effect of the collector tilt angle on thermal efficiency and stratification of passive water in glass evacuated tube solar water heater. *Applied Energy*, 155:648–659, 2015.

[145] W. Ye, D. Zhu, and N. Wang. Effect of the inclination angles on thermal energy storage in a quadrantal cavity. *Journal of thermal analysis and calorimetry*, 110 (3):1487–1492, 2011.